RECYCLING OF FOUNDRY WASTE MATERIALS

by

YIRAN XIE

A thesis submitted to

The University of Birmingham

for the degree of

DOCTOR OF PHILOSOPHY

School of Chemical Engineering

University of Birmingham

January 2016

ABSTRACT

The recycling of a foundry ceramic waste from investment casting has been investigated. The waste was reduced in size by fly pressing and disc milling to d_{50} < 20 μm and cleaned by magnetic separation and acid leaching. The powder contained zircon, alumina and amorphous silica with 37, 38 and 24 wt. % ($ZrSiO_4$: Al_2O_3: SiO_2) respectively. Two products were targeted: zirconia toughened mullite (ZTM) ceramics produced with an addition of alumina and zircon based pigments developed by the removal of alumina and reaction with colourant ions.

With an addition of 23.5 wt. % Al_2O_3, a ZTM containing 30 wt. % zirconia and 70 wt. % mullite exhibiting strength, hardness, thermal shock resistance and toughness commensurate with data reported in the literature were developed. Milling in isopropanol, dry pressing and sintering at 1600 ℃ for two hours optimised the properties. The transition to ZTM appeared to be through an intermediate glassy phase and limited by the dissociation of $ZrSiO_4$. It was estimated that 70 % of the ZrO_2 was transformable tetragonal without the addition of Y_2O_3. With Y_2O_3 non-transformable tetragonal ZrO_2 was produced.

It was shown that a clean zircon powder free of Al_2O_3 was generated by reaction with $K_2S_2O_7$. Dissociation-synthesis and direct-synthesis routes were used to produce pigment. It was found that higher reaction temperature and the introduction of flux can significantly increase yellowness. The yellow produced from waste materials performed as well as those from commercial grade feeds.

ACKNOWLEDGEMENTS

I wish to express my sincere gratitude to Professor Stuart Blackburn for his constructive suggestions, valuable ideas, great patience, encouragement and endless help. I would also like to thank Professor Neil Rowson for his advice and the use of his equipment.

Special thanks should also be expressed to 'Ceramic Processing Group' for their endless assistance. Acknowledgement is also given to the Department of Metallurgy and Materials for the provision of facilities.

I am also sincerely grateful to my family, my friends and my group mates. Without their timely and cordial help this thesis would have been impossible.

TABLE OF CONTENTS

LIST OF FIGURES

LIST OF TABLES

LIST OF ABBREVIATIONS

Abbreviation	Definition
ZTM	Zirconia Toughened Mullite
SPS	Solid Phase Synthesis
DS	Dissociation Synthesis
PDZ	Plasma Dissociated Zircon
PSD	Particle Size Distribution
XRF	X-ray Fluorescence
XRD	X-Ray Diffraction
SEM	Scanning Electron Microscopy
EDS	Energy Dispersive X-ray Spectroscopy
B3B	Ball-on-3-Ball
DSC	Differential Scanning Calorimetry
BSE	Back Scattered Electrons
SE	Secondary Electrons
RGB	Red Green Blue
CW	Ceramic Waste
AWP	Attrition Milling in Water Powder
BIP	Ball Milling in Isopropanol Powder
PVB	Polyvinyl Butyral
DBP	Dibutyl Phthalate

CHAPTER I INTRODUCTION

The foundry industry is economically important. From 2004, the output of the industry has grown continuously at 2.4 % per annum (1). With this growth in output, the amount of the waste materials generated has also increased. But, presently most foundry waste refractories are sent to land fill or used in road aggregates. This situation not only has an associated financial cost, but may also harm the environment in the long term (2). Methods of recycling foundry waste streams may alleviate this situation.

Refractory materials have commonly been considered as a potential recycling target products for the solid ceramic waste streams being emitted from foundries (3). Zirconia toughened mullite (ZTM) has drawn attention since it was first patented in high temperature refractory industry in 1964. ZTM ceramic composites have excellent refractoriness, thermal shock resistance, low thermal expansion behaviour, good fracture strength and toughness, strong creep resistance and chemical stability (4). Different production routes for the manufacture of ZTM have been developed, of these the $ZrSiO_4$ and Al_2O_3 high temperature solid phase reaction sintering method is the most widely used and researched (5). Compaction and extrusion techniques are commonly used for shaping ceramic materials into desire shapes. ZTM bricks, tubes and rolls are widely used in metallurgy, glass and construction industries (4).

Zircon ($ZrSiO_4$) based pigments are the only pigments that can generate three primary colours (red, yellow and blue) with the same base material (6). This means

any colour can be produced by proportionally mixing the red, blue and yellow pigments which make zircon based pigments attractive to the industry. The most common example of its application is the colourful patterns on tableware and tiles. High temperature solid state reaction is the normal method to introduce colourant ions into the zircon structure to develop colours.

1.1 Project Aims and Objectives

This study aims to utilise the foundry ceramic waste materials by developing them into commercially viable products. A local foundry plant generates tons of ceramic wastes each month and all go to land fill. Currently, there are no sophisticated techniques that can be used to recycle these materials. By developing a universally applicable approach to convert the foundry waste materials into useful products can not only reduce the financial cost, but also benefit the environment in the long term.

Different analytical methods are used in order to identify the composition of the ceramic waste materials. Based on the composition, ZTM refractories and zircon based coloured pigments are selected as the target products for this study.

For the purpose of finding a scalable process to convert waste solids to powders, different ceramic solid processing techniques are investigated. Various ceramic powder shaping methods are used for manufacturing products in desired shape. High temperature solid state reaction sintering behaviour and thermal, mechanical, structural properties of the finished products are compared in order to optimise the fabrication procedures.

1.2 Thesis Layout

This thesis starts with a literature review which initially looks into the current situation of the foundry industry and investment casting process. The properties, synthesis methods and microstructures of the zirconia toughened mullite are described with the focus on the influencing factors during the reaction sintering process. Section 2.3 introduced two types of zircon based pigments with their properties, production approaches and formation mechanisms described. The review can allow for a better understanding of these two different forms of target products. This allows feasible routes to convert the ceramic waste materials into useable products to be explored. In order to do so, the ceramic solid processing techniques including crushing, various types of milling, magnetic separation, acid leaching were reviewed followed by ceramic shaping techniques which include dry compaction and paste extrusion.

Chapter 3 describes the analytical methods that were used to characterise the materials by focusing on their principles, experimental instrumentation and testing details. The raw ceramic waste materials used in this study are also described and analysed with an emphasis on their composition and morphology.

A detailed description of how the ceramic waste solid components were converted to fine clean powders through a series of treatments using different processing techniques is given in Chapter 4. Crystal phase analysis results for the treated powder are also discussed in this chapter.

Chapter 5 and 6 focused on the development and characterisation of refractory products. The powder formulation is given in Section 5.2.1 followed by a further description of the processing steps required to prepare mixture powder blend suitable for use in the selected shaping processes. Details of dry compaction and extrusion routes are described. The reaction sintering conditions are also discussed in Chapter 5. Details of the 8 representative samples which were chosen from the 36 developed materials are describe in Section 6.2 followed by a comprehensive analysis of the ZTM samples. The different properties of the samples are compared and discussed.

The production method of the zircon based yellow pigments is given in Chapter 7. A visual exhibition of different shades of yellow colour pellets is provided by using digital correction. The quantification method for the yellowness of the samples is also discussed in this chapter.

The main conclusions and possible future work are discussed in Chapter 8.

CHAPTER II LITERATURE REVIEW

This chapter begins by introducing the investment casting process which generated the foundry waste which forms the feedstock to this investigation. The known constituents of the waste allow it to be considered as a source of raw material for the manufacture of zirconia toughened mullite refractories and as a source of zircon for the manufacture of coloured pigments. Thus a description of zirconia toughened mullite composite material and zircon based pigments follows. A range of ceramic processing techniques that might be used to manufacture these materials are also reviewed.

2.1 Foundry Waste and Investment Casting

2.1.1 Current Situation of Foundry Waste

A foundry is a factory that produces metal castings. The foundry industry is high energy consuming and is known to cause pollution as a result. The energy consumed by the foundry industry is estimated to take up 25 % - 30 % of the total energy consumption of all manufacturing industries (7). The most concerned pollutants generated from the process are solid and volatile wastes. According to statistics, the total amounts of pollutant emission are: dust emission 5.5×10^{6} tons, airborne emission 2.25×10^{11} m^3, sand waste 1.25×10^{9} tons, and waste residue 3.25×10^{7} tons (8).

There are different approaches to deal with foundry waste including minimizing waste generation, reusing waste materials, and converting waste materials into

commercially viable products (9). Even so, large amounts of foundry waste are still being produced every year which has led to large expenditure including various government administration fees, local administration fees, expenses to prevent environmental hazards and expenses on transportation (2). New environmental laws and regulations make the expenses of waste disposal even higher each year (2). About 2 % to 9 % of the manufacturing cost is typically spent on waste disposal in the foundry industry (7).

A survey conducted in the USA has listed the ten foundry waste streams of most concerned which are: sand system wastes, mould and pouring emissions, melt furnace emissions, shake-out emissions, storm water runoff, unfired core waste, core room emissions, cleaning room dust, shot blast dust and emission control water (10). It can be seen that waste sand disposal is the primary concern of most manufacturers. Of course these statements relate to foundry activity in general and the waste streams of individual foundries will vary depending on the specific activities being undertaken.

The main hazards generated by foundry sands are dust pollution, chemical pollution, soil desertification and land occupation (10). The large amount of fine particles may cause air pollution. Once the foundry waste sand goes to landfill, the toxic organic contents may cause long term pollution to soil and water.

There are mainly three approaches to recover foundry waste sands: thermal method, attrition method and wet method (11). However, all these methods have issues of their own (Table 2.1).

Table 2.1 Foundry sand recovery methods (11)

Methods	Equipment	Issues
Thermal method	Furnace	High energy consumption
Attrition method	Attrition mill; Crusher	Low recycling efficiency
Wet method	Water wash	Large space occupation; Secondary pollution; High invest costs

For small scale foundry operations, there are many obstacles for reusing the sands, including the large size of equipment, and limited budget available for the reutilization (8).

Other efforts are also being made to recycling the foundry waste sands. Different approaches have been discovered to turn the sands into other marketable resources, such as cement, asphalt, concrete and construction materials (12).

The above discussion is based on an all industry review and focuses on the large volume issues of foundry sand. In this thesis the concept of reuse of the foundry refractory waste is narrowed to the more specialist field of investment casting where the moulds are sintered ceramics rather than bonded sand.

2.1.2 Investment Casting Process

Investment casting is also known as lost wax casting which is the oldest casting technique that can dated back to 5000 years ago (13). The advantage of investment casting is the ability to cast complicated structural components with high accuracy and smooth surface finishes. This can significantly reduce the usage of metallic materials (14). A typical investment casting process is shown in Figure 2.1.

The process can be generally divided into 8 steps (14):

Step 1: Wax patterns are produced from the master pattern of the target products. The pattern can be made from other materials such as plastic, but wax is more widely applied due to its low melting point and its potential of reutilization. The size of the mould needed for producing wax patterns needs to be carefully calculated, taking into consideration the shrinkage of the materials used in the following steps. It may take multiple trials to decide the proper size, resulting in a high cost for the mould.

Step 2: The wax patterns are attached to a bar, which serves as a sprue, with a pouring cup on one end to create a ‘pattern tree’ or ‘cluster’.

Step 3: The pattern tree is dipped into refractory slurry which consists of ceramic powder, water and binder to obtain several ceramic layers on the surface of the pattern tree and then passed to step 4. The process is repeated to reach the desired thickness of the ceramic pattern.

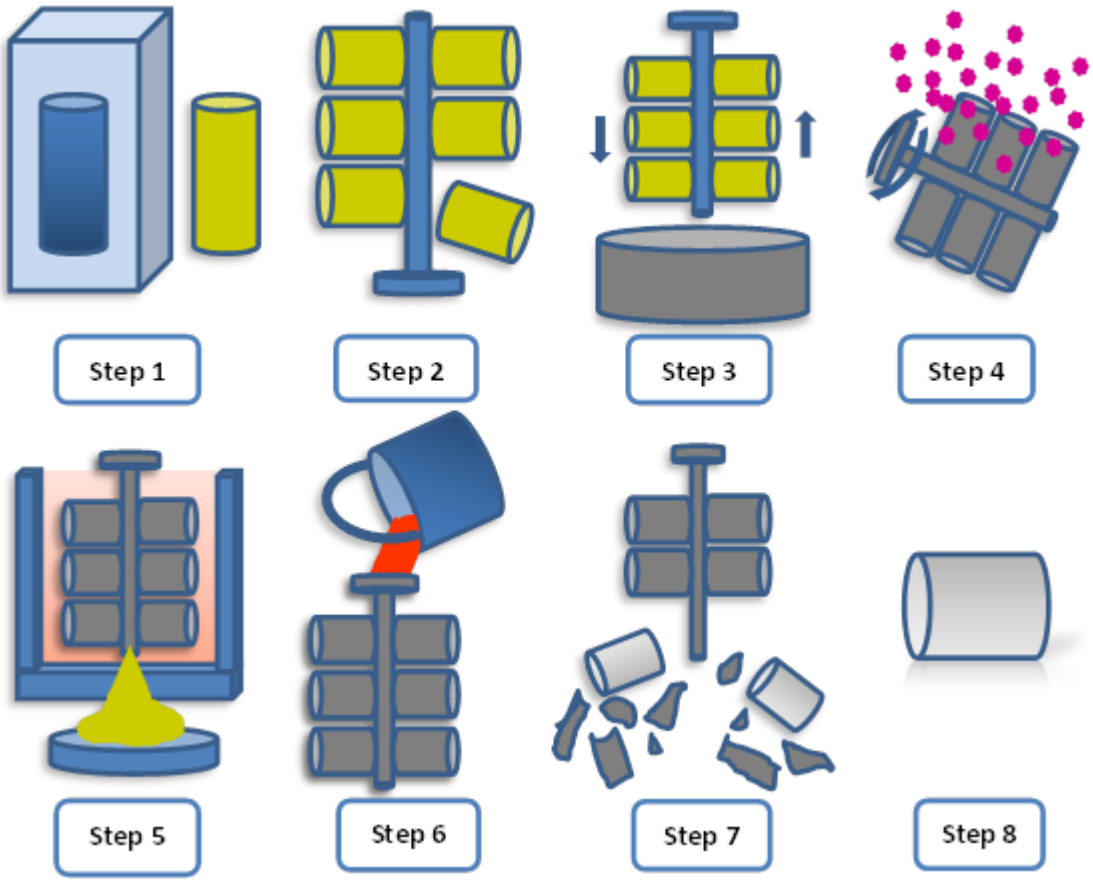

Figure 2.1 Schematic diagram of investment casting process; Modified from (14)

Step 4： The cluster once coated with slurry is stuccoed by placing it in a rainfall of fluidised bed-sander, to cover it with coarse ceramic particles. This step also needs to be repeated until the shell is sufficiently thick.

Step 5： The cluster is placed into a furnace to melt the wax out and also sinter the ceramic shell to create the mould for casting. This step is where most shell failure occurs due to the difference of thermal expansion rate between the wax and the shell materials.

Step 6： The molten metal is poured into the ceramic shell and allowed to cool down to solidify the metal casting.

Step 7：The ceramic shell is destroyed to release the metal casting using methods which included vibration or water jets.

Step 8：The procedure is finished by operations such as polishing, grinding or sand blasting to create the final products which are smooth and identical to the original pattern.

During this process, a large number of low fired ceramic shell wastes and post casting ceramic shell wastes are generated in steps 5 and 7, respectively. Most of these materials are currently land filled but offer potential for recycle or recovery (3).

The composition of the shells produced will vary depending on the metal being cast. One common form however is a combination of silica, alumina and zircon with other additives (15). Shells of this basic formulation are common when processing higher temperature alloys including steel and nickel alloys for the medical and the aerospace industries. The constituents of these materials are used in other areas of refractory manufacture and in the production of coloured minerals and the possibility of conversion to useful materials rather than going to land fill should be considered.

2.2 Zirconia Toughened Mullite

2.2.1 Mullite, Zirconia and Zirconia Toughened Mullite

The term refractory is used to describe the materials which have physical and chemical properties which allow them to be used in high temperature environments

(normally over 1580 ℃) (16). Most refractories are inorganic non-metal materials which have applications in metallurgy, chemical engineering, petroleum and manufacturing industries. 50 % to 60 % of refractories are used in the metallurgy industry (17).

Zirconia refractories are widely used due to their excellent properties including high melting temperature, high corrosion resistance, good thermal shock resistance and high chemical stability. Zirconia provides long term usage in oxidizing atmospheres at high temperature (typically 1500 ℃ to 2200 ℃) (18).

Composites containing zirconia and other oxides may also have high melting temperatures (Table 2.2) (19). However, due to the high cost of zirconia, zircon is widely used to produce a eutectic mixture (Table 2.3) (20).

ZrO_2 phase transformation helps to improve fracture toughness and strength of ceramic composites if the conditions are favourable (19). By adding ZrO_2 into materials such as mullite, Si_3N_4, SiC, their toughness can be increased significantly and this technology has been applied in the refractory manufacturing processes to improve thermal stability.

Mullite ($3Al_2O_3 \cdot 2SiO_2$) has low thermal expansion coefficient, strong creep resistance and good chemical stability which make it very suitable for high temperature application (4). However, as an engineering material, it has relatively low strength and toughness at room temperature which limits its application. When using the traditional method of sintering Al_2O_3 and SiO_2, the mullite grains enlarge massively as temperature increases, leading to decreased strength and toughness (21).

Although the low elastic modulus and thermal expansion coefficient that theoretically grant mullite good thermal shock resistance, the anisotropy of large mullite clusters under thermal expansion results in cracks when the temperature drops suddenly (22). Therefore, fine particle size and impediment of grain growth can improve the formation of mullite with good mechanical properties (23).

Table 2.2 Zirconia-oxide composites

Oxides	Molecular formula	Melting temperature (℃)
BaO	$BaO{\cdot}ZrO_2$	2620
CaO	$CaO{\cdot}ZrO_2$	2350
MgO	$MgO{\cdot}ZrO_2$	2150
Al_2O_3	$ZrO_2{\cdot}Al_2O_3$	1885

Table 2.3 Zirconia-oxides eutectic mixtures

Oxides	Molecular formula	Temperature to form eutectic mixture (℃)
MgO	$MgO{\cdot}ZrO_2{\cdot}SiO_2$	~1793
Al_2O_3	$Al_2O_3{\cdot}ZrO_2{\cdot}SiO_2$	~1675
CaO	$CaO{\cdot}ZrO_2{\cdot}SiO_2$	~1582
BaO	$BaO{\cdot}ZrO_2{\cdot}SiO_2$	~1573
Na_2O	$Na_2O{\cdot}ZrO_2{\cdot}SiO_2$	~1793

Additives can improve the properties of mullite composites by reducing the propagation of cracks. For instance, by adding ZrO_2, the thermal shock resistance, corrosion resistance, mechanical strength and toughness of mullite are effectively improved. Zirconia mullite can be formed in various chemical compositions, in which the content of ZrO_2 can range from 7 % to 40 % (4). K. Hemra and P. Aungkavattana suggest that 30 % ZrO_2 and 70 % mullite gives the best properties (24). In this composite, spherical zirconia particles homogeneously distributed in the acicular mullite matrix were observed.

2.2.2 Zirconia Toughened Mullite Synthesis Methods

There are three methods commonly reported to produce zirconia toughened mullite (ZTM) composites. Each method gives a different microstructure and thus results in different properties.

Prochazka et al. first reported in 1983 that a zirconia toughened mullite composite was synthesised by directly sintering a fused mullite and zirconia fine powder mixture (25). The ZrO_2 phase could significantly densify the structure and retarded the mullite grain growth. Thus a densified mullite matrix with intergranular ZrO_2 was formed.

Zanelli et al. used Al_2O_3, SiO_2 and ZrO_2 powder mixture to produce zirconia toughened mullite (26). Mullite, corundum and zirconia polymorphs were identified in the sintered products. The Al_2O_3/SiO_2 ratio significantly affected the properties of the fired samples. One third of the zirconia was dissolved in a glass phase during the reaction process.

$ZrSiO_4$ and Al_2O_3 reaction sintering is the most common method to produce zirconia toughened mullite. In 1964, Kordyuk and Gullko produced ZTM by using alumina and natural zircon and indicated that the reaction (Equation 2.1) started at 1397 ℃, and reacted intensively at 1447 ℃ (4). However, as the toughening effect of ZrO_2 had not yet been discovered at that time, this reaction was only taken as a study on the phase equilibrium of the ZrO_2/ Al_2O_3/ SiO_2 system.

$$2ZrSiO_4 + 3Al_2O_3 \rightarrow 2ZrO_2 + 3Al_2O_3 \cdot 2SiO_2 \qquad (2.1)$$

Rupo et al. conducted research on the densification behaviour of $ZrSiO_4$ and Al_2O_3 system (27). Phase change and reaction kinetics of the solid phase reaction were also studied. Particle rearrangement and particle reshaping were found as two main factors that affect the sintering process.

Claussen and Jahn applied special sintering techniques which separated the sintering process and reaction process (28). Mullite zirconia composites from the solid phase reaction between $ZrSiO_4$ and Al_2O_3 were produced with a flexural strength of 269 MPa and toughness of 4.5 $MPam^{1/2}$.

2.2.3 Description of Reaction Sintering Process

To study the reaction sintering process, the most common method used is X-ray diffraction to identify the temperatures of zircon dissociation and mullite formation. Equation 2.2, 2.3 and 2.4 are usually applied to quantitatively describe the extent of this reaction in order to achieve a better illustration of the phase transition and reaction process (29, 30).

$$X_1 = \frac{I[m - ZrO_2(111)] + I[t - ZrO_2(111)]}{I[m - ZrO_2(111)] + I[t - ZrO_2(111)] + I[ZrSO_4(200)]} \quad (2.2)$$

$$X_2 = \frac{I[mullite(210)]}{I[mullite(210)] + I[ZrSiO_4(200)]} \quad (2.3)$$

$$X_3 = \frac{I[mullite(210)]}{I[mullite(210)] + I[Al_2O_3(113)]} \quad (2.4)$$

where I indicates the intensity of X-ray diffraction peek; m and t indicate monoclinic and tetragonal respectively. The values of X_1, X_2 and X_3 are 0 in the unreacted state. The value of X_1 and X_2 are 1 when reaction is complete. If the generated amorphous SiO_2 reacts immediately with Al_2O_3, the expected changing rate of X_1 and X_2 are the same. If there is time delay in the mullite generating reaction, the rate of change of X_2 should be lower than that of X_1 during the whole process of reaction. X_3 represents the extent of mullite formation after $ZrSiO_4$ dissociates.

2.2.4 Influencing Factors of Reaction Sintering Process

2.2.4.1. Impact of Raw Materials and Al_2O_3/SiO_2 Ratio

Boch and Giry (31) used three different types of $ZrSiO_4$: stoichiometric $ZrSiO_4$, SiO_2 enriched $ZrSiO_4$ and ZrO_2 enriched $ZrSiO_4$. They demonstrated that the composition of $ZrSiO_4$ influences the densification and the reaction process. Additionally, the particle size of $ZrSiO_4$ also influences its dissociation temperature.

Zircon influences the reaction sintering process after its dissociation, for example the content of SiO_2 and its surface conditions, while the impact of Al_2O_3 is mainly determined by its own properties. Tiwari et al. conducted research on this by using

three different types of aluminium precursor: crystalline Al_2O_3, amorphous Al_2O_3 and γ-AlOOH (32). They demonstrated that $ZrSiO_4$ dissociates between 1400 ℃ and 1450 ℃ in the samples containing crystalline Al_2O_3, while in the other two samples $ZrSiO_4$ dissociates before reaching 1350 ℃.

Research conducted by Koyama et al. proved that the particle size of crystalline Al_2O_3 can affect the reaction rate and densification (33). Al_2O_3 powders with a mean particle sizes of 0.38 μm and 0.45μm were used in their work. Mullite was completely formed at lower temperature by using the finer alumina powder. The results also showed that higher density products can be produced by reducing the particle size of the raw materials.

2.2.4.2 Impact of Additives on the Reaction Sintering

Liquid phase additives allow $ZrSiO_4$ to dissociate at relatively low temperature. The reaction and densification process can occur simultaneously and be completed in a shorter period. However, the liquid additives tend to cause agglomeration which results in poor material performance (34). In comparison, solid phase additives can improve the microstructure without introducing unwanted phases.

There are three commonly used additives: CaO, MgO, and TiO_2 represented by X in Equation 2.5 below:

$$3Al_2O_3 + 2ZrSiO_4 + X \rightarrow 3Al_2O_3 \cdot 2SiO_2 + 2ZrO_2 + \text{extra phase} \qquad (2.5)$$

Miranzo et al. conducted a systematic research on the impact of solid additives on reaction sintering (35). They claimed that solid additives can improve the densification due to the formation of an intermediate liquid phase.

2.2.5 Microstructure of Zirconia Toughened Mullite

Several researchers demonstrated that relatively larger mullite grains can be developed by using the zircon and alumina reaction sintering method (30, 36, 37). The solid additives can lead to even larger mullite grains with both spherical intragranular and intergranular ZrO_2.

On the other hand, no intragranular zirconia can be found in mullite and zirconia direct sintering method (18). The mullite grains are relatively small in this type of ZTM. These differences were possibly caused by the appearance of amorphous mullite during the sintering process.

The presence of intragranular ZrO_2 is the most distinctive characteristic of the microstructure developed from $ZrSiO_4$ and Al_2O_3 reaction sintering route. Intragranular zirconia can also be found in ZTM produced by sintering Al_2O_3, SiO_2 and ZrO_2. The intragranular ZrO_2 tends to remain tetragonal instead of transforming to monoclinic ZrO_2 at room temperature (38).

2.2.6 New Development on Reaction Sintering Technique

Lathabai et al. combined the Reaction Bonded Aluminium Oxidation (RBAO) technique with the reaction sintering technique to prepare ZTM composites by using the Al / Al_2O_3 / $ZrSiO_4$ system (39). The green body was sintered for 2 hours at

1550 ℃, and the product had 95 % relative density and 8 % linear shrinkage due to the oxidation of the aluminum.

2.3 Zircon Based Pigments

2.3.1 Introduction of Ceramic Pigments

The research and development of ceramic pigments has a long history. In the mid-19th century, synthetic ceramic colours appeared for the first time due to the development of science and technologies such as chemistry and chemical engineering (40). The emergence of the new types of pigments occurred at the time when crystal chemistry was flourishing as a new discipline, which played an important part in the theoretical development of ceramic pigments research.

Traditional ceramic pigments generally comprised of metallic oxides, sulphides, sulphates, phosphates, silicates, aluminates, chromates, and natural minerals, which do not meet the requirements for ceramic decoration (6). The required properties include covering capacity, glossiness, light resistance, heat resistance and resistance to solvent. With more practical applications of crystal chemistry and deeper understanding of ion-exchange and catalysts, the colour range of ceramic pigments has been extended. After World War II, a series of new ceramic pigments were developed from transition metal compounds and rare earth compounds (41).

2.3.2 Properties and Categorisation of Zircon Based Pigments

Zircon based pigments has rapidly developed due to their excellent performance, which includes high corrosion resistance and heat resistance (42). They also have very good tinctorial power (staining properties) and stability.

The required amount of zircon based pigments in the glaze, which is 3 to 6 wt. %, is lower than the equivalent spinel pigments, but with better colour rendering (43). Additionally, Zircon based colours are not sensitive to other materials in the glaze, thus remain bright and vivid.

Table 2.4 Lattice type zircon pigments

Transition element	**Colour**	**Rare earth element**	**Colour**
V	Light turquoise	Pr	Yellow
V, P	Bright purple	Pr, Mg	Orange red
V, Mn	Navy blue	Pr, Mo	Yellow
Cr	Prasinous	Nd	Light purple
Cr, Co, Ca	Light purple	Tb	Yellow
Mn	Grey, Pink	Ce	Ivory yellow
Co	Bluish green	Ce, Pr	Orange
Ni	Yellow green	Ce, Pr, Mg	Orange red
Ni, Co	Grey	Ce, Nd	Bluish violet
Cu	Light turquoise	Ce, Tb	Yellow
		Ce, Er	Pink

With the same zircon basis, the blue, yellow and pink pigments have good miscibility which can generate a wide range of different colours by mixing. At present, zircon based pigments are the only pigments that can generate the three primary colours (red, yellow, blue) with same base material (6).

Zircon based pigments can be classified into two types based on their crystal structures and phase contents.

Lattice type pigment indicates the colour ions are dissolved in the $ZrSiO_4$ lattice to exhibit colours, such as zircon vanadium blue and zircon praseodymium yellow. A list of common lattice type zircon pigments are shown in Table 2.4 (44).

Table 2.5 Encapsulated type zircon pigments

Encapsulated	**Colour**	**Encapsulated**	**Colour**
Fe_2O_3	Coral	V2S	Grey
CdS	Yellow	(Co, Zn)Al_2O_3	Blue
Cd(S, Se)	Red	TiO2-$NiSbO_4$	Yellow
(Cs, Hg), (S, Se)	Orange	$PbCrO_4$	Yellow
(Cd, Zn)S	Yellow	Cu	Green
Cd(S, Te)	Light red	Au	Bluish violet
PbS	Grey	Ag	Greyish purple
SnS	Grey	Pb	Grey
MoS_2	Grey	(Au, Ag, Zn)	Reddish violet
$Mo(S, Se)_2$	Grey		

Encapsulated type pigments have two mixed crystal phases. The coloured compound or colloidal metal is encapsulated by $ZrSiO_4$ crystal, for example zircon cadmium-selenium red. Table 2.5 shows some encapsulate pigments (44).

2.3.3 Synthetic Methods of Zircon Based Pigments

There are commonly three methods to produce zircon based pigments depending on the origins of the ZrO_2.

2.3.3.1 Solid Phase Synthesis

Solid Phase Synthesis (SPS) method uses natural baddeleyite (ZrO_2) or industrial grade zirconia and silica (SiO_2) as starting materials (45). Colourants such as V_2O_5, NH_4VO_3, Pr_6O_{11}, or $FeSO_4 \cdot 7H_2O$ are added into the system and the mixture are sintered at 900 to 1600℃ with mineralizing agents such as NaF, NaCl, NH_4Cl to produce pigments (6). In general, it is very difficult to synthesis encapsulated pigments from ZrO_2 and SiO_2 by using the solid phase method.

2.3.3.2 Dissociation Synthesis

The Dissociation Synthesis (DS) method dissociates $ZrSiO_4$ by a series of chemical treatments, adding the colourants and mineralisers to generate the zircon based pigments. The dissociated products are highly reactive and well distributed which result in the low synthesis temperature and high colour intensities.

2.3.3.2.1 Alkali Fusion Method

The crystal structure of zircon is very stable, and when temperature reaches 1540℃, zircon starts to dissociate into ZrO_2 and SiO_2 (18). This thermal dissociation method consumes high energy which makes it unfavourable in industrial manufacturing. Zircon reacts to alkali metal oxide under high temperature, and generates a mixture containing ZrO_2 and SiO_2 after removing free alkali metals (46). These materials can be directly used to produce zircon based pigments due to their high reactivity. Excessive amount of alkali salts can form a eutectic state with the colourants, which may prevent the colourant ions going into the zircon structure (47). Therefore, the alkali salts need to be removed by acid treatment to enable the production of pigments.

There are several commonly used alkali fusion agents, including Na_2CO_3, NaOH, KOH and LiOH. It has been proved by experimentation that sodium salts yield better results as alkali fusion agents than potassium salts (48). Taking NaOH and Na_2CO_3 for example, the reactions are:

$$ZrSiO_4 + 2NaOH \xrightarrow{900\ ℃} Na_2ZrSiO_5 + H_2O \quad (2.6)$$

$$ZrSiO_4 + Na_2CO_3 \xrightarrow{900\ ℃} Na_2SiZrO_5 + CO_2 \quad (2.7)$$

To ensure the $ZrSiO_4$ can be dissociated completely, excess amount of NaOH or Na_2CO_3 are normally used. With these salts higher temperatures and longer dwelling times can increase the conversion rate.

Acid treatment is normally applied using inorganic acids (HCl and H_2SO_4).

During treatment with HCl, Na_2ZrSiO_5 is mixed with water, and highly concentrated HCl is introduced to react with Na_2ZrSiO_5 until pH reaches 6 to 7, which normally takes 24 hours to complete (48). The products are washed with water to remove excessive amount of NaCl, during which a certain amount of SiO_2 is lost due to its reaction with water converting it into H_2SiO_4. This may cause difficulties in controlling the ratio of SiO_2 and ZrO_2 (49). The reaction scheme is:

$$Na_2ZrSiO_5 + 4HCl \rightarrow SiO_2 + ZrOCl_2 + 2NaCl + H_2O \qquad (2.8)$$

During treatment with sulphuric acid, Na_2ZrSiO_5 powder is added to a 5 % H_2SO_4 aqueous solution and left to react for 3 to 4 hours until insoluble $(ZrO_2)_xSO_3$ is formed (48). $(ZrO_2)_xSO_3$ is then separated from the solution by vacuum filtration and dried.

$$xNa_2SiZrO_5 + H_2SO_4 \rightarrow (ZrO_2)_xSO_3 + xNa_2SiO_3 + H_2O \qquad (2.9)$$

In comparison with HCl, H_2SO_4 can lead to a more complete reaction, is a simpler process and requires shorter preparation time. $(ZrO_2)_xSO_3$ can be used directly for further processing (49).

Through this two-step process, zircon becomes dissociated which means the structure of zircon has been opened up forming SiO_2 and ZrO_2. As a result the colouration ion (V^{4+} or Pr^{4+}) can enter the crystal structure to make the colour.

Previously generated $(ZrO_2)_xSO_3$ and Na_2SiZrO_5, along with certain amount of fused silica powder and colourant (Pr_6O_{11} or VO_2) are mixed together. The mixture reacts at high temperature (> 900 ℃) to form the pigment. Equation 2.10 represents the

reaction scheme (49). A further water wash process is needed for removing sodium sulphate and thus leaving only zircon based pigment powders.

$$Na_2SiZrO_5 + (ZrO_2)_xSO_3 + SiO_2 \rightarrow (x+1)ZrSiO_4 + Na_2SO_4 \qquad (2.10)$$

2.3.3.2.2 Plasma Dissociated Zircon Method

Despite the effectiveness of the alkali fusion method, plasma dissociated zircon synthesis method is also widely used. PDZ (plasma dissociated zircon) is made by passing commercial zircon sand through a plasma torch (50). The reaction equation is shown below.

$$ZrSiO_4 \xrightarrow{6000\ K} ZrO_2 + SiO_2 \qquad (2.11)$$

Zircon sand dissociates at very high temperatures (around 2000 K if exposed sufficiently long but at around 6000K when the exposure is short) in this method and rapid cooling (500 $K \cdot min^{-1}$) gives a fine dissociated structure (51). The PDZ method produces highly reactive monoclinic zirconia and amorphous silica (52, 53). Colourant chemicals such as vanadium oxide, iron oxide or praseodymium oxide are introduced and sintered with by PDZ. During the sintering process, ZrO_2 and SiO_2 will react to form $ZrSiO_4$, which allows the colouration ion (V^{4+} or Pr^{4+}) to substitute some Zr^{4+} ions in the lattice to make the colour (54).

2.3.3.3 Sol-Gel Synthesis

Soluble zirconium salts such as $Zr(NO_3)_4 \bullet 5H_2O$, $ZrOCl_2 \bullet 8H_2O$, $Zr(SO_4)_2 \bullet 4H_2O$, or $Zr(CH_3COO)_4$ and silica gel are used as starting materials which are dissolved in water together with the colourants and react under acid environment at 1000°C to form the

encapsulated pigments (55, 56). Most encapsulated pigments are prepared using this method because of its improvement on their performance and properties.

2.3.4 Formation Mechanism of Zircon Based Pigments

2.3.4.1 Zircon Formation by Direct Sintering

There are two mechanisms reported on how the reaction of SiO_2, ZrO_2 and mineralisers can generate zircon.

The first mechanism demonstrates that SiO_2 reacts with mineraliser and generates SiF_4 which dissociates on the surface of the reactants and reacts with ZrO_2 producing $ZrSiO_4$ (45). This process is represented by:

$$3SiO_2 + 4NaF \rightarrow SiF_4 \uparrow + 2Na_2SiO_3 \quad (2.12)$$

$$SiF_4 \uparrow \rightarrow Si^{4+} + 4e^- + 2F_2 \uparrow \quad (2.13)$$

$$Si^{4+} + 4e^- + ZrO_2 + O_2 \uparrow \rightarrow ZrSiO_4 \quad (2.14)$$

The other mechanism suggests that after SiF_4 is generated, it diffuses together with O_2 and reacts with ZrO_2 to generate $ZrSiO_4$ (45). This process is shown by Equations 2.15 to 2.17.

$$3SiO_2 + 4NaF \rightarrow SiF_4 \uparrow + 2Na_2SiO_3 \quad (2.15)$$

$$SiF_4 \uparrow + ZrO_2 + O_2 \uparrow \rightarrow ZrSiO_4 + 2F_2 \uparrow \quad (2.16)$$

$$2F_2 + SiO_2 \rightarrow SiF_4 \uparrow + O_2 \uparrow \quad (2.17)$$

2.3.4.2 Formation of Zircon Based Lattice Type Pigments

To produce zircon based lattice pigments, ZrO_2 is reacted with the colourants, forming an intermediate product of ZrO_2-MO which then reacts with SiO_2 to form zircon based lattice type pigments (57). For example, to produce zircon vanadium blue, the evenly mixed materials are heated, causing the mineraliser and V_2O_5 melt together. As the temperature increases, part of the V^{4+} goes into ZrO_2 structure. With a further increase in temperature, SiO_2 reacts with ZrO_2 which generates $ZrSiO_4$, during which process the vanadium ions are retained in the zircon crystal structure, thus lattice type pigments are generated (58).

2.3.4.3 Formation of Zircon Based Encapsulated Type Pigments

Generally, it takes two steps to form zircon based encapsulated type pigments (59). Zircon cadmium-selenium red is taken as an example here to illustrate the process.

In the first step, SiO_2, ZrO_2 and mineraliser react to form $ZrSiO_4$. During this phase, very fine $ZrSiO_4$ crystal grains are generated and so are the Cd (S_xSe_{1-x}) crystal particles (60).

In the second step, Cd (S_xSe_{1-x}) crystals are encapsulated by $ZrSiO_4$ crystals. This can be explained by the liquid state sintering theory. $ZrSiO_4$ grains are rearranged with the existence of Na_2SiO_3 in liquid phase, during which process the $ZrSiO_4$ grains encapsulate some of the Cd (S_xSe_{1-x}) grains, and therefore the zircon based encapsulated red pigment is produced (60).

2.4 Size Reduction Methods

Size reduction generally takes place in stages. The energy required to reduce particle size follows Hukki's law which is an overarching theory linking Kick, Bond and Rittinger approaches which cover coarse, mid and fine comminution processes, respectively (61, 62). Various machines can be selected to move down the curve. In this thesis the selected devices are a fly press, a vibratory disc mill, a ball mill and an attrition mill. On a commercial scale the fly press might be replaced with a jaw, roll or gyratory crusher and the vibratory disc mill by a large vibratory ball mill for example.

2.4.1 Fly Pressing

A fly press is a form of screw press which generates pressure by a screw driven ram.

Fly pressing is a generic form for sample crushing systems like those shown in Figure 2.2 (63). It can be divided in two types. One is flywheel press and the other one is weighted arm press. There is no difference between these two types of fly press in terms of mechanical principles. Both of them generate static pressure by converting the rotation of the wheel or handle into a downward plunger motion (64).

Although very similar in practice there are several differences (63). First, the flywheel press is more compact than the weight arm press of the same size. Second, as can be seen from Figure 2.2, because of the shape of the equipment, if the press is not mounted at the correct height, the swinging iron ball of the weight arm press could

be dangerous to people nearby the machine when operating. Finally, the flywheel press is easier to operate as the wheel can be easily rotated from any position.

The history of the fly press can be traced back to first century A.D. It is believed that the Romans first used a wooden fly press for the olive oil and wine production industries. In the middle of 15th century A.D. the fly press was used in the printing industries. The Power-Fly-Press was invented for heavy duty usage while the small manual models were used for lighter applications (65).

Figure 2.2 Two types of fly press – Flywheel press (left) & Weight arm press (right) (63)

Fly pressing is used in many different industries and can be used for processing of various refractory materials. They are commonly used for a metalworking including forging, pressing, punching and coining (66).

The output from a fly press is limited and the crushing process can easily be scaled up if required by the use of mineral comminution equipment such as jaw, gyratory, roll or cone crushers.

2.4.2 Vibratory Disc Milling

2.4.2.1 Introduction of Vibratory Disc Mill

Vibratory disc mills are mainly used for laboratory size reduction. They can be used for grinding fibrous, brittle, medium-hard and hard materials, such as refractories, plant parts, electronic components and minerals. Normally, the maximum feed size of the laboratory vibratory disc mill should be less than 15 mm, and the particle size can be reduced to less than 100 μm in 1-2 minutes processing time (67).

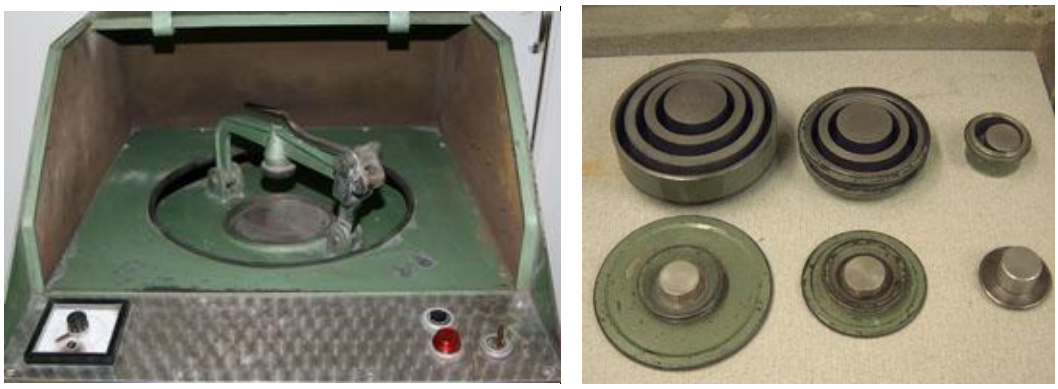

a **b**

Figure 2.3 Vibratory disc mill

a) Vibrating base and clamping mechanism, b) grinding chambers with lids removed showing the internal ring and block arrangement.

As can be seen from Figure 2.3, the vibratory disc mill mainly contains two functional parts. One is vibration plate with a locking lever (Figure 2.3-a) and the other is the grinding set (Figure 2.3-b) which consists of a grinding jar with cover, containing a cylindrical block and 0-2 rings depending on the size of the jar, typically capacities range from 50 to 250 ml.

Typically, the grinding sets can be made chromium steel, zirconia, tungsten carbide and agate (67).

2.4.2.2 Functional Principles of Vibratory Disc Mill

The samples are loaded into the grinding sets and then firmly fixed on the vibration plate by the locking lever. As can be seen from Figure 2.4-a, the plate circular horizontally vibrates along with the grinding set. Therefore, the centrifugal force drives the moving components and the interaction between them, the grinding dish and the powder cause grinding of the powder. There are three types of forces generated, which are pressure, impact and friction (Figure 2.4-b) (68). Thus the powder was crushed due to the collision between the rings. Furthermore, when the material passed under the rings, attrition forces were also applied which allowed finer grinding. With high vibration speed (usually 700 – 1500 rpm), the materials are easily comminuted to a relatively fine powder in a very short time period (normally 30-90 seconds) (67).

This method of grinding is not scalable for larger production but dry vibration mills are known which could be used. Wet vibration mills are also known for example the

vibro-energy system by William Boulton Ltd (69). It is however more common to use large tumbling mills for this scale of reduction.

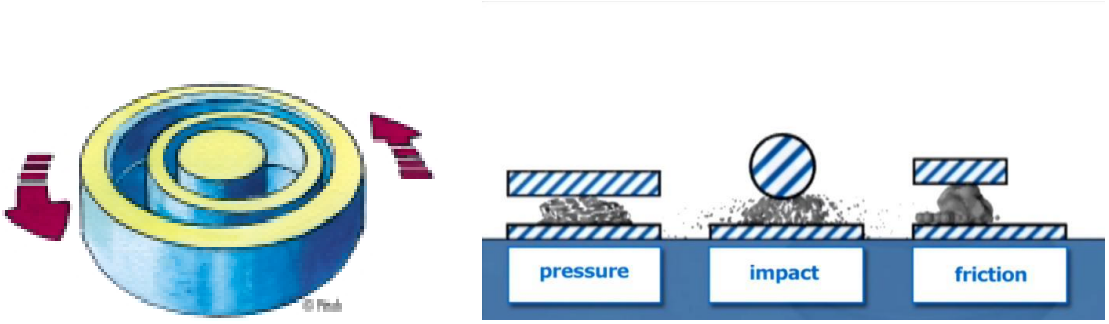

a b

Figure 2.4 Functional principles of vibratory disc mill (68)

a) The oscillations of the base create a circular action of disc movement causing the powder trapped between them to be ground. b) the mechanisms active in the disc mill

2.4.3 Ball Milling

2.4.3.1 Functional Principles of Ball Mill

Ball mills are widely used from laboratory scale to large industrial operations. Ball mills in industry are normally used to grind materials to a size suitable to be the feed to an attrition line (70). The laboratory ball mill tends to be a removable pot which is rotated on a roller table. The speed is adjusted to suit the mill volume and diameter.

All types of ball mills are operated on the same principle which is shown in Figure 2.5 (71). A cylindrical chamber with its axis mounted horizontally is rotated at a speed such that the contents within are forced to move. The grinding chamber is filled to about 30 % of its volume with spherical media of a size set by the application (72).

The mill is run at a speed such that the media is raised on the rotating wall of the chamber and cascades to strike the toe of the media remaining in the base of the mill. The critical speed is normally calculated where the media remains stuck to the wall of the chamber due to the centrifugal forces. The mill is typically run at about 80% of the calculated critical speed (73).

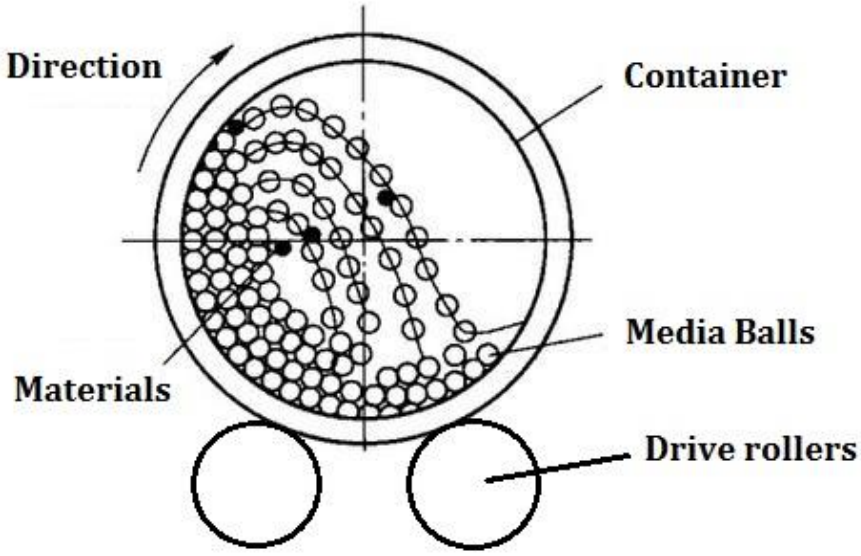

Figure 2.5 Schematic Diagram of Ball mill; Modified from (71)

2.4.3.2 Influencing Factors of Ball Mill Performance

There are several factors that can affect the ball milling behaviour.

Material-to -media ratio indicates the weight ratio between processed materials and media balls which can significantly affect the milling efficiency. Xiao demonstrated that a 10: 1 material-to-media ratio can provide more efficient milling than 5:1, 15:1 and 20:1 ratios (74).

The media ball size also directly affects the milling behaviour. Larger balls can generate higher impact, but provides smaller total contact area. Empirical equations are available to calculate the optimum media size (71, 75). A typical empirical equation is shown in Equation 2.18.

$$\mathrm{B} = \sqrt{\frac{FW_i}{KC_s}\sqrt{S\sqrt{D}}} \tag{2.18}$$

where B is the media ball diameter; F is the D_{80} of feeding material; C_s indicates the percentage of milling critical speed; S is specific gravity of the feeding material; D indicates the diameter of the mill cylinder; and K is a constant which relates to the shape of the media (76).

Dispersants can also influence milling efficiency. Zhou et al. discussed how the milling behaviour is affected by adding certain amount of ethanol as dispersant (77). Smaller mean particle size can be achieved by introducing proper amount of dispersant, but excessive volume of dispersant may reduce the milling efficiency.

Faster rotating speed means more energy can be delivered to the feeding material. However, it does not mean the higher the rotating speed the higher the efficiency. If the speed excesses the critical speed, the media balls will be stuck on the wall. The critical speed of a ball mill can be calculated by Equations 2.19.

$$n_c = \frac{1}{2\pi}\sqrt{\frac{g}{R-r}} \tag{2.19}$$

where n_c is the critical speed; g is the gravity; R indicates the radius of the ball mill container; and r is the radius of the media ball (78).

The media ball may introduce contaminations into the feed material. Thus the material of the media ball is very important. For ceramic processing, alumina and zirconia media balls are most commonly used in laboratories (72). For the similar reason, the material of the container may also affect the milling results. Normally, porcelain containers in different sizes are used for ceramic powders in the laboratory environment (73). Alumina based brick liners are common in the industrial milling of ceramics (70).

An important factor in ball milling process is milling time (79). Generally, the particle size reduces exponentially with the milling time. This means the particle size will not change after certain milling time.

Other factors may influence the ball milling behaviours include milling temperature, atmosphere, and additives (72).

2.4.4 Attrition Milling

2.4.4.1 Functional Principles of Attrition Mill

Attrition mills are a special class of comminution equipment which are widely used for fine grinding. They can be used for grinding most brittle materials including plastics, glass, pigments, minerals and ceramic powders (80).

As can be seen from Figure 2.6 (81, 82), the attrition mill mainly contains three functional parts: a vertical, stationary, cylindrical grinding chamber; a gas flow system that can provide different grinding atmosphere (i.e. N_2, He) and a water cooling system. A vertical rotating impeller with horizontal agitators is placed in the

chamber which can be fixed on the bearings of the main body of the machine. Typically, the removable inner grinding chamber is made of ceramic or polymer materials with outer chamber shell are usually made by steel (81). The rotating shaft is generally made by metal with polymer coatings or ceramic. The last component is the grinding media which are available in different sizes and materials, such as hardened steel, zirconia, alumina or tungsten carbide (82). In attrition milling the media are spherical. Generally, the amount needed of the media balls is half of the volume of the inner chamber(81).

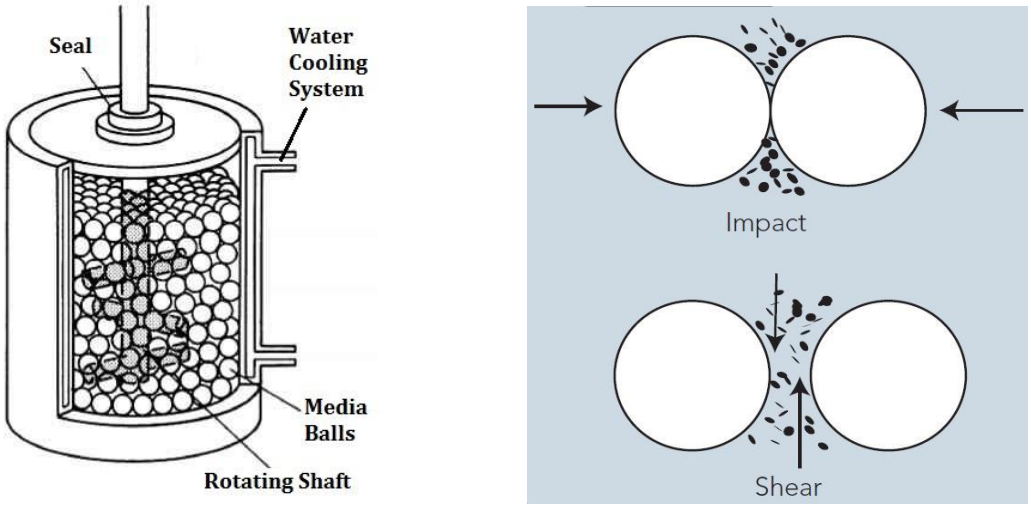

Figure 2.6 Schematic diagrams of an attrition mill and the generated forces (81, 82)

During the milling process, the rotating impeller stirs the media balls and the material slurries which allow the particles and balls move freely. These movements mainly generate two types of forces which are impact force and shear force (83). As can be seen from Figure 2.6, the material particles are ground under these two forces and thus the size of the particles is reduced.

Typically, the maximum feed size of a high speed attrition mill is less than 75 μm and these particles can be reduced to typically less than 0.5 to 2 microns depending on the material (84).

2.4.4.2 Influencing Factors of Attrition Mill

Like ball mills, the attrition milling process is also affected by specific gravity, initial feed material size, material-to-media ratio, media ball size and rotating speed (85, 86). In attrition milling, the grinding time is directly related to the diameter of media balls and agitator speed (Equation 2.20) (87).

$$\mathrm{T} = \frac{KD^2}{\sqrt{N}} \tag{2.20}$$

where T is the grinding time to reach a certain mean particle size; K is a constant which depends on slurry materials, media materials and mill model; D indicates the diameter of the media balls; and N is the shaft rotation speed.

Generally, smaller media size and higher agitator speed can enhance the working efficiency of the attrition mill. However, more energy will be consumed by increasing the shaft speed. The media ball size is also required to be within a certain range (85). Very small media size can generate very limited impact force which may lead to longer processing times.

2.4.4.3 Comparisons of Mills

Generally, attrition milling can reduce particles to a finer size than most common milling processes including vibratory and ball mills. Figure 2.7 (80) shows a comparison of effectiveness of these three different types of mills.

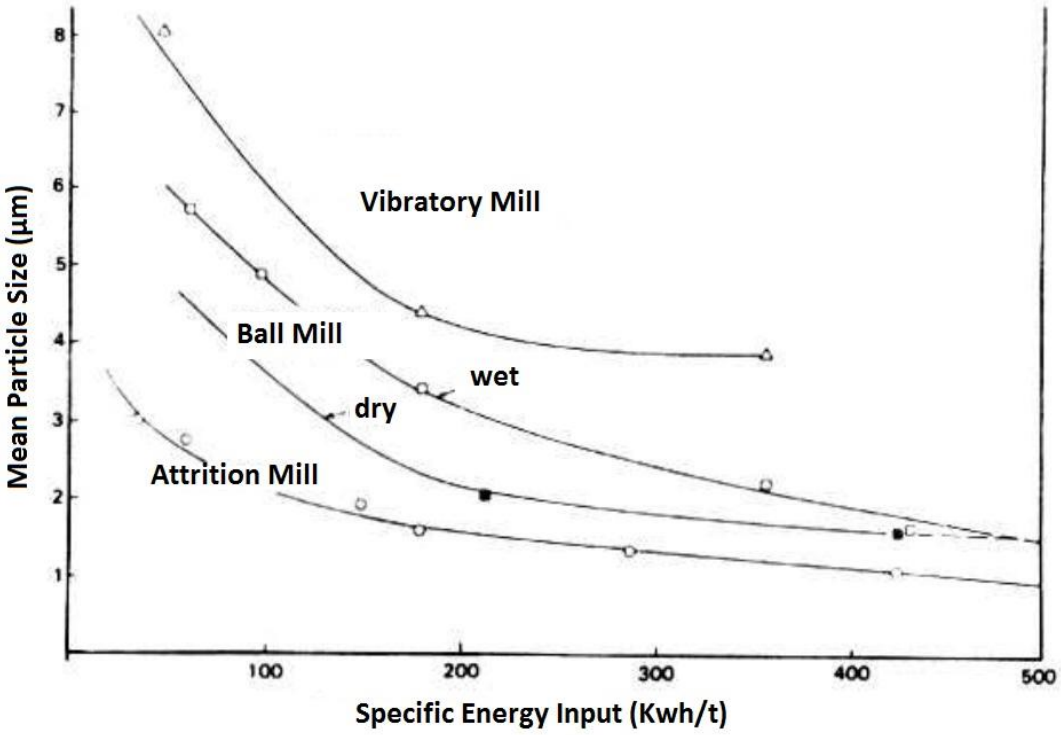

Figure 2.7 Comparisons of effectiveness of vibratory mill, ball mill and attrition mill (80)

As can be seen from the figure, with the same amount of energy consumption, the attrition mill can grind the particles to a much finer median size. Additionally, with more energy input, the attrition mill can reduce the particle size to a very fine size while the other two types of mill do not have this ability.

2.5 Purification Methods

2.5.1 Magnetic Separation

Magnetic separation is a physical technique which utilizes the magnetic force to segregate materials with different magnetic properties from a mixture. This method is widely used in many industries including ceramics processing, mining and waste water treatment (88).

2.5.1.1 Principles of Magnetics

Some materials can exhibit magnetic properties in a magnetic field. The intensity of the magnetisation can be demonstrated by Equation 2.21

$$\mathrm{J} = \frac{M}{V} \tag{2.21}$$

where the J is the magnetic intensity; M indicates the magnetic moment of the material; and V is the volume of the substance (89).

The magnetisation intensity is directly proportional to the external magnetic field strength which can be described by Equation 2.22.

$$\mathrm{J} = \kappa_0 H \tag{2.22}$$

Thus $$\kappa_0 = \frac{J}{H} = \frac{M}{VH} \tag{2.23}$$

$$x_0 = \frac{\kappa_0}{\delta} = \frac{M}{\delta V H} \tag{2.24}$$

where κ_0 is the volumetric dimensionless magnetic susceptibility which indicates the degree of magnetisation of a material; H is the strength of the applied magnetic field; x_0 is the mass magnetic susceptibility of the material; and δ is the density of the material (89).

$$B_0 = \mu_0 H \tag{2.25}$$

$$\mathrm{B} = \mu_0(H + J) = \mu_0(H + \kappa_0 H) \tag{2.26}$$

where B_0 is the magnetic induction in vacuum; μ_0 is the magnetic permeability in vacuum; B is magnetic induction (89).

Equations 2.25 and 2.26 show the relations of magnetic induction, magnetic permeability and magnetic field intensity in vacuum and medium environment respectively.

2.5.1.2 Magnetism of Materials

Every macroscopic object has magnetism to some extent. According to the characteristics exhibited in the presence of an external magnetic field, all materials can be divided into three categories: ferromagnetic, paramagnetic and diamagnetic (90). The differences of magnetic properties of materials are the basis of the magnetic separation technology. Figure 2.8 shows the magnetisation intensity of these three types of materials in an applied magnetic field.

The ferromagnetic materials can gain extremely high magnetization intensity even in a weak magnetic field. When the external magnetic field is removed, the ferromagnetic materials can remain magnetised. The magnetic susceptibilities of

these materials can reach 10^{-3} magnitude at normal temperature (91). Iron, cobalt, nickel are all ferromagnetic materials.

The main character of paramagnetic materials is that when there is an external magnetic field applied, they will be slightly attracted into the magnetic field and show extremely weak magnetism. The magnetic susceptibilities of paramagnetic materials are normally very low, about 10^{-5} magnitude at room temperature (89). There are a lot of paramagnetic materials including transition elements, rare earth elements, aluminium and platinum plus many compounds (92).

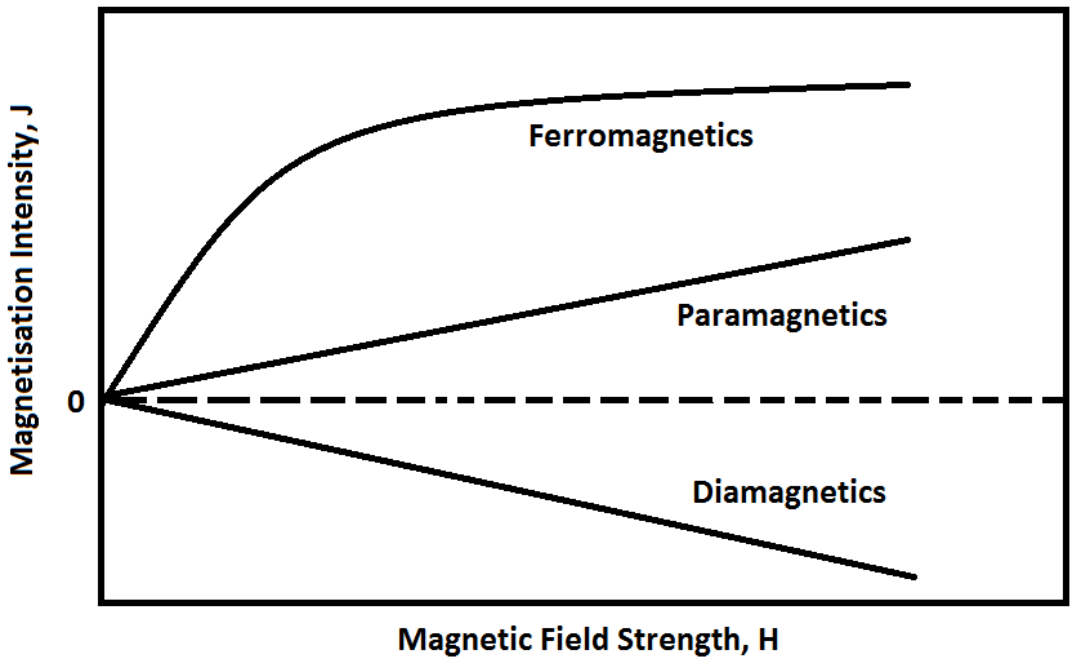

Figure 2.8 Magnetisation intensity of ferromagnetic, paramagnetic and diamagnetic materials in an applied magnetic field; Modified from (90)

Unlike with the paramagnetic materials, diamagnetic materials will generate an opposite magnetic moment to the external magnetic field. This means when an external magnetic field is applied to the diamagnetic materials, they will be repelled

from the field. The diamagnetism of these materials is generally quite weak, the magnetic susceptibilities are around -10^{-5} in normal temperature. Copper, silver, gold and some other metals are diamagnetic materials (93).

2.5.1.3 Principles of Magnetic Separation

In magnetic separation process, when the material mixture enter the separation area, the magnetic particles are magnetised by the non-uniform magnetic field, thus the particles are attracted on the separator. The particles are simultaneously subjected to magnetic force and competitive force which including gravity, resistance and friction (94). The magnetic separation can only be achieved when the magnetic force is greater than competitive force.

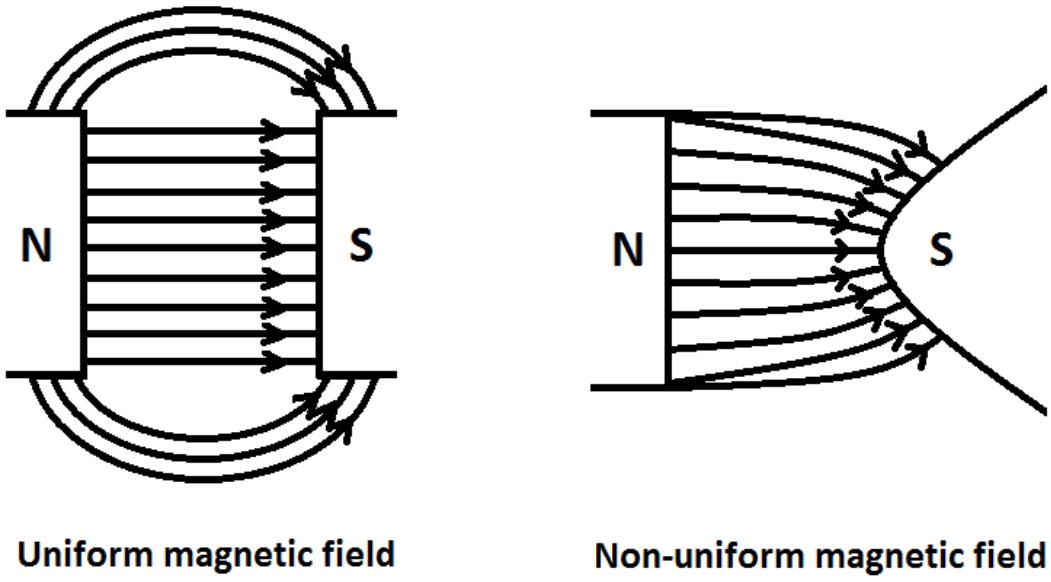

Figure 2.9 Schematic diagram of uniform and non-uniform magnetic field (89)

The two types of magnetic field (uniform and non-uniform) are shown in Figure 2.9.In a uniform magnetic field, the field intensities and field directions remain the same at any location which can be demonstrated by Equation 2.27 (89).

$$\frac{dH}{dx} = 0 \tag{2.27}$$

In a non-uniform magnetic field, the field strength and field direction are constantly changing with position. This non-uniformity can be demonstrated by magnetic field gradient which means the changing rate of field strength along with space shift (Equation 2.28) (89).

$$grad\ H = \frac{dH}{dx} \tag{2.28}$$

The magnetic force applied on a magnetic particle in a non-uniform magnetic field can be calculated by Equation 2.29 (89).

$$F_m = \mu_0 \kappa_0 HV \frac{dH}{dx} \tag{2.29}$$

It can be seen that the magnetic field strength is required to be adjusted according to the magnetism and particle size of the feeding material. For example, the ferromagnetic materials will be easily attracted and attached to a reflectively weak magnetic field (400 – 600 gauss) while the other two types of materials will pass through. In addition, by passing through a strong magnetic field (6000 – 20000 gauss), paramagnetic materials and diamagnetic substances can be parted (91). Moreover, by controlling the strength of the external magnetic field, materials with different grades of paramagnetism can be separated.

The magnetic separation can only be achieved in a non-uniform magnetic field. This is due to the magnetic particles only being subjected to torque in a uniform magnetic field. The magnetism particles are affected by magnetic force and torque at the same time in a non-uniform magnetic field which will cause the magnetic particles to rotate and move to the field gradient increasing direction and finally attach to the pole surface (94).

2.5.1.4 Types of Magnetic Separator

Various types of magnetic separator have been developed with specific features to meet different separation requirements. Table 2.6 shows the specifications of commonly used magnetic separators (95).

Table 2.6 List of magnetic separators; Modified from (95)

Type	Product Name	Features
Aluminium separation	Conveyor type aluminium separator	Assists recycling by separating crushed wastes and hand-sorted wastes.
Comb	Combe type magnet	For removal of iron from bulk materials.
Drum	Barrel separator	For barrel polishing.
	Drum separator	Casing provided for easy installation.
	Large permanent magnetic drum	Works well for large iron pieces and a large amount of iron pieces to collect.
	Permanent magnetic drum	Most suitable for removing iron from bulk materials and can be incorporated in equipment.
Eccentric pole type	Nonferrous separator	Assists recycling by separating and collecting shredded dust.
High magnetic force electromagnetic	Induction type high magnetic force separator	For removal of weak magnetic bulk materials. 2.6 T (26kg) max.
	Cross belt type high magnetic force separator	Small capacity and less mixture of raw materials in removed iron.
	Induction type separator	Effective for removing iron from casting sand.
	Electromagnetic filter	Effective for removing iron from fine materials (powder).

Table 2.6 List of magnetic separators; Modified from (95)

High speed drum	High speed drum separator	For high grade sorting and collection of magnetic substances.
Plate	Plate magnet	Chute-mounted type with stainless steel surface.
		Chute-mounted type. Attracted iron pieces held firmly.
Pulley	Electromagnetic pulley	Usable as a conveyor head pulley and high iron removal rate.
	Permanent magnetic pulley	Usable as a conveyor head pulley. For a large diameter, the electromagnetic type is recommended.
Small	Magnetic bar	Capable of being incorporated in any place.
	Grid type magnet	For collection of small iron pieces mixed in small amount. Installed at hopper outlet port or in duct.
Suspension	Suspended plate magnet	Large attractive force.
		Powerful type having large attractive force.
	Round electromagnet for iron removal	Natural air cooling and enclosed type for less mixture of iron pieces.
	Suspended electromagnet for iron removal	Oil cooling type for less mixture of iron pieces.
	Suspended electromagnetic separator	Natural discharge type and continuous operation.
	Suspended permanent magnetic separator	Energy saving and auto discharge type for shallow conveyors.
Tubular	Tubular separator	Removal of iron pieces during transfer of bulk materials in a pipe.

2.5.2 Acid Leaching

2.5.2.1 Chemistry of Acid Leaching

Leaching is usually known as extracting in the chemical process industry. In the leaching process, the solid to be leached is mixed with a suitable liquid solvent which removes the undesirable materials into solution while the desirable substances are left in solid form (96). Separation of the solution and the solid gives the purified solid. Both inorganic and organic materials are normally used in this process (97). This technique is widely used in the chemical, biological, mineral and food processing industries (98).

The leaching process can be physical and chemical methods while acid leaching is one of the chemical methods. The materials will commonly be digested in an inorganic acid in a tank or other suitable vessel. The acid will react with the contaminating materials and dissolve them into the aqueous phase in the form of ions. During this process, various types of chemical reactions happen, for example decomposition, replacement and complex reactions. The general reaction equations for metal digestion are given below (96).

$$\mathrm{M} + x\mathrm{H}^{+} \rightarrow \mathrm{M}^{\mathrm{x}+} + \frac{x}{2}\mathrm{H}_2 \tag{2.30}$$

$$\mathrm{MO}_{\mathrm{x}} + 2x\mathrm{H}^{+} \rightarrow \mathrm{M}^{2\mathrm{x}+} + x\mathrm{H}_2\mathrm{O} \tag{2.31}$$

$$\mathrm{MZO}_{\mathrm{x}} + \mathrm{H}^{+} \rightarrow \mathrm{M}^{\mathrm{y}+} + \mathrm{H}^{+} + \mathrm{ZO}_{\mathrm{x}}^{\mathrm{y}-} \tag{2.32}$$

As can be seen from Equation 2.30, metallic elements such as iron, zinc, nickel are oxidized by the hydrogen ion which means the solid phase metal is converted to metal ion and transferred into the solution. The reaction given by Equation 2.31 demonstrates that hydrogen ions can react with some metallic oxides to form metal ion and water molecules due to water being more stable. A large number of oxides can react with acid following the scheme given in Equation 2.31, for instance iron oxide, magnesium oxide. Many metal oxide salts can be dissolved by acid following the scheme shown by Equation 2.32 as well, such as calcium carbonate, magnesium carbonate.

A number of inorganic acids including sulphuric acid, hydrochloric acid and hydrofluoric acid, nitromuriatic acid can be used in the process according to the

composition of the mixture. For example, nitric acid is usually used for leaching reducing substances due to its strong oxidizing property (99).

Among these inorganic acids, sulphuric acid is the most common and widely used solvent in the leaching process. Dilute sulphuric acid has a weaker oxidizing property than nitric acid, and is less evaporable and expensive than hydrochloric acid (100). All these properties make sulphuric acid ideal for processing normal metal – non-metal mixtures.

2.5.2.2 Influencing Factors of Acid Leaching

There are three important factors that affect the acid leaching process which are particle size, acid type and concentration and reaction temperature (96).

Generally, finer particles can increase the reaction speed due to more liquid-to-solid contact area (101). Massaci et al. suggest that the effects of decreasing particle size would become negligible when the particles are smaller than a cirtical size due to the reaction speed being more affected by the porosity of the reacting material (102).

Terry and Monhemius compared the reactivity of different inorganic acids and gave the order as $H_2SO_4 \approx H_3PO_4 > HClO_4 > HNO_3 \approx HCl$ (103). For the same acid, normally higher acid concentration results in higher extraction rate in the same time period.

Boads and Abdel-Aal found out that the leaching efficiency is proportional to temperature in the range of 30 to 60 °C (101, 104).

Commonly, 5 wt. % sulphuric acid is used for leaching free metal and metallic oxides from ceramics. This process is normally performed at 20 – 80 °C and lasts 4 - 24 hours depending on the composition of materials (96).

2.5.2.3 Acid Leaching Kinetics

Generally, the acid leaching speed is controlled by either chemical reaction rate or physical diffusion rate. The calculations of the rate constants are shown in Equation 2.33 and 2.34 respectively (105).

$$K_c t = 1 - (1 - x)^{\frac{1}{3}} \tag{2.33}$$

$$K_d t = 1 - \frac{2}{3}\ x - (1 - x)^{\frac{2}{3}} \tag{2.34}$$

where K_c is chemical reaction controlled rate constant; K_d is diffusion controlled rate constant; t indicates the reacting time; x is percentage of reacted metal material.

The acid leaching process can be more accurately monitored and controlled by obtaining the kinetic constant (106).

2.6 Shaping Methods

2.6.1 Dry Compaction

2.6.1.1 Dry Pressing Process

Dry pressing is a common method for shaping ceramic powders where relatively simple geometries are required. It can be automated to allow for large volume

production. It is for these reasons that the process is attractive for forming simple shapes from powders (6).

The dry compaction process is conducted by using a die set which is usually made of metallic materials, such as hardened steel. The die set consists of a die, a lower punch, an upper punch (107).

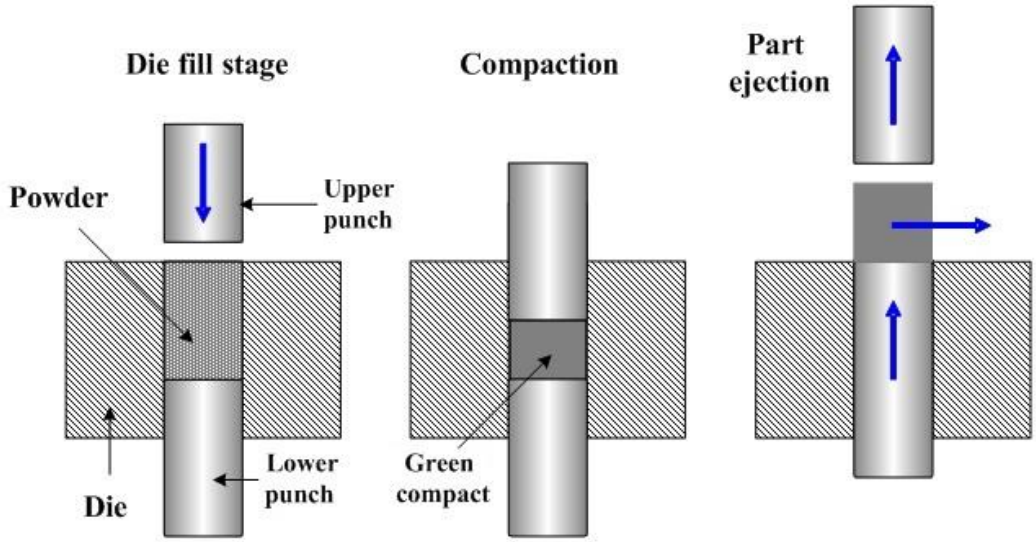

Figure 2.10 Schematic diagram of dry pressing process; Modified from (107)

As can be seen from Figure 2.10 (107), during the compaction process, firstly, the lower punch and die are set in place. The proper amount of powder is fed into the die chamber. The upper punch is forced into the die and compaction takes place as force increases. The pressure is transmitted to the powder which compacts the powder into the desire shape. After the load reaches a certain value, the fabrication process is completed. On completion of the compaction phase a force is applied on the bottom punch which ejects the green compact out of the die. Thus a green compact of the desired dimensions is obtained. This process can be surmised into an

order of events described as particle rearrangement, deformation, fragmentation, bonding, decompression and ejection (108).

2.6.1.2 Principles of Dry Compaction

Dry pressing behaviour is closely related to the properties of the powders (6). A powder with spherical shaped particles can increase the flow properties during the process. Higher moisture in the powder causes cohesion and adhesion during the compaction procedure.

There are various forces which are applied to the specimen in process which including friction, distribution, compaction and ejection force (109).

Friction develops between particles due to their rearrangement during the process. It is more noticeable when low loads are applied. There are also frictional forces developed when the particles were pressed against the die wall. This type of frictional force is more significant in high pressing loads (107).

Several researchers have carried out work to investigate the distribution forces during uniaxial pressing process and Equation 2.35 shows the relationship between the various forces involved in the process (109-111).

$$F_A = F_L + F_D \tag{2.35}$$

where F_A is the force applied on the upper punch; F_L indicates the force transmitted to the lower punch; and F_D is the friction force on die wall.

The compaction force at upper punch differs from the compaction force at lower punch. Thus, the mean compaction force (F_M) is normally used for describe the compaction process which can be calculated using Equation 2.36 (109).

$$F_M = F_A + \frac{F_L}{2} \tag{2.36}$$

The ejection force indicates the minimum force needed to eject the compacted pellet out of the die. It is mainly affected by the die wall friction and material-die wall adhesion (107).

There are two main equations used to modelling the dry compaction process which are Heckel equation and Kawakita equation (112).

Heckel equation demonstrates the relations between material density and applied pressure which is expressed by Equation 2.37 (113). Generally, the higher the porosity of the material, the higher the applied force is needed to compact it into pellet (114).

$$H = \ln\frac{1}{1-D} = \mathrm{kP} + A \tag{2.37}$$

where H indicates the Heckel value; D is relative density of the powder; P is the applied pressure; k and A are constants related to the plasticity of the material and particle rearrangement respectively.

Kawakita equation describes the relations between volume reduction of the powder and applied pressure which is shown in Equation 2.38 (115).

$$\frac{P}{C} = \frac{P}{a} + \frac{1}{ab} \tag{2.38}$$

where P is the applied pressure; C indicates the degree of volume reduction of the compacted powder; a is the total volume reduction (Carr's index); and b is a constant inversely related to the strength of the particles.

As can be seen from the equation, the initial volume evaluation plays a key role when applying this model.

2.6.2 Extrusion

Extrusion is a widely used shaping process by forcing a paste through a die. Almost any cross sections of the extruded material can be developed by changing the die typical shapes including rods, tubes, honey-combs and other complicated shapes (116).

2.6.2.1 Formulation of Paste

The ceramic powders need to be converted into paste form for extrusion processing. Paste systems generally consist of two parts, solid phase and liquid phases, while the gas phase sometimes exists in small volumes which can influence the properties of the paste and the extrudate (117). The rheology of a paste is affected by various factors including the rheology of the liquid phase and properties of the particles, such as packing behaviour, size, shape and surface chemistry (118).

The liquid phase can usually be regarded as the binder system. The liquid phase acts as a lubricant by lowering the frictional forces, and allows particles flow past each other (119). It can also bind particles together by bridging the gaps between them. The liquid phase often contains a major liquid binder, a minor binder, lubricant and

plasticiser (120). Minor binder, lubricant and plasticiser are carried by the major binder. The viscosity of the major binder can be improved by the minor binder in the green state to increase strength. The flow properties of the paste are improved by plasticisers and lubricants (121).

2.6.2.2 Extrusion Process

Figure 2.11 shows the schematic diagram of a ram extrusion process. As can be seen, the extrusion device consists of a barrel, die and ram. The paste is placed in the barrel in between the die and ram. A continuous pressure or speed is applied on the ram to force it moving towards the die and the paste is extruded through the die and out of the barrel. Thus an extrudate with continuous cross section is generated.

Pastes are known to exhibit visco-plastic behaviour which results in visco-plastic flow during the extrusion process. The Herschel-Bulkely equation (Equation 2.39) describes this type of flow (122).

$$\sigma = \sigma_0 + K\,\dot{\gamma}^n \tag{2.39}$$

where σ is the shear stress; σ_0 is the yield stress, γ is the shear rate; and K is a parameter of the flow equation.

The extrusion force can be described by Equation 2.40 (116).

$$\mathrm{F} = A_0 k \ln\frac{A_0}{A} \tag{2.40}$$

where F is the extrusion force, A_0 is the cross section area of the barrel; A is the cross sectional area of the extrudate and k is an extrusion constant related to paste material and temperature.

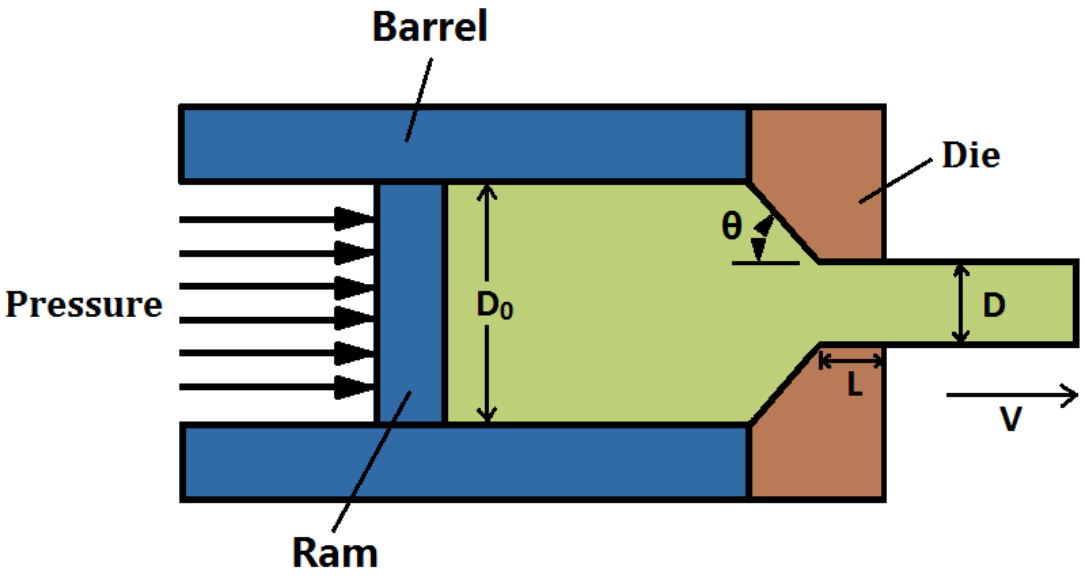

Figure 2.11 Schematic diagram of a ram extrusion process, where D_0 is the diameter of the barrel; θ is the die angle; L is length of the die; D is the diameter of the die and V is the velocity of the ram

Benbow reviewed Berghaus reported that the flow behaviours of very stiff ceramic paste can be explained by the metal extrusion theory due to the similarities of the paste (123). A pressure drop will appear when the paste entering the die.

Benbow and Bridgwater modelled the paste flow behaviour by Equation 2.41 (124).

$$\mathrm{P} = (\sigma_0 + \alpha V^m) \ln \frac{A_0}{A} + \frac{ML}{A} \quad (\tau_0 + \beta V^n) \tag{2.41}$$

Where P is the pressure drop causing by paste entering the die; σ_0 represents the yield stress; α is a constant related to the velocity; V represents extrusion velocity

and m is the power law term; M indicates the circumference of the die land, τ_0 is the die wall initial yield stress; β is the die land velocity factor and n is the die land velocity exponent. This model relies on the paste being treated as having complete slip at the wall.

Benbow and Bridgwater suggested that defects formed during extrusion process fall into two categories: flow defects and phase migration (123).

Flow defects refer to the structural imperfections of the extrudates occurred during the extrusion process. Phase migration indicates the phenomenon that the liquid phase tends to flow prior to the solid phase during extrusion process. This is due to the reason that under a pressure gradient, the liquid phase moves at a higher rate than the solid phase. Phase migration can lead to extrusion failure and equipment damage (125). A signal processing method has been employed to detect the defects formed in the process of extrusion (126).

CHAPTER III METHODS AND MATERIALS

3.1 Introduction

The previous chapter has reviewed the investment casting process and demonstrated that the foundry waste materials are inevitably growing with the expansion of the foundry industry. The current situation of recycling foundry waste materials has also been reviewed (Section 2.1). Different production methods and usage of zirconia toughened mullite composites have also been reviewed (Section 2.2). In addition, a background knowledge of zircon based pigments has also been introduced (Section 2.4).

The sample processing methods and procedures will be given in Chapter IV, V and VII. In this chapter, all the analytical methods used will be described covering their principles of operation, experimental equipment and procedures. Furthermore, the foundry waste materials used in this project will be described based on the analysis undertaken.

3.2 Analytical methods

3.2.1 Measurement of particle size distribution

3.2.1.1 Introduction of particle size distribution

In many theories on particle behaviour the particles are assumed to be spherical (127). However, in practice, most of the particles are irregular in shape. Therefore,

the irregular particle size is usually described as the equivalent spherical diameter by volume which has the same or very similar physical properties as the irregular particle being measured (128).

Particle size distribution (PSD) demonstrates the proportion of the particles according to the size in a powder sample. Typically, the value is presented on a volume or mass basis (128). The mass median diameter (MMD), D_{50}, is a commonly used value to characterize a powder sample. The physical significance of D_{50} is that 50 % of particles are larger than this value. It can be regarded as the average particle diameter (129).

The PSD of a sample is a very important factor in understanding the physical and chemical behaviour of ceramic powders. The PSD may affect solid state chemical reaction processes and mechanical strength developed in the final ceramic (6). Therefore, measuring and controlling the PSD during the process can significantly change the properties of the product.

3.2.1.2 Principles of laser diffraction method

There are several techniques which can be used to measure the PSD of a sample, for example, sieve analysis, optical counting methods and laser diffraction. Among these techniques, the laser diffraction method is most widely used for particles under 100 µm due to its advanced data analysing and automation (129).

During the propagation of the light, the wave-front is affected by apertures or particles it passes or contacts that have a similar wavelength scale, thus light

diffraction and scattering occur (129). The distribution of the diffracted intensity and scattered intensity is affected by the wavelength and the particle size. Therefore, by using parallel monochromatic laser light source, the angular distribution of the diffracted and scattered light is only related to the particle size (129).

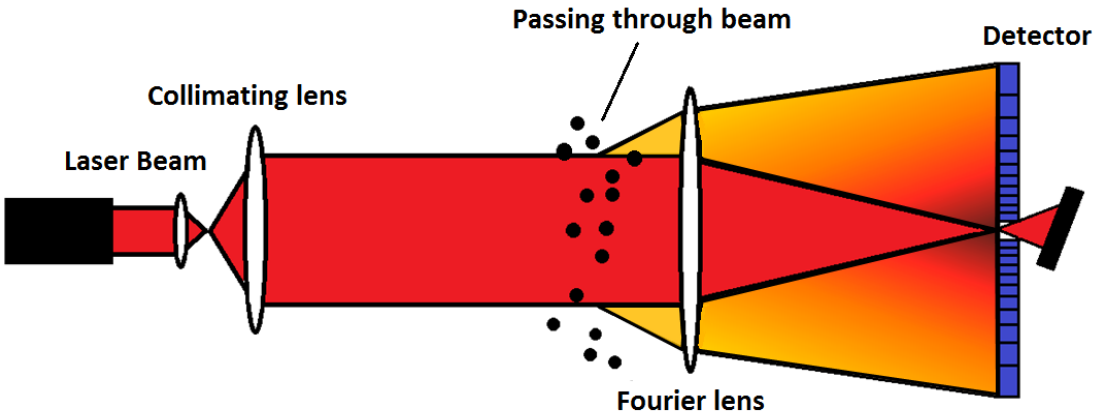

Figure 3.1 Schematic diagram of the laser diffraction method; Modified from (130)

As can be seen from Figure 3.1, the laser beam travels through the collimating lens to ensure the light is parallel (130). Then, the laser beam passes through a suspension of particles where the light is scattered and diffracted. The angle of diffraction is inversely proportional to the particle size, which means the smaller the particle, the larger the angle, and vice versa. By measuring the angle and the intensity of the diffracted light, and then analysing the data according to the Mie theory (131), the particle size distribution can be calculated and reported.

3.2.1.3 Experimental instrument and procedure

In this study, the measurement of PSD was carried out by using a SYMPATEC HELOS SUCELL laser diffraction laboratory particle size analyser. This device could measure

the PSD of suspensions in the range of 0.3 µm to 875 µm (132). This device used a HeNe laser beam of 632.8 nm wavelength as the light source, along with high quality Fourier lens and detector. An ultrasonic dispersion system was employed to ensure optimum results.

The SYMPATEC model used in this work can only measure suspended particles. The suspensions were prepared by typically mixing 1 g of the sample with 4 ml of deionised water containing 1 drop of dispersant (silicone oil). The sealed container was shaken and put in ultrasonic bath for approximately 5 minutes to allow the powder to disperse in the fluid. Normally, 3 drops of suspension were used for each PSD measurement. Each sample was repeated 3 times to ensure the results were reliable.

3.2.2 X-ray Fluorescence Elemental Analysis

3.2.2.1 Introduction of X-ray Fluorescence

X-ray Fluorescence (XRF) quantifies the secondary X-rays generated from the material of interest when that material is irradiated by a high energy source (X ray, electron or ɣ radiation) (133). If X-rays are used as the high energy source, they are regarded as the primary X-rays. Every element can be excited by the high energy primary X-rays and emit secondary X-rays which exhibit characteristic energies and wavelengths. By measuring the energy intensity as a function of wavelength of the X-ray fluorescence, elementary composition and concentration can be determined (134). According to theory, all the elements heavier than beryllium can be analysed (135). However, due to the limitation of the testing instrument, normally the

effective measurement range is from fluorine (F) to uranium (U) (133).

The XRF method emerged as a technique about 80 years ago and has developed in to a sophisticated method. It has several advantages over other elemental measurement techniques including high efficiency, non-destructive, high precision, wide applicability (solid, powder, liquid samples). XRF has been widely used in various fields, such as metallurgy, geology and construction (136).

3.2.2.2 Principles of XRF

X-rays are a type of electromagnetic radiation which is generated by the electron transition between two energy levels in atoms. The wavelength range of X-rays is between γ-rays and ultraviolet rays and has a typical value from 0.01 to 10 nanometres (137).

The phenomenon of X-ray fluorescence is generated from the internal changes of the atoms. A stable atom is composed by nucleus and electrons which move in fixed orbits based on their own energy level. However, when the inner electrons (for instance, K-shell electrons) are exposed to high energy X-rays, they will get excited and break away from their own orbit. Thus, the released electrons will leave a hole in the lower orbit which causes instability of the atom structure. As a result, the electrons from higher energy orbit (for example, L-shell electrons) will cascade into this hole to keep the electronic structure stable. Because there is an energy difference between the two orbits, the energy will be released in the form of secondary X-rays during this process (134). The schematic diagram of X-ray fluorescence is shown below in Figure 3.2.

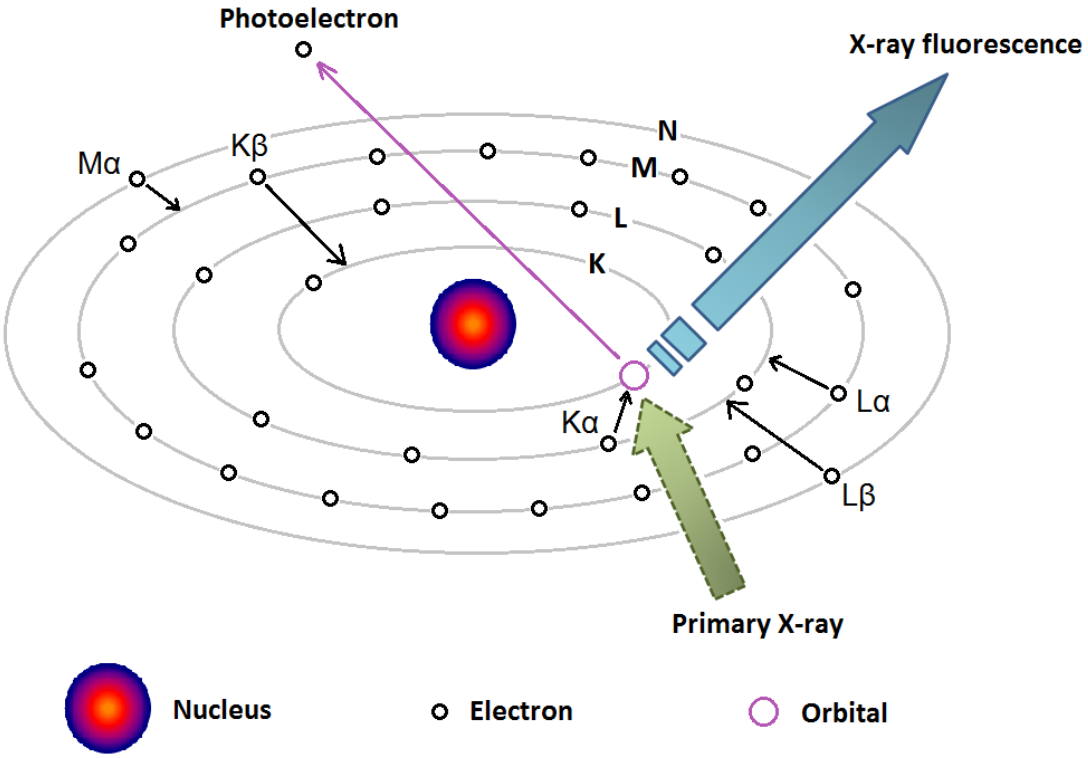

Figure 3.2 Schematic diagram of X-ray fluorescence; Modified from (137)

Every element can emit X-rays with characteristic wavelength when the inner electrons are exposed to high energy radiation. According to Moseley's law, the wavelength of X-ray fluorescence (λ) is related to the atomic number of the element (Z) (138). The mathematic relation is shown below:

$$\lambda = K(Z - s) - 2 \tag{3.1}$$

where the *K* and *s* are constants that depend on the type of lines. As can be seen from Figure 3.2, normally, the L-shell to K-shell transition is called K_α line, and the M-shell to K-shell transition is called K_β line, and so on.

According to the quantum theory, the X-rays can be regarded as a type of photon flow, the energy of the fluorescent radiation can be described by Plank's law:

$$E = h\nu = \frac{hC}{\lambda} \quad (3.2)$$

where: *E* stands for the energy of the photon (unit: keV); *h* is Planck constant; *v* is the frequency of the light wave; *C* is the velocity of light (136). Therefore, by measuring the wavelength or the energy of the X-ray fluorescence, the elements can be analysed. In addition, the intensity of the X-ray fluorescence is related to the proportion of the element present, thus, the full elemental composition of the materials can be analysed (134).

3.2.2.3 Experimental instrument and procedure

The concentration of elements can be calculated either by analysing the wavelength or the energy of the X-ray fluorescence. Thus, there are two types of XRF devices, which are the wavelength dispersive X-ray fluorescence (WD-XRF) spectrometer and energy dispersive X-ray fluorescence (ED-XRF) spectrometer (137).

In this study, the elemental analysis was carried out on a BRUKER S8 TIGER WD-XRF spectrometer. A schematic diagram of the WD-XRF spectrometer is shown in Figure 3.3. As can be seen from the diagram, an X-ray source generates high intensity X-rays and irradiates the sample surface. The excited X-ray fluorescence passes through the collimator to the dispersive crystal. The dispersive crystal separated the photons to single-wavelength radiation by diffraction, the diffracted wavelengths are detected. By adjusting the position of the crystal, X-ray fluorescence of all wavelengths can be detected and thus all the elements in the sample can be analysed (136).

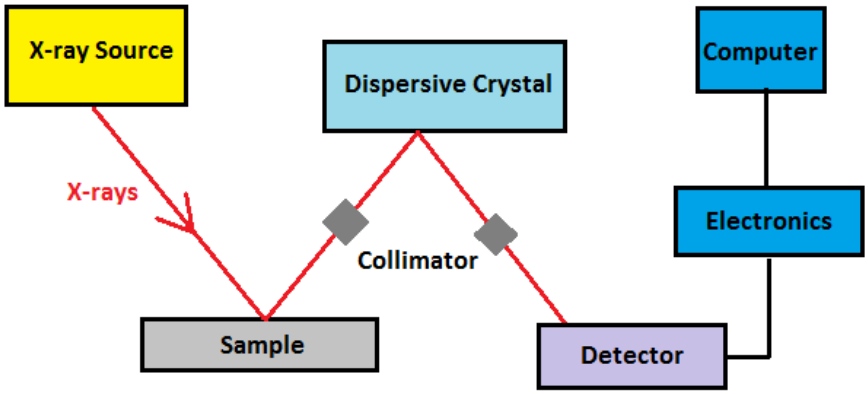

Figure 3.3 Schematic diagram of WD-XRF spectrometer

In this study, typically about 7 g powder samples and 1.4 g wax (CEROX Licowax C Micropowder) were mixed and ground. The resultant mixture was pressed to form a 34 mm diameter pellet as testing specimen. In order to achieve more accurate results, 'Best Scan' (20 min scanning time) was applied to all measurements. Each sample was tested 3 times to ensure the reliability of the results.

3.2.3 X-ray Diffraction Phase Analysis

3.2.3.1 Introduction of X-ray diffraction

X-ray diffraction (XRD) is an analytical method that can identify the crystal structure and chemical bounds of materials. The wavelength of X-rays and the spacing between the atomic planes of the crystals are similar (139). Therefore, crystals can be regarded as a diffraction grating for the X-rays. When a monochromatic beam of X-rays irradiates on the surface of crystals, it will be scattered by the atomic layers of the crystals. The scattered wave will interfere with others as a result of producing diffractions. At certain angles the diffracted waves will be in phase and observable to a detector. By analysing the X-ray diffraction patterns, the crystal structure can be

obtained (140).

From the 1970s, with the development of high intensity X-ray generators, combined with high sensitivity detector and computer analysis, XRD became one of the most effective approaches to investigate the microstructure of crystalline materials (141). XRD is the most dominat method in phase analysis, qualitative analysis and quantitative analysis of crystal materials. It is widely used in the fields of metallurgy, chemical and general materials.

3.2.3.2 Principles of XRD

X-rays are a type of optical radiation which generated by atomic transition when the inner electrons are bombarded by high-speed stream of electrons. There are two main types of X-rays which are continuous X-rays and characteristic X-rays (141).

As stated above, crystals can be regarded as a grating of X-rays which cause interference effects of the coherent scattering. This means the intensity of the X-rays will be either enhanced or weaken by this effect. The most intensive beam is called X-ray diffraction (142).

The X-ray diffraction follows Bragg's law which can be described by the equation below:

$$n\lambda = 2d\sin\theta \tag{3.3}$$

where in the equation: n stands for diffraction series which can be any positive integer; λ is the wavelength of the X-ray; d is the spacing between parallel atomic planes; θ is the angle of incident X-rays (140). The schematic diagram of Bragg

diffraction is shown below in Figure 3.4.

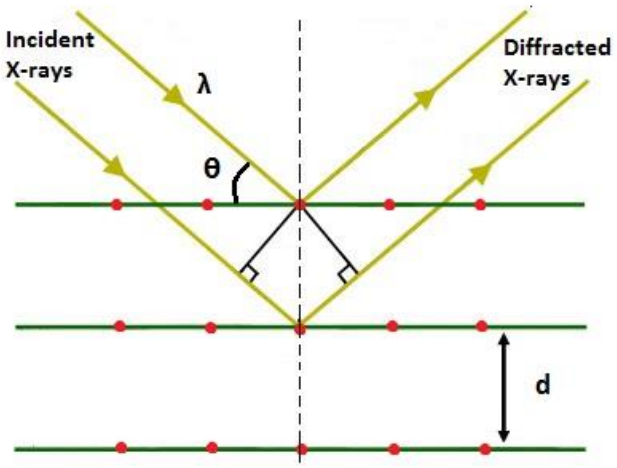

Figure 3.4 Schematic diagram of Bragg diffraction

Based on Bragg's law, it can be seen that the X-ray diffraction can be used for analysing the crystal structure of powder samples (polycrystals) or identifying the elements of single crystals (143).

For crystal structure analysis, by exposing the samples to X-ray with a fixed wavelength (characteristic X-ray), the X-rays will be reflected on each crystal face which meet the conditions of the Bragg's law. By measuring the θ value, the d (interplanar spacing) can be calculated and, the crystal structure deduced (141).

A schematic diagram of the working principles of the X-ray diffractometer is shown in Figure 3.5 (143).

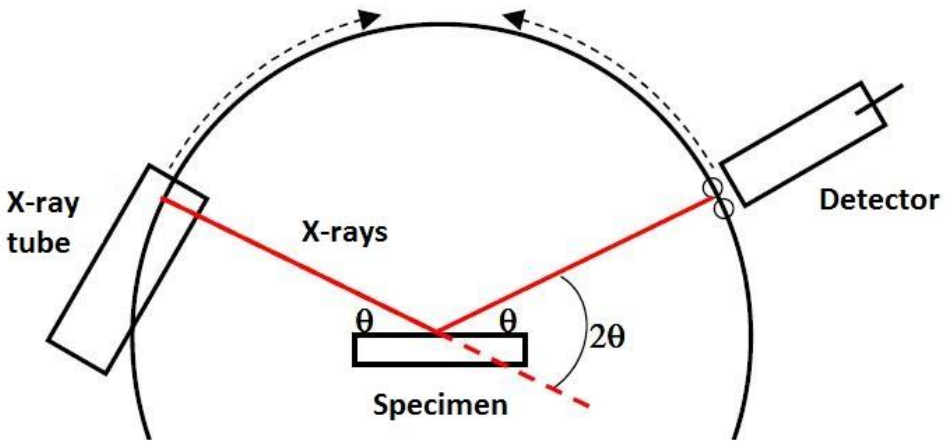

Figure 3.5 Schematic diagram of X-ray Diffractometer; Modified from (140)

As can be seen from the diagram, a specimen which contains a set of random crystals of small size was placed on the holder and exposed to a monochromatic X-ray beam. According to Bragg's law, the X-ray was diffracted by certain sets of parallel lattice planes. In a θ: θ instrument, the sample stayed still while the X-ray tube rotated at θ·min^{-1} and the detector was rotating at 2θ·min^{-1}. By detecting all the X-ray diffraction which satisfied the Bragg's equation, the intensity versus 2θ diffraction pattern was generated (141). By comparing the pattern to the database, the crystal structures of the materials could be determined.

3.2.3.3 Experimental instrument and procedure

In this study, all the crystallographic results were obtained by using an INEL EQUINOX 3000 X-ray diffractometer. Both ground powder samples and smooth surface pellet specimens were used as specimens in the XRD analysis to identify the phases in the materials. The K_α lines of copper (CuK_α, λ = 0.15418 nm) were used as the X-ray source. The XRD patterns were obtained by the computer in the formation of Intensity against 2θ graph. By using the software '!Match', the patterns were

compared with 'The Inorganic Crystal Structural Database' (144). Thereby, the crystal structures of the samples were recognized.

3.2.4 Scanning Electron Microscopy and Energy Dispersive X-ray Spectroscopy Analysis

3.2.4.1 Introduction of Scanning Electron Microscopy and Energy Dispersive X-ray Spectroscopy

The Scanning electron microscope (SEM) allows detailed morphological observation (145). SEM uses a focused electron beam to scan the specimen. The electron beam and sample interact with each other to generate various effects. The main effect is the emission of secondary electrons from specimens which can produce surface topography signals. The signals are gained in chronological order during the scanning by the detector and analysed to form an image (146).

SEM has several advantages compared to the optical microscope. First, it can achieve very high magnification which can be adjusted from 20 to 200,000 times continuously (147). Second, the images are two dimensional with a large depth of field which can show the fine structure of uneven surfaces. Third, the specimens are easily prepared (148).

At present, most SEMs are equipped with energy dispersive X-ray spectroscopy (EDS). EDS can provide elemental analysis of the sample by detecting and analysing the characteristic X-rays which emitted from the sample. EDS has high efficiency as it can analyse the X-rays emitted from all the elements at the same time while the

wavelength dispersive X-ray spectrometer (WDS) can only measure one element after another (149).

SEM is used widely in biology, chemistry and medical science areas (150).

3.2.4.2 Principles of SEM and EDS

The physical principle of SEM is based on the interaction between electrons and materials. When a high energy focused electron beam is scanning the sample, various physical signals are aroused. By detecting, analysing, amplifying and imaging these signals, the surface morphology of the samples can be generated (145).

As can be seen from Figure 3.6, when a high energy focused electron beam is bombarding on the surface of a specimen, several signals are generated from the excited area, including secondary electrons, backscattered electrons, auger electrons, transmitted electrons, characteristic X-rays, continuous X-rays, and other electromagnetic radiations (145).

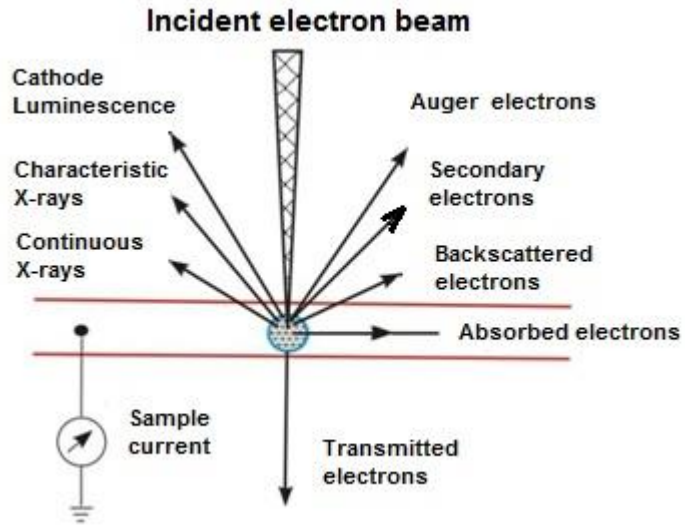

Figure 3.6 Interactions between electrons and sample; Modified from (145)

Secondary electrons (SE) refer to the extranuclear electrons which are emitted during bombardment by the incident electron beam. The secondary electrons typically have a surface area of 5 - 10 nm^2 with energy of 0 - 50 eV (150). Because the secondary electrons are emitted from sample surface, the incident electron has not been reflected. Thus, the area which produces secondary electrons is basically the same as the irradiated area. This means the resolution of the secondary electron image is very high. The yield of secondary electrons does not change greatly with the atomic number (150). It mainly depends on the surface appearance.

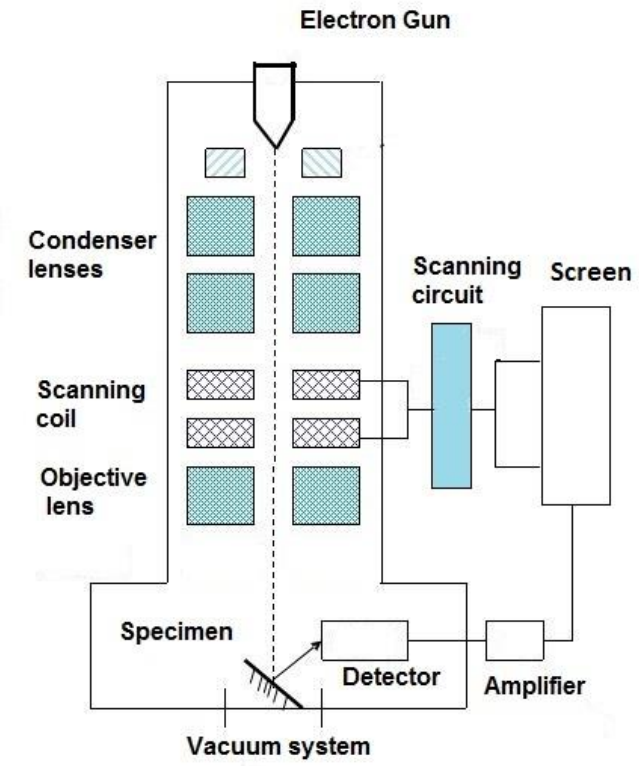

Figure 3.7 Structure and schematic diagram of SEM; Modified from (147)

Backscattered electrons (BSE) are the reflected incident electrons from the atoms of the sample. It includes elastic scattering and inelastic scattering (145). Elastic

backscattered electrons are reflected from the nucleus while the inelastic backscattered electrons are rebounded by the extranuclear electrons. The amount of elastic backscattered electrons is far more than the inelastic ones. The resolution of the backscattered electron image is lower than the secondary electron image. The yield of backscattered electrons is increased with the atomic number. Therefore, this signal can be used to observe the distribution of various elements (151).

The principles of characteristic X-rays generation are similar to X-ray fluorescence. The only difference is the incident radiation in this case is an electron beam rather than X-rays. By detecting these signals, the elements in the sample can be identified (149).

SEM uses various types of detector according to the different mechanism of signal formation to analyse many physical and chemical properties of the sample. Structure chart of a typical SEM is shown in Figure 3.7 (147).

A typical SEM comprises a power system, vacuum system, electron optical system, signal acquisition and display system. As can be seen from Figure 3.7, the electron gun which is equipped with a tungsten filament cathode emits an electron beam which is focused by electrode grids to form a light beam source with around 50 nm diameter. The electron beam passes 2 pairs of condenser lenses under 2 – 30 KV acceleration voltage which can converged the beam to a spot of 5- 10 nm^2 and focused on the surface of specimen (151). There are pairs of scanning coils above the objective lens which control the electron beam scanning on the surface. The high energy electron beam interacts with sample and produces various signals (for

example secondary electrons, backscattered electrons and characteristic X-rays). These signals are received by different kinds of detectors, following by amplification processes to adjust the brightness of the screen (150). When the electron beam is focusing on a point of the sample, there is a luminescent spot on the screen correspondingly. By scanning from upper left to lower right, one image can be produced.

EDS equipment is usually incorporated in SEM systems for qualitative and quantitative elemental analysis. The working principle of EDS is quite similar to WD-XRF (refer to Section 3.2.2.3) (149). The simplified schematic diagram of EDS is illustrated in Figure 3.8.

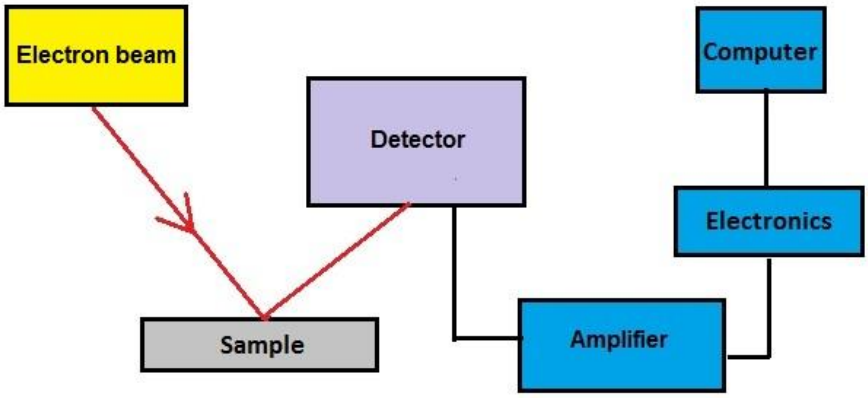

Figure 3.8 Schematic diagram of EDS

Compared with WDS, there is no dispersive crystal in the EDS and it uses silicon semiconductors as detector to convert the energy of the photons to voltage signals. EDS can analyse quicker than WDS but less accurate (149). Due to its high efficiency, portability, EDS is widely used in combination of SEM, especially with backscattered electron image.

3.2.4.3 Experimental instrument and procedure

In this study, a PHILIPS XL-30 ESEM was used to observe the morphology of the samples while an OXFORD X-ACT EDS was used to identify the elemental distribution within the SEM images.

The ESEM stands for environmental SEM which is equipped with field emission guns that can produce a higher brightness electron beam with smaller spot size compared to the conventional SEM (152). Moreover, the ESEM can analyse materials under various conditions, for example humid or oxygen atmospheres.

In this study, both powder and solid samples were observed under SEM and EDS. There were three types of samples, unprocessed specimens, polished specimens and thermal etched samples. The details can be seen in Table 3.1.

Table 3.1 Details of SEM specimens

	Unprocessed Sample	**Polished Sample**	**Thermal Etched Sample**
Risen Mounting	N/A	Epoxy resin	Epoxy resin
Polishing	N/A	Four-step polishing	Four-step polishing
Thermal Etching	N/A	N/A	1.8 hours
Coating	Gold	Gold or Carbon	Gold

The unprocessed specimens were mainly used to gain information about raw materials and also on the fracture surface of the products after mechanical strength testing (refer to Chapter 6).

In order to get clearer images, with more information about phase distribution and more accurate EDS results, the samples were polished (148). In this study, typically samples were embedded in about 9.3 g liquid epoxy resin with hardener. The specimens were left over 24 hours to cure to give a sample which was 30 mm in diameter and 15 mm in height. Specimens were polished by 4 steps which are detailed in Table 3.2.

Table 3.2 Polishing details

	Step 1	**Step 2**	**Step 3**	**Step 4**
Disc	MD-Piano	MD-Allegro	MD-Largo	MD-Cloths
Solution	Water	9 µm (grain size) Diamond Solution	3 µm (grain size) Diamond Solution	1 µm (grain size) Diamond Solution
Time	20 min	10 min	10 min	2 min

The polishing process was carried out by using a STRUERS MD-Grinding Disc Set and STRUERS Diamond Suspension Set on a STRUERS Laboforce-3 grinding and polishing machine. By changing the grinding discs and reducing the grain size of grinding solutions step by step, the samples were polished to a mirror like surface finish.

For revealing the grains size and grain boundaries, a thermal etching process was conducted for most samples (148). After the polishing process, the samples were

taken out from resin pellets by dissolving (in acetone) and cutting without damaging the polished surface.

Although the thermal etching conditions were varied for specific materials, because most samples had very similar composition, a general thermal etching progress could be developed. Several samples of a typical product were selected and then different thermal etching programmes applied by starting with sintering 0.5 hour at 100 ℃ below original sintering temperature (148). After this, the specimens were observed under SEM and the optimal conditions were determined. The result of the thermal etching trials are shown above in Table 3.3. It can be seen that sintering at 100 ℃ below original sintering temperature for 1.8 hours could achieve the best outcome.

Table 3.3 Results of thermal etching conditions

Treated time / Temp.	0.5 h	1 h	1.5 h	1.8 h	2 h
100 ℃ below sintering temperature	No change	Under etched	Slightly under etched	Nicely etched	Over etched

The specimens were coated with a gold film to get better images. The representative appearances of these 3 kinds of samples are shown below in Figure 3.9.

The samples were typically observed by using 20 kV filament voltages under magnification of 1500×, 3500×, 6500×, 10000× and 20000×. Secondary electron images were obtained to get the morphology of the materials. Backscattered

electron images were used to study the phase distribution in combination of EDS for elemental analysis.

Figure 3.9 Typical appearances of 3 types (unpolished, polished, thermal etched) samples

3.2.5 Measurement of Density

3.2.5.1 Introduction of Density

Density can be expressed as:

$$\rho = \frac{m}{V} \tag{3.4}$$

where ρ is the symbol of density; m is mass and V stands for volume (153). This means density is the mass per unit volume of the material.

Apparent density is the ratio of mass and total volume which includes the volume of particles, open and closed pores (154). It normally indicates the apparent density of materials in the dry condition. True density is the ratio of mass and volume of particles (154). That is to say, the volume of pores needs to be eliminated. This is a well-defined quantity as it will not change with the compaction of the materials.

Generally, no matter what the material is and what phases it is in, the density will change along with the temperature and pressure (153). This variation of density for solids and liquids is very small while it can change dramatically for gases.

3.2.5.2 Principles of density measurement

Apparent density is normally measured after the drying process at room temperature. For materials with regular shape, it can be calculated by measuring the mass and volume. The mass is usually measured by an electronic balance and the volume is measured by an electronic vernier calliper. For irregular shaped substances, the volume can be measured by liquid displacement method after filling the pores by wax or coating the shape with a protective film such as varnish (155).

True density is normally measured by a gas expansion pycnometer . It can measure the true volume of the samples based a on gas displacement technique and Boyle's law which is described by the equation:

$$V = \frac{k}{P} \tag{3.5}$$

where V stands for volume of gases; P is pressure and k is a constant. This means the volume is inversely proportional to pressure while the temperature and quantity of the gas are fixed (155). A schematic diagram of a typical gas expansion pycnometer is shown below in Figure 3.10.

A typical gas pycnometer comprises a transducer, two chambers and three valves. Firstly, the sample is loaded into the sample chamber and sealed. Then, valve 1 is opened and certain amount of gas goes into the chamber. The pressure P_1 is

recorded by the transducer. Secondly, the gas goes through the pathway into the expansion chamber when valve 2 is opened. After a few seconds, the pressure in the two chambers achieves a balance and the value P_2 is also measured by the transducer. The gas is vented out by opening valve 3. The volume of the two chambers is known by previous calibration (156).

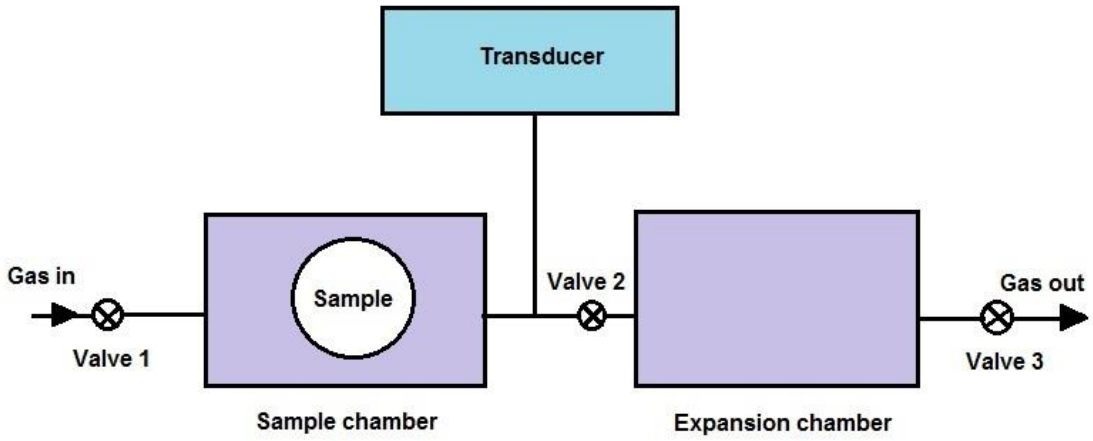

Figure 3.10 Schematic diagram of gas expansion pycnometer; Modified from (156)

Based on this information, the sample volume can be calculated by using the equation (155):

$$V_S = V_{SC} + \frac{V_{EC}}{1 - \left(\frac{P_1}{P_2}\right)} \tag{3.6}$$

where V_S is the volume of sample; V_{SC} is the volume of empty sample chamber and V_{EC} is the volume of expansion chamber. Therefore, the true density can be calculated.

Most gas pycnometer uses helium as the working gas (156). Because helium is an inert gas with very small molecular diameter it can easily diffuse and has good

permeability. Helium can fill the pores and rough surface of the sample easily and rapidly. All these properties make the measurement extremely accurate.

3.2.5.3 Experimental instrument and procedure

In this study, the samples were regular shaped as either pellets or rods were manufactured (refer to Chapter 5). Therefore, the apparent density could be calculated by measuring the weight and volume of the samples.

An A&D GALAXY HR-AZ Analytical Balance was used for weight measurement. The dimensions of the samples were measured by using a TOOLZONE 150 mm Digital Vernier Calliper accurate to ± 0.01 mm. Then the data of apparent densities was obtained.

The true density measurements were undertaken on a MICROMERITICS AccuPyc II 1340 Gas Displacement Pycnometer. Before testing, the pellet and rod samples were crushed into several small pieces by hammer in order to increase surface area and expose more pores. The samples were dried at 101 ℃ for 5 hours in a HERAEUS UT6200 Oven to vaporize the moisture. Each sample was measured by 20 testing cycles to ensure the accuracy and reliability. The final result was shown as an average value.

3.2.6 Measurement of Flexural Strength

3.2.6.1 Introduction of mechanical strength

Mechanical strength indicates the maximum load per unit area that a material can

sustain when an external force is applied. Mechanical strength can be measured by various methods and give compressive strength, tensile strength and flexural strength (Figure 3.11) (157).

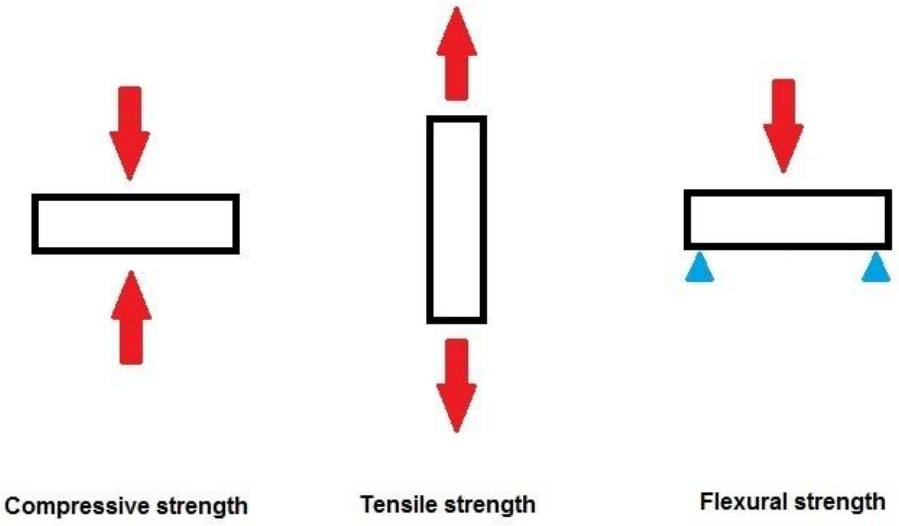

Figure 3.11 Different types of mechanical strength; Modified from (157)

Compressive strength indicates the ultimate strength when the external force is uniaxial pressure. This means when the pressure exceeds this value, it will cause ductile or brittle failure of the material (158).

Tensile strength is the ratio of maximum tension and cross sectional area when the tensile force leads a failure of the materials. It can characterize the resistance of a metallic material to homogeneous plastic deformation. For brittle materials which have very small plastic deformation, tensile strength is used to reflect the fracture resistance (159). Difficulties in fixing often prevent its application to ceramics.

Flexural strength which is also known as bending strength indicates the ultimate fracture stress in the material at the moment of rupture. That is to say when an

external force applied vertically on the axis of the solids, the object will be bended until ruptured (160). Generally, the 3 or 4 point bending or disc flexure are employed (158). The flexural strength is mainly used for analysing the mechanical property of brittle materials.

The mechanical strength of a material mainly depends on its microstructure (161). Therefore, testing the mechanical strength can help understanding the properties of different materials. Mechanical strength measurement is widely used in the ceramic, metallic and construction industries (162).

3.2.6.2 Principles of 3-point bending test

The 3-point bending test is the most widely used method for flexural strength measurement (163). A schematic diagram of 3-point bending test is shown in Figure 3.12 (164).

A test fixture for a beam comprises two supporting rollers which can be adjusted for span. Typically load is exerted on the specimen at a constant rate at the centre of the span. A rectangular or circular shaped beam is usually used for this test. Normally the support span is 10 times of the depth of a rectangular sample or 10 times of the diameter of a circular specimen (164). Combining the maximum force applied with the dimensions of the sample and test fixture, the flexural strength can be calculated by using the Equations 3.7 and 3.8 (165):

$$\sigma = \frac{3FL}{2bd^2} \tag{3.7}$$

$$\sigma = \frac{FL}{\pi R^3} \tag{3.8}$$

where the σ represents flexural strength; F is the load at moment of rupture; L is the span of between two support rollers; b and d stands for width and depth of a rectangular sample respectively; R is the radius of a circular specimen. Equation 3.7 is for rectangular samples and Equation 3.8 is for circular specimens.

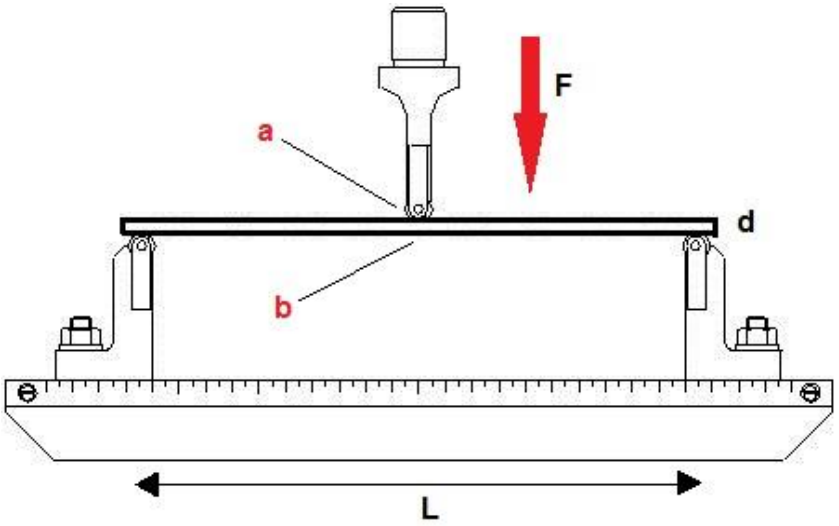

Figure 3.12 Schematic diagram of 3-point bending test; Modified from (164)

As can be seen from Figure 3.12, point 'a' of the sample is under compressive stress while point 'b' is under tensile stress. In most cases, the material fails at the point of maximum tensile stress. This means if the material is homogeneous, the flexural strength should be same as the tensile strength. However, commonly there are flaws present which will reduce the resistance to tensile stress. Thus, the flexural strength is normally higher than the tensile strength for the same material (164).

The 3-point bending test has several advantages. The testing fixture is easily manufactured and adjustable. The specimens can be rectangular or circular in cross

section which provides flexibility of sample preparation. However, this method is a uniaxial strength testing approach which may cause sensitivities about specimen geometry, loading geometry and edge defects (164).

3.2.6.3 Principles of ball on 3-ball (B3B) test

The ball on 3-ball test is a biaxial flexural strength measurement method. Compared with 3-point bending test, B3B test is not as sensitive to the test geometry, edge defects of sample and frictions between supporting balls and samples (166). This means B3B test can be more accurate (167). It can only test pellet samples within a certain range of diameter based on the dimensions of the testing fixture. A schematic diagram of B3B test is shown below in Figure 3.13.

This test fixture consists of a base with 3 hemispherical balls which are placed in an equilateral triangle arrangement and fixed to a universal testing machine. Another ball is on top of the specimen and fixed to the loading cell. A disc sample of the required diameter is then set in the centre of the 3 balls and under the upper ball. Load is applied to the central ball and specimen at a fixed rate until rupture.

According to previous work (168, 169), the required parameters of the specimen to give the optimum accuracy and reproducibility are listed in Table 3.4, where R is the radius of sample pellets; R_s is the radius of the testing balls; t is the thickness of the specimen and ν is the Poisson's ratio of the material.

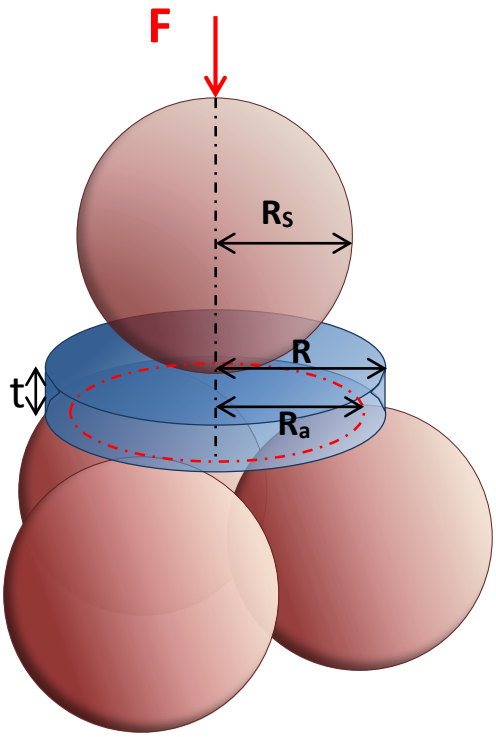

Figure 3.13 Schematic diagram of ball on 3-ball test; Modified from (170)

Table 3.4 Parameters of specimen for B3B test

Parameter	Evaluated Range
R_s/R	0.5 – 0.82
t/R	0.035 – 0.5
ν	0.10 – 0.40

The strength is calculated using (169, 171):

$$\sigma = f\frac{F}{t^2} \tag{3.9}$$

where the σ is the flexural strength; F is the load at moment of rupture; t is the thickness of the sample disc; f is the dimensionless pre-factor which determined by

the dimensions of the specimen and the Poisson's ration of the sample material. It can be calculated by using certain software (170).

3.2.6.4 Experimental instrument and procedure

In this study, both 3-point bending test and B3B test were applied to measure the mechanical strength of the products. All the tests were conducted on an INSTRON 4467 Universal Testing System.

The 3-point bending test was used for analysing the products from extrusion (refer to Section 5.4). The samples were extruded and sintered rods with a diameter of about 2.6 mm and about 35 mm in length. The support span of the test fixture was set as 30 mm. An INSTRON 2525 Series Drop-Through Static 100 N Loading Cell was used to measure the applied force.

The diameter of each rod was measured by a TOOLZONE 150 mm Digital Vernier Calliper which accurate to ± 0.01 mm and recorded before loading on the test fixture. The movement rate of testing pin was set as 1 mm per minute. The force at the moment of rupture was recorded. Each type of materials was tested 6 times to ensure the reliability. The flexural strength was calculated according to Equation 3.8.

The B3B test was conducted for measuring the strength of pellet samples which were produced by dry pressing and sintering process (refer to Section 5.4.4). The test fixture was designed and manufactured by using hardened stainless steel while the contacting balls were hardened tool steel. Figure 3.14 shows the detail of the test fixture.

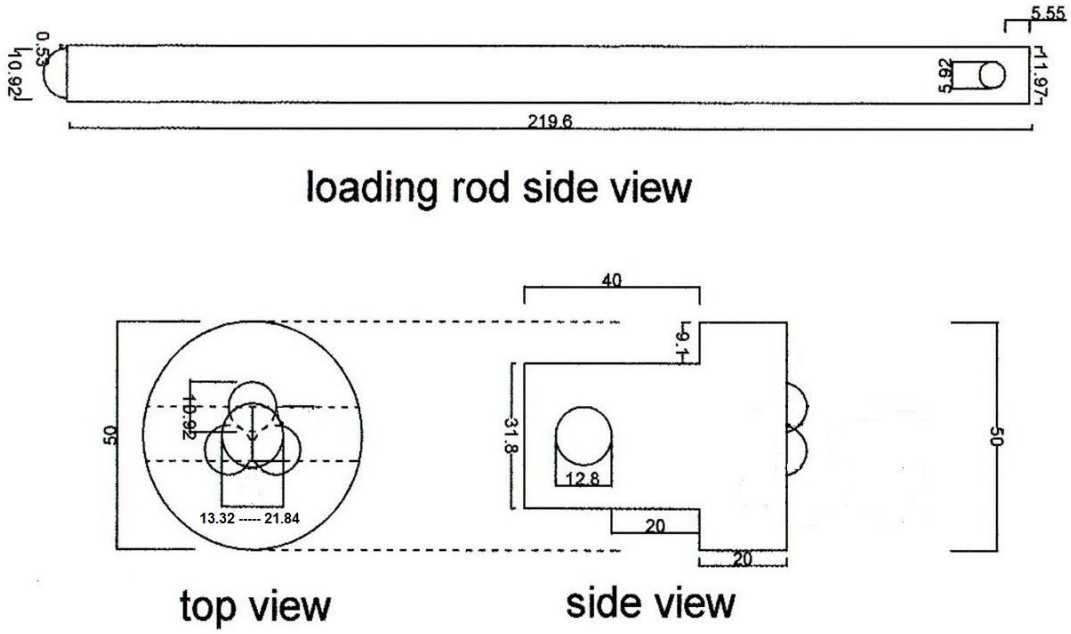

Figure 3.14 Structure diagram of B3B test fixture (UOB design)

As can be seen from the diagram, the diameter of the support balls and loading balls was 10.92 mm. The diameter range of the specimen was calculated based on Table 3.4 which gave the value range from 13.32 mm to 21.84 mm. The pellets used for the test typically had 16.00 mm to 18.00 mm diameters and 2.00 mm to 4.00 mm thickness.

The dimensions of each specimen were measured by a TOOLZONE 150mm Digital Vernier Calliper and recorded before loading on supporting balls. An INSTRON 2525 Series Drop-Through Static 30 kN Loading Cell was used for the tests with a movement speed of 1.0 mm per minute. The force at the moment of rupture was recorded. The photo of B3B testing system and a typical ruptured specimen is displayed in Figure 3.15.

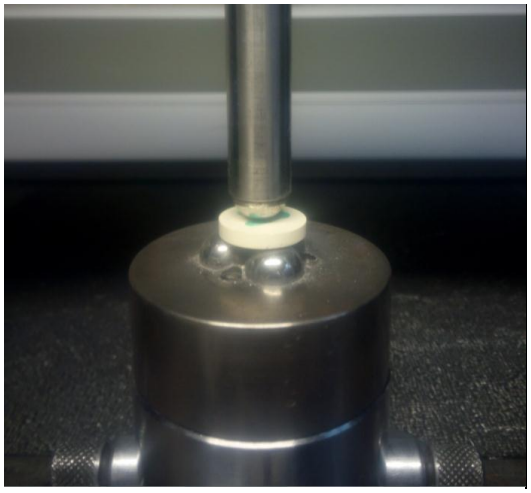
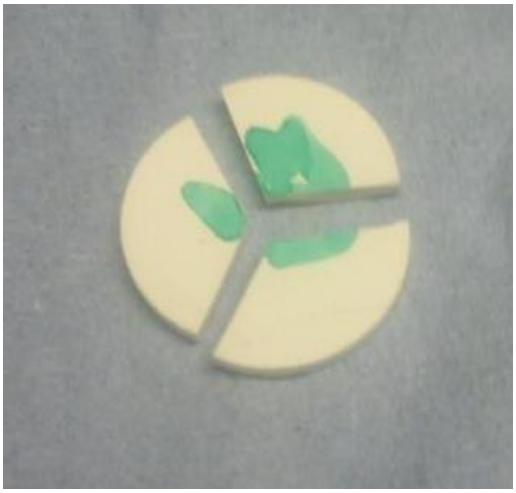

Figure 3.15 B3B testing system and a typical tested specimen (Ø =16 mm)

Each type of products was tested 6 times to ensure the reliability of the results. The Poisson's ratio of the materials was determined by using CRC Materials Science and Engineering Handbook (172). Then, the flexural strength was calculated according to Equation 3.9 by using software (170).

3.2.7 Hardness Measurement

3.2.7.1 Introduction of hardness

Hardness is a physical property of materials which indicates the ability of a solid substance's resistance to hard matter pressed into its surface when a compressive force is applied. Differences in hardness value are affected by the materials intermolecular bonds (173). However, there are several hardness measurement methods which provide different scales. Because the mechanical meanings are different among these methods, the value cannot covert from one to another directly. There are three main types of hardness testing methods which are scratch hardness, indentation hardness and rebound hardness (174).

Scratch hardness is generally used for comparing the degree of hardness between materials. The testing material is forced to scratch a metallic bar under certain load which changes the hardness gradually from one end to another. By measuring the position and the length of the scratch, the hardness of the testing material can be described. Moh's hardness is perhaps the most common scratch method which uses ten minerals as the standard for a measurement scale of ten (175). Diamond is the hardest which has been set as grade 10 while talc is the softest, grade 1. However, this method cannot be used for accurate quantitative hardness measurement as the hardness increments are not uniform when the minerals used are tested by other methods.

Indentation is the most widely used technique currently. A specified indenter is pressed into the specimen under an applied load. Then by measuring the degree of surface plastic deformation of the testing material, the hardness can be determined. Normally, the harder material is, the plastic deformation is smaller (176). There are several different indentation tests which are distinguished by indenter type, load range and time of duration. The most common ones are Vickers, Brinell, Knoop, Rockwell, Shore, Barcol hardness (175). Among them Vickers hardness test can be used for all types of materials and gives very accurate hardness values.

The two methods described above are static measures of hardness while rebound hardness is a dynamic test. A specified hammer drops from a certain height onto the testing sample and it will be bounced back. By measuring the height of the rebound, the hardness value can be determined. Rebound hardness is usually used for measuring the resistance to elastic deformation of metallic materials (174).

3.2.7.2 Principles of Vickers hardness test

The Vickers hardness test was firstly invented in 1925 at Vickers Ltd based on the principles of Brinell hardness measurement. It can measure almost every kind of solid material and it is very simple to implement. The schematic diagram of Vickers hardness test is shown in Figure 3.16 (175).

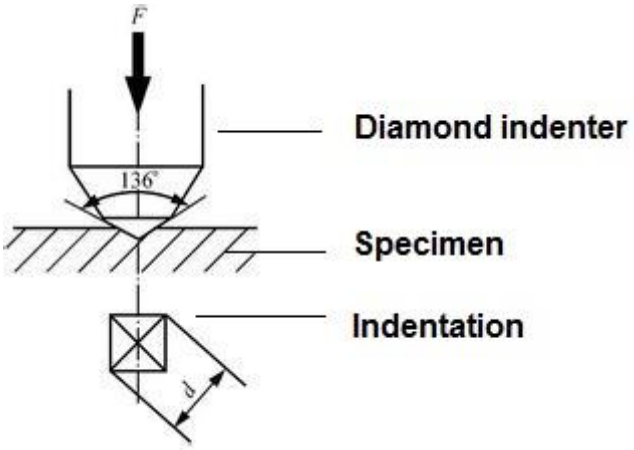

Figure 3.16 Schematic diagram of Vickers hardness test (175)

As can be seen from the diagram, Vickers hardness uses a square pyramidal diamond indenter which has a 136° included angle between two opposite surfaces. During the test, a sample is placed on the platform and then the indenter is pressed into the surface of the specimen and kept under a fixed load for a certain period. Normally, 5, 10, 15, 20, 25, 30, 50 or 100 kg loads can be applied and common loading times are 5, 10, 15, 20 seconds but can be adjusted as required (175).

After removing the indenter, a square shaped indentation is left on the surface of tested material. The length of the diagonals can be measured by using the gauge built into the Vickers hardness tester. Then the hardness value can be calculated by

Equation 3.10 (175).

$$\mathrm{HV} = \frac{2\mathrm{F}\sin\left(\frac{\theta}{2}\right)}{\mathrm{d}^2} = 1.8544\frac{\mathrm{F}}{\mathrm{d}^2} \qquad (3.10)$$

where HV is the symbol of Vickers hardness value; F is the load (kg) used during test; θ is the included angle of indenter (θ = 136°); d is the average diagonal length (mm) of the indentation. Therefore, the unit of the HV value is kg/mm^2.

The results of Vickers hardness test is normally shown in the format as:

$$\boldsymbol{aHVb/c}$$

where a is the hardness number; HV is the symbol to indicate the testing method (Vickers hardness); b shows the load value (kg) and c indicates the loading time (177). In general these should be no visible damage around the indent as this indicates material failure.

3.2.7.3 Experimental instrument and procedure

In this study, all the hardness tests were carried out on an INDENTEC 5030SKV Macro Vickers Hardness Testing Machine. The samples measured were the pellet and rod products from the refractory development process (refer to Chapter 5.).

Polished samples were prepared following the same method as the SEM (section 3.2.4.3) to ensure the testing surface were smooth and parallel.

During the tests, 10 kg was used as the loading force and the loading time was 7 seconds for all tested specimens. The lengths of diagonals were measured and

recorded by using the gauge built in the tester. Vickers hardness values were shown on the screen directly. Each sample was measured 5 times under the same condition to ensure the reliability of the results.

3.2.8 Toughness Analysis

3.2.8.1 Introduction of toughness

Toughness is a very important property of materials. It indicates the ability of a material to absorb energy during plastic deformation and fracture process. Generally the tougher a material is, the more energy is required to rupture it. Toughness can be defined as the ratio of absorbed energy and volume before fracturing. It can be expressed mathematically as:

$$Toughness = \frac{Energy}{Volume} = \int_0^{\varepsilon_f} \sigma \, d\varepsilon \qquad (3.11)$$

where σ is stress; ε is strain and ε_f is the strain upon rupture (178).

Toughness can also be expressed by a stress-strain diagram. Every material has its unique stress-strain curve. Most of materials can be categorized into two behaviours: brittle or ductile according to the stress-strain curve. The typical curves of these two types of materials are shown below in Figure 3.17 (158).

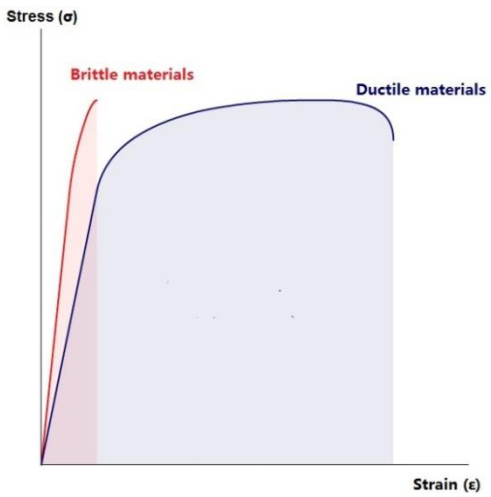

Figure 3.17 Typical stress-strain curves of brittle materials and ductile materials (158)

The area below the curve is toughness which can be calculated by using Equation 3.11. It can be seen clearly from the diagram that the area of the ductile materials is greater than the brittle materials. That is to say the toughness of ductile materials is generally higher than brittle materials.

Normally, the brittle materials can support higher stress than ductile materials which means the strength of brittle materials are generally higher. However, the strain they can withstand is commonly very low which reduces the toughness of brittle materials significantly. There is catastrophic failure but very little plastic deformation when a brittle material is ruptured. A high toughness material must have ability to resist high stress and strain (163).

3.2.8.2 Principles of fracture toughness analysis

Fracture toughness indicates the ability of a material to resist the brittle failure due to crack growth. Fracture toughness is an inherent property of a material which is independent to the external stress intensity and size of cracks (158). That is to say, if

the stress is constant, the crack should be shorter in a tougher material. Fracture toughness is widely used in the analysis of brittle materials.

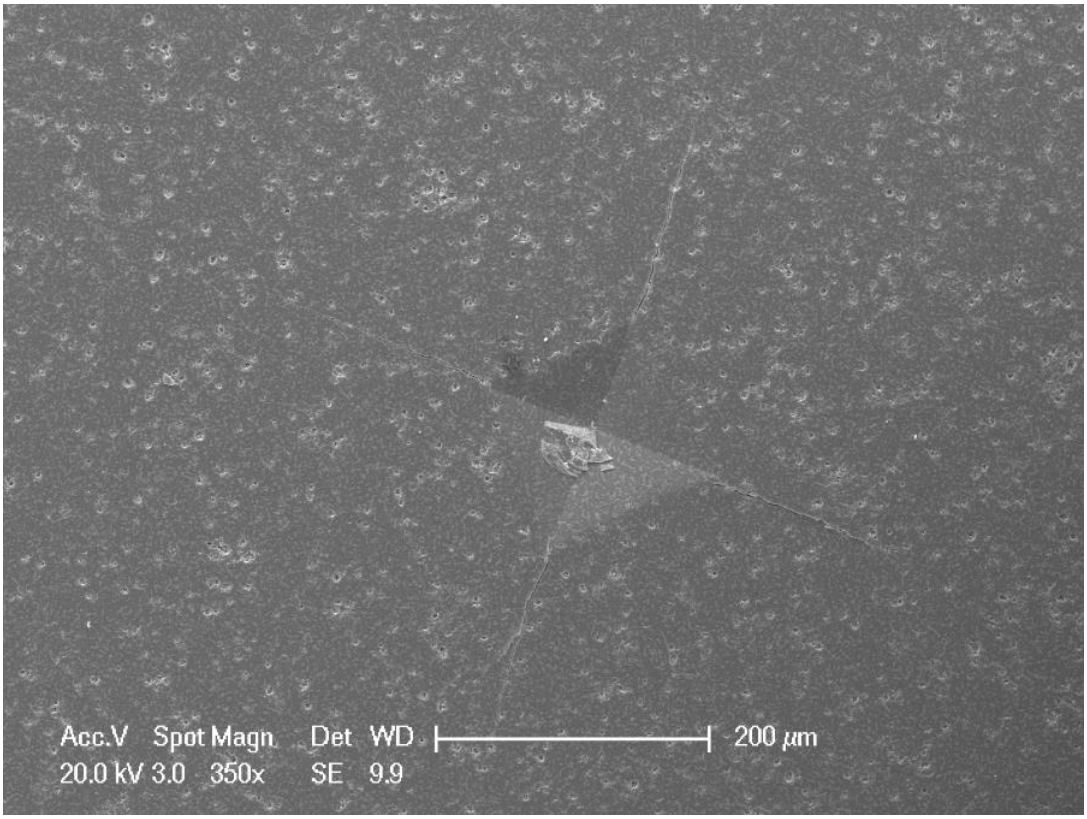

Figure 3.18 A typical indentation SEM image of brittle materials

A common approach used to measure toughness is the indentation method which uses the same equipment as hardness measurement. For brittle materials, cracks will propagate from the four vertexes of the indentation. The indentation SEM image of a typical product from this study is shown in Figure 3.18 showing the cracks of interest. Fracture toughness can be calculated based on the load and the length of the cracks. A widely used equation for the calculation is (164):

$$K_{Ic} = 0.004985 \left(\frac{E}{HV}\right)^{\frac{1}{2}} \frac{F}{C^{\frac{3}{2}}} \tag{3.12}$$

where E is the Young's modulus; F is the load (N); C is the average length of cracks (mm); HV is the Vickers hardness value (GPa). The method receives criticism in the literature when compared to more rigorous approaches such as Single Edge Notch Beam due to its subjectivity. It is acceptable to compare the toughness behaviour of the materials in this thesis to rank their performance but comparison with other works' results published in the literature should be undertaken with caution (158).

3.2.8.3 Experimental instrument and procedure

In this study, the fracture toughness was quantified by using an indentation method. The same specimens, instrument and procedure were used as the Vickers hardness measurement (refer to Chapter 3.2.7.3). During the hardness test, the length of cracks and the load value were recorded for the purpose of toughness analysis. The fracture toughness values, K_{Ic}, were calculated by using Equation 3.12. Five toughness values were generated for every specimen. The average value was shown as the result along with the error recorded as one standard deviation from the mean.

3.2.9 Dilatometry Analysis

3.2.9.1 Introduction of dilatometry

Dilatometry is an analytical method which can measure the functional relationship between dimension changes of the specimens along with the temperature variation (179).

Materials change their volume with temperature and this is called thermal expansion, an intrinsic property. Most materials expand in volume when the

temperature is increasing, and shrink with a temperature reduction (180). However, there are few materials in the opposite sense over a certain temperature range which are called negative thermal expansion materials, zirconia over limited range is an example of such a material (181).

Thermal expansion is a very important character in material science, especially for refractories. As the refractories are used in high temperature applications, different materials which are in contact with each other should match their thermal expansion behaviour as closely as possible to reduce stress and minimize failure (16).

Dilatometry can also be used for investigate other behaviours which may cause volume change of a material, such as chemical reaction, phase transformation, densification, sintering processes, glass transition temperature, softening point detection and additive influence (182).

Dilatometry can analyse most solid materials including ceramics, metals and polymers (182). Liquids can be measured in specialized systems. It has been widely used in refractory, construction and coating industries.

3.2.9.2 Principles of linear expansion analysis

All materials change dimensions in some way with temperature. Most materials expand with heating due to the increased average kinetic energy of molecules caused by heat transfer (180). The distance between molecules becomes greater and consequently the volume of the material is greater.

The degree of the thermal expansivity can be defined as the coefficient of thermal

expansion which can be divided into three types: coefficient of volume expansion, coefficient of area expansion and coefficient of linear expansion (183). Among these, the coefficient of linear expansion is the most significant and commonly used for ceramic materials.

The coefficient of linear expansion indicates the elongation per unit length with 1 ℃ or 1 K temperature rising over a certain temperature range. It can be expressed mathematically as the equation (180):

$$\alpha_L = \frac{1}{L}\frac{dL}{dT} \tag{3.13}$$

where α_L stands for the coefficient of linear expansion; L is the original length; dL is the change of length and dT is the change temperature. The unit of α_L is 1 $℃^{-1}$ or 1 K^{-1}. This process is demonstrated in Figure 3.19.

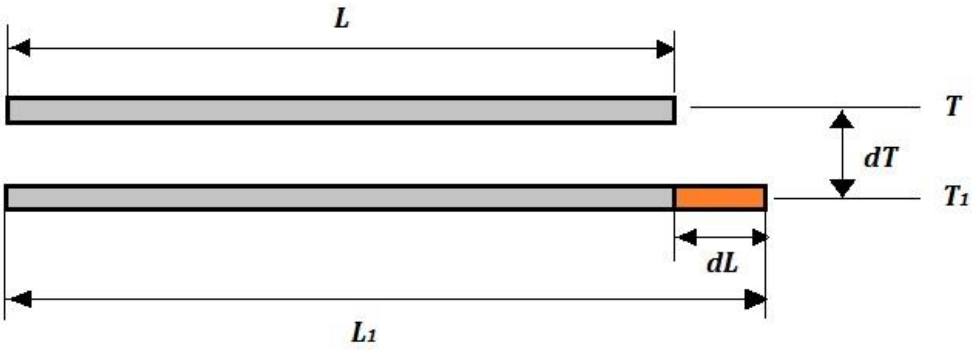

Figure 3.19 Schematic diagram of linear expansion; Modified from (180)

Accordingly, the coefficient of area expansion and the coefficient of volume expansion can be demonstrated as Equations 3.14 and 3.15, respectively (180).

$$\alpha_A = \frac{1}{A}\frac{dA}{dT} \tag{3.14}$$

$$\alpha_V = \frac{1}{V}\frac{dV}{dT} \tag{3.15}$$

Most ceramic materials are isotropic, which means the linear expansion coefficients are same in all directions. This means the other two coefficients can be calculated by using the relations below (180).

$$\alpha_A = 2\alpha_L \tag{3.16}$$

$$\alpha_V = 3\alpha_L \tag{3.17}$$

From these equations, it can be seen clearly that the thermal expansion behaviour of a ceramic material can be studied by identifying the linear expansion coefficient.

There are several factors that can affect the linear expansion coefficient of a material (181):

a. Materials composition, including chemical composition, crystal structure and bond energy. Normally, materials with high bond strength have relatively low linear expansion coefficient. Materials with different crystal structure usually have different linear expansion coefficient.
b. Phase transformation; when a phase change occurs, it can be reflected by the linear expansion behaviour. Generally, the linear expansion coefficient is relatively high in the phase transition temperature range.
c. Porosity. Pores inside the materials can reduce the bond among the grains which can make the material expand more.

3.2.9.3 Experimental instrument and procedure

There are several types of dilatometer, such as capacitance dilatometer, connecting rod dilatometer, optical dilatometer and laser dilatometer (183). The connecting rod dilatometer which is also known as push rod dilatometer is the most common linear expansion measurement method. Generally, it can be divided into horizontal and vertical dilatometer types according to the position of sample. A schematic diagram of a typical horizontal push rod dilatometer is shown in Figure 3.20.

As can be seen form the diagram, it is mainly composed by a sample holder, a furnace, a transmission rod and a displacement sensor. Additionally, a water cooling system and a gas flow system are often incorporated.

The sample is horizontally placed against the end of the holder and the transmission rod is brought in contact with the sample. The sample, holder and rod are heated simultaneously under a pre-set programme. The connecting rod measures the linear changes of the sample and transmits the information to a displacement sensor. Due to the reason that the rod and holder also expands with the temperature change, a correction process is required prior the tests (184).

The system was used to measure the linear expansion coefficient of the sintered refractory products (refer to Chapter 5) and to investigate the chemical reaction and sintering behaviour during the product formation process.

All the tests were conducted on a NETZSCH DIL 402 C Horizontal Pushrod Dilatometer which covered a temperature range of 20 ℃ to 1600 ℃ (practical range: 20 ℃ to

1540 ℃). A standard aluminium oxide (corundum) sample was used for correction prior to the tests.

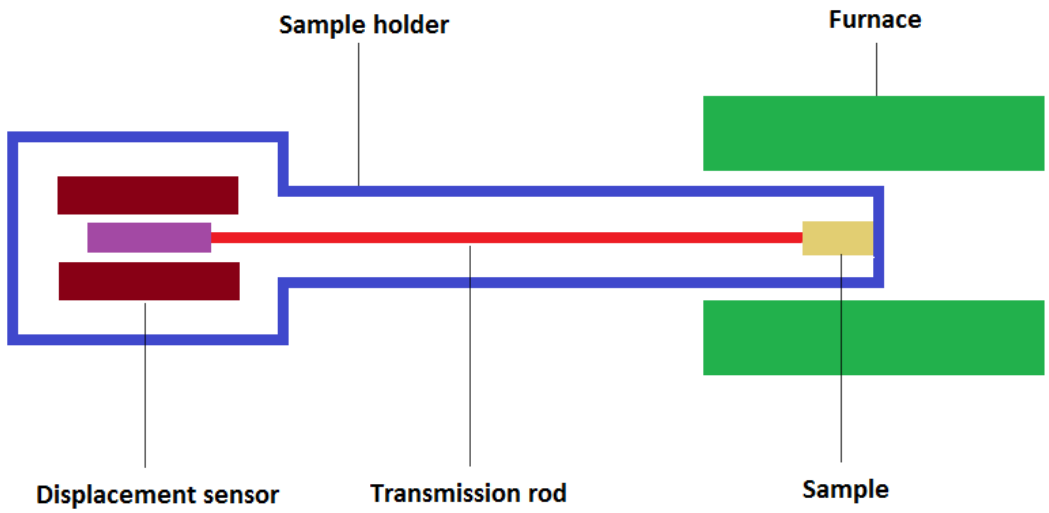

Figure 3.20 Schematic diagram of a typical connecting rod dilatometer; Modified from (180)

The specimens used for dilatometry analysis were pressed by a 13 mm die. Typically, about 8 g powder was used to form a round pellet with 13 mm diameter and about 9 mm height before sintering.

For the linear expansion coefficient measurement, the specimens were sintered in a LENTON 1700 Chamber Furnace by following the programmes of refractory product development process (typically at 1600 ℃ for 2 hours) (refer to chapter V). Then the samples were tested in the dilatometer with a programme which was set to run in three phases: temperature rose at 4 ℃ per minute from room temperature to 1540 ℃; stayed at 1540 ℃ for 1 hour and then cooled down at 10℃ per minute to room temperature.

For the sintering process investigation, the samples were sintered in a LENTON 1700

Chamber Furnace at 1000 ℃ for 1 hour to give the specimen sufficient strength to hold shape. The low fired specimens were tested in the dilatometer with a programme which was set to run in three phases: temperature rose at 3 ℃ per minute from room temperature to 1540 ℃; stayed at 1540 ℃ for 1 hour and then cooled down at 10℃ per minute to room temperature.

Due to the reason that the compositions of the products were very similar, the measurement for each sample was repeated twice.

3.2.10 Differential Scanning Calorimetry (DSC) Analysis

3.2.10.1 Introduction of DSC

DSC measures the input power difference (in form of heat) between a reference material and the specimen as a function of temperature (185). The sample and reference are heated using a certain temperature control programme and always remain at the exact same temperature. The heating rates required for sample and reference to achieve the same temperature at the same time are recorded by the compensators. The relationships between the heating rates and temperature can be analysed.

DSC has now developed to measure various thermodynamic parameters and kinetic parameters, such as specific heat capacity, heat of reaction, reaction rate and sample purity (186). DSC can measure different types of samples including inorganic and organic materials over a wide temperature range from -150 ℃ to 2000 ℃ (187).

3.2.10.2 Principles of DSC

The main principle of DSC is that when a chemical reaction, phase transformation or glass transition occurs, the sample will absorb or release a fixed amount of heat per unit mass (188). The compensator can measure the output power difference between the sample and reference to maintain them at the same temperature. A few typical energy changing processes are (189):

a. No reaction or transition. The heating rates are only related to the specific heats of the samples and references. It shows the base line of a DSC test.
b. Crystallization. During this process, the samples normally release certain amount of heat which will produce an exothermic peak on the DSC curve.
c. Oxidation reaction. This process also releases heat and produces an exothermic response.
d. Decomposition reaction. A certain amount of energy is needed for the materials to break the chemical bonds and an endothermic peak will be recorded on the DSC curve.
e. Fusion. The heat flux is increased to provide the energy required. An endothermic peak will be shown on DSC curve during this process.

Results are shown as a DSC curve where the abscissa axis is temperature or time and the ordinate axis is the heat flux. The area under a peak can be used to calculate the enthalpy of the transition by using (185):

$$\Delta H = KA \tag{3.18}$$

where ΔH is the enthalpy value; K is the calorimetry constant and A is the area of the peak. *K* is specific to each device and can be determined by testing a standard sample.

A schematic diagram of a typical DSC instrument is shown above in Figure 3.21. The sample and reference are placed in the chamber and heated under a temperature control programme. Whenever the temperature difference between the sample and reference appears, the compensator will adjust the input electric current to keep them at the same temperature. Thus, the functional relationship between the thermal power difference and the time is recorded. If the temperature rises at a fixed rate, the functional relationship between the thermal power and the temperature is known (185).

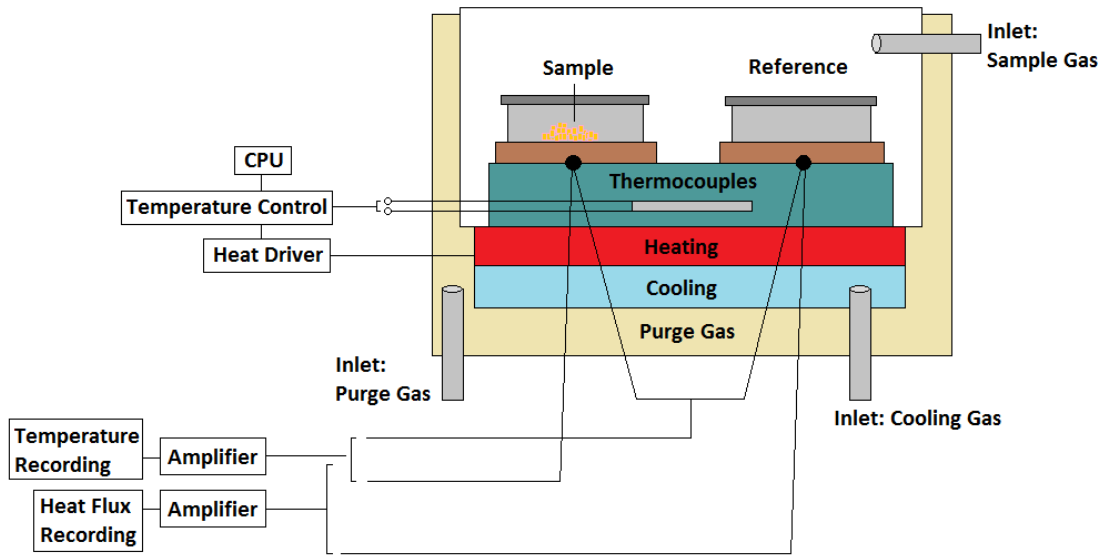

Figure 3.21 Schematic diagram of a typical DSC instrument; Modified from (185)

3.2.10.3 Experimental instrument and procedure

In this study, all the samples were measured on a NETZSCH DSC 404 F1 Pegasus High-

Temperature Differential Scanning Calorimeter. This instrument provided an operating temperature range from room temperature to 1600 ℃ by using a silicon carbide furnace.

Typically, 0.2 g of powder was used as the specimen which was tested in a 85 µl aluminum oxide crucible. The testing programme was set to run in three phases: temperature was raised at 3 ℃ per minute from 1000 ℃ to 1600 ℃; stayed at 1600 ℃ for 1 hour and then cooled down to room temperature naturally. Each sample was tested twice and the DSC curve was obtained.

3.2.11 Thermal Shock Resistance Analysis

3.2.11.1 Introduction of Thermal Shock Resistance

When the surrounding temperature of the material is suddenly increasing or decreasing, there will be significant temperature difference between the surface and interior of the material, which will cause very high thermal stress. This phenomenon is called thermal shock (190).

Thermal shock resistance indicates the maximum temperature change or the maximum times of certain temperature change the materials can sustain without failure. It is known that the thermal shock resistance of a brittle material is related to its properties such as elastic modulus, fracture toughness, sample size, thermal expansion coefficient (107).

Due to the various shapes of the sample and different experimental methods, the thermal stress generated inside the materials are changing with time. There is no

objective true value of the thermal shock resistance of a material which can be measured by a certain testing method (191).

A commonly used method for analyse the thermal shock resistance of ceramic materials is comparing the fractural strength before and after the quenching process (190). This method is usually applied by heating the ceramic specimens to a certain temperature and quenching in the water at room temperature which followed by drying and flexural strength testing process.

3.2.11.2 Experimental instrument and procedure

In this study, the sintered compact pellet refractory samples were placed in a LENTON 1700 Chamber Furnace heated and retained at different temperatures (220 ℃, 420 ℃, 820 ℃, 1220 ℃) for 0.5 hours. The specimens were taken out at the testing temperatures and dropped in about 5 L of water.

After 30 minutes, the samples were taken out from the water and placed in a HERAEUS UT6200 Oven at 101 ℃ for 4 hours to dry. Ball on 3-ball flexural strength test was carried out as described in Section 3.2.6 for the quenched sample. Each sample was repeated 5 times to ensure the results were reliable and the average value was calculated.

3.3 Raw Foundry Waste Materials

In this project, all the ceramic waste materials were donated by a local foundry plant. Generally, the plant produces 5 tons of these waste materials per calendar month. Specifically, these foundry waste materials were generated from an investment

casting process (Section 2.1). The appearance of the raw ceramic waste is shown in Figure 3.22.

As can be seen from Figure 3.22, the ceramic waste pieces were delivered with a range of different sizes and shapes. The materials had a layered structure. Typically, the pieces were about 200 mm in length and 50 mm in width. The weight of the waste pieces ranged from approximately 100 g to 300 g.

The microstructure of the material is shown in Figure 3.23 which suggests that the waste materials were generated from a typical investment casting process. It also indicates these ceramic components were products of colloidal silica and zircon based shell system.

It can be seen that the colour of the ceramic waste is cream white. It means that these waste shells were fired at low temperature (approximately 900℃ – 1200℃) and had not been used in the casting process. That is to say, there was no metal contamination in these materials.

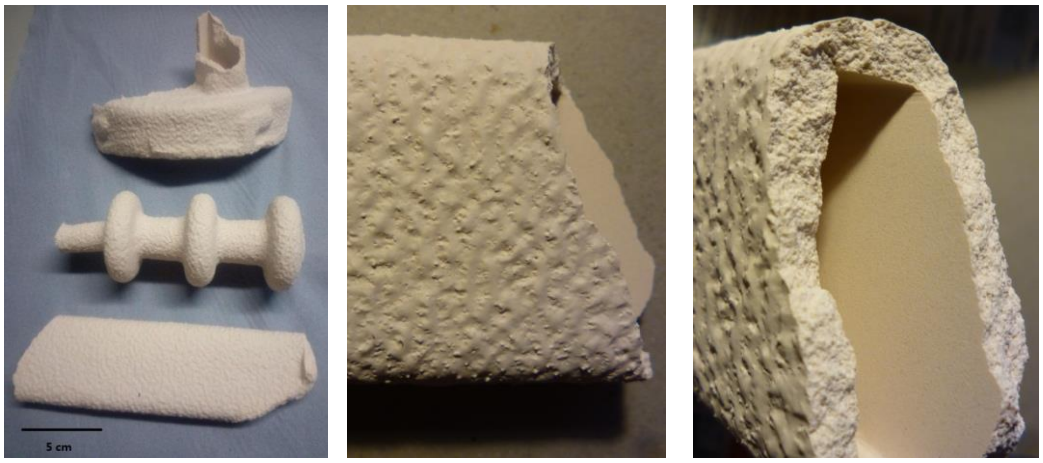

Figure 3.22 Raw foundry ceramic waste materials

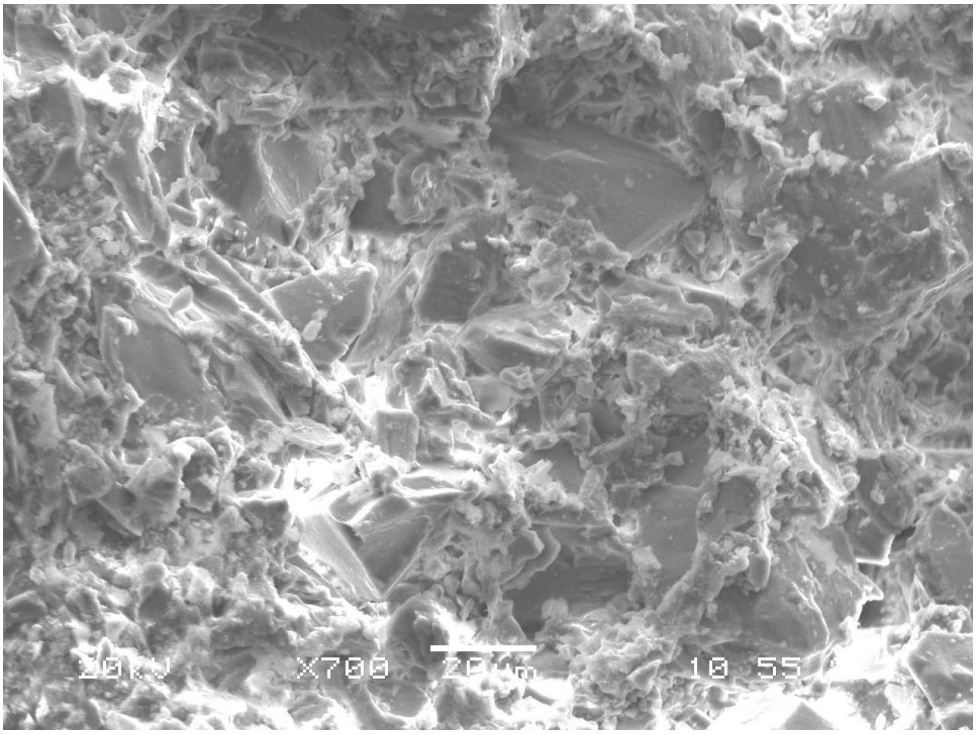

Figure 3.23 SEM image of a ceramic waste sample

3.4 Conclusions

This chapter describes the various characterization methods that were used in the study, including PSD, XRF, XRD, SEM, EDS, density, fractural strength measurement, Vickers hardness test, toughness calculation, dilatometry, DSC and

The physical and chemical principles behind these analytical techniques were described and the working principles of the experimental instrument were demonstrated. Information on the devices used to conduct the experiment was provided, and the sample preparation processes and experimental procedures were described.

Finally, the raw ceramic waste components were characterized with the appearance,

dimension, weight and microstructures (SEM image) given.

CHAPTER IV PRE-TREATMENT OF THE FOUNDRY WASTE MATERIALS

4.1 Introduction

The previous chapter introduced the foundry waste materials used in this project. The analytical methods conduced to characterize the samples were also described.

In order to produce a suitable feedstock for making either refractory materials or coloured minerals, pre-treatment of the raw foundry waste was required. The methods and processes used for this pre-treatment are described in this chapter.

4.2 Fly pressing process

In order to analyse the ceramic waste materials and to produce a feed for further processing, the ceramic pieces were crushed to a coarse powder. The first step was to crush the ceramic waste components into small pieces. From Figures 3.22 and 3.23, it is known that the ceramic wastes were sintered at low temperature typically between 800 °C to 1100 °C and were not used for casting, thus the mechanical strength of the waste components were relatively low (about 20 – 30 MPa) (13). Based on this, a fly press was selected to crush the raw ceramic waste materials. Commercially a jaw or roll crusher could perform a similar duty.

4.2.1 Experimental apparatus

The amount of the waste materials (20 kg) need to be processed was not large. Due to the friability of the waste and the relatively small volume, a manual fly press was employed. The equipment used in this procedure was a NORTON #6 Single Sided Weight Arm Fly Press which had a 301 kg total weight that could provide up to 60 kN load.

Due to the high hardness of the ceramic waste materials, a hardened stainless steel plate was used. This was built into a tray designed to catch the crushed pieces. A 2.00 mm sieve was used to ensure all the crushed ceramic waste pieces were smaller than this size which formed a reasonable feed to the next vibratory milling step.

4.2.2 Experimental procedure

3 to 5 pieces of ceramic waste materials were put into the stainless steel tray each time according to the size of the fragments. The volume of the ceramic waste was insured to be less than 30% of the total volume of the stainless steel tray.

The plate was put under the die of the fly press. The handle of the fly press was rotated with certain speed to move the die downwards to crush the ceramic pieces. This process was repeated several times until all the ceramic waste materials on plate were crushed to the required size.

The crushed ceramic waste was screened on a 2.00 mm sieve. The waste which did not pass the sieve were gathered and put back to the press. The crushed -2mm material was collected.

Roughly 300 g of ceramic components were fed to the press and about 60 % (180 g) were crushed to powders which passed the sieve on each press treatment. The crushing process was repeated until all the ceramic waste materials passed the sieve. All 20 kg of the feed material were processed by the method.

4.3 Vibratory disc milling process

4.3.1 Experimental apparatus

Approximately 20 kg of -2.00 mm ceramic waste was reduced to less than 100 µm in preparation for both the required analysis and further processing. A vibratory disc mill was used for this purpose due to its high efficiency and its known ability to produce materials of high final fineness with good reproducibility.

The instrument used in this process was a TEMA Siebtechnik vibratory disc mill (Model: TS 1000). The dimensions of the instrument is 836 x 1220 x 780 mm (W x H x D) and the weight is 210 kg (without grinding set). The maximum vibrating speed of this model was 970 rpm. Due to the amount of the samples, a 250 ml grinding set was selected. However, there were only chromium steel grinding vessels available which would lead to metal (iron) contamination.

The 250 ml grinding set was composed of a grinding vessel with cover, two grinding rings and a die. The useful volume of this set is 250 ml which can operate on a minimum 80 ml to a maximum 250 ml of feed. The dimensions of the grinding set are show in Table 4.1.

Table 4.1 Dimensions of the 250 ml chromium steel grinding set

	Outer Diameter (mm)	Inner Diameter (mm)	Height (mm)
Vessel	210	200	55
Large Ring	163	143	50
Small Ring	134	102	50
Die	80	80	50

4.3.2 Experimental procedure

Due to the capacity of the mill being 80 – 250 ml, around 150 ml powders were ground with each run. The feed was measured and placed uniformly in the gap between the large grinding ring and the vessel wall. With the lid in place the assembly was clamped into the mill.

Considering the hard but brittle nature of the ceramic feed, the maximum vibration frequency of 970 rpm was applied for 60 seconds for each run. After the milling, the rings and die were removed, and the powders were transferred into a 10 L clean sample storage drum.

Due to the strenuous vibration during the process, some of the mechanical energy was converted to thermal energy which causes the temperature of the grinding set rise to about 50 °C. If the temperature went higher, it may have caused greater electrostatic attraction between the powders which would reduce the efficiency of

the milling process as a result. The high temperature may also have damaged the equipment. Therefore, the grinding set was left to cool down for 5 minutes between each run, cooling was rapid as the specific heat capacity of the chromium steel is relatively low.

The aforementioned process was repeated for 40 times and all 20 kg ceramic coarse powder was ground to analytical fineness.

4.3.3 Particle size distribution

The particle size distribution of the milled powder is shown in Figure 4.1. Measurement was conducted on a SYMPATEC HELOS SUCELL laser diffraction laboratory particle size analyser using the methods described in Section 3.2.1.3.

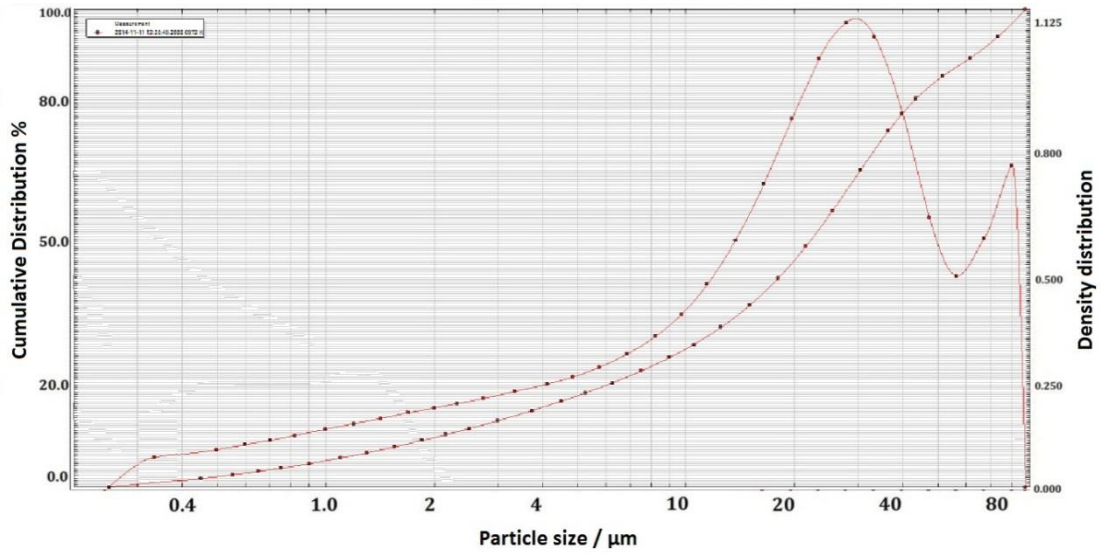

Figure 4.1 PSD of ground powder

As can be seen from the chart, the median size of the particles (D_{50}) was 21.33 µm. About 10% of the particles had a size (D_{10}) smaller than 2 µm, while 90% of the

particles (D_{90}) were smaller than 50 µm. The maximum value of the particle size was about 88 µm.

The above PSD results suggested that the powder was relatively fine and suitable for initial chemical and physical examination.

4.4 Magnetic Separation

The process of fly pressing and vibratory disc milling introduced magnetic iron due to wear of the crushing and grinding surfaces by the hard ceramic waste (XRF and XRD analysis will demonstrate the phases of the ceramic waste in section 4.4.4 and 4.5.4 respectively). The typical Vickers hardness values of different materials are listed in Table 4.2 (159). This iron was in two forms: discrete particles and smeared iron on the surface of the ground ceramic. A magnetic separation method was selected to remove a proportion of the free iron contamination.

4.4.1 Experimental apparatus

For a particle of iron to be removed from a non-magnetic bulk powder a magnetic field is applied. That field must also have a gradient to induce the magnetic particle to move (91). Magnetic separators apply this concept to separate ferromagnetic and paramagnetic materials from non-magnetic particulate feed. A wide range of devices are available with different field intensities and gradients. These devices are widely used for removing magnetic contaminations or free iron from mixtures in ceramic, mining and food processing industries (89) .

Table 4.2 Examples of HV values for various materials (159)

Materials	Value
Iron	30 – 80 HV
Carbon steel	55 – 120 HV
Chromium steel	140 – 200 HV
Zircon	1300 HV
Alumina	1800 HV
Diamond	10000 HV

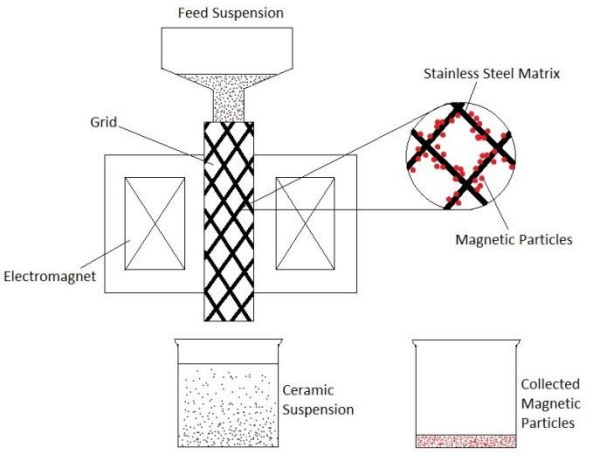

a **b**

Figure 4.2 Grid magnetic separator and schematic diagram

According to the intensity of the magnetic field which the device can generate, the machines can be divided into normal or high magnetic force separators. On the basis of the mechanisms and sizes, the separator can be divided into several types. Here because the volumes to be processed were small maximum efficiency rather than yield was sought, thus a wet high intensity separator was selected.

In this study, the 20 kg of iron contaminated feed was passed over a wet high intensity magnetic separator. The wet system gave a cleaner output than dry or lower intensity methods such as the ore shoot system (94).

A BOXMAG RAPID normal strength grid magnetic separator was selected (Figure 4.2-a). This instrument was made by Rapid Magnetic Ltd. with a maximum output of 250 V and 5 A. The equipment comprised a feeding hopper, a stainless steel grid, an electromagnet and a control panel which includes a voltmeter and a current meter.

As can be seen from the schematic diagram (Figure 4.2-b), the suspension was fed from the vertical gravity feeding port, and passed through the magnetic field which was generated by poles of the electromagnets. The intensity of the magnetic field can be adjusted by controlling the output amperage (0 – 5 A). The mesh selected has a profile which induces a high field gradient. The magnetic particles are attracted to the stainless steel matrix and remain there while the ceramic particles passing through. When the field is removed, the free iron and ceramic particles with smeared iron can be separated from the matrix by washing.

4.4.2 Experimental procedure

Initial trials showed that the most effective separation was achieved with the volts set at 250 V and the amps at 5 A. The system was assembled clean and the magnets tuned to the required settings.

A suspension of 30 g of ceramic waste powder in 250 ml of water was passed through the mesh residing in the pole channel. The pour was maintained at a steady rate with the suspension stirred well to present the particles to the magnetic field in as evenly distributed way as possible. This allowed optimized separation. The underflow was collected in a 1000 ml beaker. Once all the slurry had passed, 200 ml water was used to rinse the funnel and grid.

The 1000 ml beaker with ceramic suspension was removed and replaced by another 1000 ml empty beaker. The output voltage was adjusted to 0 % and switched off. The magnetic particles were washed from the grid by flushing down with 200 ml water 3 times. The ceramic suspension was transferred in a 10 L plastic sample drum while the magnetic material was discarded after being weighed. The collected iron was dried at 100 °C to attain the mass balance data. Typically, about 1.6 g iron was removed from 30 g of ceramic waste materials in this process.

The above process was repeated about 20 times, until the 10 L drum was almost full yielding about 600 g ceramic powders (original weight) in the suspension. The drum was retained to allow the ceramic particles to sediment. After 24 hours, the water was decanted and the wet ceramic powder was retained.

4.4.3 X-ray Fluorescence Analysis (XRF)

Approximately 50 g of treated ceramic waste powder was dried in an oven at 110 °C for 8 hours. XRF analysis was carried out to identify the elemental composition of the powder. The principles, experimental instrument and testing procedures are detailed in Section 3.2.2.

Table 4.3 XRF results of ceramic waste powder after magnetic separation

Result(s)		Units	
Sample Basis			Dried 110 deg C
Silicon Dioxide	SiO_2	%	24.08
Titanium Dioxide	TiO_2	%	<0.01
Aluminium Oxide	Al_2O_3	%	37.89
Iron (III) Oxide	Fe_2O_3	%	0.18
Calcium Oxide	CaO	%	0.03
Magnesium Oxide	MgO	%	0.03
Potassium Oxide	K_2O	%	<0.01
Sodium Oxide	Na_2O	%	0.17
Phosphorus Pentoxide	P_2O_5	%	0.07
Chromium (III) Oxide	Cr_2O_3	%	0.02
Manganese (II,III) Oxide	Mn_3O_4	%	<0.01
Zirconium Oxide	ZrO_2	%	36.57
Hafnium (IV) Oxide	HfO_2	%	0.80
Lead Oxide	PbO	%	<0.02
Zinc Oxide	ZnO	%	<0.01
Barium Oxide	BaO	%	<0.01
Strontium (II) Oxide	SrO	%	<0.01
Tin (IV) Oxide	SnO_2	%	<0.01
Copper Oxide	CuO	%	<0.01
Yttrium Oxide	Y_2O_3	%	0.08
Thorium (IV) Oxide	ThO_2	%	0.01
Uranium (V VI) Oxide	U_3O_8	%	0.03
Loss on Ignition		%	0.41
Loss on Ignition Temperature		°C	1025
Total		%	100.37
Sulphur Trioxide	SO_3	%	<0.05
UKAS Accredited			Yes

The XRF results are shown in Table 4.3. XRF measures the elemental composition of the sample, but here the results were converted into oxide format which provides a clearer view of the constituents.

As can be seen from the table, the three main elements in the ceramic wastes were aluminium, zirconium and silicon. The content of iron, sodium, phosphorus, hafnium, and yttrium were all greater than 0.05 %. Several trace elements (< 0.05 %) were also

found in the sample including calcium, titanium, magnesium and potassium. These elements probably have no impact on the properties of the ceramic waste materials due to the contents being very low.

The magnetic separation process removed most of the iron in the ceramic powders. However, there was still about 0.18 % iron in the sample.

4.5 Acid leaching

Following magnetic separation, most of the tramp iron particles had been removed from the ceramic waste. However, almost all physical separation methods have a statistical chance of some particles not being separated, which means there were still a small amount of magnetic particles (for example smeared iron) in the ceramic powders. This may be due to the reason that with smeared iron the attraction to the magnet may not be sufficient to remove it. For example, imagine a thin layer of iron on a large particle the net magnetic force would be too small. XRF results (Table 4.3) post magnetic separation indicates that there remained some undesirable materials which could not be separated by magnetic separation (i.e. sodium, calcium and magnesium). Therefore, a further purification process was applied to eliminate those impurities. Chemical purification methods are generally considered more effective than physical ones on extracting the very small levels of contaminations in relatively fine ceramic powders.

4.5.1 Experimental apparatus

In this study, an acid leaching process was operated in a fume cupboard using normal laboratory equipment. The whole experimental arrangement can be seen in Figure 3.7. A 1000 ml glass beaker was used as the reaction vessel which contained the 5% sulfuric acid and ceramic waste suspension. A PTFE (a material with high acid and alkali resistance) coated magnetic stirring bar (70 × 10 mm) was used to keep the suspension agitated.

The beaker was placed on a hotplate stirrer (Stuart Equipment) with the specification listed in Table 4.4 (192). The hotplate stirrer can not only heat and retain the suspension at a desire temperature but also can drive the magnetic stirring bar at a specific speed. As can be seen from Figure 4.3, there was a PTFE coated thermal probe which was inserted in the suspension to retain the accuracy of temperature of the fluid by control of the hotplate.

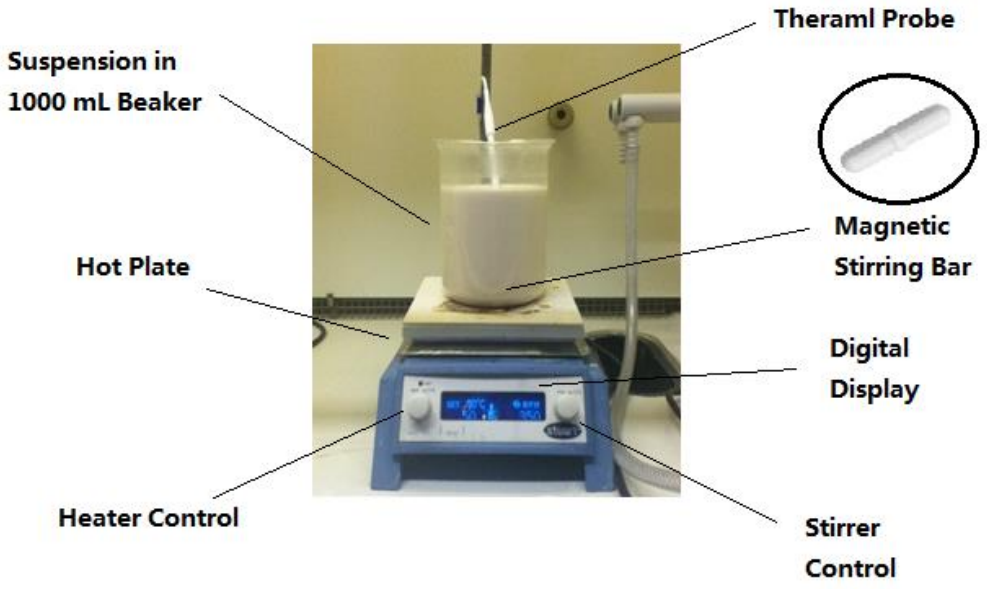

Figure 4.3 Acid leaching devices

Table 4.4 Specification of 'Stuart' hotplate stirrer (192)

Model No.	**CD162**
Plate material	Glass ceramic
Plate dimensions, mm	160 x 160
Heated area, mm	120 x 120
Max. Plate temp. °C with probe °C	450
Control accuracy with probe °C	±0.5°C
Stirrer speed, rpm	200 to 1300
Max. stirring capacity, litres	15

4.5.2 Experimental procedure

Acid leaching was performed in standard laboratory scale glassware which meant the amount of powder that could be processed per batch was limited. Moreover, a better stirring arrangement would have increased the contact between the powder and the solvent which could have resulted in a faster and more complete reaction. A commercial system would be more efficient than the system adopted here if the process were to be scaled up. The pulp density of the system was limited due to the high density of the ceramic powder mass. Free alumina and zircon have densities of 3900 $kg \cdot m^{-3}$ and 4700 $kg \cdot m^{-3}$ respectively, so the solids loading was reduced for all suspension processing.

The process was optimized by evaluating three different solids loading of 150, 250, and 350 g in 800 ml acid with the magnetic stirring speed adjusted to 200, 400, 600, 800, 1000 rpm. Table 4.5 shows the solid suspension under the different processing conditions and can be seen, for 350 g ceramic powder (23.5 w.t. %), sediments formed at the bottom of the beaker no matter what stirring speed. This suggested that some powder may have very little contact with the liquid. The device could keep the mixture in a homogeneous suspension when 250 g powder (23.5 w.t. %) was processed by using a 400 to 1000 rpm stirring speed. However, with 1000 rpm, the suspension splashed a little. Therefore, 250g ceramic waste powder in 800 ml liquid with 800 rpm rotor speed was used as the standard operating condition. Additionally, the stirrer size was critical as well to the process. The stirrer with a 100 mm length was used in this study as it is longest one that can fit in the 1000 ml beaker. The shorter stirrer (60 mm) would significantly reduce the ability to keep the suspension homogeneous.

Table 4.5 Stirring situations in different conditions

Stirring Speed / Powder weight	200 rpm	400 rpm	600 rpm	800 rpm	1000 rpm
150g	Homogeneous suspension	Homogeneous suspension	Homogeneous suspension	Small amount of splashing	Small amount of splashing
250g	Sediments at bottom	Homogeneous suspension	Homogeneous suspension	Homogeneous suspension	Small amount of splashing
350g	Sediments at bottom	Sediments at bottom	Sediments at bottom	Sediments at bottom	Sediments at bottom

The 95% sulphuric acid (produced by Sigma-Aldrich for trace analysis) was diluted to 5% sulfuric acid for the leaching process (101). According to the density (at 20 °C) and concentration, the amount of 95% sulphuric acid need for 800 ml 5% solution was calculated (Table 4.6). 24 ml 95% sulfuric acid was slowly added in 776 ml deionized water with gently mixing by a glass rod.

250 g ceramic waste fine powder was weight out and put into a 1000 ml glass beaker with a PTFE coated magnetic stirring bar at the bottom. 800 ml of 5% sulfuric acid solution was poured carefully onto the powder. The agitation speed was adjusted to 300 rpm at the start for smoothly mixing and then increased to 800 rpm to achieve the optimum condition. The PTFE thermal rod was inserted in the suspension without touching the wall or bottom of the vessel to control the temperature accurately. The temperature was set at 50 °C to accelerate the reaction speed and also increase the dissolution rate of the contaminants.

Table 4.6 Density of sulphuric acid and amount used in this process

H_2SO_4 % (wt.%)	Density ($g \cdot ml^{-1}$)	Amount (ml)
5	1.0317	800
95	1.8337	X = 800 × 1.0317 × 0.05/0.95/1.8337 = 23.69

Once the operating temperature was reached the digestion process was run for 8 hours. Then the hotplate was turned off and left in place overnight to sediment.

After the liquid above the sediment became clear, it was transferred in a waste solution collection bottle by decantation. The sediment was washed with 800 ml deionized water (stirring for 15 minutes and allowed to sediment before separating). The water washing step was conducted a number of times until the pH of the solution was about 7.0 to ensure all acid was removed.

The remaining sediment was dried at 101 °C in a laboratory forced convection oven (Heraeus UT6200) for 8 hours to let the powder dry completely to give the purified ceramic powder.

4.5.3 Iron content analysis

The level of iron being removed was monitored by analysing the liquor being generated through the leaching process.

4.5.3.1 Principles of potassium dichromate titration method

During the acid leaching process, the free and smeared iron in the ceramic mixtures reacted with the hydrogen ion (Equation 4.4) continuously (193). The iron was converted to the iron (II) ion, and thus transferred into the solution.

$$Fe + 2H^+ \rightarrow Fe^{2+} + H_2 \qquad (4.4)$$

With the reaction time, the concentration of the iron (II) ion would increase gradually. A chemical titration experiment was carried out in order to monitor the iron digestion process.

Potassium dichromate titration method is a commonly used technique to determine the concentration of the metallic ion in the solution (194). The reaction between potassium dichromate and iron (II) ion is:

$$6Fe^{2+} + Cr_2O_7{}^{2-} + 14H^+ \rightarrow 6Fe^{3+} + 2Cr^{3+} + 7H_2O \qquad (4.5)$$

As can be seen from the equation, the iron (II) ion will be oxidized by the dichromate ion and converted to iron (III) ion. Simultaneously, the dichromate ion will be transformed to chrome (III) ion and some water is generated.

An indicator is needed to determine whether the reaction is completed. Sodium diphenylaminesulfonate is the most common indicator for this reaction (193). A green colour will appear if there is iron (II) ion in the solution. After the dichromate ion has oxidised all Fe^{2+} ion to Fe^{3+}, tiny quantity of excess potassium dichromate solution will change the colour of the indicator from green to red purple immediately. Because the concentration of the potassium dichromate and the consumption volume are known, the original concentration of iron (II) ion can be calculated.

4.5.3.2 Experimental procedure

In this study, during the leaching process, 30 ml of acid solution was taken out from the beaker and placed in small containers after 1 hour, 2 hours, 4 hours, 6 hours and 8 hours.

The standard $K_2Cr_2O_7$ solution was prepared in a 1 L volumetric flask at 0.001 mol·L^{-1}. 1000 mL sulphuric acid and phosphoric acid mixture (14.7 wt. % H_2SO_4 + 12.7 wt. % H_3PO_4) was also prepared as the buffer solution to keep the pH value (pH ≈ 1) stable

during the titration process. 0.25 g of sodium diphenylaminesulfonate powder was dissolved in 50 ml water along with 3 drops of 98 w.t. % sulphuric acid to form the proper indicator.

Table 4.7 Volume consumption of $K_2Cr_2O_7$ solution for each sample

Sample taken	1 hour	2 hours	4 hours	6 hours	8 hours
Volume consumption (1^{st} test) (ml)	2.6	3.7	3.9	4.3	5.9
Volume consumption (2^{nd} test) (ml)	2.5	3.6	3.9	4.2	6.0
Average volume consumption (ml)	2.55	3.65	3.90	4.25	5.95

5 ml of acid leaching sample solution filtered from the extracted sample of the suspension was added to a 400 ml beaker, followed by 200 ml deionized water. 4 or 5 drops of indicator (sodium diphenylaminesulfonate) was added to the solution and 20 ml of the sulphuric acid and phosphoric acid mixed solution was slowly added. The acid burette was filled in with 50 ml potassium dichromate 0.0001 mol· L^{-1} solution.

The standard $K_2Cr_2O_7$ solution was added into the beaker drop by drop until the colour of the sample solution converted from green to red purple. The consumption

volume was recorded. Each sample was tested twice and the results are given below in Table 4.7.

4.5.3.3 Results analysis

From the concentration, the volume consumption of the potassium dichromate solution and the volume of the sample solution, the concentration of the iron (II) ion can be calculated (Table 4.8).

As can be seen from the table, the concentration of Fe^{2+} in the sample solution increased gradually with time. After 8 hours, the concentration of Fe^{2+} was 0.00702 mol· L^{-1} in average. This value meant that 0.314 g of free and smeared iron (0.125 w.t. % of ceramic powder) was leached in the acid solution. That is to say about 99.7 % remaining iron was removed from the ceramic powder by acid leaching process.

Table 4.8 Concentration of Fe^{2+} for each sample

Sample Taken	1 hour	2 hours	4 hours	6 hours	8 hours
Fe^{2+} Concentration (mol· L^{-1})(1^{st} test)	0.00312	0.00444	0.00468	0.00516	0.00684
Fe^{2+} Concentration (mol· L^{-1}) (2^{nd} test)	0.00300	0.00432	0.00468	0.00504	0.00720
Average Fe^{2+} Concentration (mol· L^{-1})	0.00306	0.00438	0.00468	0.00508	0.00702

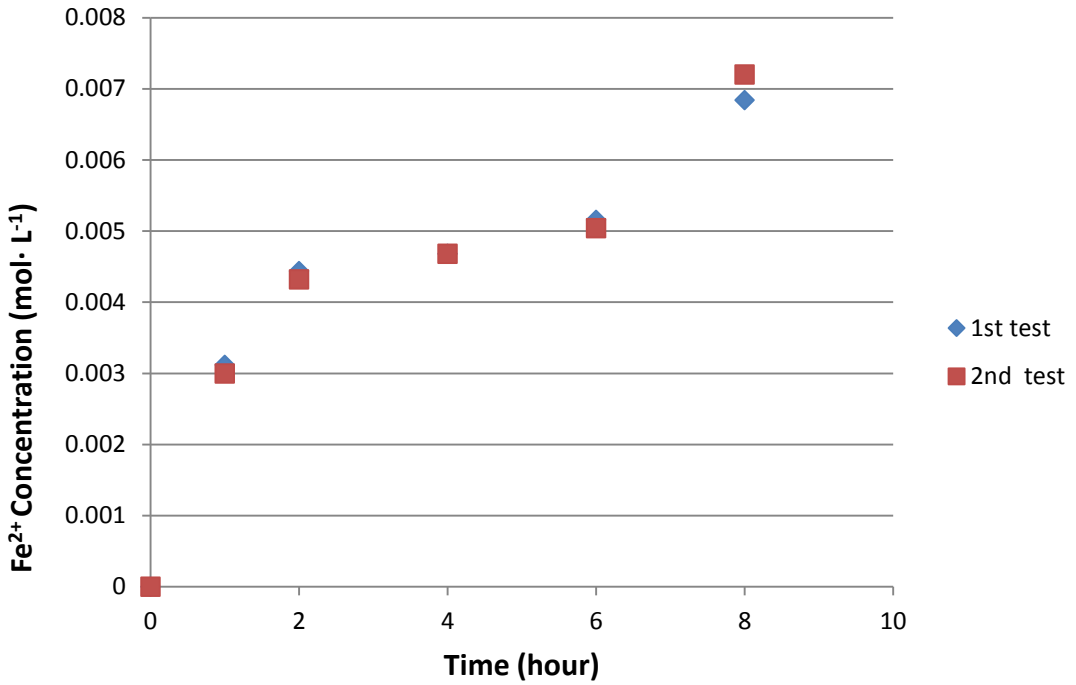

Figure 4.4 Iron content digestion curve of the leaching process

Figure 4.4 shows the iron content digestion curve of the leaching process. It can be seen that the tests repeated the same trend as the more iron was digested in the solution with reaction time. However, the Fe^{2+} concentration data did not form an ideal curve due the introduced error. Because the iron content in the ceramic was very small thus the concentration of the Fe^{2+} in the solution was very low. This means the standard $K_2Cr_2O_7$ solution must be prepared in very low concentration as well which might introduce significant error through the weighting and transferring steps. In addition, the low concentration of Fe^{2+} solution and standard $K_2Cr_2O_7$ solution also brought difficulties when identify the end point of the titration which probably introduced further error.

This titration method assumes all iron ions were in Fe^{2+} form according to Equation 4.4. However, if there were any Fe^{3+} ions in the solution, they could not be analysed

by using this $K_2Cr_2O_7$ titration method. Thus, this might introduce possible errors in the calculation as well.

According to the shrinking core model for chemical reaction control leaching process (195), the integrated leaching rate can be described by:

$$1-(1-X)^{\frac{1}{3}}=K_T t \tag{4.6}$$

where X is the fraction of reacted material, K_T is the rate constant and t is the reaction time.

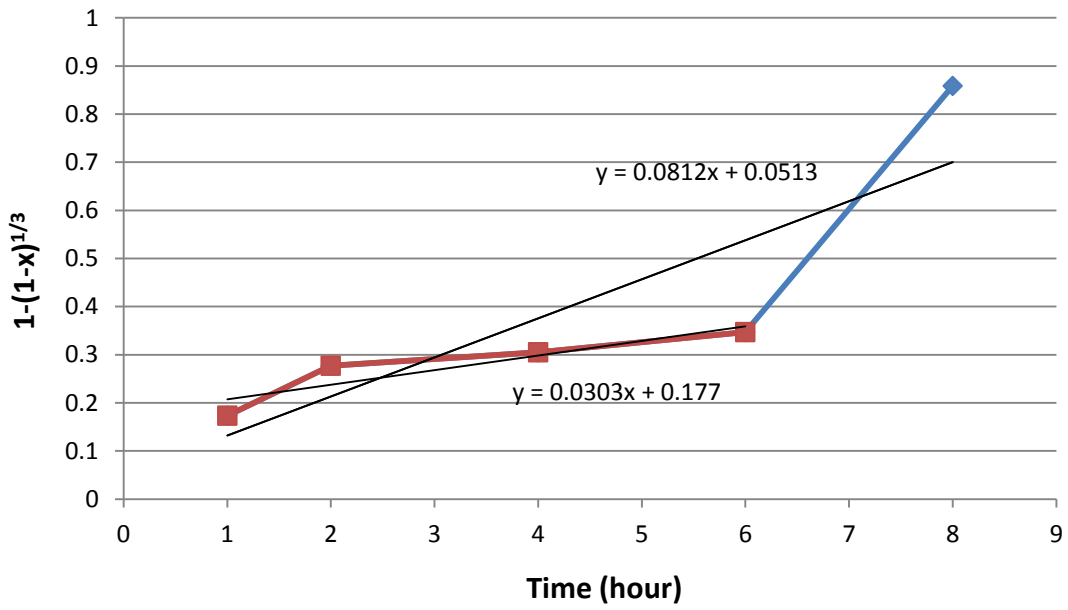

Figure 4.5 Graph of leaching rate constant (KT) identification

The data obtained were calculated and thus Figure 4.5 was generated to identify the leaching rate constant. The K_T value is 0.0303 h^{-1} when only the first four points are used in the calculation while the K_T shows as 0.0812 h^{-1} when all points are considered. The significant difference between these two values is caused by the error introduced to the system. Due to the Fe^{2+} concentration was relatively low at

the 1, 2, 4, 6 hour time mark, the first four points perhaps contain more error than the fifth point. Thus, the K_T valued at 0.0812 h^{-1} should be more accurate than the 0.0303 h^{-1} one.

Increasing the volume of the processed materials in a single run (for example 2500 g ceramic powders) could significantly increase the required concentration of the standard $K_2Cr_2O_7$ solution which should reduce the error. The error may also be reduced by repeating the tests more times (for example 6 times). However, due to limitations of the laboratory equipment size and time allotted to this study only an indication is provided of the iron reduction kinetics.

4.5.4 XRD analysis

After acid leaching, about 10 g of treated ceramic waste powder was dried in the oven at 110 °C for 8 hours and XRD analysis was carried out to identify the phase distribution. The principles, experimental instrument and testing procedures of XRD analysis used in this study are detailed in section 3.2.3.

The analysed XRD pattern of the purified ceramic waste powder is shown below in Figure 4.6. It can be seen that only zircon and alumina were detected in the sample.

However, by combing the results of the XRF test (refer to Chapter 4.4.4), it can be deduced that there were three main substances in this ceramic waste which were zircon, alumina and amorphous silica. Since XRD cannot detect amorphous materials, silica was not identifiable in the XRD analysis.

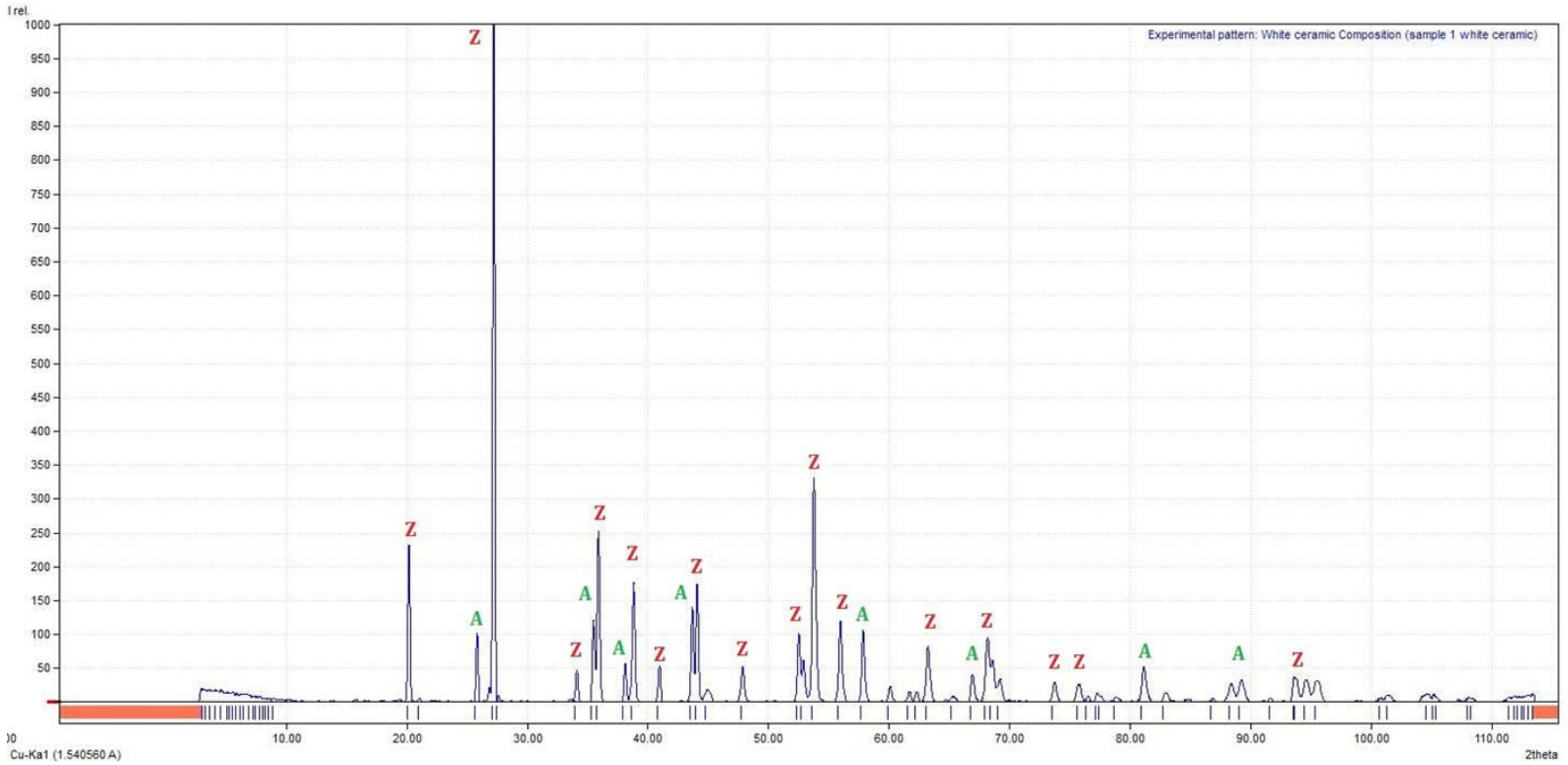

Colour	Formula	Matched Phase	Quantity
Red	$ZrSiO_4$	Zircon	55.1 %
Green	Al_2O_3	Corundum	44.9 %

Figure 4.6 XRD of acid leached ceramic waste powder

4.6 Discussion

The previous sections described the pre-treatment process of the raw foundry waste materials. Through crushing, milling, separation and leaching process, the foundry waste solids were converted to a purified ceramic powder of analytical fineness (< 100 μm).

PSD, XRD and XRF analysis were carried out to evaluate the effectiveness of the procedures. The particle size distribution, elemental composition and phase distribution of the ceramic waste materials were thus identified.

The particle size reducing processes (fly pressing and disc milling) were applied to all 20 kg of the ceramic waste materials to give a uniform feed to the later processes and thus reduce the errors that may have been introduced by sampling. Purification processes (magnetic separation and acid leaching) were carried out whenever purified ceramic waste powder was required for further experiments. The laboratory scale equipment used for magnetic separation and acid leaching were time consuming. About 2 kg of purified ceramic powder was kept as backup sample at all times during the project.

4.6.1 Particle size reducing processes

In order to convert the solids to fine powders, normally crushing and grinding processes are required. The fly press was chosen because it was ideal for small quantity of samples and easy to operate. The vibratory disc mill was the most efficient device to reduce the particle size in extremely short time.

Although these instruments fulfilled the task in a short time, some tramp iron contamination was introduced to the system due to the extreme hardness of the ceramic materials. Compared with the fly pressing, the disc milling process was much more intense and there was a visible colour change (from cream to grey) of the powder after vibratory grinding. This suggested that most of the free iron contamination was introduced in this step. This caused more reworking in the purification process. However, the tramp iron can be eliminated quite easily by magnetic separation and acid leaching due to its ferromagnetism and strong solubility in acid. Thus, these two machines were the best options in this study for particle size reducing purpose.

The process could be improved if a zirconia grinding mould was used in the disc mill, which could reduce the amount of iron contamination dramatically but it could result in contamination of the powder with a fraction of zirconia. That zirconia contamination could not be removed but would probably not influence the overall properties of the powder greatly. The use of a ceramic grinding system might mean the magnetic separation step could be removed from the process.

4.6.2 Purification processes

4.6.2.1 Combination methods

As stated above, the particle reducing process introduced in tramp iron contamination and there were other impurities such as dioxides which need to be eliminated before any further recycling process is considered. Thus, the magnetic

separation and acid leaching techniques were combined to purify the ceramic powder.

Only using the magnetic separation would lead to incomplete purification due to the statistical nature of the separation mechanism. Not only it could eliminate most of the unwanted oxides, but it also would leave a little amount of free iron in the mixture (iron spotting and colouration in the finished products would be the most probable consequence of this).

The acid leaching technique could give a ceramic powder which was essentially clean, but it was not able to dissolve all the impurities at a low acid concentration (i.e. 5 w.t. % - 10 w.t. %). An experiment was conducted to prove this by using 250 g vibratory disc ground powder (non-magnetically treated) at the same acid condition (5 w.t. % H_2SO_4, 50 °C, 800 rpm, 8 hours) as described in Section 4.5. A thin layer of grey particles remained which could be separated by a bar magnet. Theoretically, increasing the concentration of the acid solution (maximum 70 wt. % sulphuric acid) could eliminate all the contamination without the magnetic separation process (96). However, this would raise the operating cost dramatically and cause more safety issues in terms of practical application.

To sum up, the combination of magnetic separation and acid leaching techniques was the most practical and ideal method to decontaminate the ceramic waste powders.

4.6.2.2 Sedimentation rather than vacuum filtration

As described in the experimental procedure for magnetic separation and acid leaching, the suspensions were allowed to sediment for 8 hours before decanting. Theoretically vacuum filtration would be a better option as it should be more efficient and loss free (196). A schematic diagram of vacuum filtration is shown in Figure 4.7.

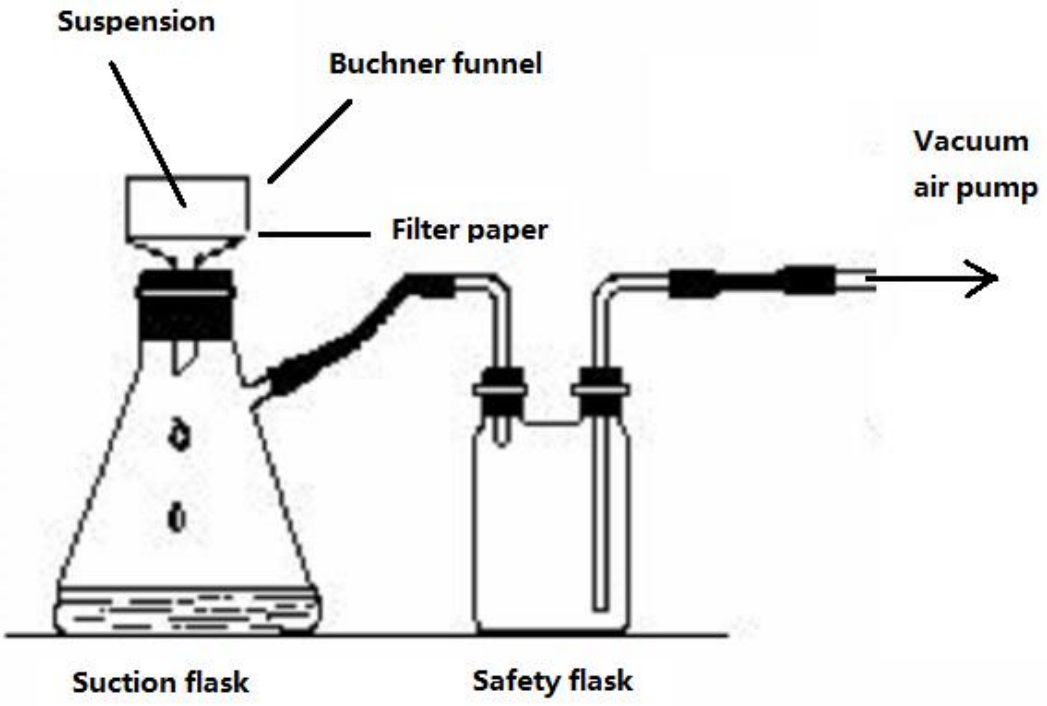

Figure 4.7 Schematic diagram of vacuum suction filtration; Modified from (196)

As can be seen from the figure, the vacuum pump will reduce the pressure in the flask and result in a pressure difference across the suspension in the Buchner funnel. This would accelerate the filtration velocity and allow rapid drying. However, in this study, because the ceramic powder was quite fine (according to the PSD result in next chapter), the particles would form a dense layer blocking the liquid passage.

A verification experiment was undertaken by using this device. It took about 30 minutes to filter 100 ml of ceramic suspension. Through this simple experiment, it was shown that the sedimentation method was more efficient in this particular scenario than vacuum filtration.

4.7 Conclusions

A pre-treatment process of the ceramic waste was developed and is summarized in the flow chart given in Figure 4.8.

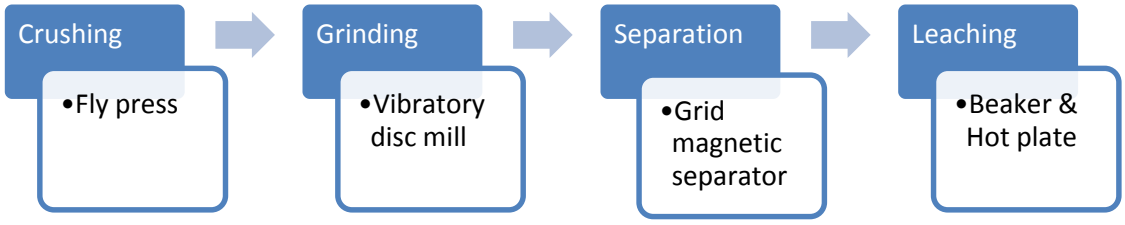

Figure 4.8 Flow Chart of pre-treatment processes

For each process, the theoretical foundation of techniques was given. The experimental apparatus were defined and the procedure described. The finished powder had a chemical composition suitable for further processing into ceramic (refractory) components and as a precursor for the manufacture of coloured zircon.

CHAPTER V REFRACTORY DEVELOPMENT

5.1 Introduction

The previous chapter described the pre-treatment processes which converted the ceramic waste solids to powders. Particle size analysis, chemical composition analysis and crystal phase analysis were conducted and reported in addition to the procedures for manufacture (Section 4.4 & 4.7).

This chapter describes how the ceramic waste powders can be developed into new refractory products. Specifically, the processes of pellet pressing and rod extrusion production which include calculations of the required amount of additives to give the final composition, the mixing and milling processes, the pellets pressing process, the paste forming process, the drying process and the sintering process will be covered. The detailed experimental conditions, data and information on the devices used will be shown.

5.2 Powder Formulating and Further Processing

5.2.1 Calculation of adding materials

From the XRF, EDS and XRD results (Section 4.4 & 4.7), the elemental composition and crystal phase distribution of the ceramic waste powders were obtained. The ceramic waste contained mainly three phases: zircon ($ZrSiO_4$), alumina (Al_2O_3) and amorphous silica (SiO_2), giving a system comprising four main elements: silicon, aluminium, zirconium and oxygen.

Knowing the composition of the ceramic waste, and the target refractory chemistry, in this case zirconia toughened mullite (ZTM), where the idealized composition of ZTM is described in Section 2.2. The compositional adjustments can be calculated. The reaction equations for this route are given as Equation 5.1 and 5.2. As can be seen, the main materials of the ceramic waste can be fully utilized to generate ZTM refractory material.

$$2ZrSiO_4 + 3Al_2O_3 \rightarrow 3Al_2O_3 \bullet 2SiO_2 + 2ZrO_2 \quad (5.1)$$

$$2SiO_2 + 3Al_2O_3 \rightarrow 3Al_2O_3 \bullet 2SiO_2 \quad (5.2)$$

The elemental content of the waste powders needs to be brought into the right ratios to allow the reactions of Equations 5.1 and 5.2 to go to completion.

From the XRF data and the molar weight of SiO_2, ZrO_2 and Al_2O_3, the mole ratio of these elements can be calculated which are shown in Table 5.1.

Table 5.1 Calculation of elemental ratio

	Amount (wt. %)	Molar Weight ($g \cdot mol^{-1}$)	Elemental moles per 100g sample (mol)	Mole Ratio
SiO_2	24.08	60.08	Si = 0.401	1.35
ZrO_2	36.57	123.22	Zr = 0.297	1
Al_2O_3	37.89	101.96	Al = 0.742	2.50

The elemental requirements to produce ZTM are given by:

Elemental mole ratio in the waste materials: Si : Zr : Al = 1.35 : 1 : 2.5 ➔

Mole ratio of alumina and silica in the waste ceramic: $Al_2O_3 : SiO_2 = 0.925 : 1$

Target mole ratio of alumina and silica in the ZTM: $Al_2O_3 : SiO_2 = 3 : 2$

Assuming the ceramic waste has a weight of 10 g: $Al_2O_3 = 0.0401 \times 1.5 - 0.0371$

$= 0.02305$ mol

Converted to weight: $Al_2O_3 = 2.351$ g (for 10 g ceramic waste)

Therefore, for every 10 g ceramic waste powder, an addition of 2.35 g Al_2O_3 powder would be needed. In theory, if these materials reacted completely, all the alumina (original and added), zircon, silica will be converted to a useful new zirconia toughened mullite refractory product. The composition of the refractory produced by this method will be 29.6 wt. % ZrO_2 and 70.4 wt. % mullite (19 % ZrO_2 and 81 % mullite in volume).

In this study, ALMATIS Alumina CT 3000 LS SG was selected as the additive source powder due to its high purity (Al_2O_3 = 99.8%), high reaction activity and small particle size (D_{50} = 0.5 μm).

5.2.2 Mixing & Milling Processes

The prepared formulation was ground to give the required properties. This gives intimate mixing of the two powders, and reduces the particle size of the mixture to give the reactivity necessary for the sintering process to go to completion.

5.2.2.1 Attrition Milling

In this study, a UNION PROCESS Szegvari Attritor System HD-01 Lab Attrition Mill was used to conduct mixing and milling actions. A 1400 ml zirconia inner grinding tank and a zirconia rotating shaft were used chosen along with around 500 ml zirconia media balls ($\Phi = 5\text{mm}$). All these parts were made of zirconia due to its high toughness, high specific gravity and was non-contaminating to the ceramic materials used in this process (apart from perhaps a slight increase in the zirconia content).

Table 5.2 Attrition mill operating conditions

Materials	Amount
Media Balls ZrO_2 (Φ = 0.5 mm)	500 ml
Ceramic Powders (original ceramic waste + alumina)	247g (200 g + 47 g)
Liquid (Water or Isopropanol)	300 ml

During the experiments, firstly, the grinding shaft and tank were fixed to the main body of the machine. 500 ml media was added to the chamber along with 247 g of powder feed. Around 300 ml milling liquid which in this study was either water or isopropanol was poured slowly into the chamber. The mill was cooled during

operation using a water jacket. Typically, the grinding speed was set as 250 rpm, and the milling time was 8 hours. These conditions are summarised in Table 5.2.

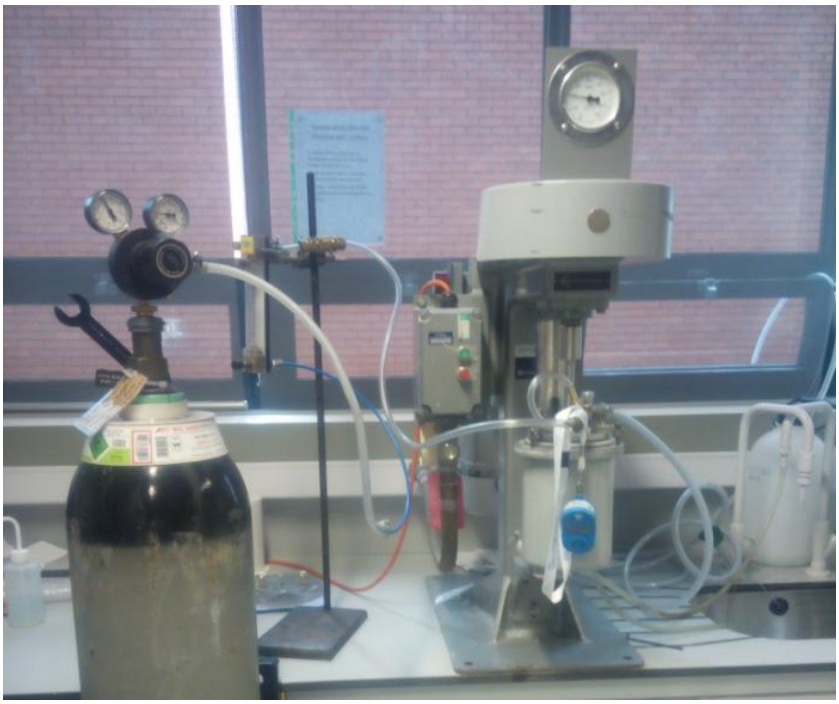

Figure 5.1 Attrition milling system by using isopropanol

When isopropanol was used a gas flow system was included to reduce explosion risk. Figure 5.1 illustrates the arrangement. Nitrogen gas was used to flood the top of the mill and a flow of 1 litre per minute was used to carry volatiles from the mill. An oxygen detector was placed by the mill to ensure the lab atmosphere was safe. Other conditions remained the same as when milling in water.

After the milling process was completed, the mixtures were passed through a 1 mm sieve to separate the slurry and media balls. The water based slurries were dried at 101 °C in a laboratory forced convection oven (Heraeus UT6200) for 16 hours, to let the powder dry completely. The isopropanol based slurries were dried at 39 °C in

the oven which was located in the fume cupboard for 8 hours to let the powder dry completely. The particle size was tested for each batch.

5.2.2.2 Particle Size Reduction

During the attrition milling process with water as fluid, 1 ml of slurry was taken from the mill after 2, 4, 6 and 8 hours time to determine the particle size distribution.

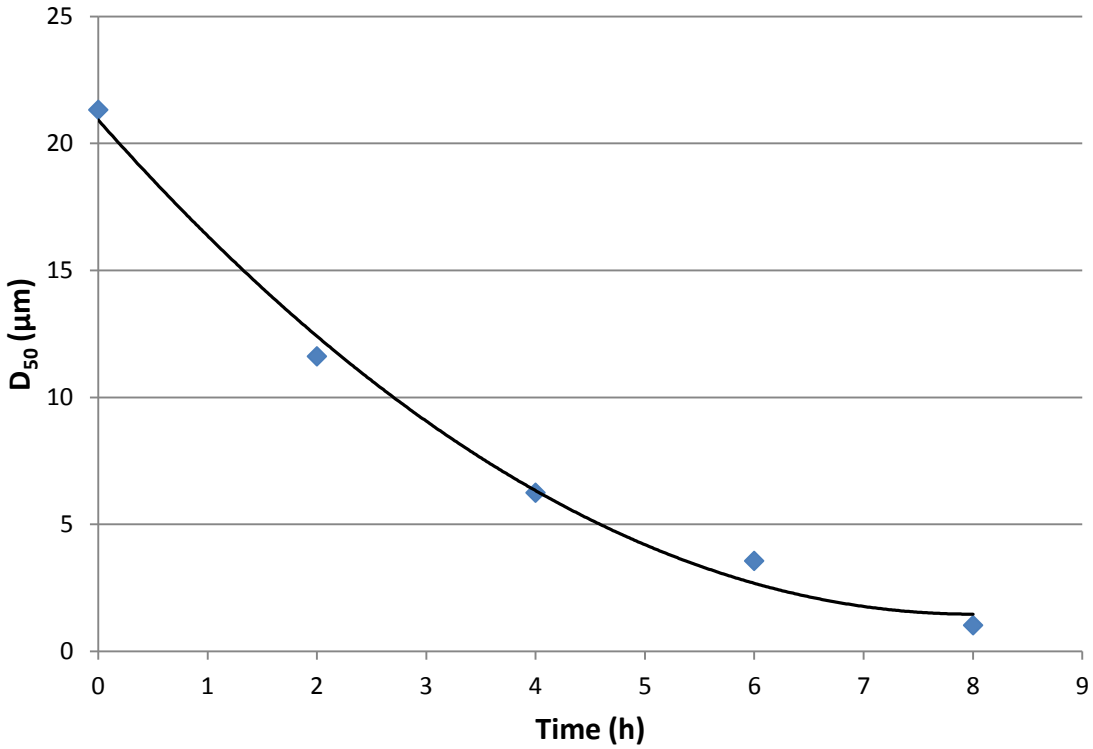

Figure 5.2 Particle size reductions during attrition milling process

Figure 5.2 shows the mean particle size of the powder as a function of milling time in water. The D_{50} value decreased exponentially with the milling time. The mean particle size dropped to about half (11.62 µm) of the original value in 2 hours. After a further 6 hours milling, the particles reached the desired mean size of around 1.03 µm.

5.2.2.3 Ball Milling

In this study, a GLEN CRESTON CA12var Roller Ball Mill was used to further process the ceramic powders. Normally a 250 ml plastic cylinder was used for small quantity processing and a 1000 ml porcelain container was selected to process larger amounts of material. Zirconia media balls ($\Phi = 5\ \mathrm{mm}$) were used in this procedure.

The ball mill was not as effective at reducing the particle size compared to the attrition mill. For example, it took about 72 hours to reduce the feed to the required size where it took just 8 hours in the attrition mill. Thus, in this research, the attrition mill was used for milling while the ball mill was used as a simple method for mixing with the powders with dispersant to remove any agglomerates formed in earlier operations.

As shown in Figure 5.1, the attrition milling system with isopropanol was very complex to operate. With the ball mill it was possible to run with alternative liquids because the chamber was sealed during the batch process. The ball mill was ideal for testing the effect of changing milling liquid.

After aqueous attrition, the dried powder (about 250 g per experiment) was mixed with 300 ml isopropanol in a 1000 ml porcelain container and milled for 4 hours. The resultant slurry was poured through a 1 mm sieve to remove the media and dried in an oven for 8 hours at 39°C in a fume cupboard. All the dried powders were pushed through a 500 μm screen in readiness for pressing.

5.3 Powder Compact Product Development

5.3.1 Dry Pressing Process

In this study, all the uniaxial dry pressing experiments were conducted on an INSTRON 4467 Universal Testing System. A SPECAC Atlas 20 mm (diameter) An Evaluable Pellet Die Set was used to fabricating general sample pellets for mechanical strength testing (refer to Chapter 3.6), hardness testing and SEM analysis (Figure 5.3). A SPECAC Atlas 13 mm (diameter) Evaluable Pellet Die Set was chosen for preparing dilatometry samples. A SPECAC Atlas 5 mm (diameter) Evaluable Pellet Die Set was used for DSC sample preparation. The details of dry pressing conditions are shown in Table 5.3.

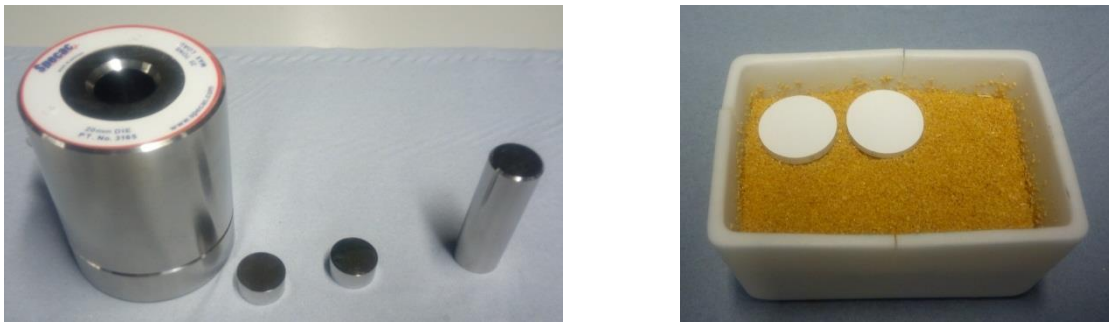

a **b**

Figure 5.3 Photos of 20 mm die set (a) and 20 mm green compact pellets (b)

Table 5.3 Details of dry pressing conditions

Die Set	Powder Amount (g)	Maximum Load (kN)	Loading Rate (mm/min)	Pellet Quantities	Purposes
20 mm	2.5	16	1	10	General
13 mm	4.5	16	1	3	Dilatometry
5 mm	0.3	10	1	2	DSC

5.3.2 Sintering Process

The 20 mm and 13 mm green compact pellets obtained from the dry pressing process were sintered. In this study, the green pellets were put on a bed of zirconia setting powders (supplied by Unitec Ceramics) which provided evenly heat transfer during the sintering process. The setting powder was retained in a 140 ml rectangular alumina crucible (L × W × H = 84 mm × 58 mm × 41 mm) (Figure 5.3). Occasionally, cracks were found on the edge of the fired pellets if sintering undertaken without the zirconia set powder which indicated the negative influence of uneven heat transfer. All the sintering processes were conducted in a LENTON UAF 17/27E 1700 Chamber Furnace.

Mullite is a high temperature phase and its formation from a powder diffusion route, such as the one used here requires temperatures in excess of 1500°C. To evaluate the influence of temperature and sintering conditions on the products development different temperature regimes were evaluated. The conditions are listed in Table 5.4.

Table 5.4 Details of sintering programmes

Sintering Temperature (°C)	Heating Rates (°C·min^{-1})	Dwelling Time (Hours)	Cooling Rates (°C·min^{-1})
1540	10	2	10
1600	3; 10	2	3; 10
1685	10	2	10

5.4 Extrusion Product Development

Extrusion technology was also developed to allow new refractory products to be produced. The extrusion process allows the creation of products with fixed complicated cross section but in different lengths. The shapes of the extrudates are varied and can be rods, tubes and bricks (116).

In this study, two different paste formulation systems were developed. One was an aqueous based paste system, and the other one was an organic based paste system. Both paste types were evaluated through the extrusion process and their subsequent processes to form rods. The properties and microstructures of the fabricated parts were compared to the products produced by dry pressing.

5.4.1 Paste Formulation

5.4.1.1 Solid phase materials

In this study, two types of ceramic powders were used to form the pastes. The first was a ceramic waste powder mixed with alumina 3000 SG by attrition milling in

water and dried. This powder is denoted AWP standing for attrition milled in water powder. The second powder was AWP further processed by grinding in a ball mill with isopropanol. This powder feed stock is denoted BIP, standing for ball milled in isopropanol powder.

The particle size and distribution data of these two types of ceramic powders was evaluated. The results are show in Figures 5.4 and 5.5 respectively.

As can be seen from these two figures, AWP has a d_{50} of 1.03 µm and BIP 0.80 µm. This small difference in d_{50} suggests both powders are well dispersed and mixed but BIP is slightly more deagglomerated and possibly finer ground. The shapes of the curves are very similar and both have a relatively narrow distribution according to the breadth value shown in Table 5.5 (127).

The relatively fine particle size and narrow distribution should help the particles to disperse and mix easily and form a uniform paste.

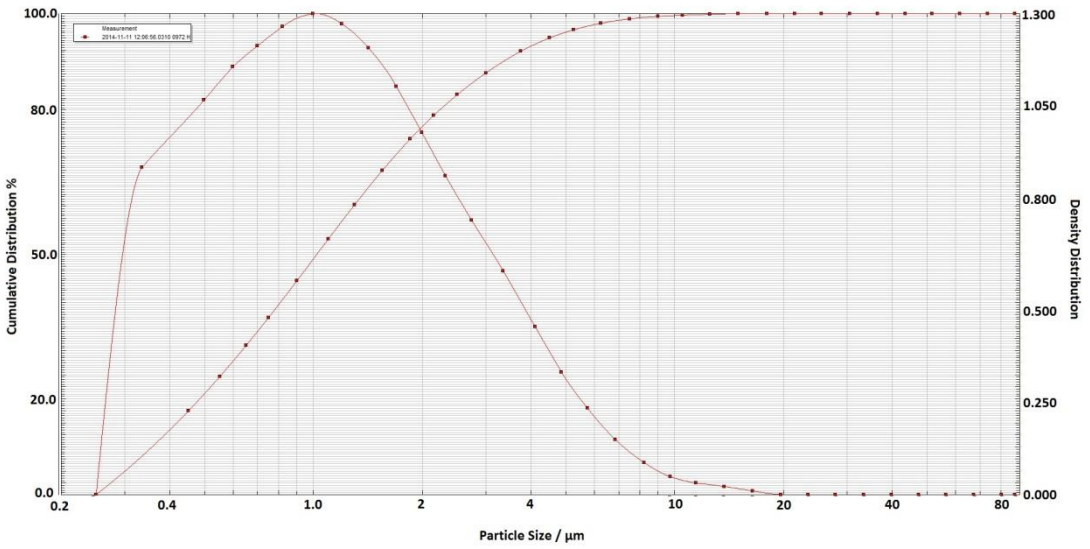

Figure 5.4 Particle size distribution of the powder produced by attrition milling in water (AWP)

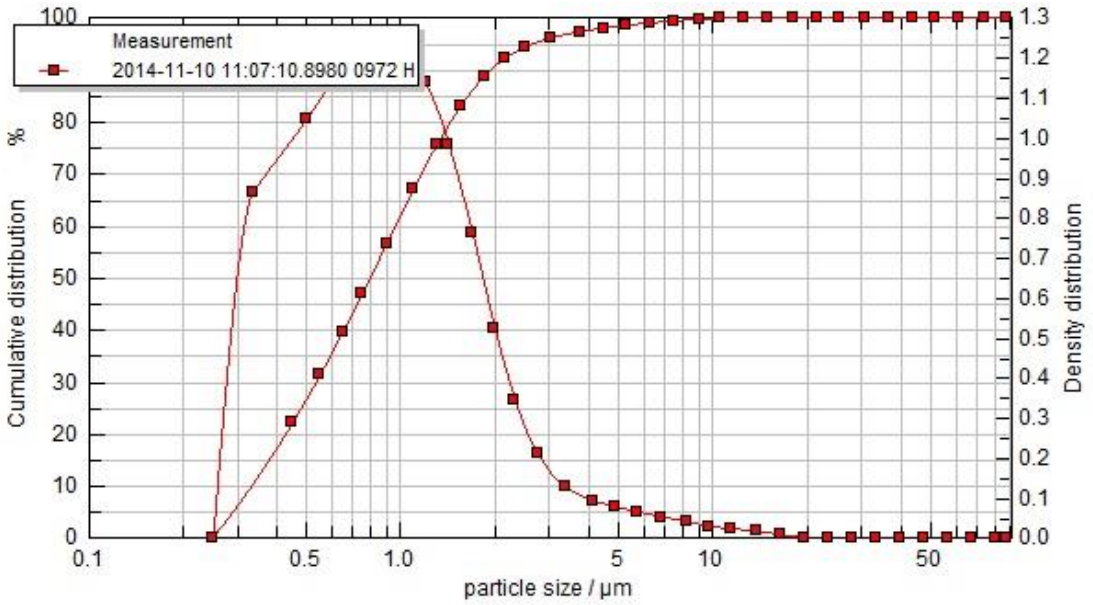

Figure 5.5 Particle size distribution of the AWP powder additionally treated by ball milling in isopropanol (BIP)

Table 5.5 Particle size data of 4 samples

Sample	D_{10} (µm)	D_{50} (µm)	D_{90} (µm)	D_{99} (µm)	Breadth $\frac{D_{90}-D_{10}}{D_{50}}$
AWP	0.37	1.03	3.39	7.90	2.93
BIP	0.34	0.80	1.97	6.85	2.04

5.4.1.2 Formulation of aqueous based paste

The formulation of the aqueous based paste system which developed by the author is shown in Table 5.6. The METHOCEL K15M which is a hydroxypropyl methylcellulose (HPMC) used in this study was supplied by DOW, U.S.A and the glycerol was supplied by Fisher Scientific, UK with a purity of 99+ %.

Table 5.6 Formulation of aqueous based paste system

	Materials	**Amount**	**Mass Fraction (Liquid Phase)**
Solid phase			
AWP or BIP	Ceramic Waste	200 g	N/A
Liquid Phase			
Major Binder	Water	40 mL	91.0 %
Minor Binder	Methocel K15M	3.5 g	8.0 %
Plasticiser	Glycerol	0.5 mL	1.0 %

The binder system consists of water, Methocel K15M and glycerol as functional components. The major binder phase, water, had a low viscosity thus may have caused phase separation of the paste. The minor binder, Methocel K15M, was required to modify the rheology of the binder system to prevent phase separation and also improve the strength of the green extrudates. The Methocel K15M is a cellulose ether powder which is soluble in water giving a pseudoplastic visco-elastic fluid. Methocel K15M has a viscosity of 15000 mPa·s with 2% in water at 20 ℃ (197).

To prevent cracks which developed during the drying process glycerol was added to reduce the volatilization rate of the liquid phase. The liquid phases would volatilize more uniformly and the green extrudate dried evenly.

5.4.1.3 Formulation of organic based paste

The formulation of organic based paste is given in Table 5.7. The B30H PVB (polyvinyl butyral) and B60H PVB used in this study were supplied by Kuraray, Europe. The DBP (dibutyl phthalate) and stearic acid were both supplied by Sigma-Aldrich, UK with an assay of 99+% and 98.5+% respectively. This formulation of the organic binder system was based on a formulation developed by the Functional Materials Group (University of Birmingham)(198).

Table 5.7 Formulation of organic based paste system

	Materials	**Amount**	**Mass Fraction (Liquid Phase)**
Solid phase			
AWP or BIP	Ceramic Waste	200 g	N/A
Liquid Phase			
Major Binder	Cyclohexanone	40 mL	64.7 %
Minor Binder	B30H Polyvinyl Butyral	10 g	16.2 %
Minor Binder	B60H Polyvinyl Butyral	10 g	16.2 %
Plasticiser	Dibutyl Phthalate	1.1 g	1.8 %
Lubricant	Stearic Acid	0.67 g	1.1 %

The major binder cyclohexanone is a saturated cyclic ketone with six carbon atoms. It is a colourless organic compound with argillaceous smell. Cyclohexanone is a common organic solvent which can dissolve most organic chemicals. Similar to water, it also has a relatively low viscosity (2.02×10^{-3} Pa·s) and volatility (199). Cyclohexanone is sensitive to the environment which allows to control drying of the green extrudates by changing the humidity levels.

The B30H PVB and B60H PVB are two different grades polyvinyl butyral which have different molecular weights 30 and 60 M respectively. Polyvinyl butyral is not soluble in water but soluble in most organic solvents including ethanol, acetone and cyclohexanone. The specification of these two types of PVB can be found in Table 5.8 (200, 201). The most significant difference is that B60H has a higher viscosity than B30H. The two PVB in combination provide a balance of viscosity. B30H can be considered as the minor binder while B60H PVB adds stiffness to allow the paste to retain its shape.

Table 5.8 Properties of two types of PVB (200, 201)

	Non-volatile content (wt. %)	**Content of polyvinyl alcohol (wt. %)**	**Content of polyvinyl acetate (wt. %)**	**Dynamic viscosity 10% solution in ethanol (mPa·s)**
B30H PVB	≥ 97.5	18 – 21	1 – 4	35 – 60
B60H PVB	≥ 97.5	18 – 21	1 – 4	160 – 260

Dibutyl phthalate is the most commonly used plasticizer for PVB which can weaken the bonds and at the same time increase separation of the polymer molecules to enhance plastic deformation (202).

Stearic acid is an octadecanoic acid which is a white crystalline solid at room temperature. The nonpolar chain of steric acid molecule provides solubility in organic solvents while the polar head of its molecule can easily be attached to inorganic molecules. Thus it is thought to ease the interaction between the organic carrier and the powder system. It can reduce the agglomeration of the powder and improve the homogeneity of the paste.

5.4.2 Kneading: Paste Forming Process

The raw materials in the pastes need to be combined to form the paste. In this work kneading was performed on the ingredients to force the mixing of the powders and liquids. Both binder systems were mixed at room temperature with cooling to prevent frictional heating. It has been shown that the mixing operation has a significant influence on the paste performance and the procedure is detailed in the following sections (116).

5.4.2.1 Experimental Apparatus

Z-blade mixers are widely used in food, ceramic and pigment industries for materials kneading processes. In this study, a WERNER & PFLEIDERER Z-blade Kneading Machine (Type: DUK05KSPV) was used to conduct the mixing operations. Photographs of the outside and inside structures of the Z-blade mixer are shown in Figure 5.6. As can be seen, the machine was composed by a sealable kneading

chamber and a water cooling system. The water cooling system ensured the mixing process was conducted at a constant temperature which reduced the evaporation of the liquid phase and maintained the accuracy of the formulation.

(a) **(b)**

Figure 5.6 Outside (a) and inside (b) of the Z-blade kneading machine used in this study

There were two 'Z' shaped mixing blades which rotated at different speeds to provide different shear rates and allow the passing of material one to another. The chamber had a volume of approximately 2 litres was sealed to prevent the materials loss during the mixing procedure.

5.4.2.2 Experimental Procedures

For the aqueous based paste system, the dry ingredients (ceramic powders and Methocel K15M) (Section 5.4.1) were weighed and added into the mixing chamber and dry mixed for five minutes. Five minutes dry mixing time was selected to allow

the required mixing but minimise the wear on the blades and contamination of the powders.

The liquid phase ingredients, water and glycerol, were added and the mixture kneaded for 30 minutes. During the process, any materials which stuck on the surface of the chamber and blade were scraped off every 5 minutes to ensure all the materials were mixed thoroughly. The mixed paste was stored in the fridge. Pastes were stored for 24 hours before use and no longer than 5 days.

The organic based paste system followed the same procedure of the aqueous one by adding the solid materials (ceramic powders, B30H PVB, B60H PVB and stearic acid) first, followed by dry mixing for 5 minutes. Then the liquid chemicals (cyclohexanone and DBP) were introduced in the chamber and left to knead for 30 minutes. The manual check frequency was reduced to every 10 minutes to reduce the materials loss as the organic liquids were volatile. The paste was put into a sample bag and stored in the fridge for at least one hour before extrusion. This was done following the findings of R. Wildman's PhD thesis (University of Birmingham) (203).

5.4.3 Extrusion Process

The principles and theories of paste extrusion were discussed in Chapter 2.6. This section will focus on the experimental apparatus and procedures used.

In this study, all the extrusion processes were conducted on an INSTRON 4467 Universal Testing System with 30 kN load cell. A ram extruder set was used to produce the rod samples. As can be seen in Figure 5.7, the extruder set was

composed by a barrel, a ram, a fixing ring and several substitutable dies. There were two dies used in this study which were 1 mm and 3 mm in diameter (L/D = 1).

The selected die was attached at the end of the barrel and fixed by the retention ring. About 100 g of paste was filled into the barrel which had a 25 mm inner diameter. A wooden rod was used to press the paste in the barrel to make sure the paste was compacted. The ram was inserted in the barrel and a load frame was used to push the paste from the assembly. The pastes were extruded with a fixed ram speed of 10 $mm \cdot min^{-1}$.

Figure 5.7 Photo of extruder set

Both aqueous based paste and organic based pasted were extruded by using 1 mm and 3 mm diameter dies. These rods were cut into samples with 20 mm and 40 mm length respectively. This was due to the required sample aspect ratio for the 3-Point

bending test (10:1 ratio length to diameter). The selected length allowed for sintering shrinkage.

5.4.4 Drying Process

The cut rods were placed on a V grooved alumina plate to allow the sample to dry uniformly. Figure 5.8 shows the rod samples with 3 mm diameter produced from an organic based paste.

The rods made from water based paste were dried at room temperature for 24 hours. The surface and end of the rods were smooth and no cracks were visible.

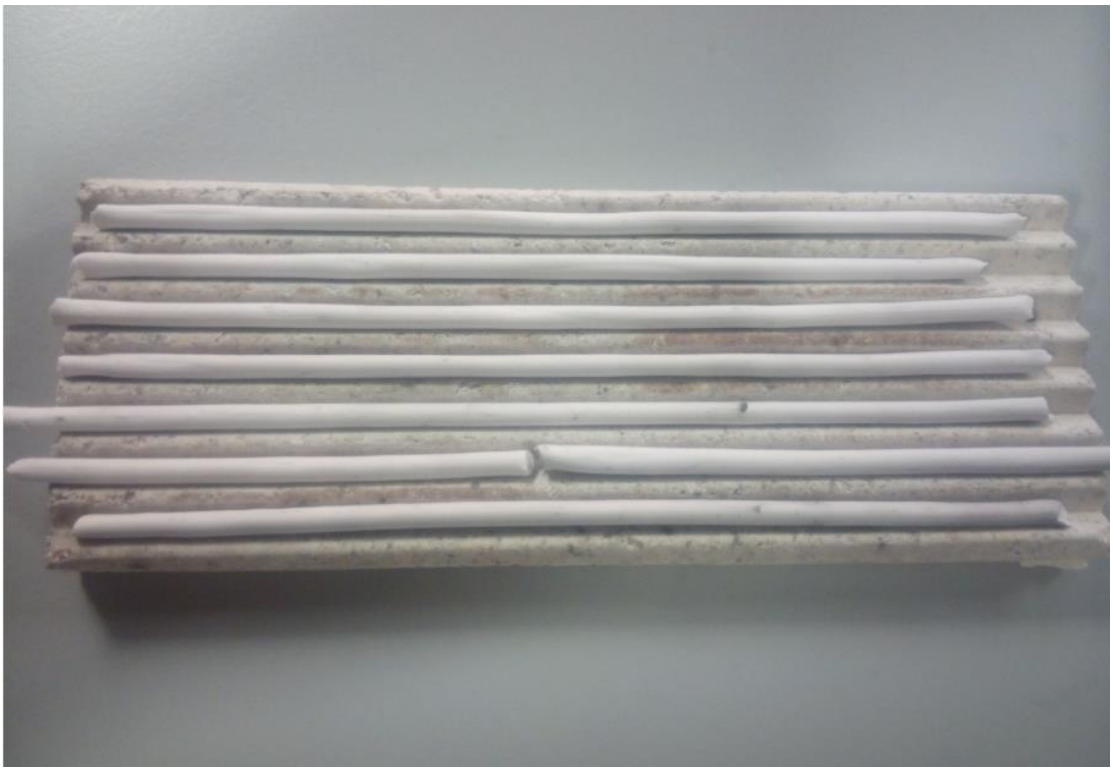

Figure 5.8 3 mm green rod samples made from an organic based paste

Rods made from pastes with an organic binder all developed cracks on the surface when drying in a room environment. Therefore, a Votsch Environment Oven was employed to fix the temperature and humidity during the drying process.

Table 5.9 Drying conditions of rods made from organic based paste

Condition / Diameter	Room environment	60 % Humidity 20 ℃	70 % Humidity 15 ℃
1 mm Rods	Some Cracks	Few cracks	No cracks
3 mm Rods	Many Cracks	Many Cracks	Many Cracks

As can be seen from Table 5.9, there were many cracks on the surface of the rods with 3 mm diameter no matter what drying conditions were employed. The 1 mm rods could be dried without observable cracking if the temperature of drying was reduced and the humidity increased. Crack-free samples of 1 mm diameter were produced at 70% humidity and 15°C. All the organic based samples were examined after 48 hours drying under these conditions.

5.4.5 Sintering Process

The dried green rod samples made from both aqueous and organic based paste were further processed by sintering in the furnace in order to form the zirconia toughened mullite composition.

In this study, the green rods were removed from the V-shape alumina plate after drying and firing on zirconia setting powder. All the sintering processes were conducted in a LENTON UAF 17/27E 1700 Chamber Furnace. As can be seen from

Table 5.9, different sintering programmes were carried out to establish the optimum firing cycle for refractory products being developed.

Table 5.10 Details of sintering programmes

Sintering Temperature (°C)	Heating Rates (°C·min^{-1})	Dwelling Time (Hours)	Cooling Rates (°C·min^{-1})
1600	3 or 10	2	3 or 10
1685	10	2	10

CHAPTER VI CHARACTERISATION OF REFRACTORY PRODUCTS

6.1 Introduction

In the previous chapters the conversion of an investment casting waste ceramic to refined refractory products has been described. The material was first coarse ground and cleaned before fine milling and chemical adjustments were undertaken to produce a feedstock material suitable for shaping. Shaping was undertaken either by dry pressing or extrusion. Two types of binder system were employed in the extrusion process.

This chapter will illustrate how a series of refractory formulations were evaluated and how a set of representative products were selected to allow comparison of the processing methods and product properties. Different analytical methods (described in Chapter 3) were applied to characterise the products.

The results of these characterisation tests including particle size distribution, density, shrinkage, mechanical strength, phase content, hardness, thermal expansion and sintering behaviour, thermal dynamic behaviour, microstructure, morphology and thermal shock resistance will be described and analysed.

6.2 Refractory Product System and Representative Samples

To compare the properties of the products produced from ceramic waste, commercial raw materials were used and passed through same processing

procedures which included the use different milling devices (attrition mill and ball mill), milling fluid (water and isopropanol) and sintering temperatures (1540, 1600 and 1685 ℃). Fused silica, supplied by the same local foundry plant, UK with 97 % purity as the ceramic waste, and alumina, supplied by ALMATIS, UK with 99.9 % purity, powders were used to develop mullite refractories. Zirconium oxide, supplied by Sigma-Aldrich, UK with 99 % purity and aluminium oxide powders were used to produce zirconia toughened mullite refractories.

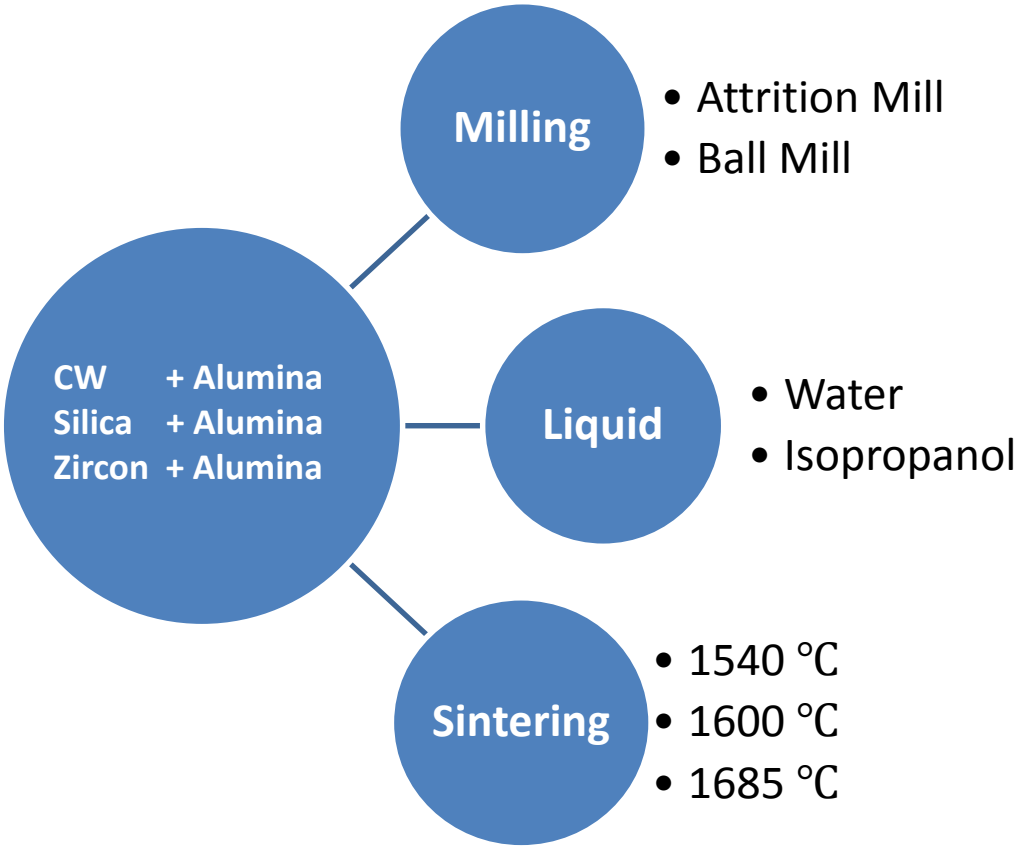

Figure 6.1 Compact pellet refractory product system (CW is Ceramic Waste)

The extrusion products were developed by using attrition milled in water waste powder (AWP) and ball milled in isopropanol powder (BIP) using either water or

organic based binder systems and sintering temperatures of 1600 or 1685 ℃. (Refer to Section 5.4 for details)

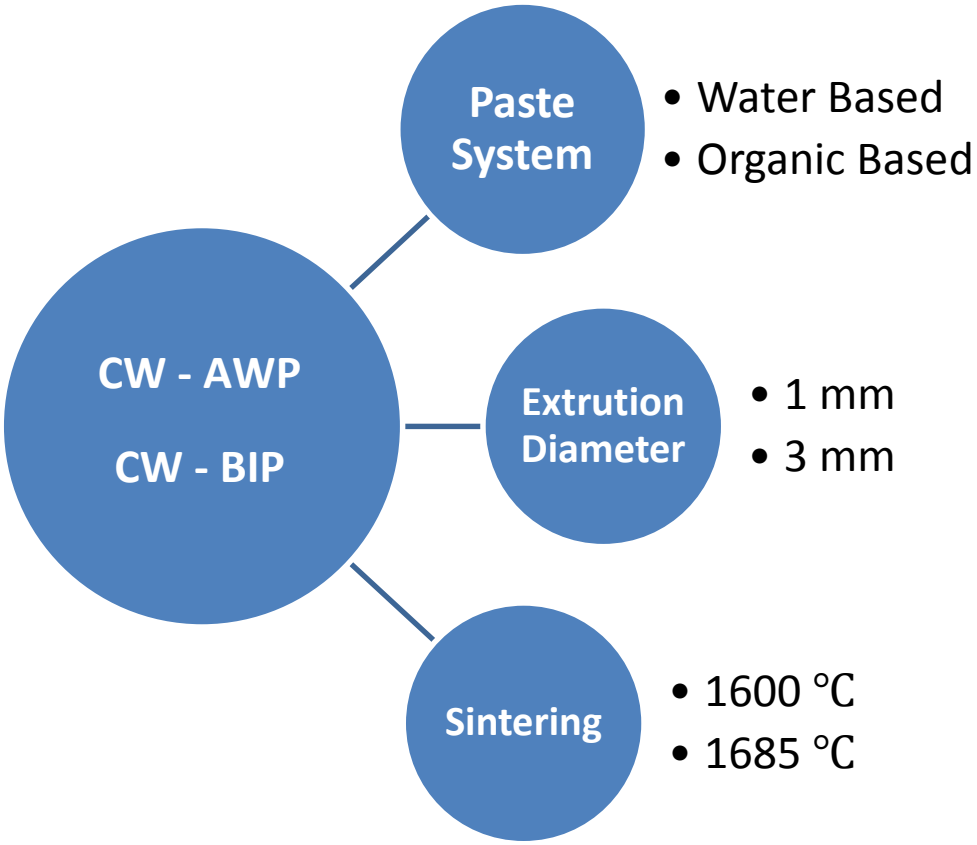

Figure 6.2 Extrusion refractory product system (CW is Ceramic Waste)

Figure 6.1 and Figure 6.2 shows the compact refractory product and extrusion refractory product permutation diagrams respectively. As the aim of this study was to develop materials by using ceramic wastes, and due to device and time limitations, not all products under each condition were evaluated. For example, silica and alumina pellets were not sintered at 1540 ℃; the commercial powders (SiO_2 + Al_2O_3 and $ZrSiO_4$ + Al_2O_3) were not directly processed in isopropanol by attrition milling and there was no organic paste extruded as 3 mm rods due to adverse cracking during the drying process.

All these pellet products and extrusion products combined together formed the whole refractory sample system. There were totally 36 different products. The whole sample lists with detailed production conditions can be found in Appendix A.

The weight and dimensions of the samples were recorded, thus the density and shrinkage data calculated. The mechanical strength tests were also carried out at least 5 times for each material, and the average value of flexural strength was obtained. Full list of results of all 36 samples are shown in Appendix B.

Table 6.1 Details of 6 representative samples

Product Number	Name	Type	Raw Materials	Milling	Sintering (heating rate)
Ceramic waste compact samples					
8	PCA1685	Compact Pellet	Ceramic Waste + Alumina	Ball milled in isopropanol	1685 ℃ (10 ℃·min^{-1})
19	PCA1600	Compact Pellet	Ceramic Waste + Alumina	Ball milled in isopropanol	1600 ℃ (10 ℃·min^{-1})
Commercial material compact samples					
24	PSA1600	Compact Pellet	Silica + Alumina	Ball milled in isopropanol	1600 ℃ (10 ℃·min^{-1})
28	PZA1600	Compact Pellet	Zircon + Alumina	Ball milled in isopropanol	1600 ℃ (10 ℃·min^{-1})
Ceramic waste extrusion samples					
30	EWH1600	Extrusion rod	Water Based Paste	Attrition milled in water	1600 ℃ (10 ℃·min^{-1})
34	EWI1600	Extrusion rod	Water Based Paste	Ball milled in isopropanol	1600 ℃ (10 ℃·min^{-1})

By comparing the density and flexural strength results, 6 samples were then selected as representative products. These 6 samples were chosen from different raw

materials, processing routes, sintering temperatures and product types which formed the lowest to highest density and flexural strength differences in the full sample set.

Other analytical tests were conducted on these samples to give a comprehensive understanding of the properties of the refractory products. Table 6.1 shows the details of the 6 representative samples selected.

In this table, the sample is identified with its own number and coded name. 'P' represents a pressed pellet product; 'C' identifies waste ceramic; 'A' indicates commercial alumina; 'S' stands for commercial silica; 'Z' indicates commercial zircon; 'E' identifies an extruded product; 'W' indicates a water based paste; 'H' stands for water as milling fluid; and 'I' shows that the powder system was 'ball milled in isopropanol'. 'Ball milled in isopropanol' was an additional step to 'attrition milled in water' to reduce the agglomeration developed during the drying process (refer to Section 5.2). The number in the code name indicates the sintering temperature that was applied. Therefore, for example, sample No.19 shows code name PCA1600 which stands for pellet product made by ceramic waste and alumina sintered at 1600 ℃; No.34 has code name as EWI1600 which means it was an extrusion product produced by using ball milling in isopropanol powder through a water based paste system and sintered at 1600 ℃.

In order to compare and analyse certain properties of the products (for instance, dilatometry and micro-structure), two additional samples were produced by changing some conditions of sample No.19 (PCA1600) manufacture. The details of the two resultant products are shown in Table 6.2

Table 6.2 Details of 2 additional samples

Product Number	Name	Type	Raw Materials	Milling	Sintering (ramp rate)
Additional ceramic waste compact samples					
35	PCAY1600	Compact Pellet	Ceramic Waste + Alumina + Yttria	Ball milled in isopropanol	1600 ℃ ($10\ ℃{\cdot}min^{-1}$)
36	PCA1540	Compact Pellet	Ceramic Waste + Alumina	Ball milled in isopropanol	1540 ℃ ($10\ ℃{\cdot}min^{-1}$)

The No.35 (PCAY1600) product contained an addition of 1.78 wt. % of yttrium (III) oxide in the starting materials in order to generate yttria stabilized zirconia in the refractory structure. No.36 (PCA1540) used same manufacturing conditions as No.19 (PCA1600), but applied a lower sintering temperature of 1540 ℃.

Comparisons between sample No.8 (PCA1685), No.19 (PCA1600) and No.36 (PCA1540) showed how different sintering temperatures influenced the properties of the product. Comparing sample No.24 (PSA1600), No.28 (PZA1600) and No.19 (PCA1600) illustrated how the zirconia form changed the properties of mullite and how commercial zircon and waste ceramic as the raw material source affected the final product. Comparisons between sample No.19 (PCA1600) and No.34 (EWI1600) can showed the differences between compacted products and extruded products. The powder milling and drying processes were reviewed by comparing sample No.30 (EWH1600) and No.34 (EWI1600). Sample No.35 (PCAY1600) was designed to demonstrate the effects of yttria as a stabilizer for zirconia in the zirconia toughened mullite system.

Some general trends can be found from reviewing the data in Appendix B. First, no matter what raw materials were used, the 'ball milled in isopropanol' processed powder mostly yielded higher density and strength than samples produces only by attrition milling in water. Comparisons between No.30 (EWH1600) and No.34 (EWI1600) will confirm this in following sections.

Generally, sintering at 1600 ℃ produced better quality samples (higher density and mechanical strength) than at 1540 ℃ and 1685 ℃. Comparisons of No.8 (PCA1685), No.19 (PCA1600) and No.36 (PCA1540) will confirm this in following sections. The reasons will be investigated by analysing other test results (for example, SEM and dilatometry). It can also be observed that the heating rate (3 ℃·min-1 and 10 ℃·min-1) did not affect the product properties. Therefore, all the selected samples were sintered using 10 ℃·min^{-1} as this heating rate reduced the processing time and energy cost.

Appendix B also shows that the water based paste system products have slightly better mechanical strength than the organic based ones. As demonstrated in Table 5.8, the organic paste system products were very restrict by the drying condition and easily developing cracks. This propensity to crack was the most probable cause of the underperformance of the organic system. Therefore, the selected extrusion samples both used the water based system.

6.3 PSD Analysis

After the powders were processed and ready to be incorporated into either the dry pressing or pastes formulations, the particle size distributions were characterised to

ensure the particle size and particle size distribution of each sample was similar. The powders were complex mixtures of materials, but the major fraction was always zircon (about 70 wt. %), thus the optical model for zircon was set for all the samples except for sample No.24 (PSA1600) where 'Silica' was the selected optical model.

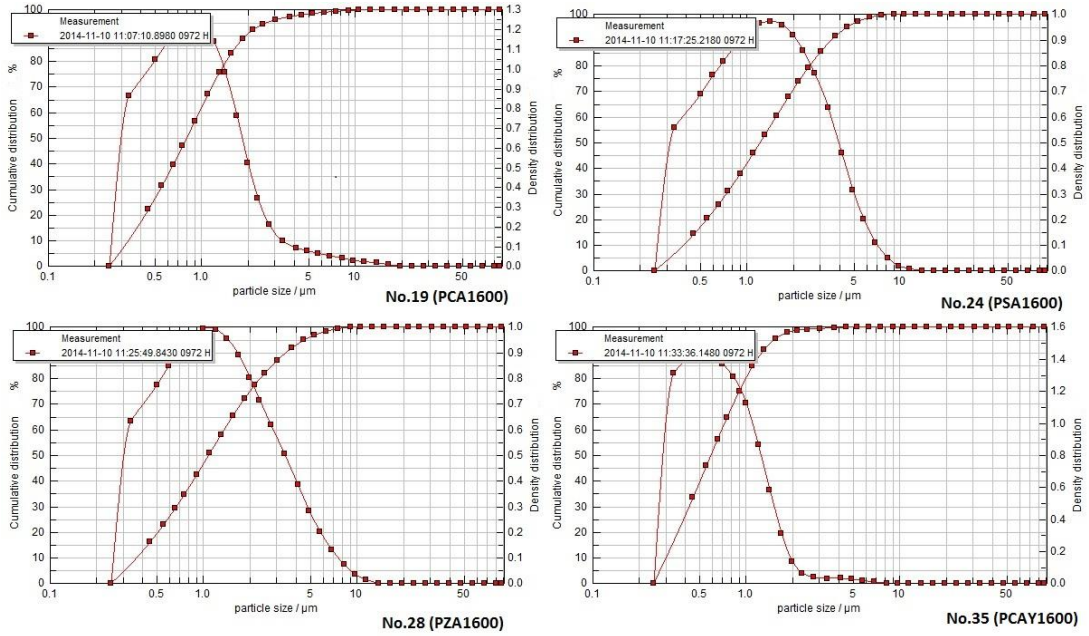

Figure 6.3 Particle size distribution of product No.19 (PCA1600), No.24 (PSA1600), No.28 (PZA1600) and No.35 (PCAY1600)

Figure 6.3 shows the particle distribution of product No.19 (PCA1600), No.24 (PSA1600), No.28 (PZA1600) and No.35 (PCAY1600). The product No.8 (PCA1685), No.34 (EWI1600) and No.36 (PCA1540) used the exactly same powder as No.19 (PCA1600) and had the same particle size distribution. The instrument used could not measure particles smaller than 0.3 µm, so the left hand tail of the graph was drawn by the software automatically which may give a false impression.

Table 6.3 Particle size data of 4 samples

Product Number	D_{10} (µm)	D_{50} (µm)	D_{90} (µm)	D_{99} (µm)	Breadth $\frac{D_{90}-D_{10}}{D_{50}}$
Ceramic waste compact samples					
19	0.34	0.80	1.97	6.85	2.04
Commercial material compact samples					
24	0.39	1.22	3.58	6.82	2.61
28	0.37	1.08	3.49	7.35	2.89
Additional ceramic waste compact samples					
35	0.31	0.59	1.27	2.65	1.63

The particle sizes of these four samples were all similar. Details of the particle sizes are recorded in Table 6.3. It can be seen that the mean particle size of No.19 (PCA1600), No.24 (PSA1600) and No.28 (PZA1600) were around 1.00 µm, and 99 % of the powder was smaller than approximately 7.00 µm.

Powder No.35 (PCAY1600) was made by taking original No.19 (PCA1600) powder with additional 1.7 wt. % yttrium (III) oxide and further grinding for 4 hours and this resulted in the mean particle size and maximum particle size being smaller than the other three powder feed stocks.

The distributions of these four powders were considered similar. Given the limitations of the method for measuring mixed phase systems, they all appear to be mono-modal and the shape of the curve implies that they were well dispersed. (128).

From the breadth figures, No.24 (PSA1600) and No.28 (PZA1600) had the widest distribution, while No.19 (PCA1600) was narrower and No.35 (PCAY1600) the narrowest distribution. This implies the particles were more closely sized in No.19 (PCA1600) and No.35 (PCAY1600) which may lead to more effective reaction during sintering process.

6.4 Density and Shrinkage

The weight and dimensions of all the samples were measured before and after the sintering process and the apparent density and area shrinkage were calculated. The true density of the selected samples was also measured and recorded by helium pycnometer (refer to Section 3.2.5).

Table 6.4 shows the average value of area shrinkage, apparent density and true density of the 8 samples. Tests for each sample were conducted 5 to 10 times and the data shown in the table is the average value. The standard deviation for each value is shown after the "±" symbol.

The standard deviation value for all the samples in Table 6.4 is relatively small compared to the measured value. This means the numbers are narrowly spread which indicates the systems error is low.

Table 6.4 Shrinkage and density of 6 representative samples and 2 additional samples

Product Number	Name	Average Area Shrinkage	Average Apparent Density ($kg \cdot m^{-3}$)	Average True Density ($kg \cdot m^{-3}$)	Density Ratio
Ceramic waste compact samples					
8	PCA1685	32% ± 0.95%	3470 ± 70	3720± 2	93.28%±0.73%
19	PCA1600	33% ± 0.76%	3580 ± 50	3660 ± 4	97.81%±0.54%
Commercial material compact samples					
24	PSA1600	11% ± 0.53%	2220 ± 30	2850 ± 5	77.89 %±0.38%
28	PZA1600	13% ± 1.72%	2950 ± 15	3810 ± 3	77.43%±1.62%
Ceramic waste extrusion samples					
30	EWH1600	31% ± 1.03%	3450 ± 80	3690 ± 8	93.49 %±1.33%
34	EWI1600	32% ± 0.99%	3520 ± 80	3640 ± 2	96.70%±1.04%
Additional ceramic waste compact samples					
35	PCAY1600	34% ±0.06%	3590 ± 40	3670 ± 5	97.82%±0.55%
36	PCA1540	31% ±0.15%	3240 ± 90	n/a	n/a

As can be seen from the table, the ceramic waste generated products (No.8, No.19, No.30, No.34, No.35 and No.36) have similar area shrinkage rates which are from 31 % to 34 %, similar apparent densities which range from 3450 $kg \cdot m^{-3}$ to 3590 $kg \cdot m^{-3}$ and true density values from 3640 $kg \cdot m^{-3}$ to 3720 $kg \cdot m^{-3}$. This is to be expected as the basic chemical formulations are closely similar by design.

Comparing the density ratio, it can be seen that product No.8 (PCA1685) and No.30 (EWH1600) have lower values than other ceramic waste generated refractory products indicating greater included porosity.

Both samples produced from the commercial materials - No.24 (PSA1600) and No.28 (PZA1600) had lower shrinkage ratios of 11 % and 13 %, apparent densities of 2220 $kg \cdot m^{-3}$, 2950 $kg \cdot m^{-3}$ and density ratio of 77.89 %, 77.43 % respectively.

The true density of No.24 (PSA1600) was 2850 $kg \cdot m^{-3}$ and is significantly lower than other samples as it contains only mullite with no toughening zirconia. The density ratio indicates that the mullite formed from the fusion of alumina and silica leads to a microstructure which is porous in nature. The microstructure of mullite formed by this process route is known to be porous due to grains growing in different directions during the sintering process (4). The reaction of zircon to form the zirconia toughened mullite appears to modify the sintering process allowing densification to a much higher level. The process is complicated by the reaction but it is known that the presence of zirconia can influence the grain growth mechanism of toughened materials. When the zirconia was formed during the reaction, it probably restricted the mobility of the dissociation process and restricts excessive mullite grain growth. Therefore, a more dense mullite microstructure was formed by the influence of zirconia particles (19, 204).

Product No.28 (PZA1600) had a similar true density to the ceramic waste generated sample because it also develops zirconia toughened mullite. However, the apparent density and density ratio are much lower which indicated the structure contained more pores. This may be due to the reason that the small amount of amorphous

silica contained in the ceramic waste helped the development of a homogeneous microstructure formation. Further analysis based on microstructure observation and thermal behaviours will resolve the mechanisms in the later sections of this chapter.

6.5 Flexural Strength

6.5.1 Results Comparison

The flexural strength of compact pellet samples was measured using the ball on 3-ball method and the failure load value was recorded. The values of strength were calculated by using Equation 3.9 (refer to Section 3.2.6.3).

The extrusion products were rods of 1 mm or 3 mm diameter with span of 20 mm or 40 mm respectively. 3-point bending tests were conducted to determine the flexural strength. The strength values were calculated by using Equation3.8 (refer to Section 3.2.6.3).

Table 6.5 shows the average value of flexural strength of the selected samples based on 5 to 15 tests for each sample. The standard deviation for each average result is shown after the "±" symbol. Generally, the ceramic waste developed refractories are stronger than those made from commercial materials. Product No.19 (PCA1600) has the highest value of 349.8 MPa, and No.24 (PSA1600) the lowest strength at 62.4 MPa. To the author's knowledge sample No.19 (PCA1600) was equivalent or stronger than other zirconia toughened mullite products reported in the literature (205-210), although it must be remembered that the testing method used here may not be the same as used in the reported works.

Table 6.5 Flexural strength of 6 representative samples and 2 additional samples

Product Number	Name	Average Flexural Strength (MPa)	Sintering Temperature	Density Ratio
Ceramic waste compact samples				
8	PCA1685	100.2 ± 4.69	1685 ℃	93.28 %±0.73 %
19	PCA1600	349.8 ± 18.40	1600 ℃	97.81 %±0.54 %
Commercial material compact samples				
24	PSA1600	62.4 ± 6.75	1600 ℃	77.89 %±0.38 %
28	PZA1600	145.2 ± 10.60	1600 ℃	77.43 %±1.62 %
Ceramic waste extrusion samples				
30	EWH1600	196.4 ± 22.37	1600 ℃	93.49 %±1.33 %
34	EWI1600	296.9 ± 21.74	1600 ℃	96.70 %±1.04 %
Additional ceramic waste compact samples				
35	PCAY1600	215.0 ± 23.80	1600 ℃	97.82 %±0.55 %
36	PCA1540	283.8 ± 20.65	1540 ℃	n/a

Comparing No.8 (PCA1685), No.19 (PCA1600) and No.36 (PCA1540), it was observed that by using same materials, the strength changed dramatically with sintering temperature. This indicates that different micro structures were formed among these three samples. The strength of No.19 (PCA1600) is higher than No.36 (PCA1540) and this suggests that at 1540 ℃ the samples may not be fully sintered. The strength value of product No.8 (PCA1685) is significantly lower than the other

two samples suggesting that at 1685 ℃ some defects were developed through over sintering. These results indicate that 1600 ℃ was the optimum evaluated sintering temperature for refractory product formation from waste derived materials. Additionally, the standard deviation shows that sample No.8 (PCA1685) exhibited the least variation, but most of the data lay within 5 % to 7 % of the mean value for this group of samples.

Sample No.35 (PCAY1600) exhibited 60 % the strength of No.19 (PCA1600) which suggests yttrium oxide (1.7 wt. %) significantly changed the properties. This may due to the yttrium inducing a different sintering mechanism and modifying the zirconia phase form. This prospect will be discussed in Section 6.11.6. It can be seen that No.35 (PCAY1600) had a slightly higher standard deviation than the No.19 (PCA1600) which suggests that when the yttria reacted with zirconia developing a different microstructure, this will be borne out in the structural analysis (Section 6.11.6).

Product No.34 (EWI1600) was 50 % higher in strength than No.30 (EWH1600) indicating that isopropanol milling can improve the mechanical strength. Isopropanol can commonly reduce the amount of agglomeration which is formed during drying process. The presence of fewer and softer agglomerations mean the powders can be mixed more uniformly in the paste formulation (123).

The strength value of the strongest compact samples (No.19) is higher than the strongest extrusion products (No.34) by 17.8 %. This may be due to the extruded product containing more binder (in this case Methocel K15M). During the sintering process, when the polymers were burnt out, that process may generate more pores in the structure which can reduce the strength of the products.

6.5.2 Failure Analysis

All the material failed by brittle fracture. Typical failure curves are shown in Figure 6.4 for sample No.19 (PCA1600). The black triangles close to the peak load show the moment when pellet failed and the triangles at the base of the failure curve indicate when the test was stopped.

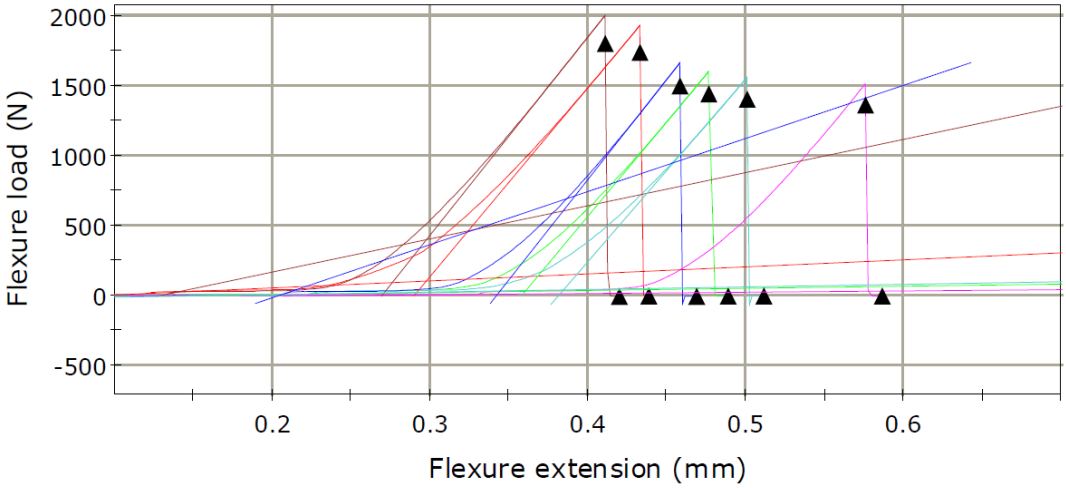

Figure 6.4 Failure curve of sample No.19 (PCA1600)

Six pellets of sample No.19 (PCA1600) were tested under the same conditions loading at 1 mm·min^{-1} with 30 kN loading cell. Due to the pellets having different thickness they failed at different loads ranging from 1400 N to 1800 N. However, the flexural deflections at break were quite similar ranging from 0.389 to 0.466 with a 0.03 standard deviation. This means all these samples exhibited brittle failure and should have same microstructure. Additionally, it shows that the repeatability and consistency of this refractory production process are very good.

There were several limitations of the method that may have contributed to errors in the results. In the ball on 3-ball test, the accuracy of sample placement was an issue.

As demonstrated in Table 3.4, the pellet samples need to have a diameter within a certain range relative to the circle on which the three lower balls rest. In this study, the model requires that the pellets have a diameter from 12.13 mm to 19.85 mm. All pellets ranged from 16 mm to 18 mm in diameter after sintering. However, there was no mechanism to ensure the pellets were placed centrally on top of the 3 balls due to the difference in diameter of each sample. This may introduce small errors in the testing system.

Most of the pellets were broken in the 900 N to 3000 N range. Therefore, the ideal loading cell would have been 5 kN but such a cell was not available. A 30 kN loading cell was chosen. However, as the capacity was much higher than the measured value, it may reduce the accuracy of the measurement. The surface finish of the specimens was as pressed and fired without any subsequent treatment, this can lead to some variance in results but the test is considered in the literature to be most suited to testing materials in this state (168, 171).

For the 3-point bending test, the sample shape and the surface finish was thought to be the main source errors. Due to the samples being extruded rods in small (1 mm or 3 mm) diameters and although care was taken in the process, they were not perfectly straight after drying and sintering process. Additionally the surface finish or the extruded samples was inconsistent. Defects on the surface of the extrudates beneath the loading point are known to cause variance in the strength data (158).

Despite all the contributing factors identified above the error gave a standard deviation ranging from 5 to 7 %. This is consistent with most refractory ceramic materials (164, 211).

6.6 XRD Analysis

The formulation was designed to develop zirconia toughened mullite refractory products (Section 5.2.1), thus the composition of the selected samples were identified using X-ray diffraction (XRD). Figures 6.5 to Figure 6.11 show the XRD patterns and analysed phase distribution results of the selected samples with the exception sample No.35 (PCAY1600).

These figures show that sample No.8 (PCA1685), No.19 (PCA1600), No.28 (PZA1600), No.30 (EWH1600) and No.34 (EWI1600) contain only zirconia and mullite indicating full conversion of zircon, amorphous silica and alumina in the raw materials to zirconia mullite.

According to the starting formulation (refer to Section 5.2.1), the theoretical phase contents of finished refractory products should be 70.4 wt. % mullite and 29.6 wt. % zirconia. In this study, XRD tests show the qualitative results of the phase analysis as a full quantitative method was not applied. However, as can be seen from the phase analysis tables, the mullite contents of these 6 samples ranged between 67 wt. % to 80 wt. % while zirconia ranged from 20 wt. % to 33 wt. %. The materials reacted following the theoretical equation (Section 5.2.1).

Sample No.24 (PSA1600) shows there was only mullite present. This suggests that silica and alumina powders were fully reacted during the sintering process.

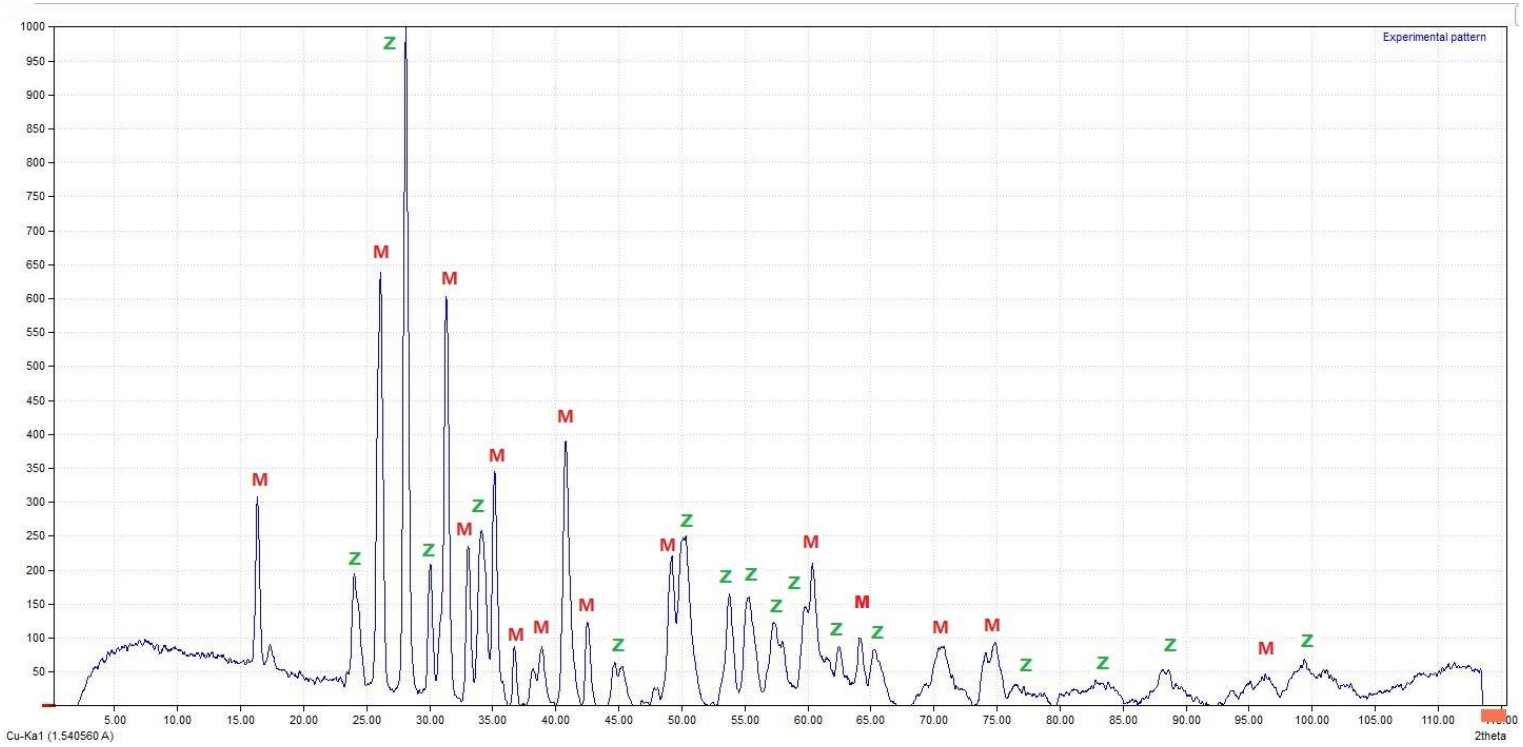

Colour	Formula	Matched Phase	Quantity
Red (M)	$Al_{2.25}O_{4.871}Si_{0.75}$	Mullite	70.9 %
Green (Z)	ZrO_2	Baddeleyite	29.1 %

Figure 6.5 XRD result of product No.8 (PCA1685)

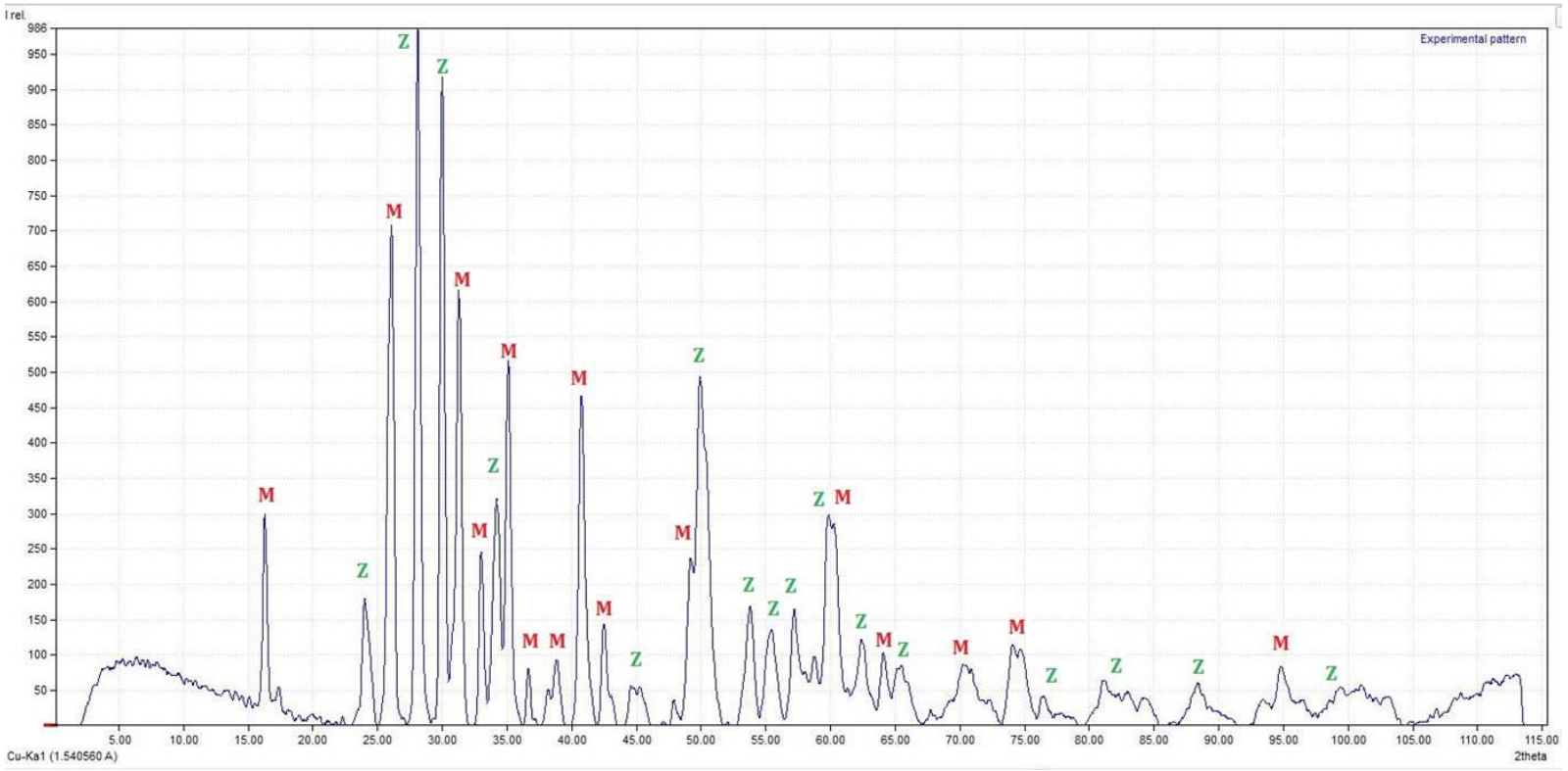

Colour	Formula	Matched Phase	Quantity
Red (M)	$Al_{2.25}O_{4.871}Si_{0.75}$	Mullite	77.2 %
Green (Z)	ZrO_2	Baddeleyite	22.8 %

Figure 6.6 XRD result of product No.19 (PCA1600)

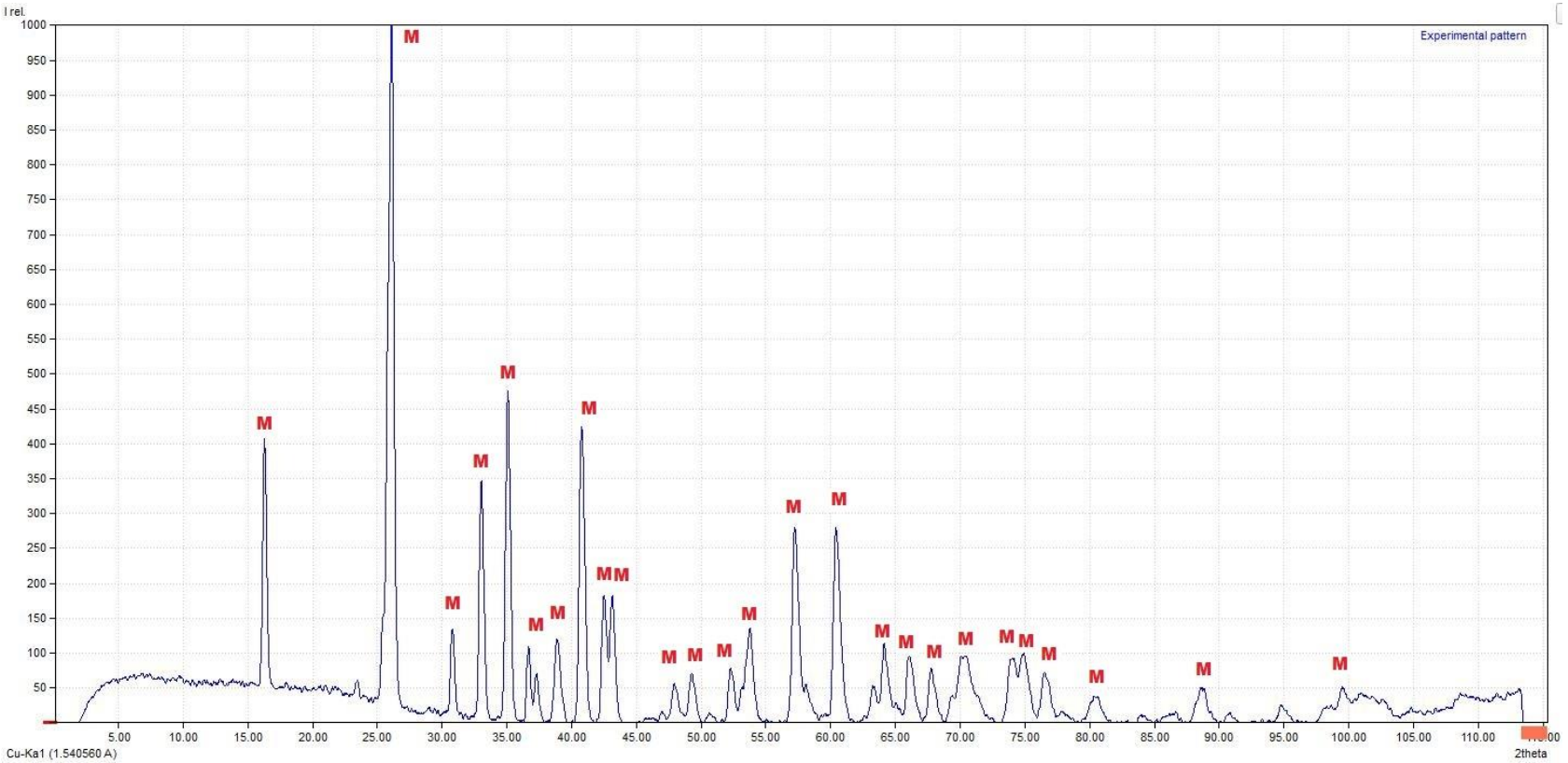

Colour	Formula	Matched Phase	Quantity
Red (M)	$Al_{2.25}O_{4.871}Si_{0.75}$	Mullite	100 %

Figure 6.7 XRD result of product No.24 (PSA1600)

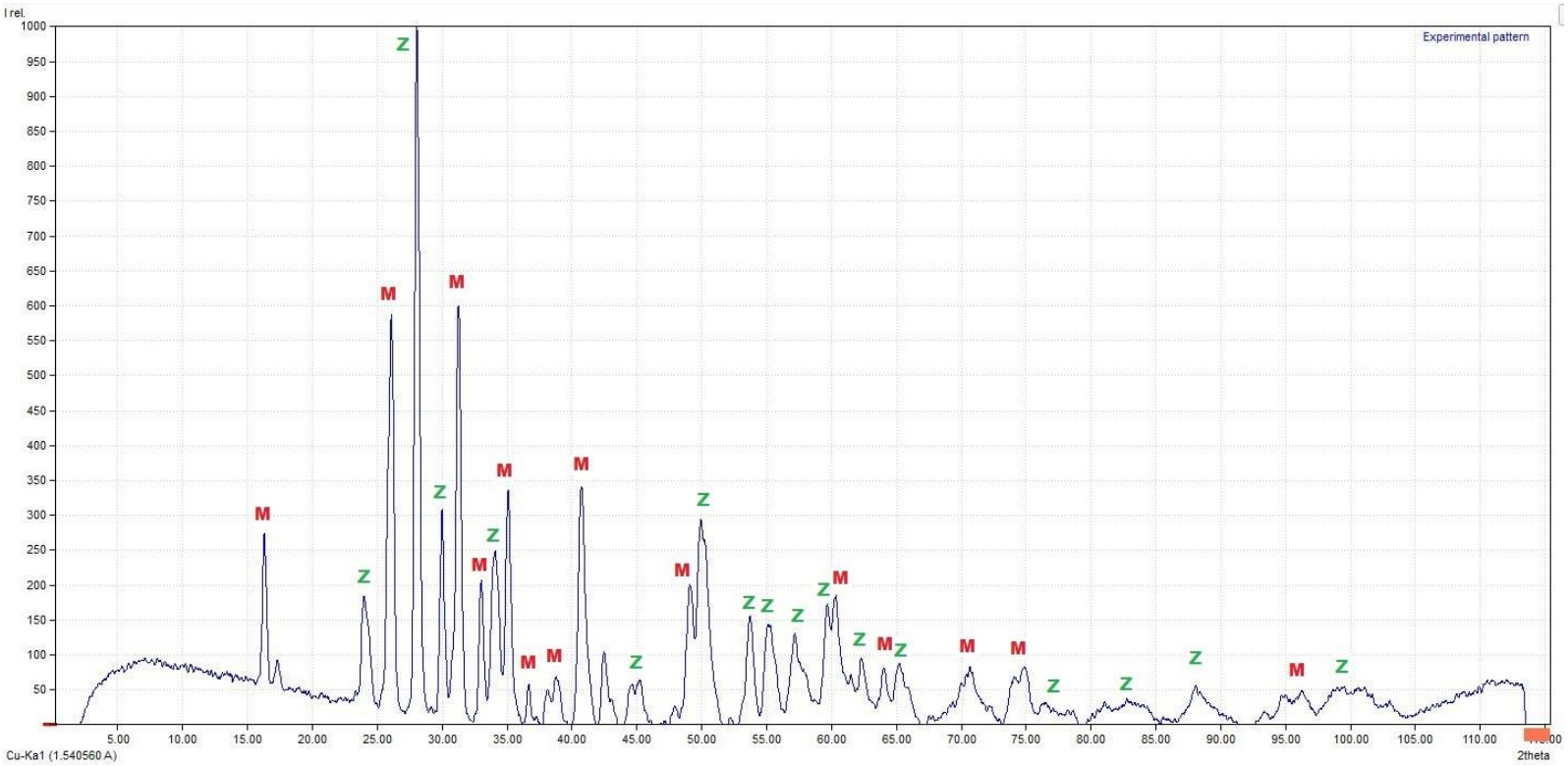

Colour	Formula	Matched Phase	Quantity
Red (M)	$Al_{2.25}O_{4.871}Si_{0.75}$	Mullite	67.3 %
Green (Z)	ZrO_2	Baddeleyite	32.7 %

Figure 6.8 XRD result of product No.28 (PZA 1600)

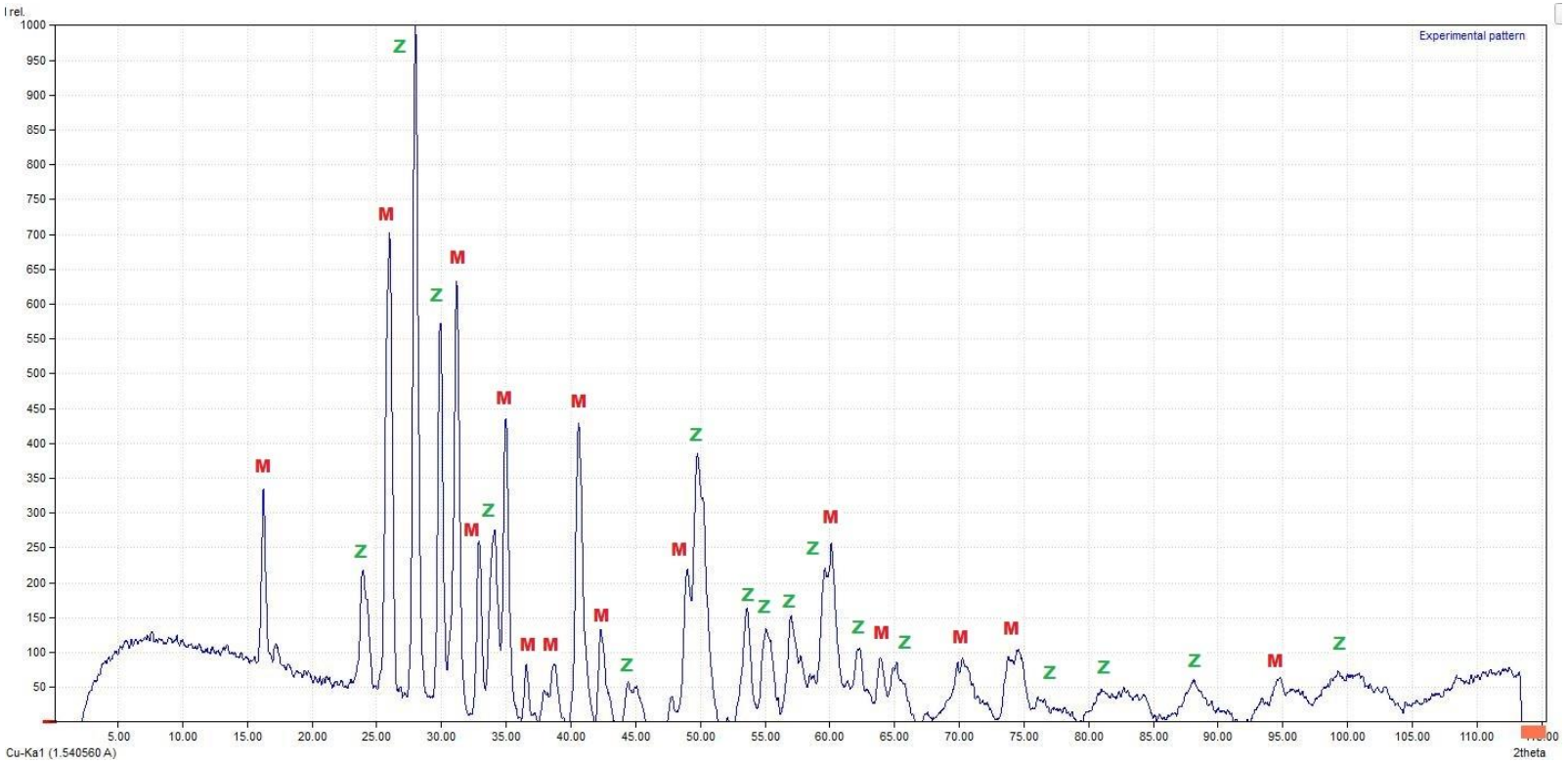

Colour	Formula	Matched Phase	Quantity
Red (M)	$Al_{2.25}O_{4.871}Si_{0.75}$	Mullite	80.1 %
Green (Z)	ZrO_2	Baddeleyite	19.9 %

Figure 6.9 XRD result of product No.30 (EWH1600)

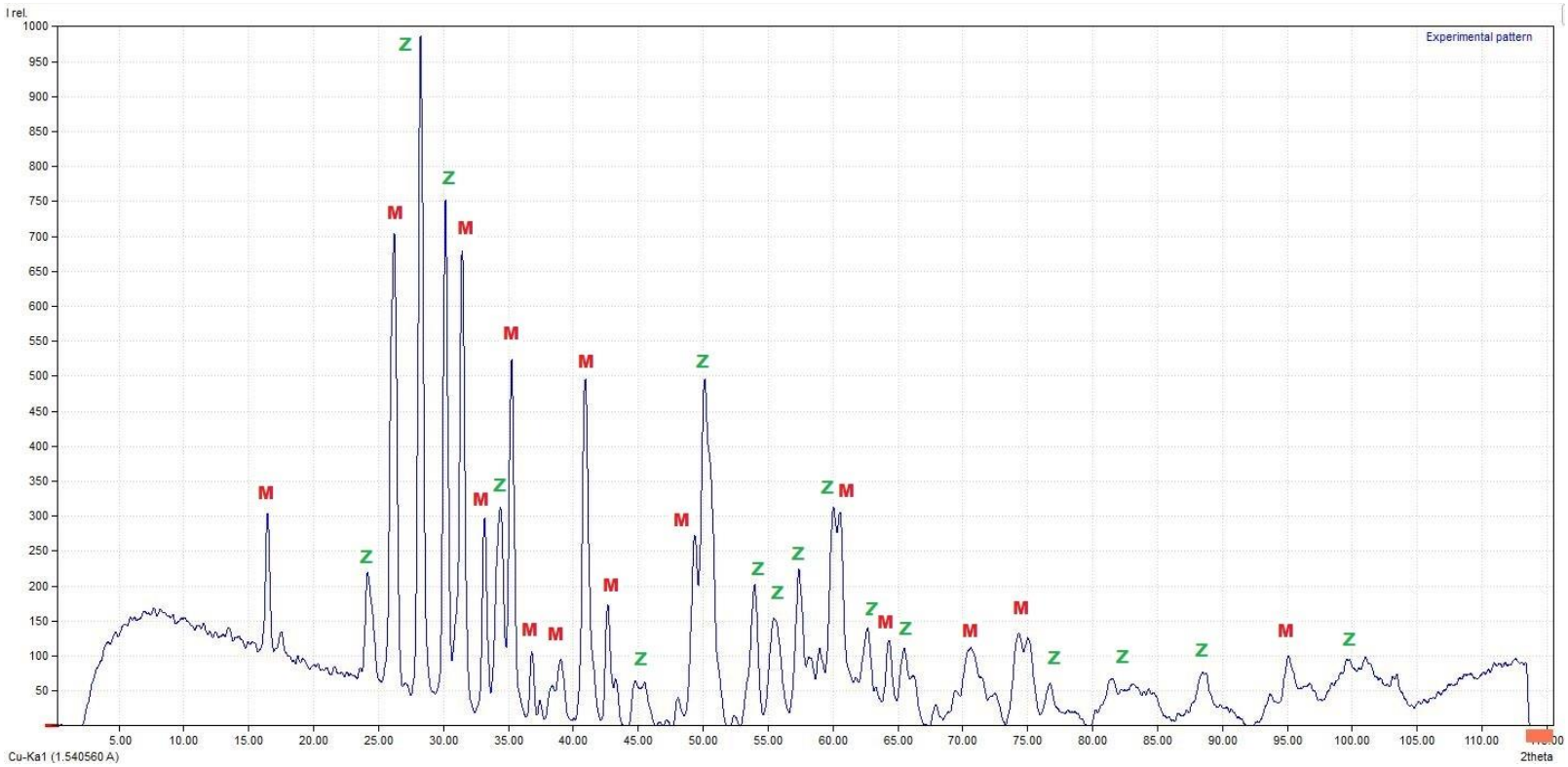

Colour	Formula	Matched Phase	Quantity
Red (M)	$Al_{2.25}O_{4.871}Si_{0.75}$	Mullite	72.8 %
Green (Z)	ZrO_2	Baddeleyite	27.2 %

Figure 6.10 XRD result of product No.34 (EWI1600)

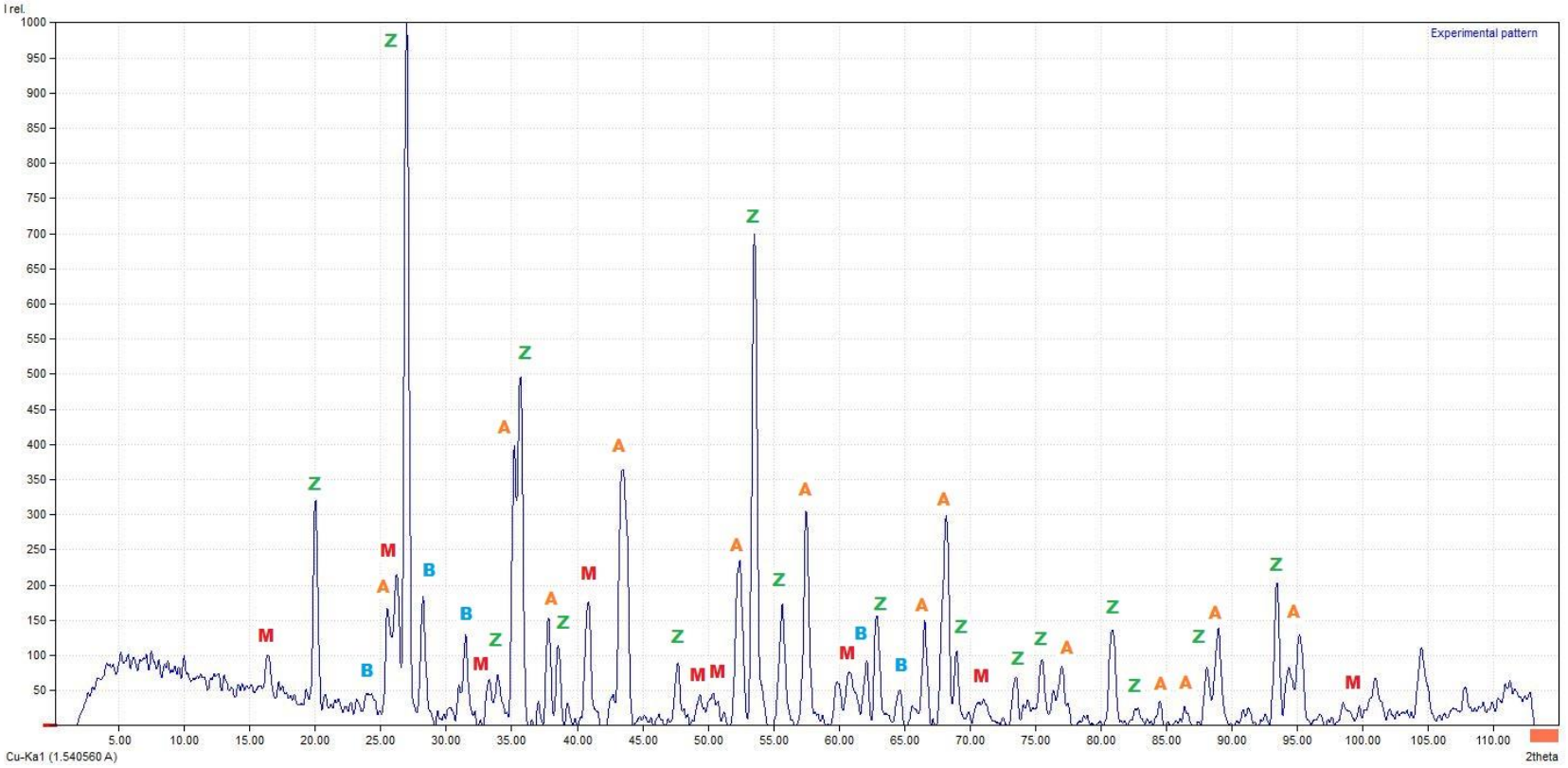

Colour	Formula	Matched Phase	Quantity
Orange (A)	Al_2O_3	Aluminium oxide	44.8 %
Green (Z)	$ZrSiO_4$	Zircon	26.9 %
Red (M)	$Al_{2.25}O_{4.871}Si_{0.75}$	Mullite	23.1 %
Blue (B)	ZrO_2	Baddeleyite	5.2 %

Figure 6.11 XRD result of product No.36 (PCA1540)

Figure 6.11 shows that sample No.36 (PCA1540) had a more complex composition which contained alumina, zircon, mullite and zirconia. By comparing the results with No.8 (PCA1685) and No.19 (PCA1600), it can be concluded that sintering at 1540 ℃ did not provoke full decomposition of the zircon. Furthermore, it indicates that the reactions were progressing by zircon dissociation first followed by mullitisation of the silica and alumina phases. Zircon dissociation appears to be the rate-determining step due to there being no cristobalite found in the XRD pattern. This suggests that when the zircon dissociated into zirconia and silica, the free silica was mopped up by a near instant reaction with alumina to form mullite which resulted in a mixture of unreacted alumina and zircon and the newly formed zirconia and mullite phases.

6.7 Dilatometry

6.7.1 Thermal Expansion

A horizontal dilatometer was used to identify the thermal expansion properties of the sintered refractory products. Each sample was repeated 2 to 3 times to a maximum 1540 ℃ testing temperature due to the limitation of the device (Section 3.2.9).

The dilatometry curves for the mullite product No.24 (PSA1600) are shown in Figure 6.12. As can be seen, the sample expanded almost linearly in length with temperature and shrank in a similar way as temperature reduced. The shape of the curves fits the typical thermal expansion behaviour of mullite (4). When the sample was held at 1540 ℃ for 1 hour, the curve shows the sample shrinking slightly. This situation does not indicate the sample was sintering, but is caused by machine error.

This was proved by re-test of the same sintered sample several times. Figure 6.13 shows that after 3 repeated dilatometry tests, the curve was exactly the same as the first tests shown in Figure 6.12. All samples show the same behaviour during the dwell at 1540 ℃ for 1 hour.

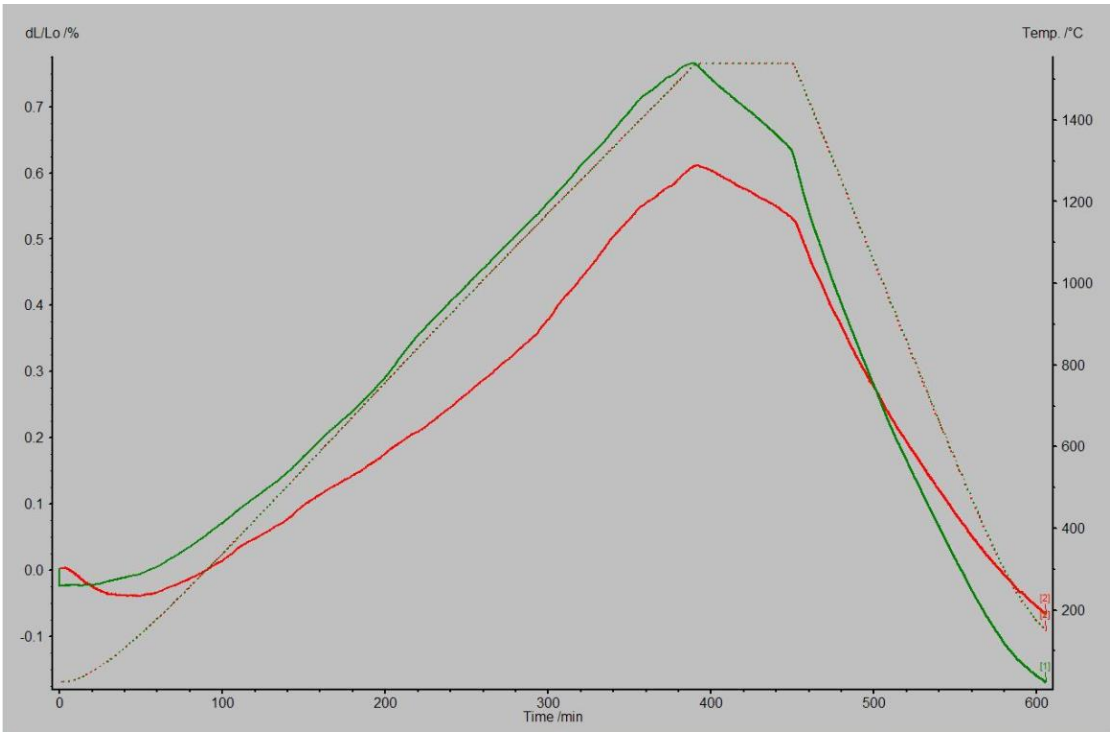

Figure 6.12 Dilatometry curves of two No.24 samples (PSA1600)

The zirconia toughened mullite samples without yttria addition No.8 (PCA1685), No.19 (PCA1600), No.30 (EWH1600) and No.34 (EWI1600) all exhibited a similar response. As an example the curves of sample No.19 (PCA1600) after sintering are shown in Figure 6.14.

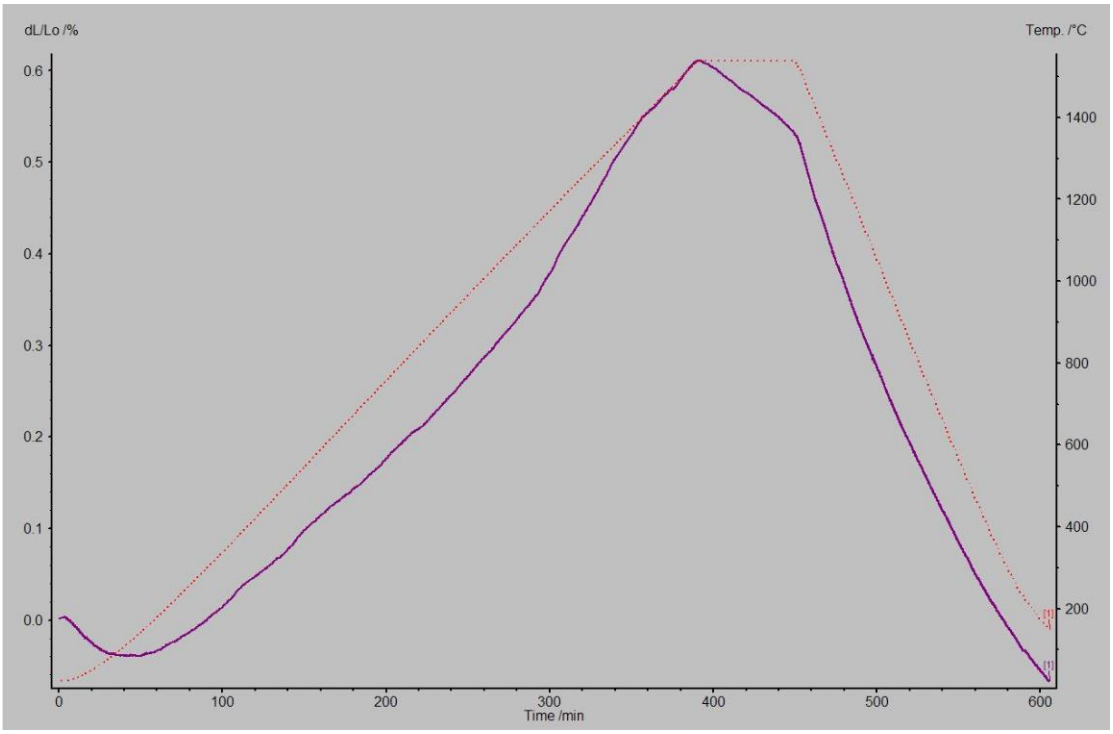

Figure 6.13 Dilatometry curve of sample No.24 (PSA1600) after three repeated tests

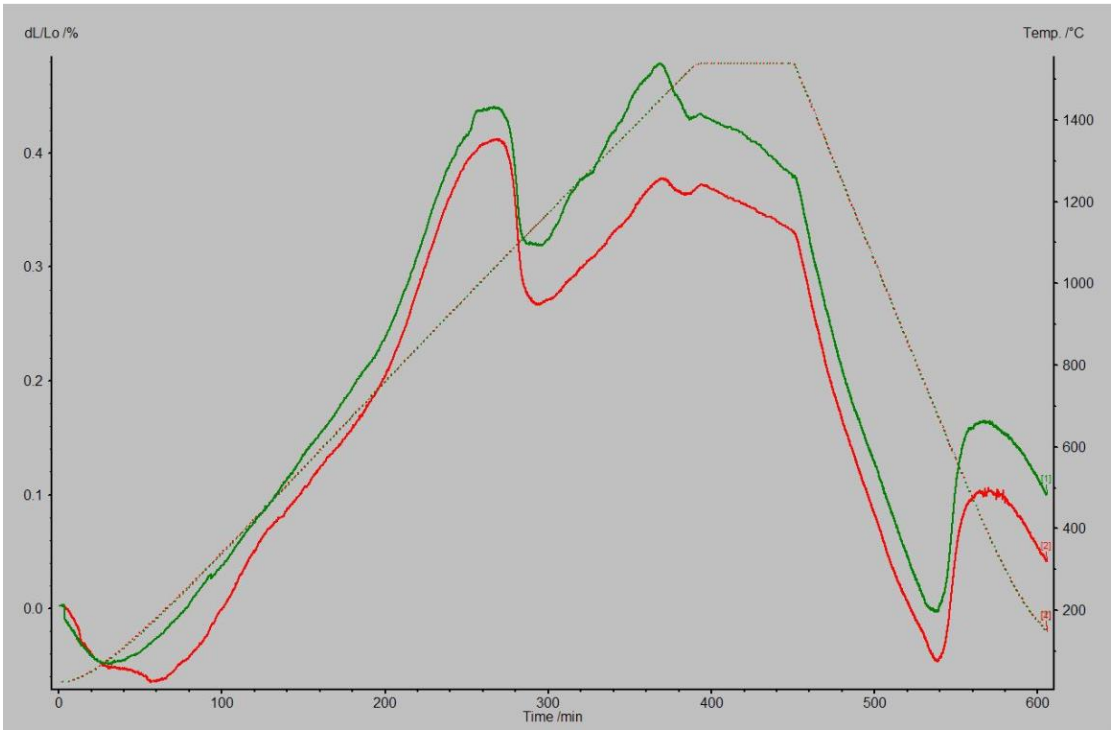

Figure 6.14 Dilatometry curves of two No.19 (PCA1600) samples

In Figure 6.14, between 1050 ℃ and 1200 ℃, the sample shrinks by about 0.1 % in length while heating continues. During the cooling process, the sample expands by the same length sharply at about 800 ℃. This expansion hysteresis is typical of unstabilised or partially stabilised zirconia ceramics (19).

The phase transformations of zirconia are shown in Figure 6.15. The monoclinic phase transforms to tetragonal zirconia with rising temperature and this is associated with 4 % volume reduction due to tetragonal zirconia has smaller lattice (18). The reverse transition takes place on cooling. At much higher temperatures the tetragonal phase transforms to cubic but there is little associated volume change in this transition.

In a pure zirconia, the volume expansion from tetragonal to monoclinic would be about 4 % which means 1.3 % linear expansion on heating. In this study, a completely reacted product should contain about 30 % zirconia which suggests if all the zirconia was in monoclinic form at room temperature about 0.39 % linear expansion would be observed. However, the tests shows only 0.1 % linear expansion which indicates majority of the zirconia (about 74 %) was in tetragonal phase at room temperature. The tetragonal phase was retained to room temperature because it is constrained by the mullite lattice and its small grain size.

Monoclinic (1173 °C) ↔ Tetragonal (2370 °C) ↔ Cubic (2690 °C) ↔ Melt

(Largest lattice) (Intermediate lattice) (Smallest lattice)

Figure 6.15 Schematic diagram of zirconia phase transformation (18)

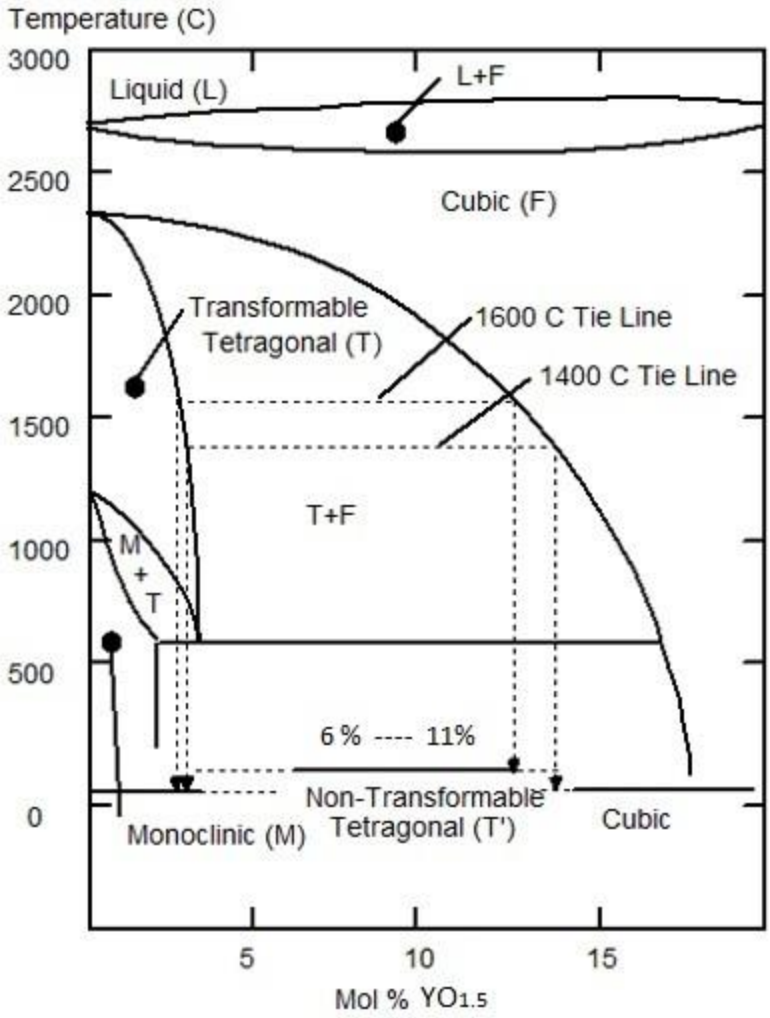

Figure 6.16 Phase diagram of yttria stabilized zirconia (212)

It is known that yttria can stabilize the crystal structure of zirconia by substituting some of the Zr^{4+} ions. Different contents of yttria result in different zirconia crystal structure being stable to room temperature. Figure 6.16 shows the phase diagram of yttria stabilized zirconia (18, 212). In this study, 6 wt. % yttria (equal to 3.34 mol. % Y_2O_3 or 6.68 mol. % $YO_{1.5}$) was added in the system to produce sample No.35 (PCAY1600). Thus, at room temperature, all the zirconia should be in a non-transformable tetragonal crystal form. This may also result in zirconia being over stabilized which probably would significantly alter the behaviour of the material.

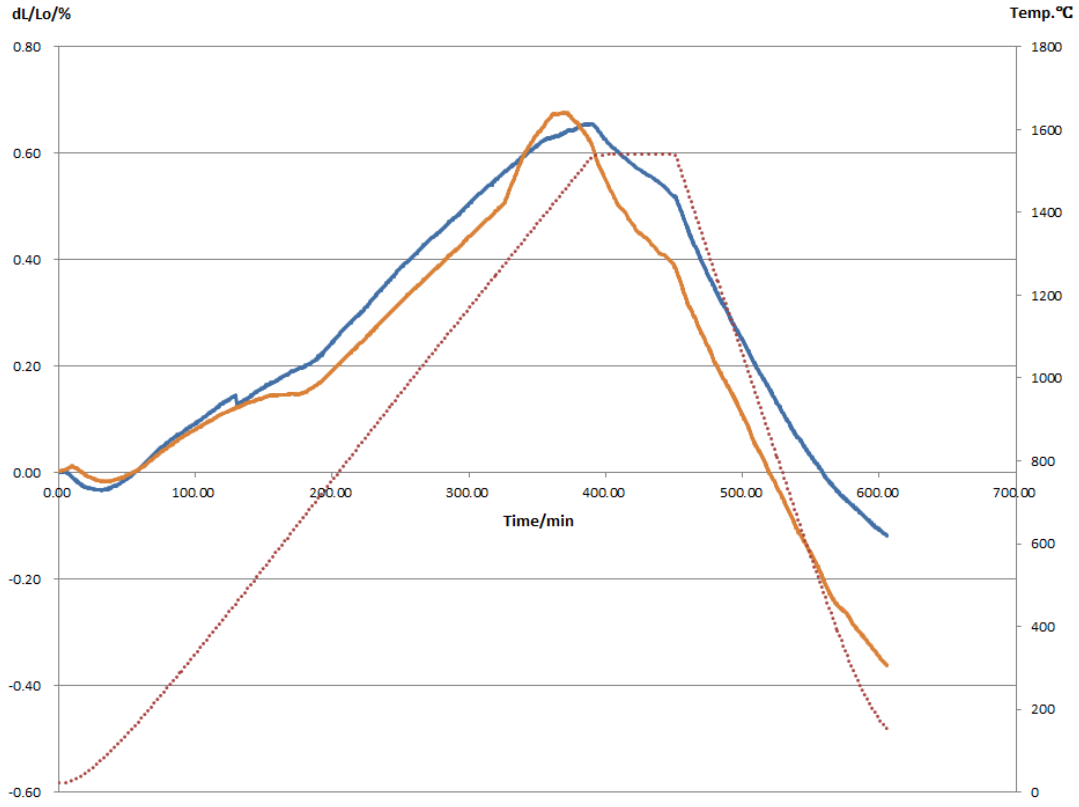

Figure 6.17 Dilatometry curves of two No.35 (PCAY1600) samples

Figure 6.17 shows dilatometry curves of two sintered samples of No.35 (PCAY1600). This confirms that the sudden shape change in No.19 (PCA1600) was caused by monoclinic to tetragonal zirconia phase transformation. It also proves that the added

yttria did react with zirconia and formed ytrria-stabilized zirconia which has a non-transformable tetragonal structure that does not change with temperature rise.

Table 6.6 Coefficient of linear thermal expansion

Product Number	Elongation at Maximum Temperature $dL \cdot L^{-1}$ (%)	Temperature Range (℃)	Coefficient ($℃^{-1}$)
Ceramic waste compact samples			
8	0.39 ± 0.007	1520	$2.57 \times 10^{-6} \pm 4.60 \times 10^{-8}$
19	0.41 ± 0.009	1520	$2.70 \times 10^{-6} \pm 5.92 \times 10^{-8}$
Commercial material compact samples			
24	0.72 ± 0.005	1520	$4.74 \times 10^{-6} \pm 3.29 \times 10^{-8}$
28	0.42 ± 0.007	1520	$2.76 \times 10^{-6} \pm 4.60 \times 10^{-8}$
Ceramic waste extrusion samples			
30	0.52 ± 0.011	1520	$3.42 \times 10^{-6} \pm 7.24 \times 10^{-8}$
34	0.45 ± 0.008	1520	$2.96 \times 10^{-6} \pm 5.26 \times 10^{-8}$
Additional ceramic waste compact samples			
35	0.42 ± 0.004	1520	$2.76 \times 10^{-6} \pm 2.63 \times 10^{-8}$

The coefficient of linear thermal expansion of each sample was calculated according to Equation 3.13 by using the recorded data. The results are shown in Table 6.6.

It can be seen that all the zirconia toughened mullite samples have similar coefficient of linear thermal expansion in the temperature range from 20 ℃ to 1540 ℃. The mullite sample 24 (PSA1600) has a coefficient value slightly lower than that reported in the literature (5.3 x 10^{-6} $°C^{-1}$)(22). This may be caused by the sample and machine error.

6.7.2 Sintering Process

The dilatometer was also used to monitor the sintering process of the green samples (refer to Section 3.2.9). Due to the limitation of machine availability, each green sample was only tested once. The maximum operational temperature of this device was 1540 ℃, thus the sintering behaviour above 1540 ℃ could not be monitored by using this method.

Figure 6.18 shows the sintering process curves of the selected 7 samples. It can be seen that the samples expanded a little as temperature initially rises. Sintering behaviour started at approximately 1100 ℃ for all samples shown by the onset of rapid shrinkage.

The reaction path in sample No.24 (PSA1600) is relatively simple compared to the other specimens as only mullite was being formed. The sintering started from 1300 ℃ and terminated at 1500 ℃. In this region the curve appears steeper and sintering is terminated at lower shrinkages than any other composition. This lower densification was observed in the commercially processed materials and attributed to mullite formation (4).

The other six samples all show that shrinkage stops and expansion occurs just before where the maximum temperature is reached. This feature is probably associated with the dissociation of zircon and subsequent growth of mullite. It is known that the formation of mullite can lead to relatively low density products through this work with sample No.24 (PSA1600) and the literature (5, 21). During reaction sintering as is occurring here it is not unknown for the material to be rather plastic in nature and for strong sintering to occur as the high temperature phase (in this case mullite) is formed (198). XRD data (Section 6.6) and SEM images (Section 6.11) show that at temperatures of 1540 ℃ full dissociation of zircon has not occurred and the dilatometry result reflect this hypothesis.

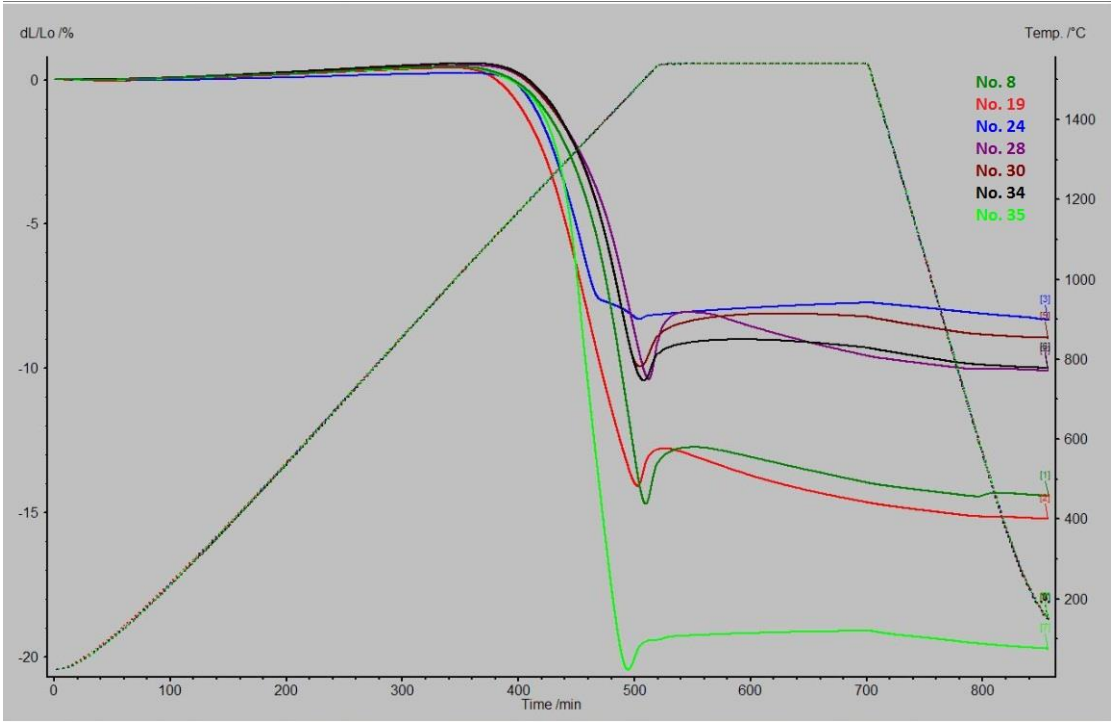

Figure 6.18 Dilatometry curve of sintering process

One other possible explanation for the expansion is the dissociation of zircon itself but it appears that the reaction of the free silica with alumina and the resulting

microstructure are the most probable cause. Densification continues slowly as the sample is held at 1540 ℃ and subsequently cooled down.

The other 6 samples all have a peak on the curve which corresponds with zircon dissociation and mullite formation. Combining with the XRD results of sample No.36 (PCA1540) showed in Figure 6.11, it can be found that zircon did not dissociate completely and thus alumina remained in the sample along with newly formed zirconia and mullite. The system was very complicated as different reactions were taking place simultaneously, and thus it is difficult to explain the dimensional changing behaviour of the sample. One possible reason could be that when the sample reached a certain temperature, the reaction rate of zircon dissociation started to accelerate which caused the sample expansion. When the temperature stopped rising and was held at 1540 ℃, the rates between reactions matched again and the sintering process continued smoothly.

The transfer from sintering to expansion in samples No.8 (PCA1685) and No.19 (PCA1600) occurred at a slightly lower temperature than in samples No.28 (PZA1600), No.30 (EWH1600) and No.34 (EWI 1600). This may be due to the particles in the dry pressed materials being more compacted by the process than in extruded samples which may lead to a lower reaction temperature through easier mass transport. It is also possible that sample No.30 (EWH1600) and No.34 (EWI1600) may contain trace amount of iron which were worn from the Z-blade mixing machine during the paste forming process. The impurities may affect the zircon dissociation behaviour (18). Impurities (about 3 %) present in the commercial zircon feedstock used in the

formulation of sample No.28 (PZA1600) could explain the differences between No. 28 (PZA1600), No. 8 (PCA1685) and No. 19 (PCA1600).

Sample No.35 (PCAY1600) has an additional 1.77 wt. % Y_2O_3 in the system which may lower the zircon dissociation and mullite formation temperature and the rate of the reaction. This suggests more materials had reacted at 1540 ℃ and sintering shrinkage was greater.

As can be seen from Figure 6.14, the zirconia phase transformation of a fully sintered sample can cause about 0.1 dL/L_0 % linear change. However, the maximum value on the Y axis of Figure 6.18 was -20 dL/L_0 % and combined with the incomplete formation of zirconia in the structure (about 25 % conversion) the transformation will not be visible in the cooling down curve.

The main limitation of the dilatometry test was the length of the sample. It required the sample to be 20 mm in length to achieve optimum accuracy. However, due to the nature of dry pressing technique and there being no binder the samples were short and weak. The samples used in this test were typically 8 mm to 12 mm in length. Errors may have been introduced due to this limitation.

6.8 DSC Analysis

In order to further analyse the reaction behaviour during the sintering process, the selected green samples were also tested by differential scanning calorimeter. Due to the limitation of available experimental time and device availability, each green sample was only tested once. The principles, experimental apparatus and procedures are detailed in Section 3.2.10.

Figure 6.19 shows the thermodynamic behaviour during the sintering process of the chosen samples. As can be seen when the device started to increase the temperature, there was a sudden drop on each curve. A reverse change occurred when the device stopped heating and was maintained at 1600 ℃. This was caused by a systematic machine error rather than anything that can be attributed to sample behaviour.

It can be seen that there are exothermic reactions resulting in peaks on these curves. From the similarity of curve shapes and the peak positions, the samples can be divided into four typical behaviours represented as:

①. Sample No.8 (PCA1685) and No.19 (PCA1600)

②. Sample No.28 (PZA1600), No. 30 (EWH1600) and NO.34 (EWI1600)

③. Sample No.24 (PSA1600)

④. Sample No.35 (PCAY1600)

The main exothermic peak in group one occurred at 1520 ℃. While in group two it occurred at 1550 ℃ and was generally sharper in profile and smaller. This indicates that the zircon dissociation and mullite formation reactions occurred with more intensity and more rapidly in samples No.8 (PCA1685) and No.19 (PCA1600). This may be due to the group one samples containing some amorphous silica which was highly active thus accelerating the reaction compared with sample No.28 (PZA1600). The more compact microstructure in pressed products than in extruded samples may also explain the differences between group one and two.

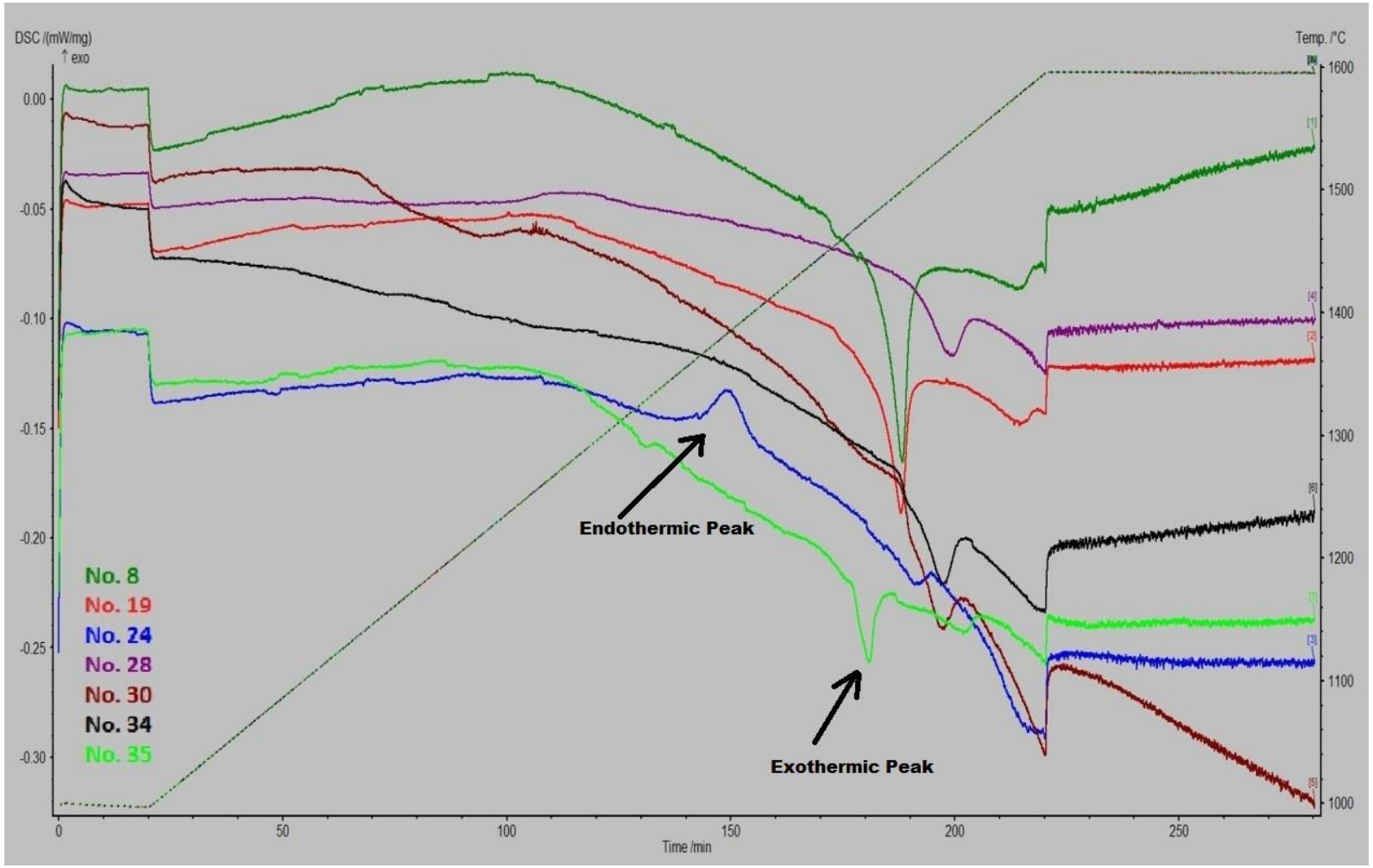

Figure 6.19 DSC curves of the selected 7 samples

No. 24 (PSA1600) has one endothermic peak at about 1400 ℃ which may indicate silica phase transformation from tridymite to cristobalite. The exothermic peak at around 1500 ℃ is indicative of the mullite formation process.

No.35 (PCAY1600) has two exothermic peaks at 1480 ℃ and 1560 ℃. The main peak at 1480 ℃ indicates the thermal dynamic behaviour of zircon dissociation and mullite formation process. The temperature of the transformation was due to the additional yttria and thus the presence of yttria may assist the reaction. The second peak represents Y^{3+} substituting Zr^{4+} in the zirconia lattice and forming more stable zirconia and releasing energy to the environment.

6.9 Hardness and Toughness

6.9.1 Hardness Results

The hardness and toughness properties of zirconia toughened mullite composites are very important as they reflect the microstructure of the materials and are significant in their selection for refractory applications. Previous research on alumina-mullite-zirconia found that the flexural strength, hardness and toughness are closely related to the composition of the raw materials and sintering conditions (26).

In this study, the hardness values were tested on an INDENTEC 5030SKV Macro Vickers Hardness Testing Machine using polished samples. Details of the measuring procedures and conditions can be found in Section 3.2.7.

The hardness tests were evaluated by applying different indentation loads including 5, 10, 15 and 20 kg. Under 5 kg load, the indentation was too small and unclear to be monitored and measured accurately. As the load increased from 10 kg to 20 kg, the hardness value H decreased linearly. This is a phenomenon commonly observed in ceramic materials (175, 213). There is no satisfactory explanation to the phenomena in the published literature to date. Some suggest that the surface grinding during sample preparation is the most plausible reason for this behaviour (174, 175).

In this study, the data were obtained by applying 10 kg load for all the samples. At least 5 measurements were conducted on each sample, and the average value was calculated. The results were converted to SI units by using Equation 3.10.

Table 6.7 shows the measured hardness value (Hv) and the calculated value (H) of the seven samples along with the flexural strength value. The standard deviation of each value is shown after the '±' symbol. Sample No.24 (PSA1600) has a 5.1 % error while the error of other samples ranged from 0.8 % and 1.8 %. This indicates that zirconia toughened mullite products have a more homogenous response (and probably microstructure) than the pure mullite sample in this study.

In order to find the relations between the two values a scatter diagram of flexural strength and hardness of the selected samples was constructed, and shown in Figure 6.20. It can be seen that the flexural strength values and hardness values exhibit a similar trend. Sample No.19 (PCA1600) has the highest values in both properties while No.24 (PSA1600) is the lowest. This is due to sample No.24 (PSA1600) being mullite only. The added zirconia has been shown to refine microstructure thus enhancing the properties significantly. Furthermore, the low densification of No.24

(PSA1600) means there were more pores in the structure which may significantly reduce the properties.

Table 6.7 Hardness of 6 representative samples and 1 additional sample (10 Kg Load)

Product Number	NAME	Flexural Strength (MPa)	Hardness (Hv) (kgf·mm^{-2})	Hardness (H) (GPa)
Ceramic waste compact samples				
8	PCA1685	100.2 ± 4.69	627.7 ± 5.27	6.2 ± 0.052
19	PCA1600	349.8 ± 18.40	1063.5 ± 12.43	10.4 ± 0.12
Commercial material compact samples				
24	PSA1600	62.4 ± 6.75	255.3 ± 13.07	2.5 ± 0.13
28	PZA1600	145.2 ± 10.60	513.4 ± 3.67	5.0 ± 0.035
Ceramic waste extrusion samples				
30	EWH1600	196.4 ± 22.37	522.7 ± 9.73	5.1 ± 0.095
34	EWI1600	296.9 ± 21.74	675.2 ± 10.68	6.6 ± 0.10
Additional ceramic waste compact samples				
35	PCAY1600	215.0 ± 23.80	1056.9 ± 18.26	10.4 ± 0.05

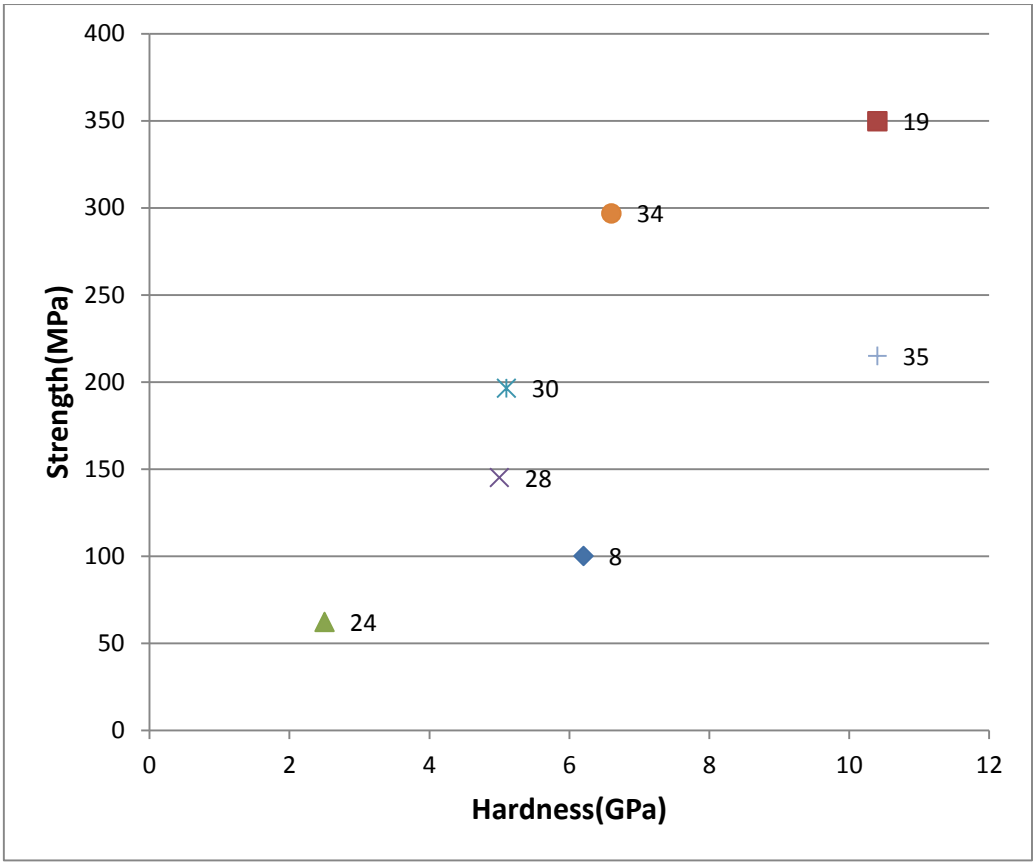

Figure 6.20 Scatter diagram of flexural strength and hardness

Sample No.35 (PCAY1600) has the second highest hardness among the evaluated products and very similar behaviour to No.19 (PCA1600). As stated earlier in the dilatometry section (Section 6.7.1), No.19 (PCA1600) has approximately 26 % monoclinic zirconia and 74 % transformable tetragonal zirconia which provide transformation toughening to the structure. However, the added yttria transferred all zirconia to non-transformable tetragonal zirconia in sample No.35 (PCAY1600) rather than monoclinic and transformable tetragonal zirconia. The reactions between yttria and zirconia may have induced grain size and shape change which may cause higher stress in the structures. This may lead to little toughening and more defects in the microstructures which will significantly impact on mechanical behaviour (proof will be shown in Section 6.10). Thus the flexural strength is reduced

by about 30 % compared by No.19 (PCA1600), but the change of grain size and shape has not affected the hardness value to the same extent.

Sample No.8 (PCA1685), No.28 (PZA1600), No.30 (EWH1600) and No.34 (EWI1600) have similar hardness values ranging from 5.0 GPa to 6.5 GPa. As stated before, probably there were some micro cracks developed between the grains which caused the significant drop in mechanical performance. These cracks can also lower the hardness value. Sample No.28 (PZA1600), No.30 (EWH1600) and No.34 (EWI1600) have low hardness values perhaps due to them having a relatively higher porosity.

6.9.2 Toughness Results

The fracture toughness was calculated using Equation 3.12. Thus, the lengths of cracks from the indentation were measured by using the microscope on the hardness testing instrument. However, due to the low accuracy of the devise and the relatively high bulk porosity of the samples, the cracks on sample No.8 (PCA1685), No.24 (PSA1600), No.28 (PZA1600), No.30 (EWH1600) and No.34 (EWI1600) could not be accurately monitored and measured. As an example of the difficulty of this type of analysis on porous materials, an indentation in sample No.24 (PSA1600) and No.34 (EWI1600) is shown in Figures 6.21 and 6.22 respectively.

As can be seen from these two figures, there were cracks developing from the corner of the indentations, but even under SEM, the length of cracks could not be monitored clearly and measured with any confidence. The pores in these materials can prevent the growth of cracks which suggests that these porous products were tougher than samples of higher density (178).

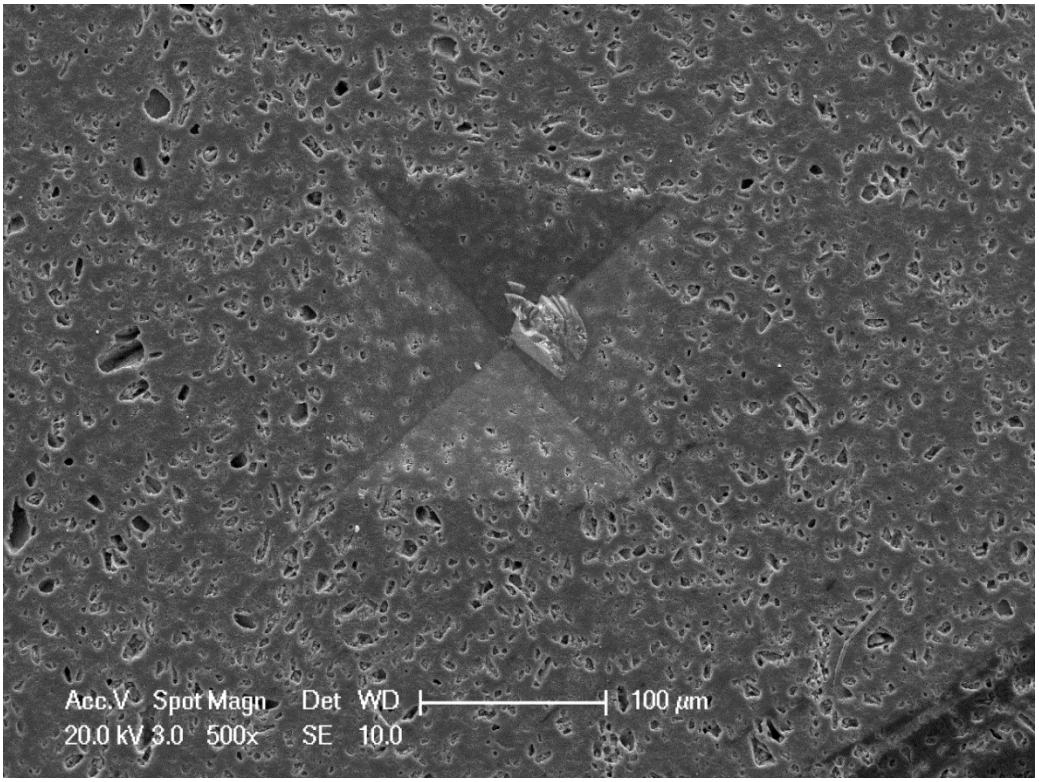

Figure 6.21 SEM image of indentation on sample No.24 (PSA1600) under 10 kg load

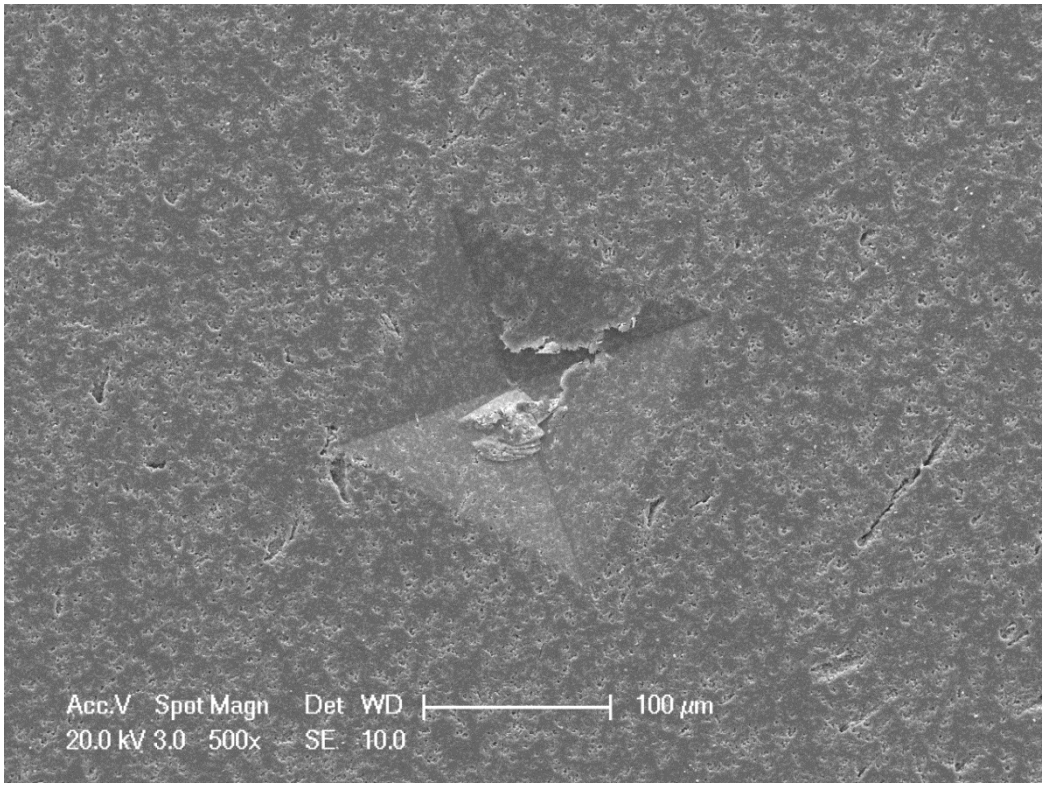

Figure 6.22 SEM image of indentation on sample No.34 (EWI1600) under 10 kg load

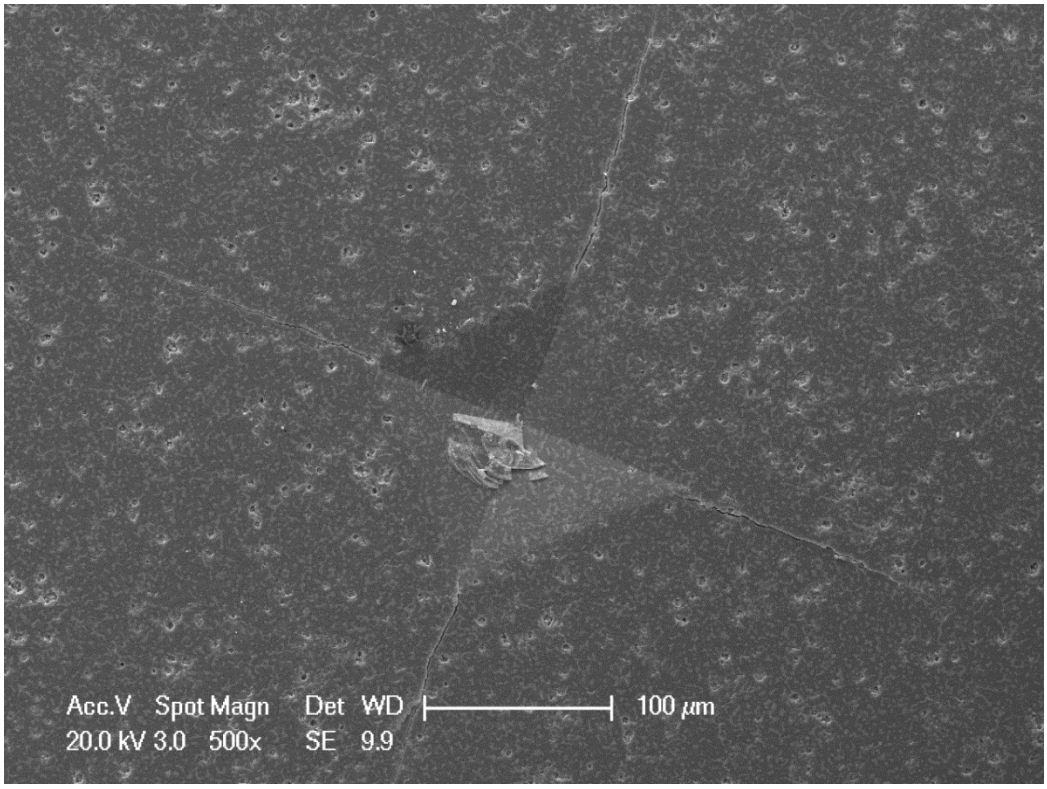

Figure 6.23 SEM image of indentation on sample No.35 (PCAY1600) under 10 kg load

Figure 6.23 shows the SEM image of indentation on sample No.35 (PCAY1600). Cracks emanated from each corner of the indentation. They could be clearly observed and measured. Sample No.19 (PCA1600) showed similar behaviour. Thus, these two samples were tested and measured at least 7 times and the values of crack length were recorded and calculated to yield a comparative toughness.

Table 6.8 shows the calculated average toughness of sample No.19 (PCA1600) and No.35 (PCAY1600). Considering the handbook fracture toughness values of zirconia and mullite are typically 13 $MPam^{1/2}$ and 2 $MPam^{1/2}$ respectively (172), the samples in this study have values in a reasonable range. It should be noted that due to the subjective nature of the observation process in this test, it can in practice only offer an indication of toughness values.

Table 6.8 Toughness of sample No.19 (PCA1600) and No.35 (PCAY1600)

Product Number	Name	Flexural Strength (MPa)	Hardness (H) (GPa)	Toughness KIC ($MPam^{1/2}$)
19	PCA1600	349.8 ± 18.40	10.4 ± 0.12	6.12 ± 0.58
35	PCAY1600	215.0 ± 23.80	10.4 ± 0.05	5.38 ± 0.63

The purpose of adding yttria to the system was stabilising the zirconia thus enhancing the toughness of the product. However, according to the results, sample No.19 (PCA1600) is a little tougher than No.35 (PCAY1600) which means the more highly stabilised zirconia has not helped to produce toughness. This may also have caused a more defective microstructure to develop.

6.10 Microstructure Analysis by SEM

In order to further reveal the reasons for the differences between samples, microstructure analysis was carried out by analysing SEM images. For each sample, a fracture surface resulting from failure during the strength tests, a polished cross-section surface and a thermal etched polished surface were observed under different electron modes and magnifications (refer to Chapter 3.2.4).

6.10.1 Different Raw Materials

The microstructure of the sample produced from SiO_2 and Al_2O_3 was compared to that of the highest strength sample produced from waste ceramic and Al_2O_3. Figure

6.24 shows the fracture surface images of No.24 (PSA1600) and No.19 (PCA1600). It can be seen that the sample produced from SiO_2 and Al_2O_3 has an inhomogeneous structure (pores distributed inhomogeneously among the mullite grains) with a fine crystalline matrix between large plates and lath like crystals. There is a significant fraction of pores (approximately 22 % according to image analysis) exhibiting a range of shapes and sizes. The zirconia toughened mullite material has clearly developed a higher density and more uniform structure during sintering. It has a finer particle size and less porosity with an overall more uniform fracture surface. This clearly shows why mullite product has a much lower fractional density and flexural strength than zirconia toughened mullite samples.

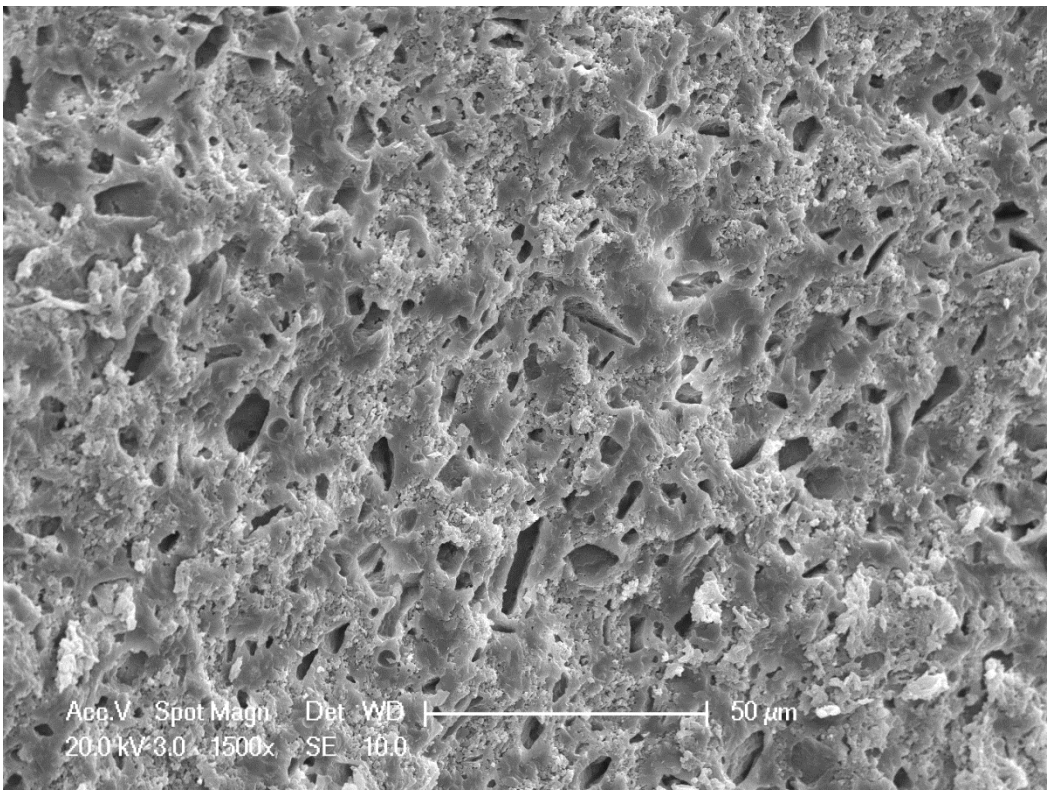

No.24

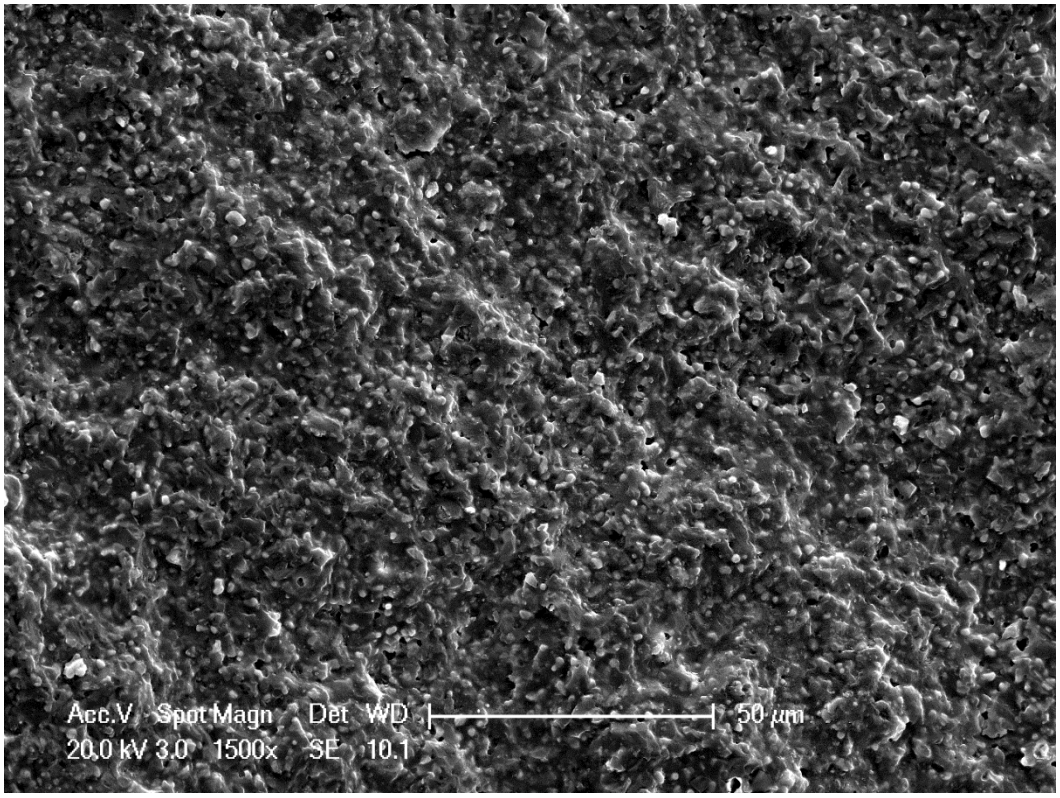

No.19

Figure 6.24 Fracture surface images of No.24 (PSA1600) and No.19 (PCA1600) (SE)

Figure 6.25 shows that sample No.19 (PCA1600) has a relatively coarse matrix of mullite, the dark particles, and finer zirconia dispersion, the bright particles, in its structure. The zirconia particles are evenly distributed in a dense mullite matrix. The zirconia grains appear rounded. It can clearly be seen that sample No.24 (PSA1600) is mono phase mullite. There is a wide range of pores from about 0.5 µm to 8 µm and they have an irregular shape. The particles are very different in terms of size; as the large lath-like crystals are about 5 µm in their largest aspect while the small ones are only about 0.3 µm. The large pores were probably caused by agglomerates remaining in the powder compact while the small pores were developed by the growth of the mullite grains. Due to the inhomogeneity of the pores and grains, line

intercept method for particle size analysis was not applied to sample 24 (PSA1600) as the error between intercept lines was too large.

The samples were all coated with gold film to give better image quality. This may cause inaccuracy in quantitative EDS tests due to the characteristic peaks of gold may overlap peaks of the sample materials, thus the EDS results reported here only provide qualitative values to confirm the elemental compositions (214).

The EDS results of No.24 (PSA1600) and No.19 (PCA1600) are shown in Table 6.9. The analysis clearly shows that sample No.24 (PSA1600) only consisted of mullite. There was no zirconium element detected in the dark areas of sample No.19 (PCA1600) which indicates a mullitic composition, while the bright grains show only zirconium and oxygen which confirm the presence of zirconia.

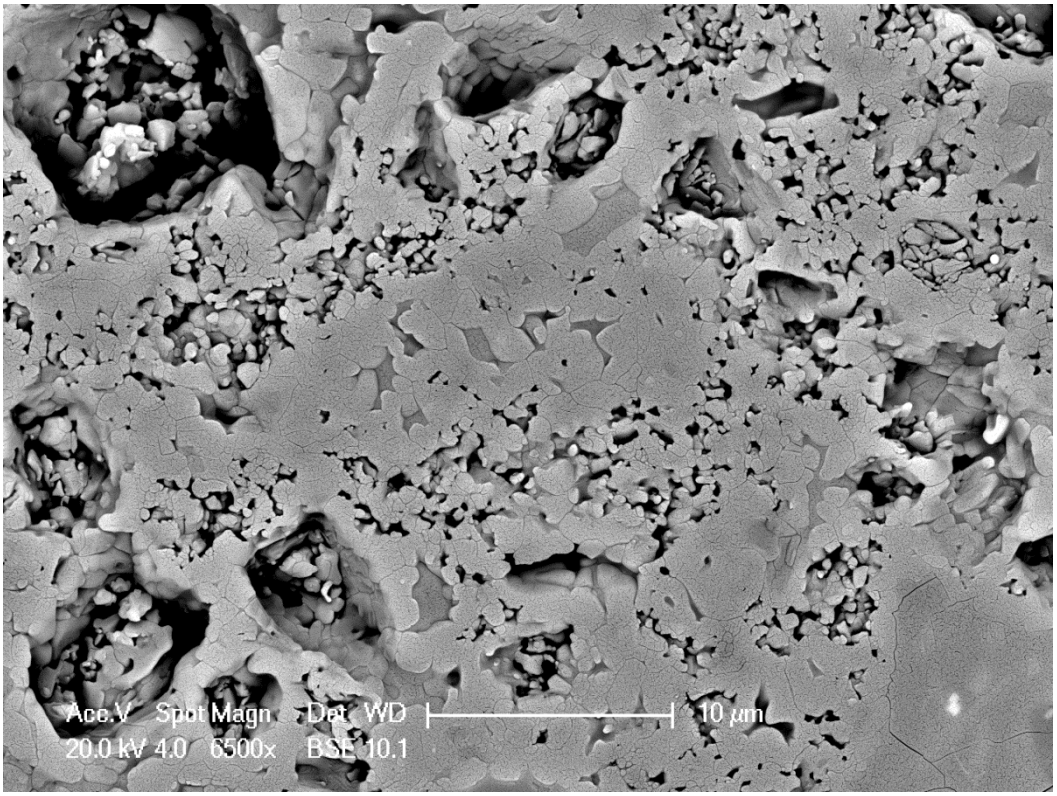

No.24

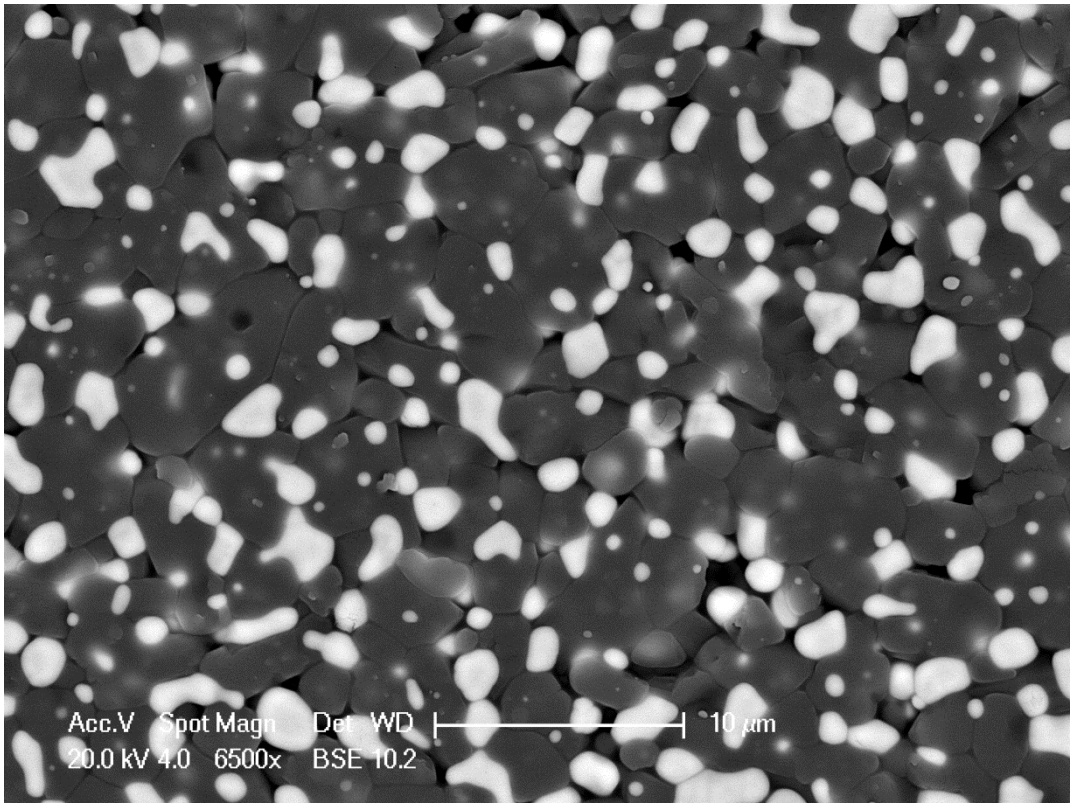

No.19

Figure 6.25 Thermally etched surfaces of No.24 (PSA1600) and No.19 (PCA1600) (BSE)

Table 6.9 EDS results of Sample No.24 (PSA1600) and No.19 (PCA1600)

Sample No.24 (PSA1600)		
Element	Weight %	Atomic %
O K	47.98	61.18
Al K	34.68	26.22
Si K	17.34	12.60

Sample No.19 (PCA1600)						
Dark Matrix				**Bright Grain**		
Element	Weight %	Atomic %		Element	Weight %	Atomic %
O K	38.44	51.88		O K	28.43	69.37
Al K	43.45	34.57				
Si K	18.12	13.85		Zr L	71.57	30.62

6.10.2 Commercial Materials and Waste Materials

For the ZTM materials different microstructures were developed under the same processing procedures and sintering conditions depending on the raw materials, and this significantly affected the properties of the materials.

Sample No.28 (PZA1600) in Figure 6.26 used the same formulation and processes as No.19 (PCA1600) substituting the waste zircon silica mix with commercial zircon sand. The fracture surfaces show quite different structures compared to No.19 (PCA1600), Figure 6.24.

The images indicate sample No.28 (PZA1600) developed bedded structures. Though the structure is quite uniform, there are a large number of small pores (about 1 μm to 3 μm) evenly distributed in the structure compared to No.19 (PCA1600). The porous structure can lead sample to lower density, strength and hardness compared with No.19 (PCA1600).

Figure 6.27 shows the thermally etched surface of sample No.28 (PZA1600). A line intercept analysis was conducted on both sample No.28 (PZA1600) and No.19 (PCA1600). The mullite grains (average 2.1 μm) and intragranular zirconia particles (average 0.6 μm) in sample No.28 (PZA1600) were smaller than those in No.19 (PCA1600) which had an average value of 3.2 μm and 0.9 μm respectively. The structure in No.28 (PZA1600) contains less intragranular zirconia than No.19 (PCA1600). The intergranular zirconia particles are clustered rather than evenly distributed in the mullite structures. This situation causes pores to develop around relatively large zirconia particle clusters.

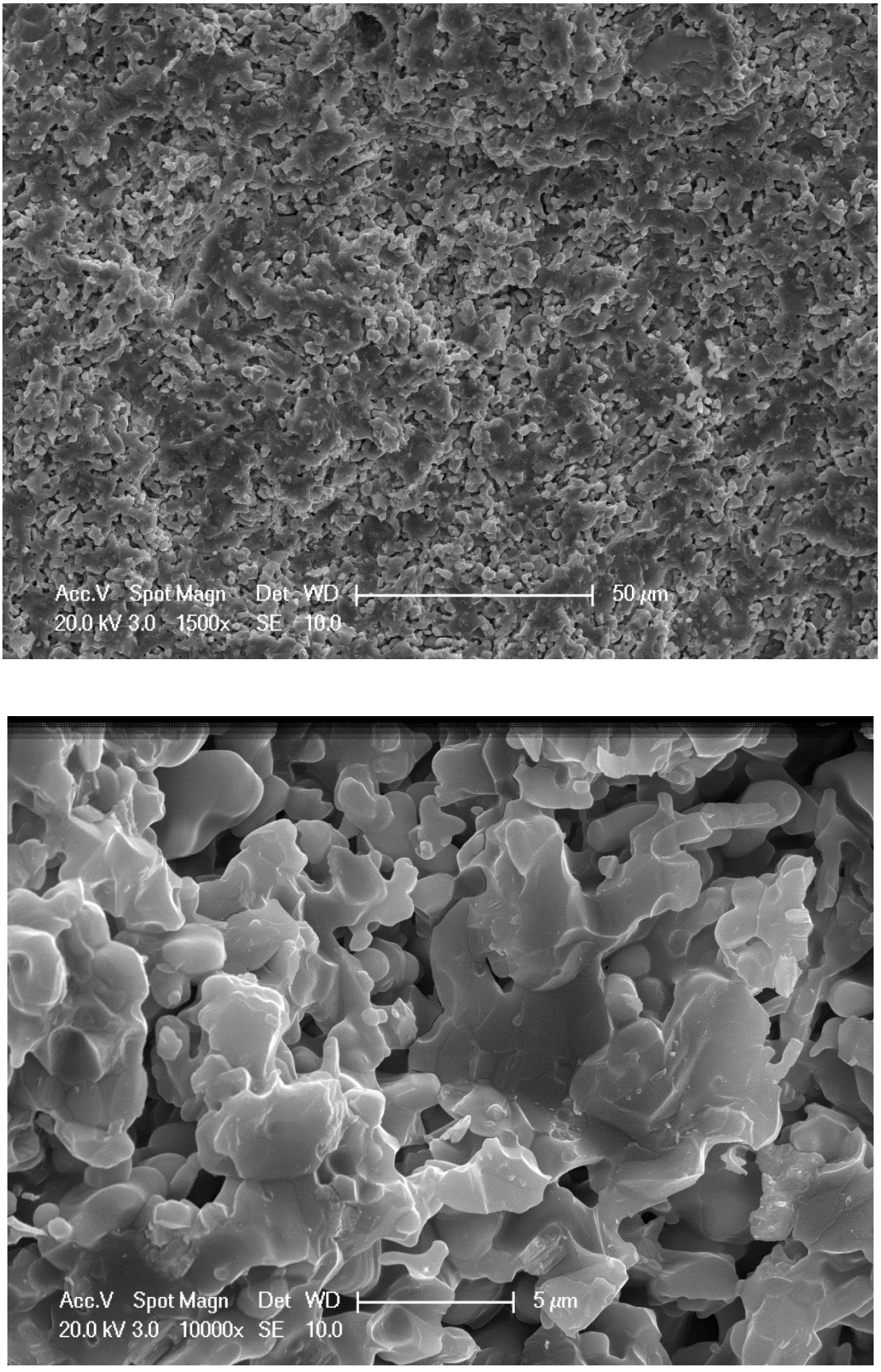

Figure 6.26 Fracture surface of No.28 (PZA1600) (SE)

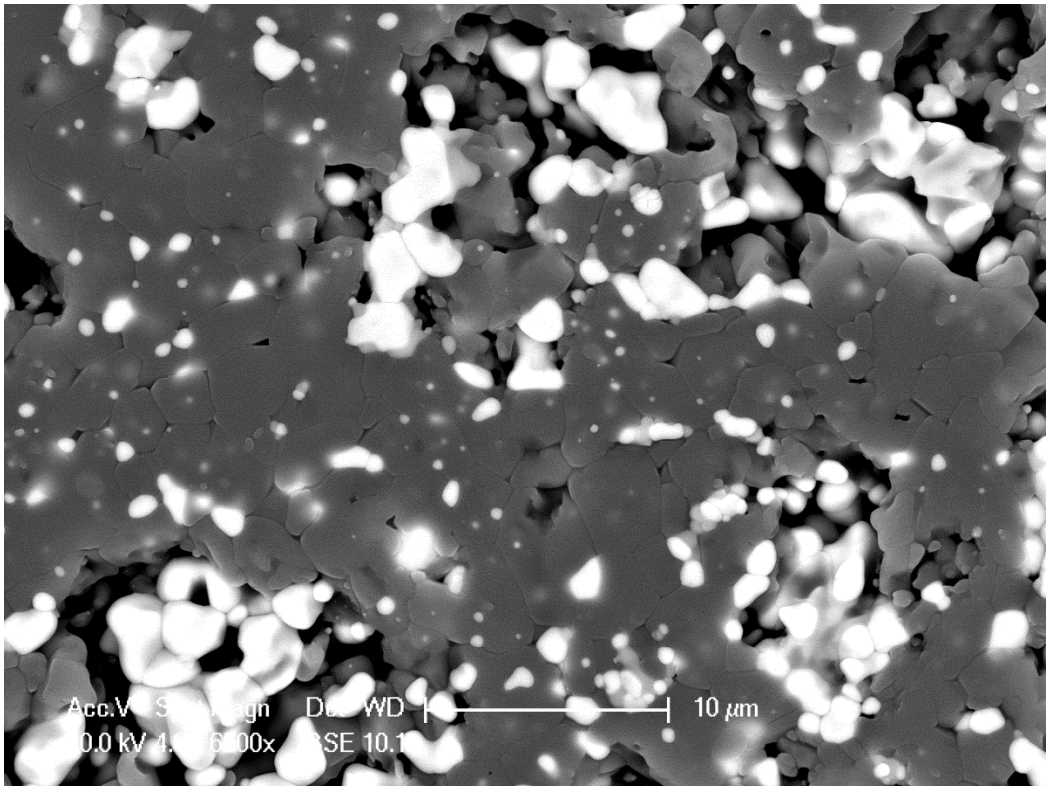

Figure 6.27 Thermally etched surface of No.28 (PZA1600) (BSE)

Table 6.10 EDS results of No.28 (PZA1600)

Sample No.28 (PZA1600)						
Dark Grain				**Bright Grain**		
Element	Weight %	Atomic %		Element	Weight %	Atomic %
O K	23.49	34.41		O K	9.98	38.72
Al K	51.00	44.30				
Si K	25.52	21.29		Zr L	90.02	61.28

The two samples were processed in the same way and had a very similar starting particle size distribution, thus the variances can be attributed to the small amount of amorphous silica in the ceramic waste. The fine free amorphous silica would be highly reactive which may have assisted in the formation of mullite and distribution of the zirconia particles. However, due the high complexity of the system, it is

difficult to explain the mechanism by which the silica helped the reaction and improved the homogeneity of the microstructure.

Table 6.10 shows the EDS results of sample No.28 (PZA1600) and confirms the mullite and zirconia composition of this material.

6.10.3 Sintering Temperatures

Sample No.8 (PCA1685), No.19 (PCA1600) and No.36 (PCA1540) used the same starting materials and processing techniques, but were sintered at 1685, 1600, 1540 ℃ respectively. This section demonstrates how the sintering temperature affects the microstructures.

Figure 6.28 compares the thermally etched surfaces of sample No.8 (PCA1685) and No.19 (PCA1600) under secondary electron mode. They both have homogenous structures with zirconia particles distributed evenly, in and between the mullite grains. It is clear that under the same magnification, the grains of No.8 (PCA1685) are much larger than the ones in No.19 (PCA1600). The line intercept method shows the mullite and zirconia have an average size of 6.0 μm and 3.2 μm, respectively in 1685 ℃ sintered product while No.19 (PCA1600) had an average value of 3.2 μm and 0.9 μm, respectively. Increasing the temperature from 1600 ℃ to 1685 ℃ has caused significant grain growth, which may lead to other effects developing in the microstructure which include fracture due to uncontrolled phase change in the zirconia (grain size too large to maintain the tetragonal form on cooling).

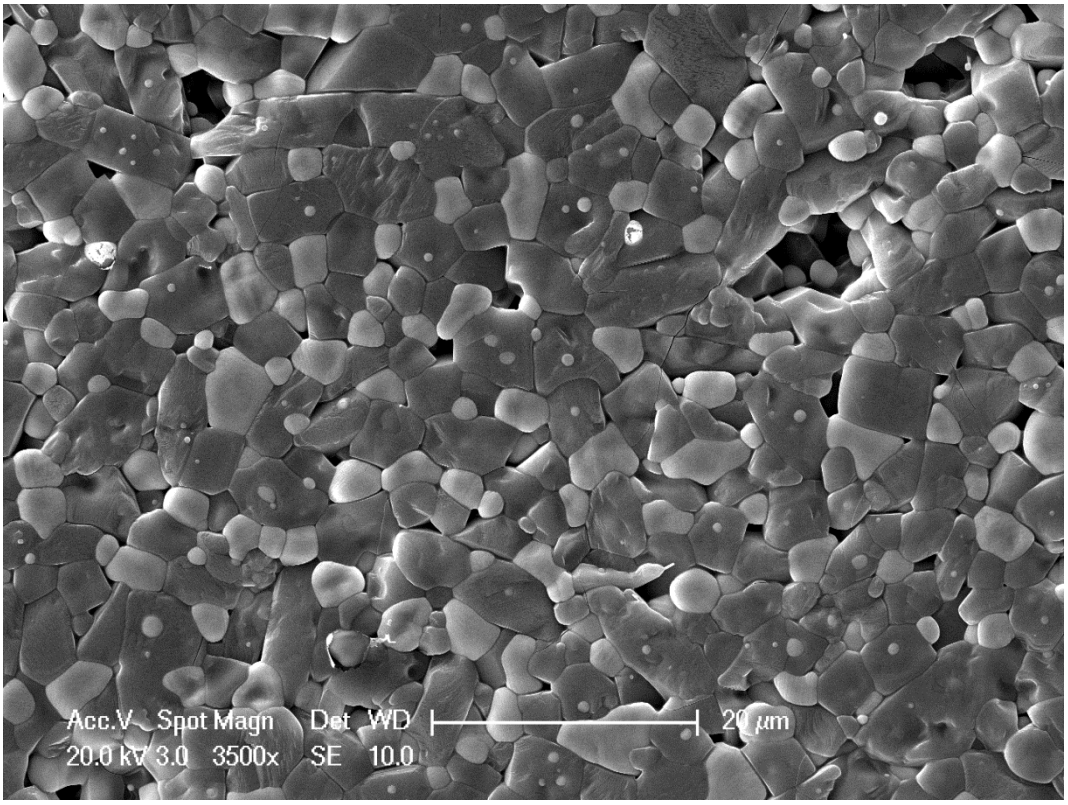

No.8

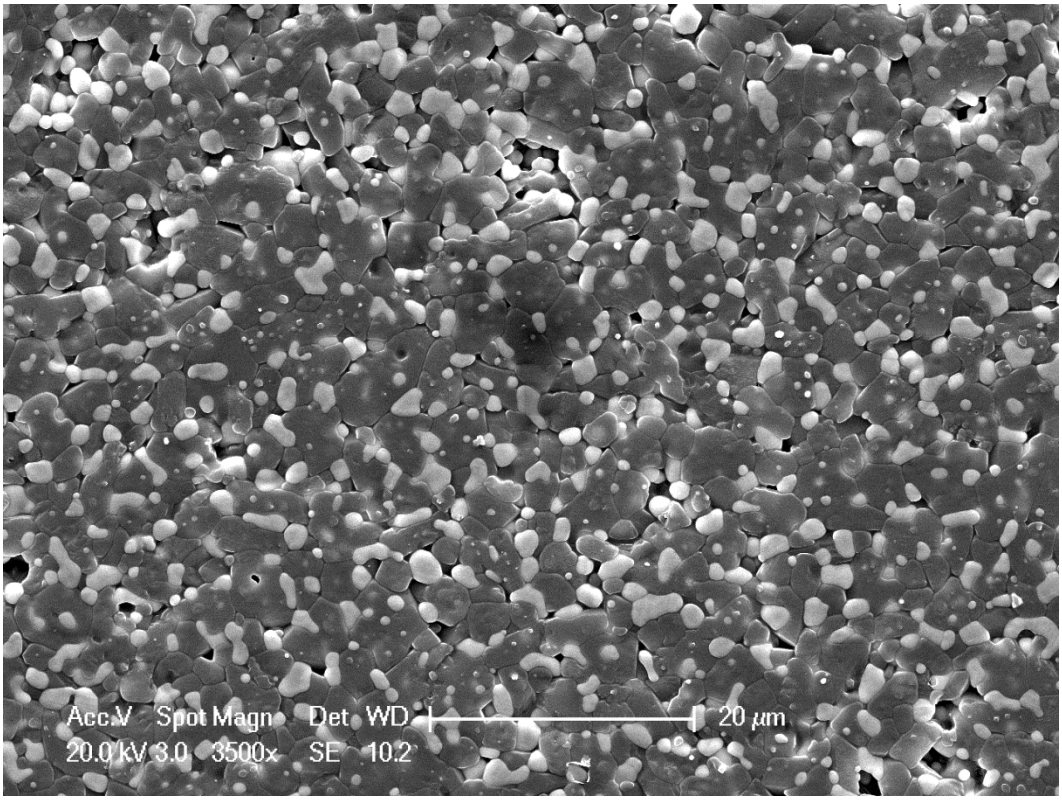

No.19

Figure 6.28 Thermal etched surfaces of No.8 (PCA1685) and No.19 (PCA1600) (SE)

Figure 6.29 shows the thermal etched surface of sample No.8 (PCA1685) under higher magnification (6500× when testing) and back scattered electrons mode. Micro-cracks within the mullite grains can be clearly observed in the image. These cracks all developed from the boundaries between relatively larger intergranular ZrO_2 particles and mullite grains. This may be due to the reason that when the temperature increased, the particles expanded significantly and causing the tensions between them to rise. However, the zirconia grains are much stronger, harder and tougher than the mullite ones, thus the mullite grains were squeezed by the larger zirconia particles. When the stress exceeded the limits that the mullite can withstand failure occurred.

Another explanation of the cracks would be due to zirconia phase transformation. As mentioned before in Section 6.7, when ZrO_2 transformed from tetragonal to monoclinic, the volume expandes significantly (4 %) (18). Such a volume expansion can cause the system in which it occurs to fail. If the zirconia is finely dispersed in another phase (mullite in this case) and the grain sizes is relative small (typically less than 1 μm) (for example sample No.19), the constraint of the surrounding matrix can prevent the zirconia transformation from tetragonal to monoclinic and so the surrounding matrix stays stable. However, the zirconia in sample No.8 (PCA 1685) had an average size of 3.2 μm which is too large for the surrounding matrix to prevent the transformation. The significant volume change lead to high stresses in the matrix which causes the cracks. These cracks significantly reduce the room temperature mechanical strength of the sample.

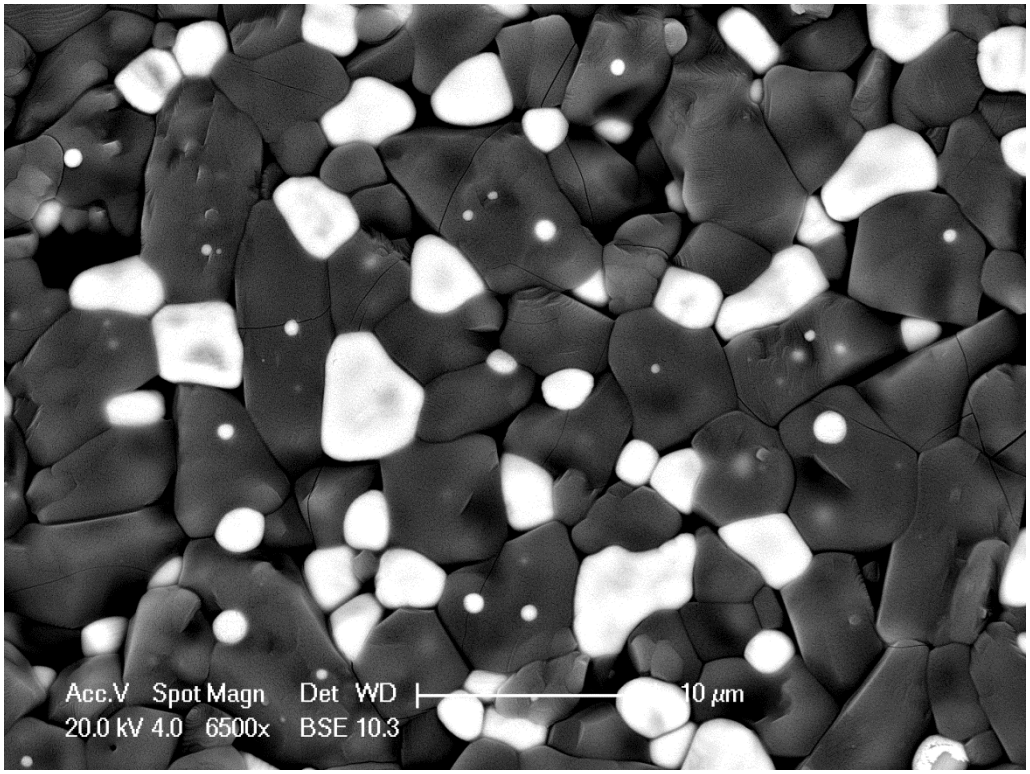

Figure 6.29 Micro cracks in sample No.8 (PCA1685) (BSE)

Table 6.11 EDS results of No.8 (PCA1685)

Sample No.8 (PCA1685)					
Dark Grain				**Bright Grain**	
Element	Weight %	Atomic %	Element	Weight %	Atomic %
O K	35.40	48.33	O K	20.87	60.07
Al K	45.06	36.48			
Si K	19.54	15.20	Zr L	79.13	39.93

Table 6.11 shows the EDS results of sample No.8 (PCA1685) which confirm the mullite and zirconia composition.

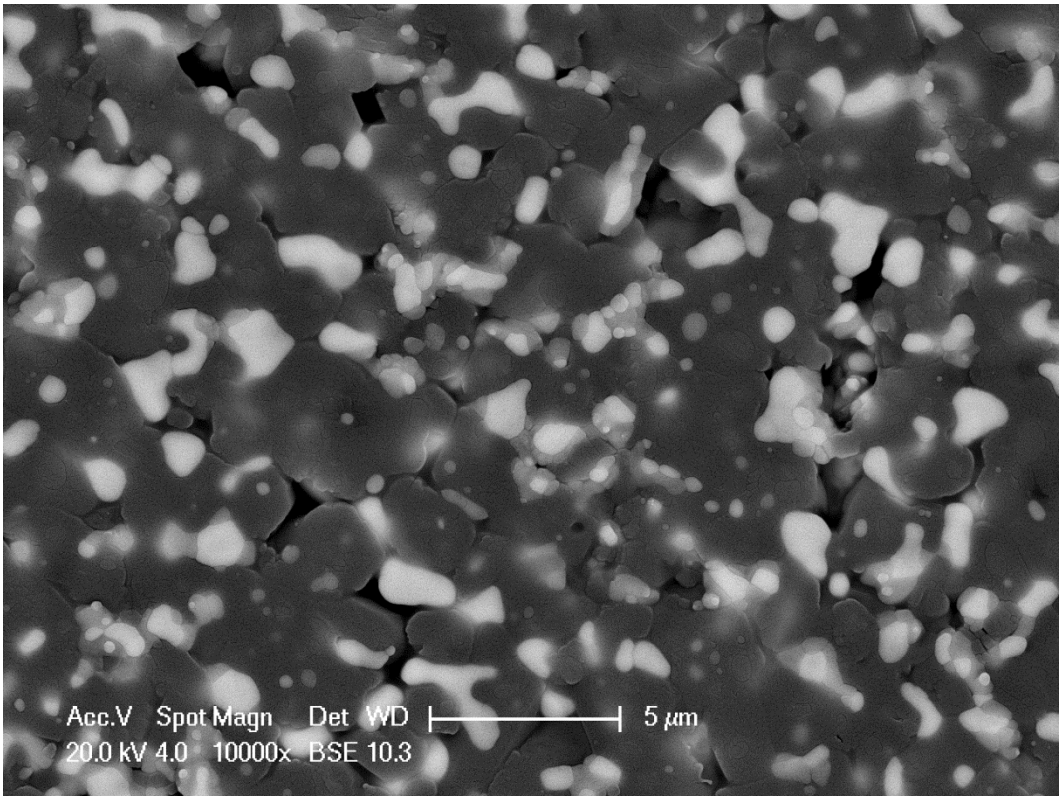

No.36

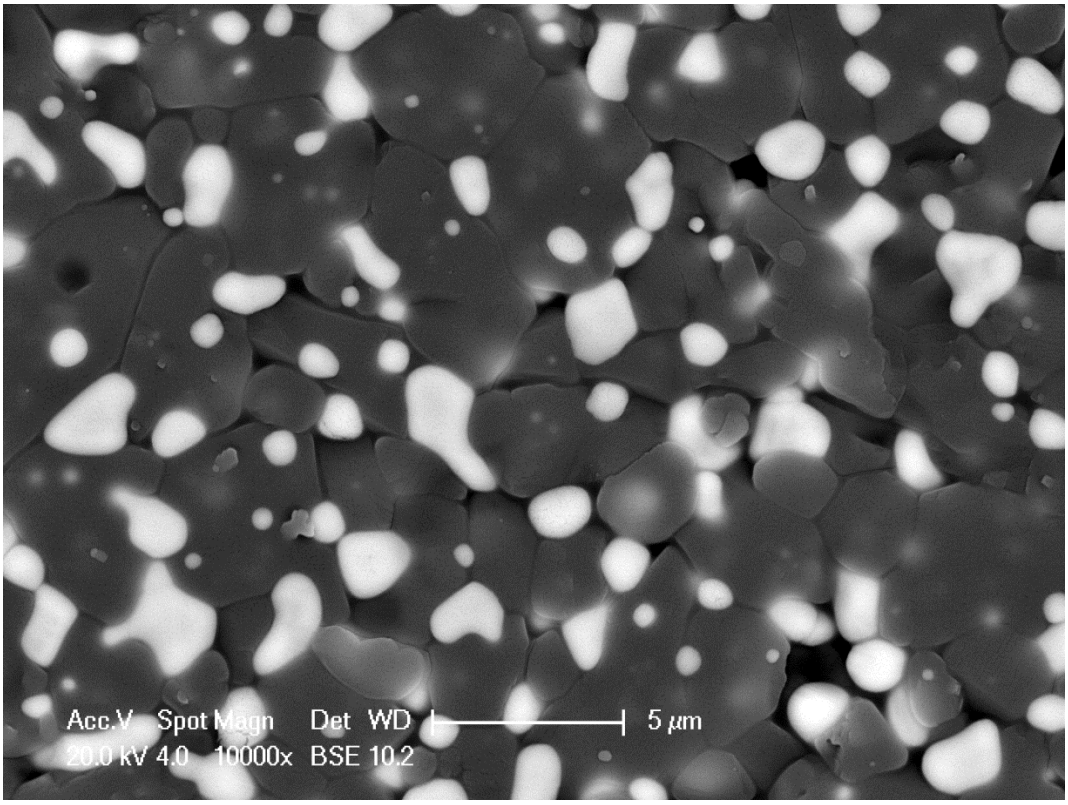

No.19

Figure 6.30 Thermally etched surfaces of No.36 (PCA1540) and No.19 (PCA1600) (BSE)

The differences between sample No.36 (PCA1540) and No.19 (PCA1600) are not easily observed. The images of polished surface of these two samples appear essentially the same. By comparing the thermal etched surface under high magnification (10000× when testing), the differences can be identified (Figure 6.30).

First, the shape of mullite and zirconia particles are spherical in No.19 (PCA1600) while in No.36 (PCA1540) the shape is elongated and more irregular. Second, the grain boundaries are not as clearly defined in No.36 (PCA1540). The intergranular zirconia particles are not well defined. Some of the intragranular bright zircon particles have light grey halos.

All these morphological features confirm that at 1540 ℃ the reaction had not gone to completion. Zirconia has not yet fully developed from sintering processes and an intermediate phase was present. When the materials are fully reacted, as in No.19 (PCA1600), the zirconia developed a more spherical appearance.

Table 6.12 EDS results of No.36 (PCA1540)

Sample No.36 (PCA1540)								
Dark phase			**Grey Phase**			**Bright Phase**		
Element	Weight %	Atomic %	Element	Weight %	Atomic %	Element	Weight %	Atomic %
O K	41.50	54.71	O K	30.68	59.64	O K	21.63	61.04
Al K	43.25	33.82	Al K	14.40	16.60			
Si K	15.25	11.46	Si K	6.56	7.26	Zr L	78.37	38.96
				48.36	16.49			

Table 6.12 shows the elemental analysis of the three identified phases in No.36 (PCA1540). The mullite and zirconia were detected in the dark phase and bright phase respectively. The grey phase surrounding the bright phase contained Al, Si, Zr

and O which chemically indicating the presence of zircon and alumina or possibly Si-Zr-Al-O glass phase as there is no evidence of two separate phases by the uniform phase contrast. This confirms the incomplete reaction which results in reduced properties and inferior behaviour as the preferred microstructure had not fully formed.

6.10.4 Product Types

Sample No.34 (EWI1600) exhibited the best extruded product properties and No.19 (PCA1600) has the best properties among the compact products. These two samples show very similar properties, while No.19 (PCA1600) outperforms in most areas to a small degree.

The fracture surface and polished surface generally show same morphological appearances between these two samples. After the samples were thermally etched, some differences were observed under relatively high magnification (6500× when in the SEM).

As can be seen from Figure 6.31, the overall structure is similar with zirconia homogenously distributed in a relatively dense mullite matrix. The shape, size and boundaries of mullite grains (about 3 μm) and intragranular zirconia particles (about 1 μm) are very similar. However, in sample No.34 (EWI1600), the intergranular zirconia is in form of a few smaller particles gathered together rather than the single rounded particles observed in No.19 (PCA1600). Several very small pores developed in between these small zirconia particle clusters. These zirconia clusters and pores

may be the cause of the properties of sample No.34 (EWI1600) being slightly reduced compared to No.19 (PCA1600).

The differences may be due to the pressed pellet being compacted more than the extrusion sample during the forming process. That is to say, extrusion process cannot provide as high stress during shaping that is impose by the dry pressing technique.

A binder system was added in during the paste forming process of sample No.34 (EWI1600). Thus during the sintering process, the introduced polymers burnt and released gas which may have caused the formation a less compact structure.

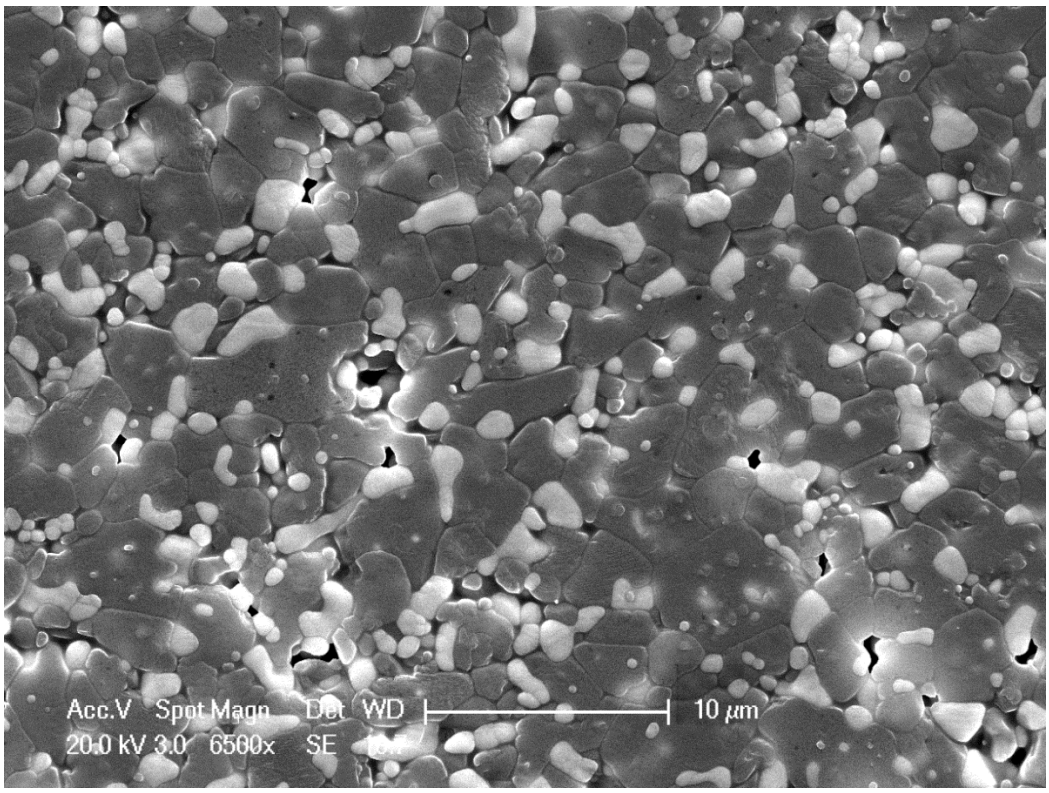

No.34

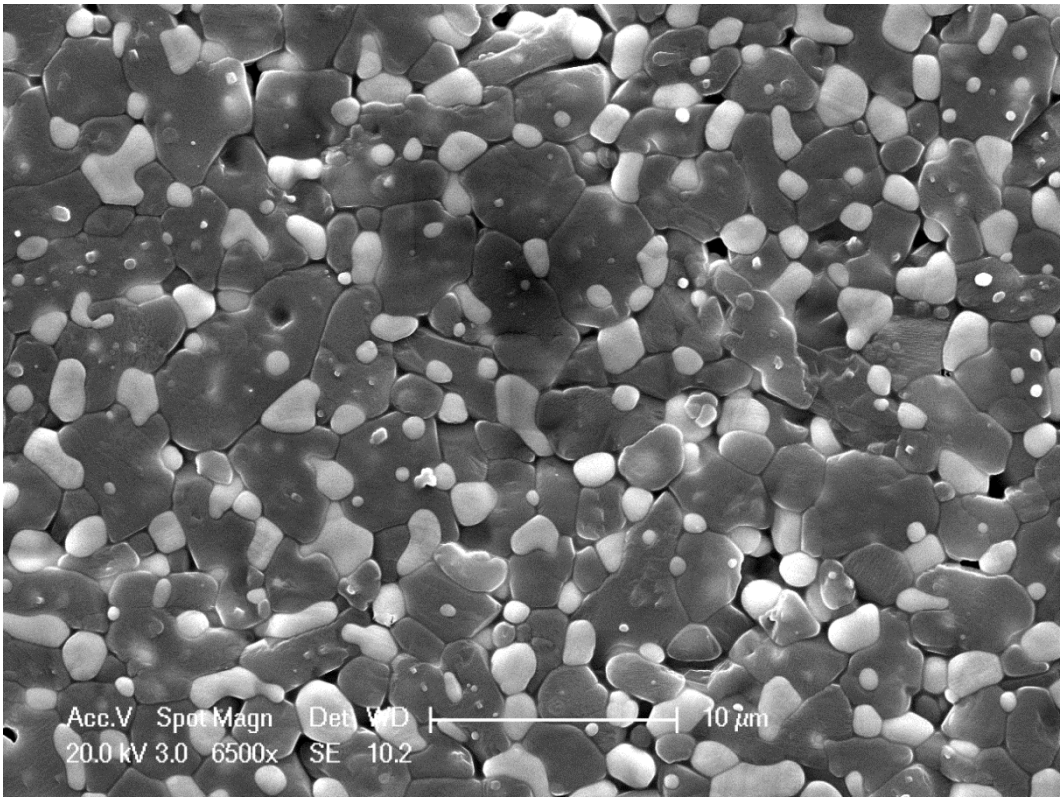

No.19

Figure 6.31 Thermally etched surfaces of No.34 (EWI1600) and No.19 (PCA1600) (SE)

6.10.5 Powder Processing Techniques

Sample No.30 (EWH1600) used a powder which was attrition milled in water while the powder used in No.34 (EWI1600) had been additionally ball milled in isopropanol to break up the agglomerates. In every other aspect the processing was the same yet some microstructural differences were observed.

Firstly, the structure of sample No.30 (EWH1600) (93.4 % dense) was less dense than No.34 (EWI1600) (96.7 % dense). There are more pores evenly distributed through the matrix. Line interception analysis shows there is less intragranular zirconia in sample No.34 (EWI1600). The intergranular zirconia particles are similar in volume, size and shape to No.30 (EWH1600).

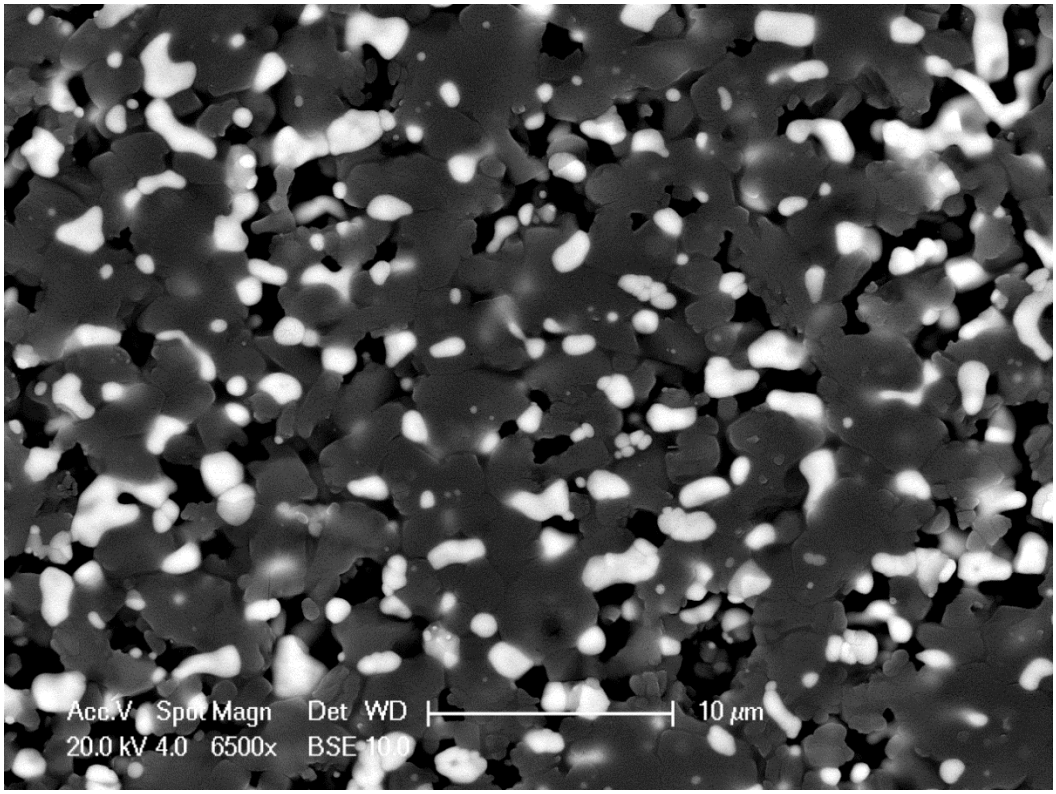

No.30

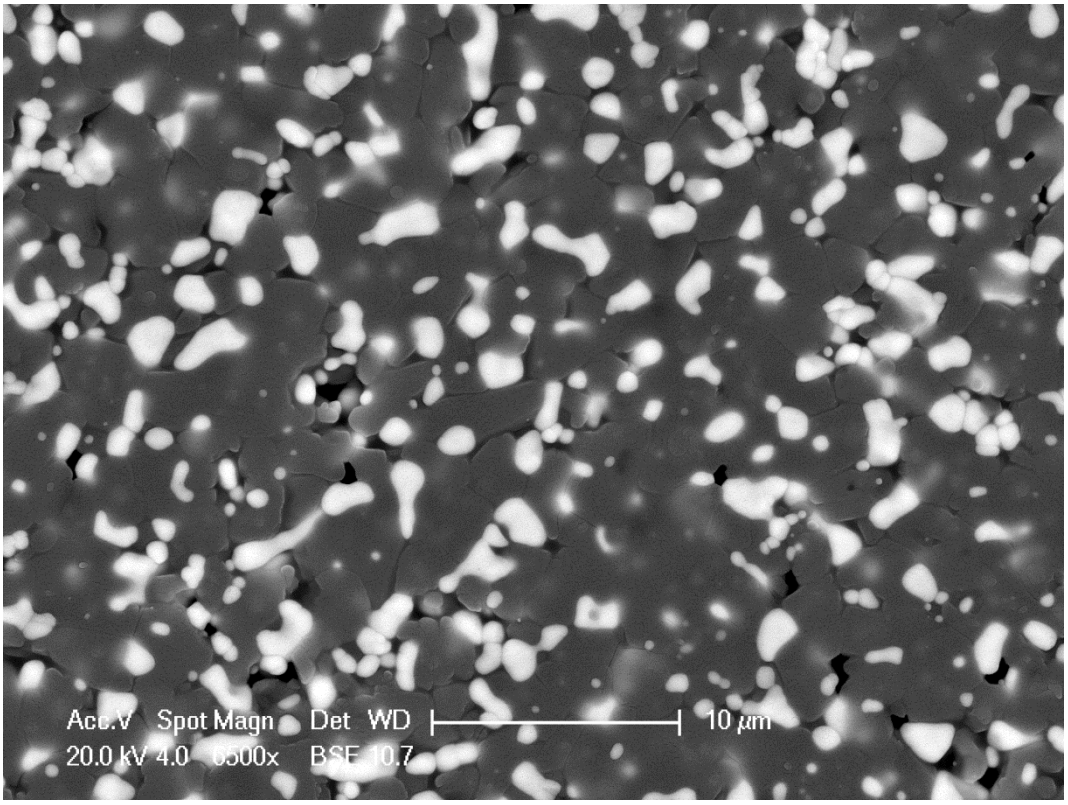

No.34

Figure 6.32 Thermally etched surfaces of No.30 (EWH1600) and No.34 (EWI1600) (BSE)

Table 6.13 EDS results of No.30 (EWH1600) and No.34 (EWI1600)

Sample No.30 (EWH1600)						
Dark Grain				**Bright Grain**		
Element	Weight %	Atomic %		Element	Weight %	Atomic %
O K	30.83	43.25		O K	36.12	76.31
Al K	45.14	37.55				
Si K	24.03	19.20		Zr L	63.88	23.69

Sample No.34 (EWI1600)						
Dark Grain				**Bright Grain**		
Element	Weight %	Atomic %		Element	Weight %	Atomic %
O K	38.50	51.65		O K	29.14	70.11
Al K	43.24	34.39				
Si K	18.26	13.96		Zr L	70.86	29.89

This phenomenon suggests that in sample No.30 (EWH 1600), small agglomerates contain about 10 to 20 grains were developed in the post attrition mill processing. In the agglomerated areas, the materials were fully reacted and a dense structure was developed but between the agglomerates, the matrix did not fully sinter such that pores remain.

This means isopropanol process can significantly reduce agglomerate formation in powders which can significantly enhanced the properties of finished products.

Table 6.13 shows the EDS results of sample No.30 (EWH1600) and No.34 (EWI1600) which confirms the mullite and zirconia composition on the dark and bright grains respectively.

6.10.6 Effects of Yttria

To change the stabilisation of the ZrO_2 forming in the zirconia toughened mullite, 1.77 wt. % yttria was added in the raw powders of No.19 (PCA1600). This addition changed the mechanical and thermal properties of the finished products. Dilatometry results indicate the monoclinic and transformable zirconia was fully converted to a non-transformable tetragonal yttria stabilized zirconia (Section 6.7).

Figure 6.33 compares the fracture surfaces of sample No.35 (PCAY1600) and No.19 (PCA1600). The overall structures are quite similar with a similar volume of pores being randomly dispersed across on the surfaces of the two materials. However, it is clear that the pores in sample No.35 (about 2 μm) are larger than the ones in No.19 (about 1 μm) according to line interception method.

Figure 6.27 shows the detailed micro structured of these two samples by polishing and thermal etching the surfaces. By comparing these two images, it can be seen that the zirconia distribution is different with the addition of Y_2O_3. The zirconia grains are in strings which appear to have formed around the mullite in sample No.35 (PCAY1600). In addition, the shape of the zirconia grains was more irregular in sample No.35 (PCAY1600) while in No.19 (PCA1600) they are near spherical.

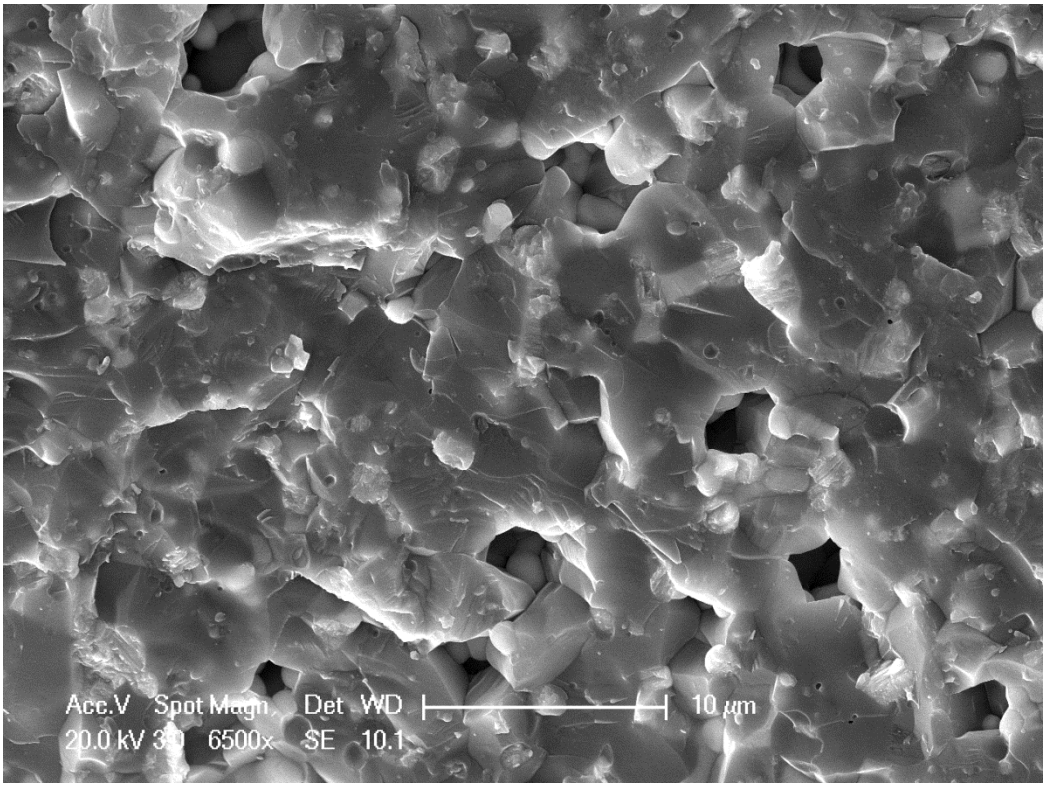

No.35

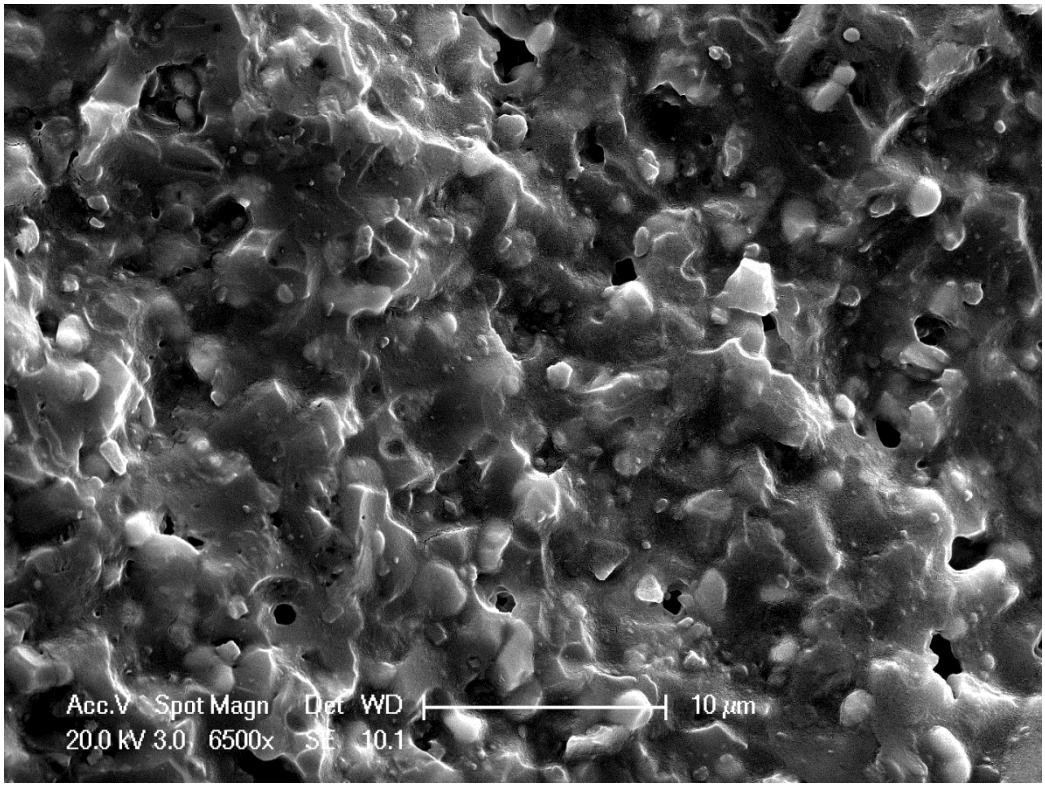

No.19

Figure 6.33 Fracture surfaces of No.35 (PCAY1600) and No.19 (PCA1600) (SE)

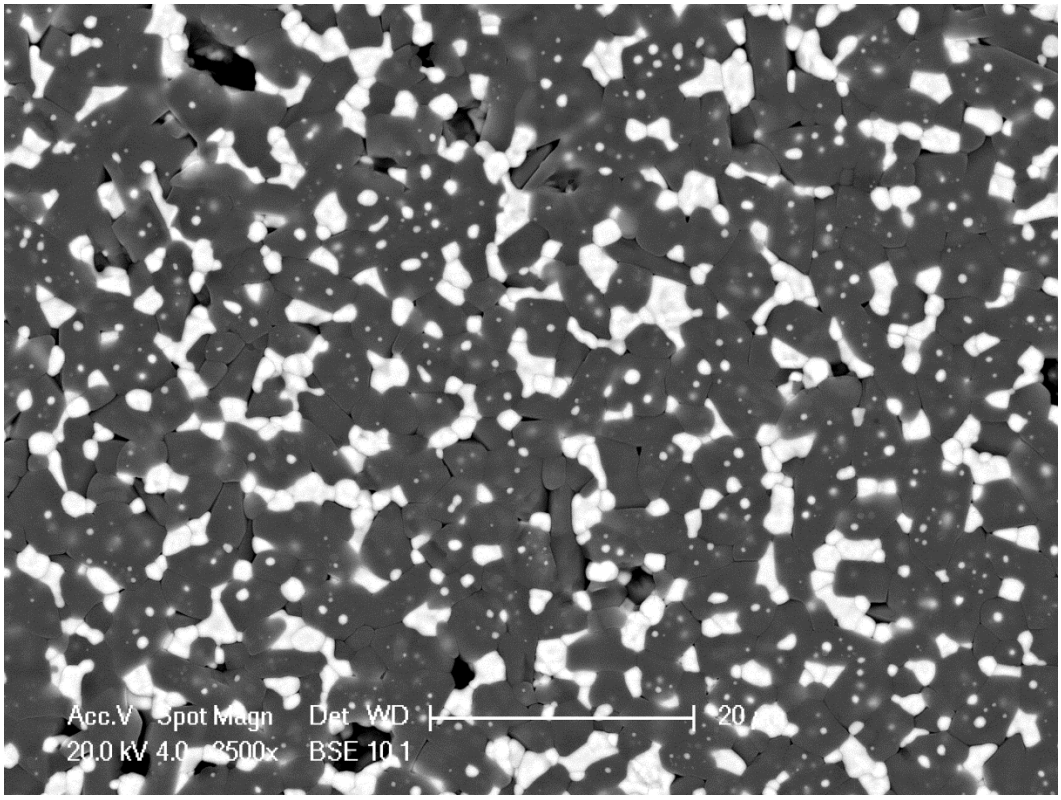

No.35

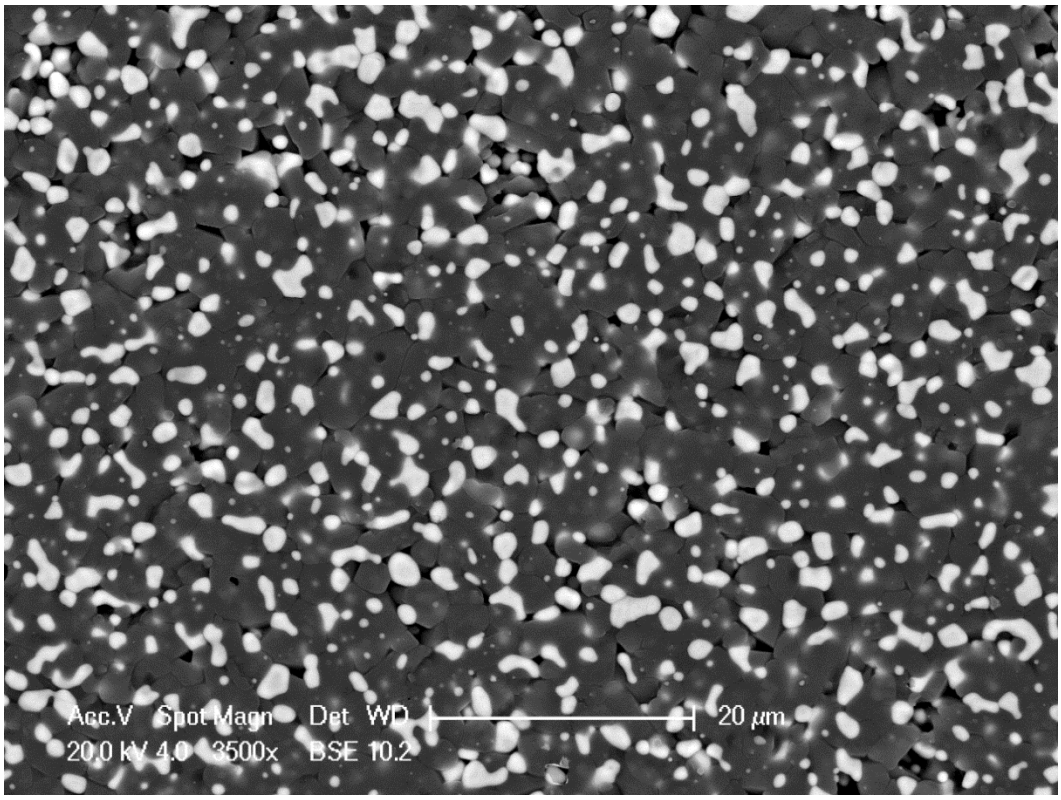

No.19

Figure 6.34 Thermally etched surfaces of No.35 (PCAY1600) and No.19 (PCA1600) (BSE)

Table 6.14 EDS results of sample No.35 (PCAY1600)

Sample No.30 (EWH1600)						
Dark Spot				Bright Spot		
Element	Weight %	Atomic %		Element	Weight %	Atomic %
O K	29.56	41.71		O K	20.74	59.83
Al K	50.32	42.11		Y L	5.67	2.94
Si K	20.12	16.17		Zr L	73.59	37.23

This may be due to the reason that the presence of yttria may change the intermediate glass behaviour. It may cause the glass phase to be formed at lower temperature with a composition Y, Zr, Si and O and thus had a different fluidity and elemental mobility (215). Therefore, if the glass were to follow round the alumina grains in the sintering process before mullitization, this structure in No.35 (PCAY1600) may develop.

Another explanation is that the Y_2O_3 somehow preferably attracted to zircon or alumina in the milling process and thus causes the powders to agglomerate in a different way which may lead to the zirconia particles formed into strings.

Table 6.4 shows the EDS results of sample No.35 (PCAY1600). As can be seen from the table, the dark spot shows Al, Si and O which confirms the mullite matrix has been formed. Yttrium is detected in the bright phase only which indicate that yttria did partition into the zirconia structure and thus the stabilized non-transformable tetragonal zirconia was formed as expected.

6.11 Thermal Shock Resistance

Only product No.19 (PCA1600) which exhibited the best properties in every aspect was evaluated for thermal shock resistance. The detailed principles and procedures are described in Chapter 3.2.11.

Figure 6.35 shows the curve of the thermal shock resistant results of sample No.19 (PCA1600). It can be seen that the flexural strength was maintained at a similar level of approximately 350 MPa when quenching from 220 ℃ to room temperature. When ΔT was 700 ℃, the strength dropped to about half of the original value and when ΔT was 1200 ℃ the remnant strength was 118.6 MPa (about 35 % of original value).

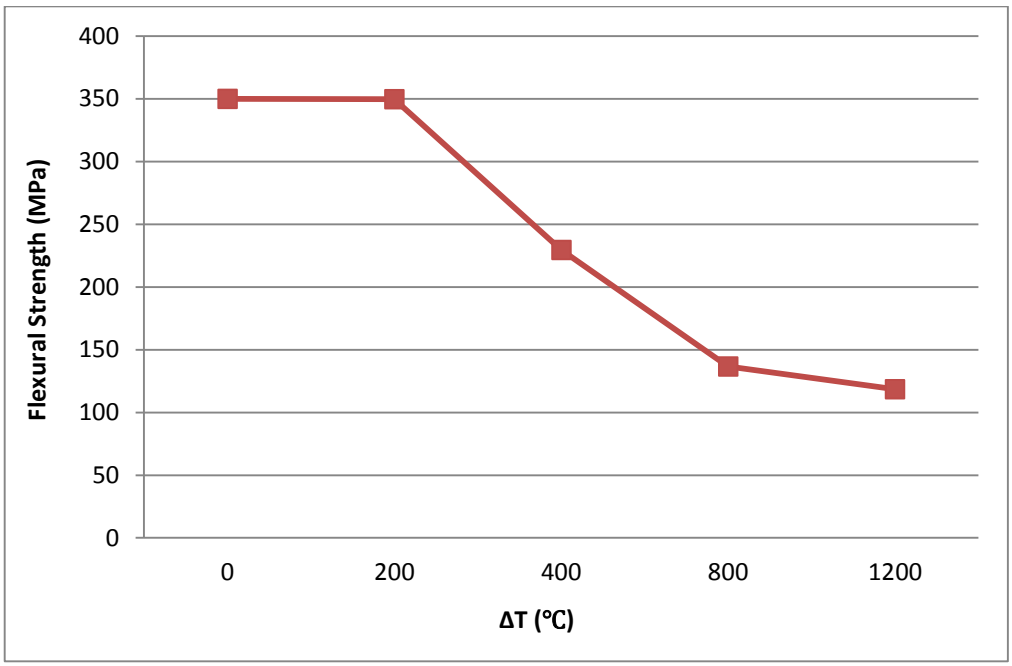

Figure 6.35 Thermal shock resistance of sample No.19 (PCA1600)

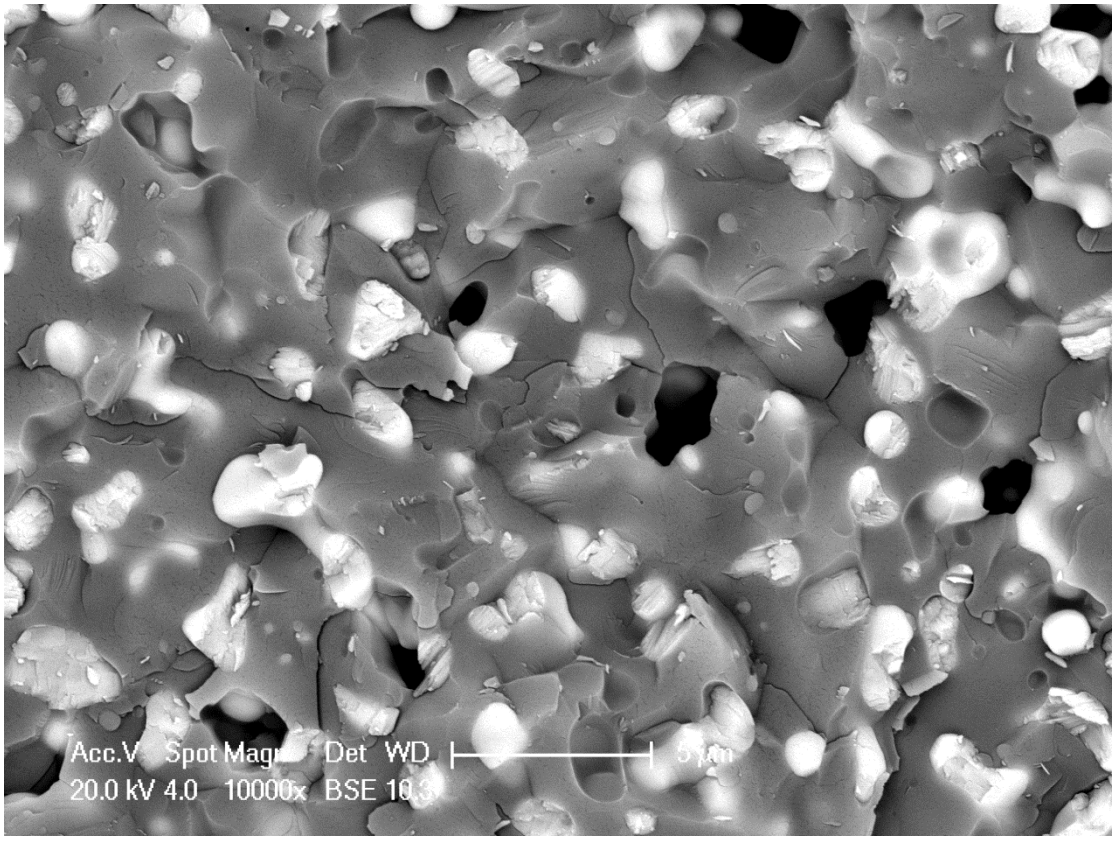

Figure 6.36 Fracture surface of ΔT = 1200 °C sample

These results show sample No.19 (PCA1600) has similar thermal shock resistance to other mullite-zirconia composite reported in the literature (37, 216).

Figure 6.36 shows an SEM image of the fracture surface of a ΔT = 1200 °C sample. It can be seen that micro cracks with length from about 2 µm to 5 µm were developed randomly in the structure. These cracks reduced the mechanical behaviour of the product as would be expected but it can be said that the material retained some significant residual strength.

CHAPTER VII COLOUR PIGMENT DEVELOPMENT

7.1 Introduction

The previous chapters demonstrated how the ceramic waste solids were processed to give clean fine powders (Chapter 4) and how the waste powders were then developed to produce zirconia toughened mullite refractory pellets and rods (Chapter 5). The properties of these refractory products were also examined and analysed (Chapter 6).

The principles, techniques and processes of producing zircon based pigments were reviewed in Section 2.3. This chapter will show how zircon based pigments can be developed from the ceramic waste powders.

The alumina elimination technique and zirconia dissociation methods developed in this study will be described. Different yellow colour forming approaches will also be demonstrated. The production system will be introduced and finally the chroma data of the yellow pigments will be examined, analysed and compared.

7.2 Alumina Elimination Process

7.2.1 Theoretical Basis

From the XRF, EDS and XRD results (Section 4.4 & 4.7), the elemental composition and crystal phase distribution of the ceramic waste powders were obtained. The ceramic waste mainly contains 3 oxide species: zircon, alumina (corundum) and amorphous silica.

From the literature, there should be no elemental aluminum in the zircon based pigments (46, 57). Alumina in the ceramic waste would severely hinder the formation of zircon based pigment colours. This is because alumina can react with silica and zircon at high temperature, thus seriously interfering with the process of the colorant ion such as Pr^{4+} and V^{4+} entering into the zircon crystal lattice. Therefore, the alumina in the ceramic waste should be eliminated as a first step.

In order to remove the alumina in the ceramic waste while retaining the zircon, $K_2S_2O_7$ can be used as the reagent. Alumina and potassium pyrosulphate react in a eutectic melting process which is shown in Equation 7.1 (217).

$$3K_2S_2O_7 + Al_2O_3 \xrightarrow{650\ ^\circ C} 3K_2SO_4 + Al_2(SO_4)_3 \qquad (7.1)$$

After the mixture has fully reacted and cooled, the K_2SO_4 and $Al_2(SO_4)_3$ can be easily dissolved in water and washed from the zircon. The alumina in the ceramic waste is thus eliminated while the zircon is retained.

7.2.2 Experimental Apparatus and Procedures

In this study, two 150 ml silica crucibles were used as the reactor which prevented reaction with active materials. Commonly used alumina crucibles would react with potassium pyrosulphate. The potassium pyrosulphate was supplied by Fisher Scientific, UK with a purity of 98 + %. The reactions were conducted in a LENTON UAF 17/27E 1700 Chamber Furnace.

Given the compositions of ceramic waste, an excess of potassium pyrosulphate was added to the waste in the ratio of 25 wt. % ceramic waste to 75 wt. % $K_2S_2O_7$

(typically 20 g and 60 g) and then powder transferred into a mortar followed by pestle mixing for 0.5 hour. The mixed powders were transferred to a 150 ml silica crucible and treated in a programmed chamber furnace. The samples were sintered at three different temperatures (450 ℃, 650 ℃, 850 ℃) for 3 hours with same heating rate (1.0 ℃·min^{-1}) and cooling rate (10 ℃·min^{-1}) to evaluate the intensity of the reaction at higher temperature.

After the firing process, the samples were dissolved in 500 ml of water at room temperature for 8 hours with continuous stirring and then filtered under vacuum. The powder was placed into an oven for drying at 101 ℃ for 12 hours. The product was examined for alumina content before further processing.

7.2.3 XRD results

In order to analyse whether the alumina was completely removed, XRD analysis was carried out to identify the phase distribution of remaining ceramic waste materials. The principles, experimental instrument used in this study and testing procedures of XRD analysis are detailed in Section 3.2.3.

The analysed XRD patterns of the products reacted at 450 ℃ and 650 ℃ are shown in Figures 7.1 and Figure 7.2, respectively.

Figure 7.1 shows that some alumina remained after reaction at 450 ℃. However, compared with Figure 4.7, the concentration of alumina was reduced which suggests the alumina was partially removed from the ceramic waste powders under these conditions.

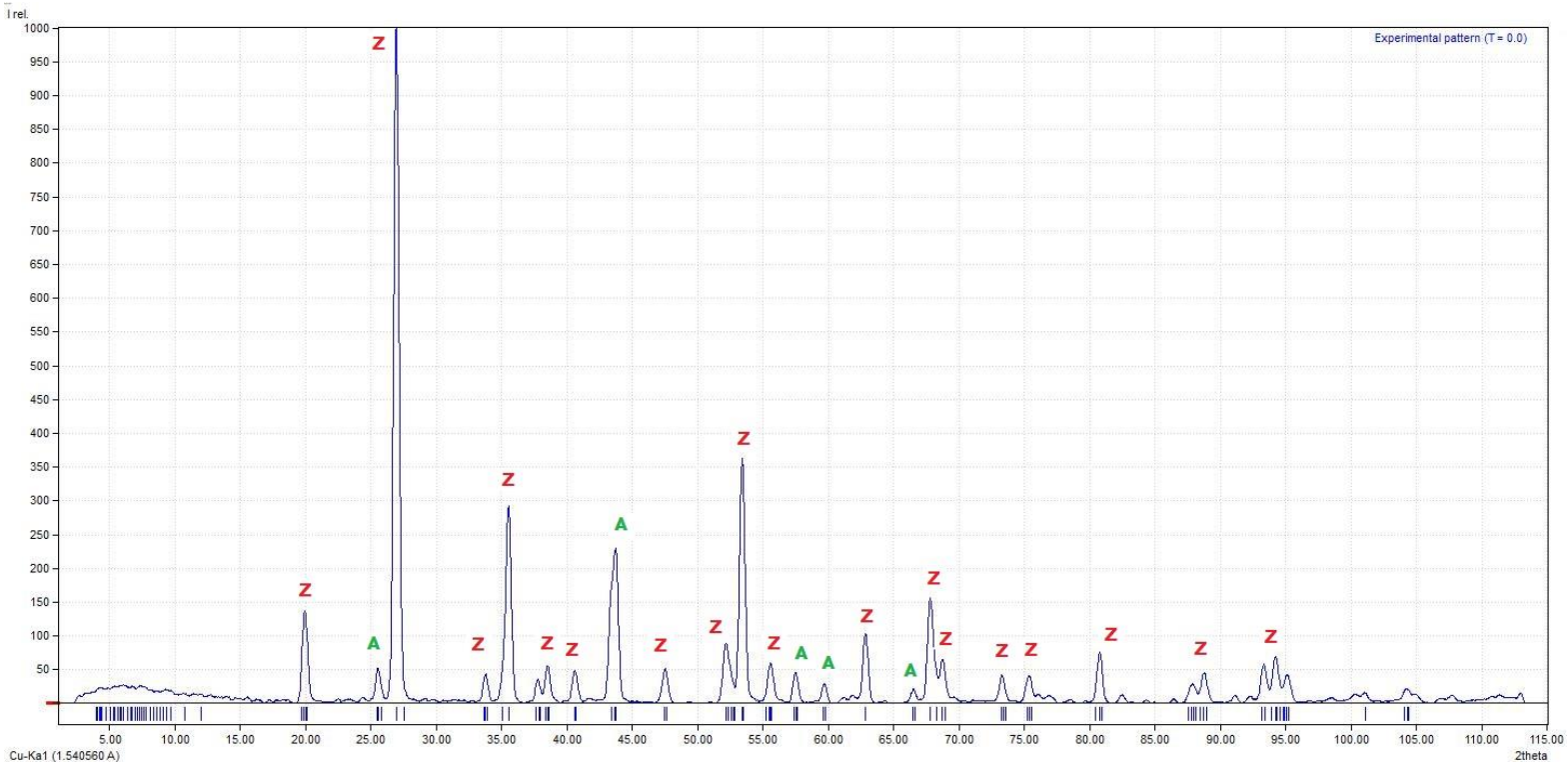

Colour	Formula	Matched Phase	Quantity
Red (Z)	$ZrSiO_4$	Zircon	63.1 %
Green (A)	Al_2O_3	Corundum	36.9 %

Figure 7.1 XRD results of 450 ℃ reacted product

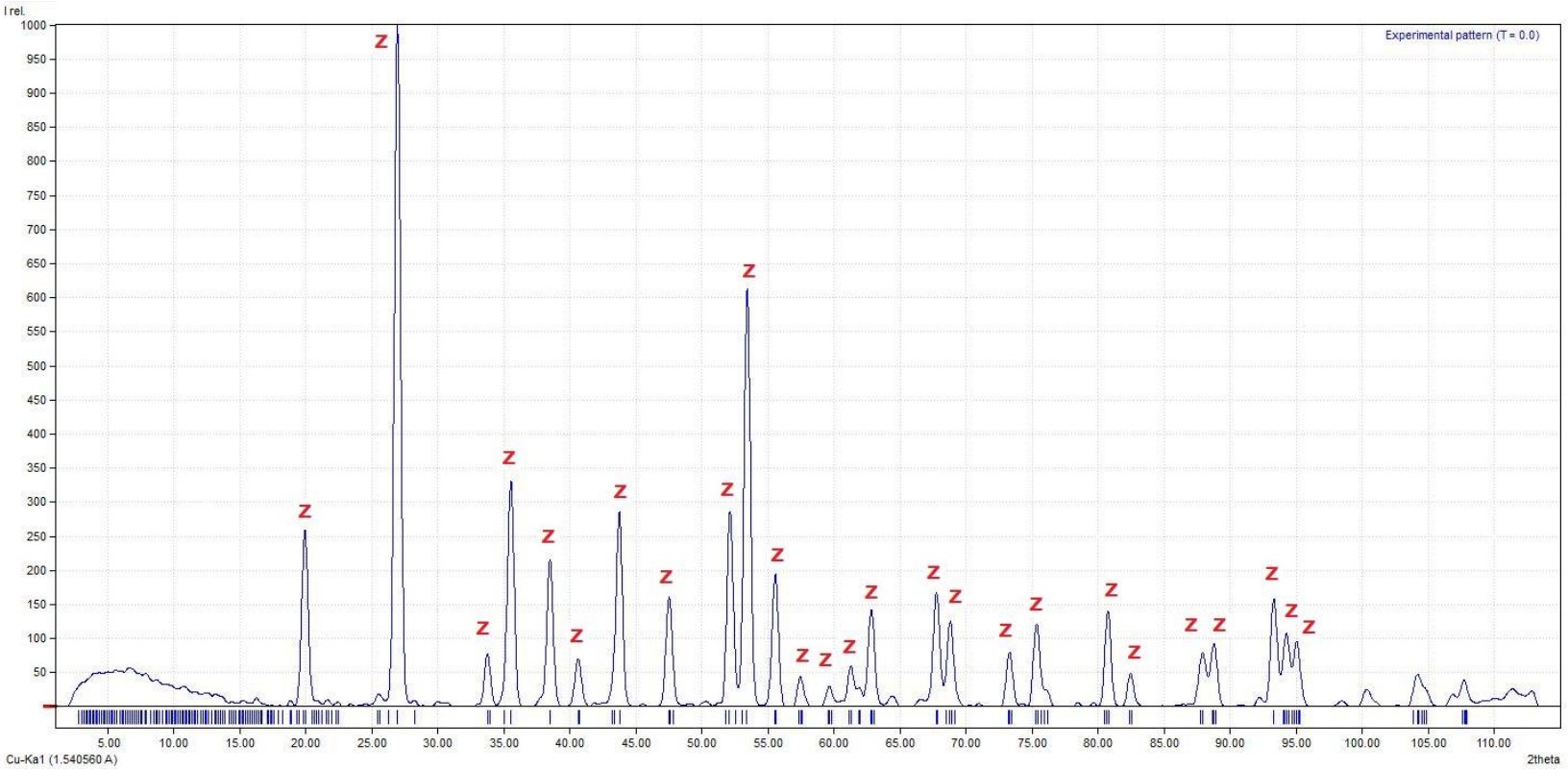

Colour	Formula	Matched Phase	Quantity
Red (Z)	$ZrSiO_4$	Zircon	100 %

Figure 7.2 XRD results of 650 ℃reacted product

Figure 7.2 shows only zircon to be present after treatment at 650 ℃ which indicates that all the alumina has been completely removed from the waste materials. The XRD result of treatment at 850 ℃ was the same as the 650 ℃ result, but not shown here.

The optimum reaction conditions were determined to be 650 ℃ for 3 hours, which allows the materials to react fully with minimum reaction temperature and thus minimum energy.

7.3 Zircon Dissociation Methods

7.3.1 Plasma Dissociation Method

7.3.1.1 Experimental Apparatus and Procedure

In this study, a Sulzer Metco F4 Plasma Gun was used to dissociate the ceramic waste. About 100 g ceramic waste was loaded into the sample chamber to test the feasibility of this method.

The powders were passed through the plasma gun with the gun operating at a condition of 35 V, 500A with a 45 $L \cdot min^{-1}$ helium gas flow. The reacted fine powders were collected on a metal net in the sample collector. The net was transferred into a beaker with ethanol followed by ultra-sonic treatment for 30 minutes. Through this process the powder was slowly and gently removed from the net. After drying in the oven at 70 ℃ for 12 hours, the dry product powder was collected.

7.3.1.2 PDZ Analysis

In order to examine the extent of dissociation, XRD and SEM were used. The XRD graph of the PDZ treated material is shown in Figure 7.3.

By comparing the result with Figure 4.7, it can be seen that the amount of alumina in the powder was the same, while the amount of zircon was reduced. Zirconia and silica can be detected in this sample as new phases compared to the untreated ceramic waste powders. This suggests that a certain amount of zircon has been dissociated (about 25 wt. %). Due to the high feed volume required (minimum 500 g), ceramic waste containing alumina was passed through the device. The losses were high and contamination was common as the gun and collector were difficult to clean. There was a significant accumulation of the previous powder in the product despite attempting to toughly clean the system before use.

The plasma treated ceramic waste powder was mounted in resin and polished to allow observation under back scattered mode. An example image of the data obtained is shown in Figure 7.4.

Figure 7.4 shows that the darkest particles are alumina and silica particles while the grey toned particles indicate zircon and the brightest grains are zirconia. To confirm this, EDS was used to identify the elemental composition of the zircon and zirconia particles which are show in Table 7.1. Free zirconia and unaltered zircon are confirmed by this analysis.

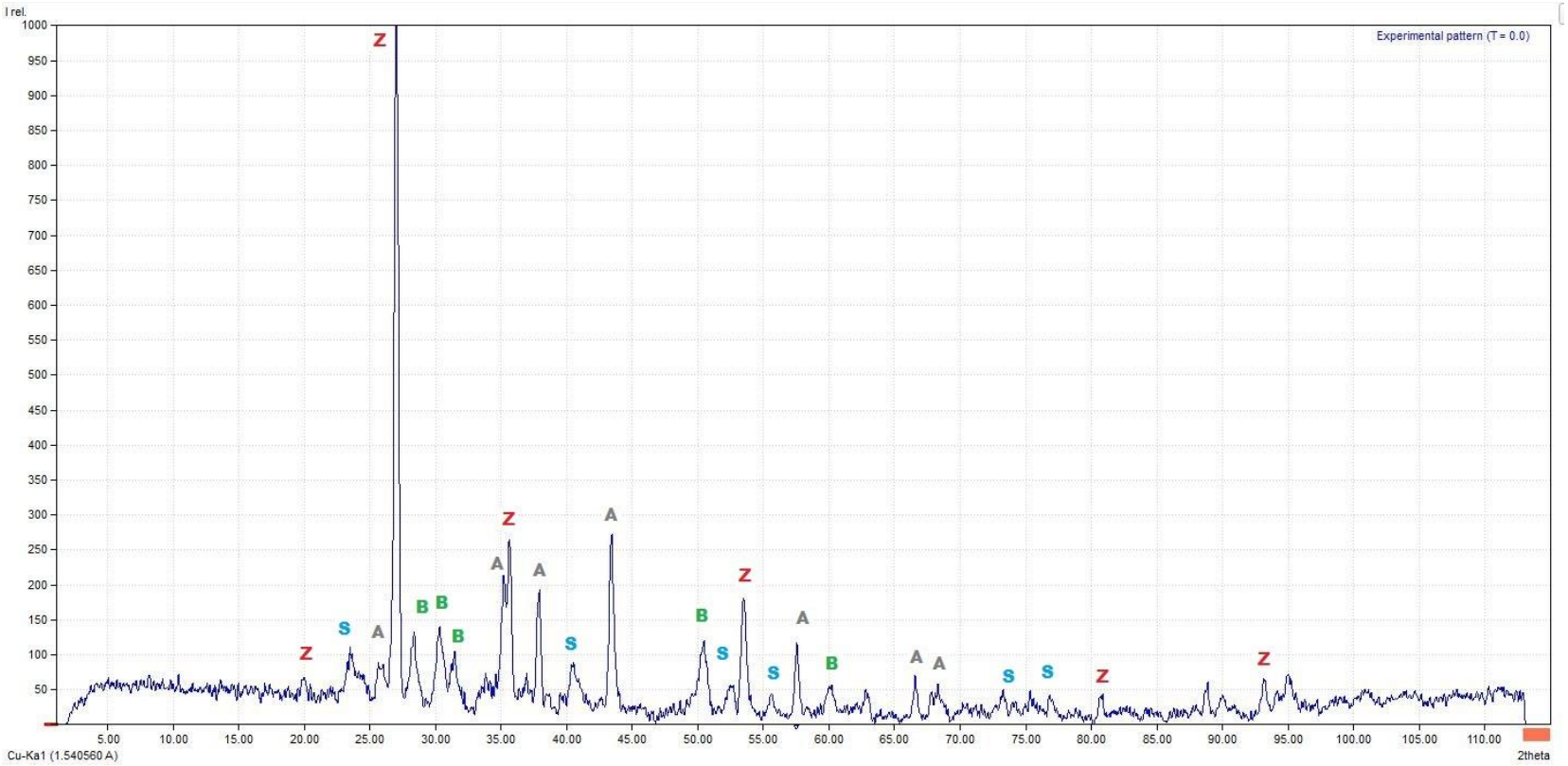

Colour	Formula	Matched Phase	Quantity
Red (Z)	$ZrSiO_4$	Zircon	33.7 %
Grey (A)	Al_2O_3	Corundum	45.8 %
Green (B)	ZrO_2	Zirconia	13 %
Blue (S)	SiO_2	Silica	7.5 %

Figure 7.3 XRD results of plasma treated ceramic waste powder

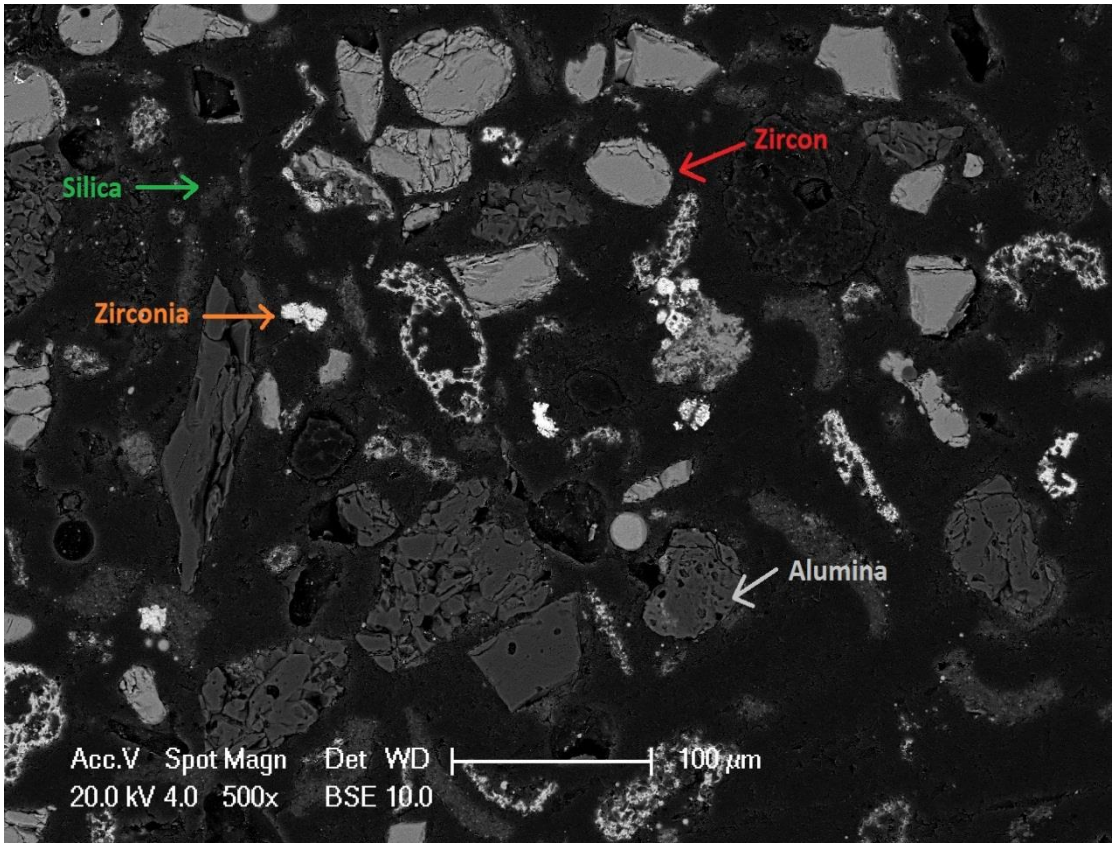

Figure 7.4 Back scatter SEM image of plasma treated ceramic waste powder

Table 7.1 EDS results of Zircon and Zirconia Spot

Zircon Spot				**Zirconia Spot**		
Element	Weight %	Atomic %		Element	Weight %	Atomic %
O K	20.82	50.60		O K	26.73	67.53
Si K	16.33	22.61				
Zr L	62.85	26.79		Zr L	73.27	32.47

Combining XRD, SEM and EDS results, it can be confirmed that a fraction of zircon has been dissociated by passing through a plasma gun but most zircon (about 75 wt. %) did not react. This may be due to the rather low power of the available plasma device. The maximum power was 600 A, but for safety reasons, the 500 A

was applied as the upper practical limit. A powerful plasma gun which can operate at power levels in excess of 2000 A could provide sufficient energy to dissociate all zircon in the ceramic waste (51, 53, 218, 219).

7.3.2 Sodium Carbonate Dissociation Method

Plasma dissociation was ultimately not successful in this study due to the limitation of the available equipment. However, it would be a process for consideration on a dedicated commercial plant. Other methods can be used to produce zircon based pigments by using zircon as raw material. Sodium carbonate dissociation is the most commonly used method and a cost effective method (42, 49).

7.3.2.1 Experimental Apparatus and Procedure

In this study, 30 g ceramic waste generated zircon powder (Refer to Section 7.2) was used per experiment to mix with 17.3 g sodium carbonate (supplied by Sigma-Aldrich, UK with a purity of 99.5 %) using a mortar and pestle. The mixture was transferred into a 250 ml alumina crucible. The sample was sintered in a programmed chamber furnace (LENTON UAF 17/27E 1700) for 3 hours with a heating rate of 10 ℃·min^{-1} up to 950 ℃ to generate Na_2SiZrO_5.

After the process was completed, about 20 g of product powder was removed and put in a 500 ml beaker which contained 400 ml 5 wt. % sulphuric acid. The solution was stirred magnetically to accelerate the reaction for 4 hours. The remaining solids were filtered from the reaction liquor and washed with de-ionized water 3 times and dried in the oven at 80 ℃ for 24 hours. This $(ZrO_2)_xSO_3$ powder was mixed with Na_2SiZrO_5, commercial fused silica and commercial colourant to form pigments. In

addition, the sintered powders were dissolved in water for 2 hours and washed 3 times to remove the Na_2SO_4. Finally, the product was dried in the oven at 101 ℃ for 24 hours.

7.4 Product System

The procedures described in section 7.3 transformed the ceramic waste powders into samples that were ready to be used in the production of zircon based pigments. In this study, yellow pigment was chosen as the product due to it being safer to produce in an open environment compared to the blue pigments produced from vanadium. Iron pink was considered, but because of the availability of the colour determination methods, the cleaner yellow pigment produced by praseodymium oxide was favoured.

In order to compare the procedures and products, three different methods were used to make yellow pigments. Each method was conducted under different conditions.

In Table 7.2, each sample produced and recorded in the system is given a number along with a coded name. For example, T1350 means the sample was made using commercial material sintered at 1350 ℃ under traditional method; DF 1050 indicates that the condition applied was direct sintering with flux being heat treated at 1050 ℃.

Table 7.2 Yellow pigment product system - Traditional Method

Traditional Method					
No.	**Name**	**Material Type**	**Formulation**	**Temperature**	**Reaction**
n/a	TC900	Commercial	$ZrO_2 + SiO_2 + Pr_6O_{11}$	900 ℃	No
n/a	TC1050	Commercial	$ZrO_2 + SiO_2 + Pr_6O_{11}$	1050 ℃	No
n/a	TC1200	Commercial	$ZrO_2 + SiO_2 + Pr_6O_{11}$	1200 ℃	No
1.	TC1350	Commercial	$ZrO_2 + SiO_2 + Pr_6O_{11}$	1350 ℃	Yes
2.	TC1500	Commercial	$ZrO_2 + SiO_2 + Pr_6O_{11}$	1500 ℃	Yes
3.	TC1650	Commercial	$ZrO_2 + SiO_2 + Pr_6O_{11}$	1650 ℃	Yes
n/a	TCF900	Commercial +Flux	$ZrO_2 + SiO_2 + Pr_6O_{11}$ + NaF + NaCl	900 ℃	No
4.	TCF1050	Commercial +Flux	$ZrO_2 + SiO_2 + Pr_6O_{11}$ + NaF + NaCl	1050 ℃	Yes
5.	TCF1200	Commercial +Flux	$ZrO_2 + SiO_2 + Pr_6O_{11}$ + NaF + NaCl	1200 ℃	Yes
6.	TCF1350	Commercial +Flux	$ZrO_2 + SiO_2 + Pr_6O_{11}$ + NaF + NaCl	1350 ℃	Yes

Table 7.2 Yellow pigment product system - Alkali Fusion Method

Alkali Fusion Method					
No.	**Name**	**Material Type**	**Formulation**	**Temperature**	**Reaction**
n/a	A900	Na_2ZrSiO_5	Na_2ZrSiO_5+ $(ZrO_2)_xSO_3$ + SiO_2 + Pr_6O_{11}	900 ℃	No
7.	A1050	Na_2ZrSiO_5	Na_2ZrSiO_5+ $(ZrO_2)_xSO_3$ + SiO_2 + Pr_6O_{11}	1050 ℃	Yes
8.	A1200	Na_2ZrSiO_5	Na_2ZrSiO_5+ $(ZrO_2)_xSO_3$ + SiO_2 + Pr_6O_{11}	1200 ℃	Yes
9.	A1350	Na_2ZrSiO_5	Na_2ZrSiO_5+ $(ZrO_2)_xSO_3$ + SiO_2 + Pr_6O_{11}	1350 ℃	Yes
n/a	AF900	Na_2ZrSiO_5+Flux	Na_2ZrSiO_5+ $(ZrO_2)_xSO_3$ + SiO_2 + Pr_6O_{11} +NaF + NaCl	900 ℃	No
10.	AF1050	Na_2ZrSiO_5+Flux	Na_2ZrSiO_5+ $(ZrO_2)_xSO_3$ + SiO_2 + Pr_6O_{11} +NaF + NaCl	1050 ℃	Yes
11.	AF1200	Na_2ZrSiO_5+Flux	Na_2ZrSiO_5+ $(ZrO_2)_xSO_3$ + SiO_2 + Pr_6O_{11} +NaF + NaCl	1200 ℃	Yes
12.	AF1350	Na_2ZrSiO_5+Flux	Na_2ZrSiO_5+ $(ZrO_2)_xSO_3$ + SiO_2 + Pr_6O_{11} +NaF + NaCl	1350 ℃	Yes
13.	AF1500	Na_2ZrSiO_5+Flux	Na_2ZrSiO_5+ $(ZrO_2)_xSO_3$ + SiO_2 + Pr_6O_{11} + NaF + NaCl	1500 ℃	Yes

Table 7.2 Yellow pigment product system - Direct Synthesis Method

Direct Synthesis Method					
No.	**Name**	**Material Type**	**Formulation**	**Temperature**	**Reaction**
n/a	D900	CW-Zircon	CW-Zircon + Pr_6O_{11}	900 ℃	No
n/a	D1050	CW-Zircon	CW-Zircon + Pr_6O_{11}	1050 ℃	No
14.	D1200	CW-Zircon	CW-Zircon + Pr_6O_{11}	1200 ℃	Yes
15.	D1350	CW-Zircon	CW-Zircon + Pr_6O_{11}	1350 ℃	Yes
16.	D1500	CW-Zircon	CW-Zircon + Pr_6O_{11}	1500 ℃	Yes
n/a	DF900	CW-Zircon + Flux	CW-Zircon + Pr_6O_{11}+NaF + NaCl	900 ℃	No
17.	DF1050	CW-Zircon + Flux	CW-Zircon + Pr_6O_{11}+NaF + NaCl	1050 ℃	Yes
18.	DF1200	CW-Zircon + Flux	CW-Zircon + Pr_6O_{11} +NaF + NaCl	1200 ℃	Yes
19.	DF1350	CW-Zircon + Flux	CW-Zircon + Pr_6O_{11} +NaF + NaCl	1350 ℃	Yes
20.	DF1500	CW-Zircon + Flux	CW-Zircon + Pr_6O_{11} +NaF + NaCl	1500 ℃	Yes
21	DCF1350	Commercial zircon + Flux	Z-045(Zircon)+ Pr_6O_{11} +NaF + NaCl	1350 ℃	Yes
22.	DCF1500	Commercial Zircon + Flux	Z-045(Zircon)+ Pr_6O_{11} +NaF + NaCl	1500 ℃	Yes

(T = Traditional Method; A = Alkali Fusion Method; D = Direct Synthesis Method; C = commercial material; F = with flux; Number = Temperature)

All the materials used in the 'Traditional Method' were commercial chemicals. These products were used as the base line materials against which the pigments made from the ceramic waste materials were compared.

As can be seen from Table 7.2, the 'Traditional Method' used commercial zirconium oxide (supplied by Sigma-Aldrich, UK with 99 % purity) and fused silica (supplied by the local foundry plant, UK with 97 % purity) as the main raw materials to form the zircon structure. Praseodymium (III, IV) oxide (supplied by Sigma-Aldrich, UK with 99.9 % purity) was used as the colourant to develop the yellow colour. NaF (supplied by Sigma-Aldrich, UK with 99 % purity) and NaCl (supplied by Sigma-Aldrich, UK with 99.5 % purity) were used as the fluxing agents which were added with the intension of lowering the reaction temperature. The experiments were carried out without flux (Product No.1 to No.3: TC1350, TC1500 and TC1650) and with flux (Product No.4 to No.6: TCF1050, TCF1200, TCF1350) at different set temperatures.

The raw material powders were mixed (typically with 5 wt. % colourant and 4 wt. % flux) together by using a mortar and pestle for 30 minutes. The mixture was transferred into a 150 ml alumina crucible and calcined in a chamber furnace. The samples were sintered at different temperatures (900 ℃, 1050 ℃, 1200 ℃, 1350 ℃, 1500 ℃ and 1650 ℃) for 3 hours with same heating rate (10 ℃·min^{-1}) to reach the soak temperature and cooled at a rate of 10 ℃·min^{-1} .

When no reaction occurred, Table 7.2 shows 'No' in the last column and the sample was not counted in the numbering system. For example, the experiments without flux sintered at 900 ℃, 1050 ℃ and 1200 ℃ showed no colour change or structural alteration to the powder. The first product to show a reaction in the 'Traditional

method' for example occurred at 1350 ℃. When the colour powder could not be collected, the conditions were not given a number in the table. For instance, the experiments with flux sintered at 1500 ℃ and 1650 ℃ showed no visual colour improvement and the materials melted on the crucible, as a result only the 1350 ℃ condition was recorded as sample No.6 in the system.

The 'Alkali Fusion Method' is most commonly used in the zircon based pigments manufacturing industry which is based on the sodium carbonate dissociation method (Section 7.3.2.1) (47-49). In this study, Na_2ZrSiO_5 and $(ZrO_2)_xSO_3$ were used which were both generated from ceramic waste materials (refer to Section 7.3.2.2). The same commercial silica, praseodymium (III, IV) oxide, sodium fluoride and sodium chloride were used as in the 'Traditional Method'. The experiments were also carried out without flux (Product No.7 to No.9: A1050, A1200 and A 1350) and with flux (Product No.10 to No.13: AF1050, AF1200, AF1350 and AF1500) following the same temperature treatment scheme.

The raw material powders were mixed typically with 5 wt. % of colourant and 4 wt. % flux together using a mortar and pestle for 30 minutes. The mixture was put into a 150 ml alumina crucible with a platinum foil liner (supplied by Sigma-Aldrich, UK with 0.05 mm thickness and 99 % purity) and then set in a programmed chamber furnace. The samples were sintered at different temperatures (900 ℃, 1050 ℃, 1200 ℃, 1350 ℃, 1500 ℃ and 1650 ℃) for 3 hours with same heating rate (10 ℃·min^{-1}) and cooling rate (10 ℃·min^{-1}).

As can be seen from Table 7.2, the 'Direct Synthesis Method' was also used to produce the yellow colour. The purpose of these experiments was to simplify the

'Dissociation - Synthesis' process and compare the products with the commercially used methods.

This method used ceramic waste derived zircon (refer to Section 7.2) as the main material to react at high temperature which may allow the colourant ion to replace the zirconium (IV) ion in the structure to develop colour. It also used the same praseodymium (III, IV) oxide as the colourant and NaF, NaCl as the flux. The experiments were carried out without flux (Product No.14 to No.16: D1200, D1350 and D1500) and with flux (Product No.17 to No.20: DF1050, DF1200, DF1350 and DF1500) under different temperatures.

Figure 7.5 Raw materials and sintered yellow pigments (product No. 20: CF 1500)

Two more experiments were carried out using commercial zircon sand (Z-045 supplied by the local foundry plant, UK) to compare the difference between commercial materials and ceramic waste materials (product No.21 and No.22: DCF1350 and DCF1500). This Z-045 zircon had a mean particle size of about 2 μm and a purity of 95+ %. The same experimental apparatus and the same mixing and sintering processes were applied in this 'Direct Synthesis Method' as used in the 'Traditional Method'.

Following the sintering process, all the numbered products, 22 in total, were transformed from grey powder to different grades of yellow coloured powders. Typical colour changes from raw materials to pigment products can be seen in Figure 7.5.

The products were then ground in a mortar and pestle for 15 minutes to break the agglomeration which developed during the sintering process. The milled powder was water-washed for 3 times in order to remove the NaF and NaCl flux and any other unwanted impurities that were soluble (for example Na_2SO_4).

Finally the powder was dried in an oven at 101 ℃ for 8 hours. The pigment powder was characterised.

7.5 Characterisation of Products

There were 22 yellow colour pigments produced using 3 different methods. Particle size distribution tests were carried out before the sintering process. A chroma test was used to identify and compare the yellowness among these finished products. Finally, SEM images of the pigment were generated to show the morphology of the pigments.

7.5.1 PSD Analysis

The raw materials were mixed with colourant and flux in a mortar for 30 minutes. At this stage the PSD test was carried out to ensure the particle size and particle size distribution of each sample was similar before further processing. Seven types of powder were tested: TC, TCF, A, AF, D, DF and DZF (Table 7.2). Each type of powder

was tested 3 times and they all showed similar patterns of distribution indicating high repeatability. The different powder types also showed similar distributions. Two typical and representative results for the TC and DF powders are shown in Figure 7.6 and 7.7. Due to the software employed in the PSD only screen shot images of results are available, thus these two images are in different presentation styles as there was a software change between the experiments.

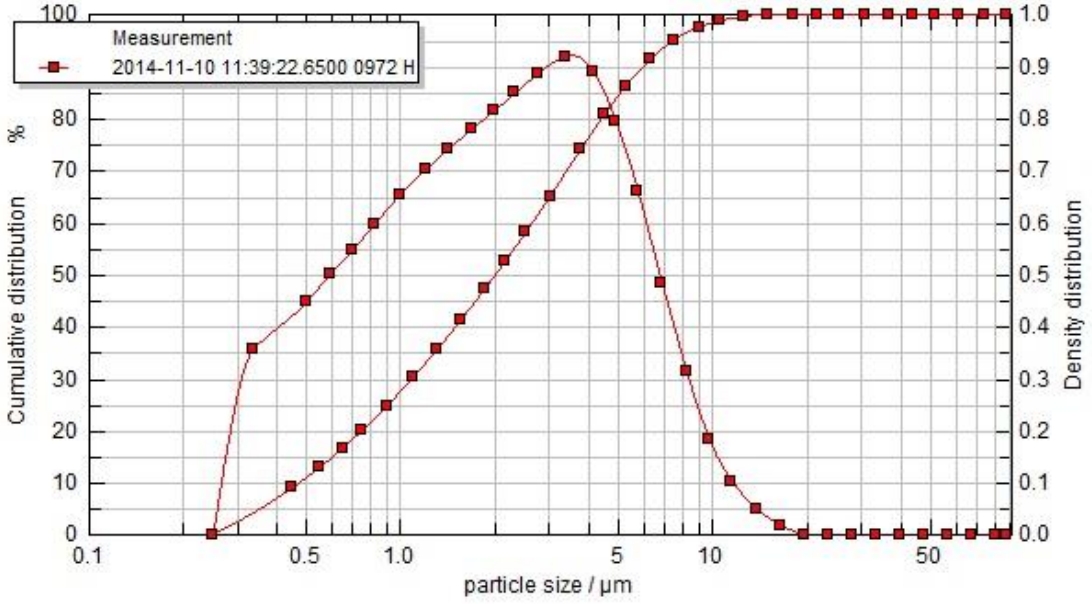

Figure 7.6 Typical particle size distribution of TC powder

As can be seen from Figures 7.6 and 7.7, the raw material mixtures for the different methods of manufacturing have a mono-modal distribution which means the powder is well dispersed (127). The mean particle size values of these two samples were very similar (2.01 µm and 2.08 µm respectively). The shapes of the curves are very similar and both have a relatively narrow distribution.

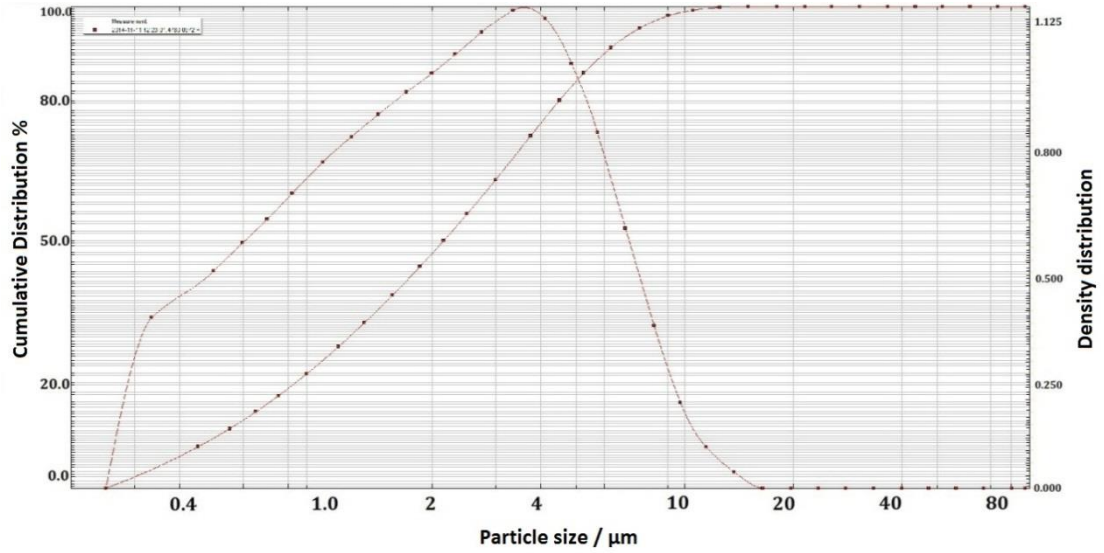

Figure 7.7 Typical particle size distribution of DF

Table 7.3 Particle size data of 4 samples

Product Name	D_{10} (µm)	D_{50} (µm)	D_{90} (µm)	D_{99} (µm)	Breadth $\frac{D_{90}-D_{10}}{D_{50}}$
TC	0.47	2.01	6.01	11.25	2.76
DF	0.49	2.08	5.98	10.31	2.64

The relatively fine particle size and narrow distribution (Breadth value in Table 7.3) would allow the materials to react efficiently and completely during the sintering process. The mean particle size value (about 2 µm) is very similar to that in published literature which stated this particle size can improve the process (47, 49). The similarity of the PSD results of each batch of raw materials ensured the properties of the products were not influenced by this factor.

7.5.2 Chroma Analysis

7.5.2.1 Experimental Apparatus and Procedures

A very important property of pigments is the chroma of the products. In this study, a self-developed method was used to identify and quantify the yellowness of the pigments.

The pigment products were in powder form which can influence the degree of yellowness due to PSD, shape and pores. In order to make the samples homogeneous and stable, the powders were pressed into pellets.

In this study, the cleaned and dried yellow pigment powders were pressed into pellets using a dry pressing technique with a 13 mm diameter die at a loading rate of 10 $mm \cdot min^{-1}$ to a maximum 10 kN load (Section 5.3). Each product was pressed to give 3 pellets.

The pellets were placed in the centre of a white paper with standard white colour, black colour and different shades of yellow colour printed to give a visual effect of the sample. An array of yellows of known RGB (Red, Green and Blue) value was printed on the paper to allow visual reference between pictures and calibration was thus possible once imported into photo processing software.

A NIKON D60 Digital Camera was used under same settings to photograph each pellet in the same position on a light table on the same day to minimize environmental difference. The camera was set at f/10 aperture; 1/13 second exposure time; ISO-100 speed and 105 mm focal length without flash light. A typical photo is given in Figure 7.8.

As can be seen the selected standard different colour circles (1 white, 5 shades of yellow and 1 black) are around the sample. But throughthe printing and photographing process, there were errors introduced in the system which meant the reproduced colour did not show the original RGB values. Thus, an adjustment method was applied to solve this issue.

Computer software Photoshop 7.0 was used to adjust the chroma of the whole photo until the white colour circle gave an RGB value of (255, 255, 255) which is the theoretical standard white value. An adjusted photo of Figure 7.8 can be seen in Figure 7.9, but of course even here the printing process used to generate this thesis will have changed the values slightly compared to the digital file images.

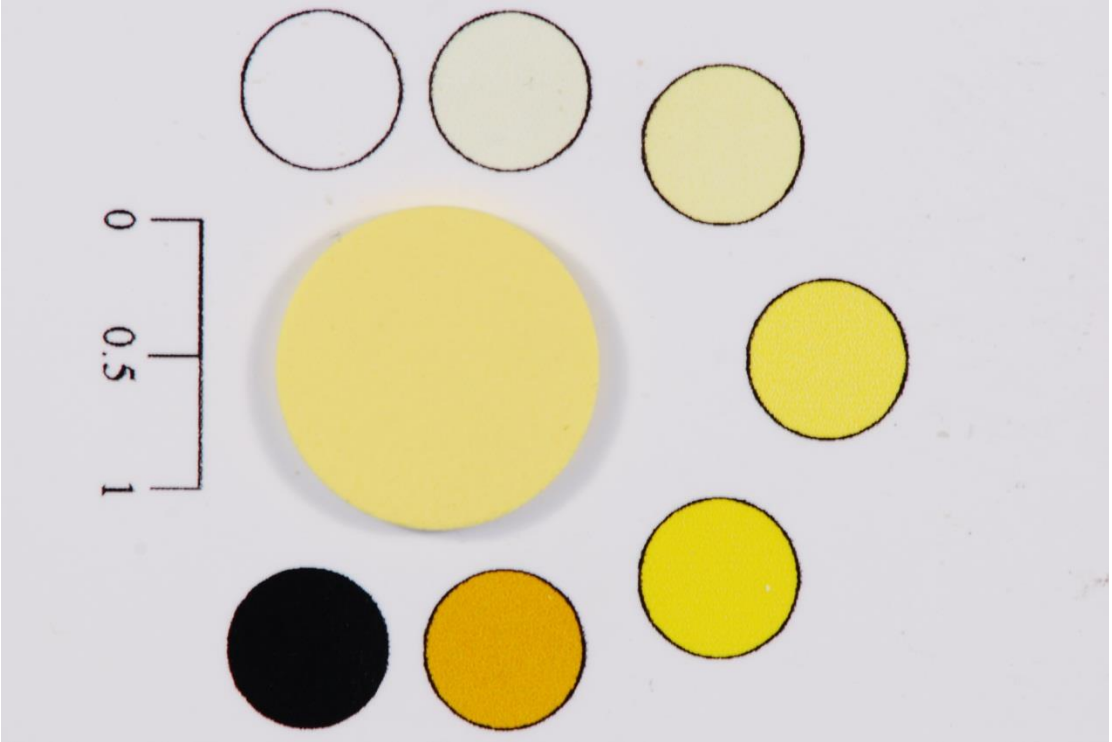

Figure 7.8 A typical photo of yellow pigment pellet (Product No.6: TCF1350)

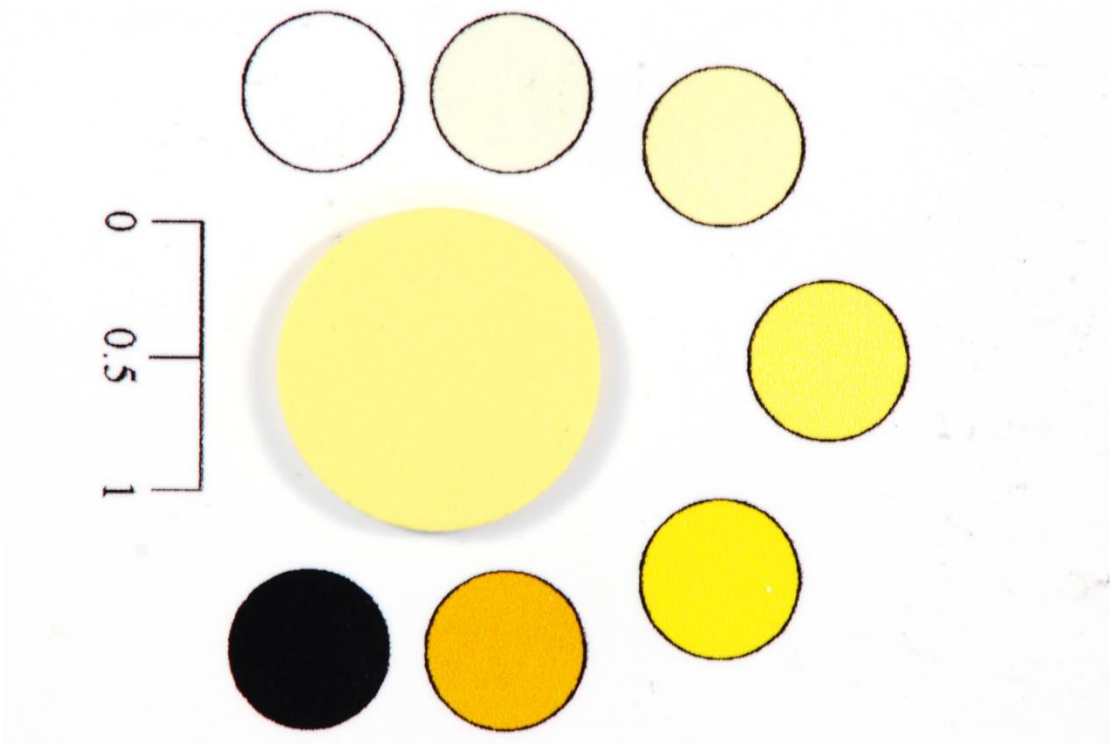

Figure 7.9 Adjusted photo of Figure 7.8 by using Photoshop 7.0 (Product No.6: TCF 1350)

The colour identifying tool of the software was used to gain the RGB value of the pellets following all the required correction being applied. Thus the yellowness of the products was quantified and the comparison among products was carried out. There were 3 pellets prepared and photographed for each kind of sample (22 types of samples and 66 pellets in total) which means 66 original photos and 66 adjusted photos were measured.

7.5.2.2 System Error

The average RGB values (based on the 66 original photos and 66 adjusted photos) of the selected standard colour circles were measured and are shown in Table 7.4 in clockwise order. The second column shows the theoretical RGB value of the 7 circles when editing the background paper before printing. After printing and photographic

processing, the average RGB value (based on 66 original photos) of each circle (third column) was changed due to the printer, ink, photographic condition and camera sensor introduced error in the system. After software adjustment, by correcting the white colour to the standard value (255, 255, 255), the average RGB value (based on 66 adjusted photos) of other colour circles (fourth column) were changed becoming closer to original value as well. Standard yellow which is Yellow 4 in the table shows about (0, -10, +24) deviation compared with the theoretical value.

Table 7.4 RGB value of selected reference colour along with processes employed to observe the colour

Colour	Theoretical RGB Value (Before Printed on paper)	Average RGB Value After Photographing (eg. Figure 7.8)	Average RGB Value After Adjustment (eg. Figure 7.8)
White	255, 255, 255	223±2, 221±1, 225±1	255±0, 255±0, 255±0
Yellow 1	255, 255, 204	223±2, 220±2, 207±2	255±0, 254±1, 232±2
Yellow 2	255, 255, 153	226±1, 220±2, 176±2	255±0, 254±1, 195±3
Yellow 3	255, 255, 102	232±1, 218±1, 89±2	255±0, 252±2, 101±1
Yellow 4 (Standard Yellow)	255, 255, 0	228±1, 211±1, 20±1	255±0, 244±2, 24±2
Yellow 5	204, 153, 0	220±5, 164± 10, 0±0	255±0, 180±3, 0±0
Black	0, 0, 0	9±1, 9±1, 11±2	10±1, 10±1, 12±1

As can be seen in Table 7.4, the measured data was within ±3 range by sampling from 66 photos which means the repeatability and the reliability of the data was very good.

By comparing the average RGB value before and after adjustment, it can be seen that the error can be reduced but cannot be totally eliminated due to each step of the process adding to the error in quantifying the system. The red value was basically corrected to 255, and green was corrected to about 244 - 255 value range. The blue colour still has about +25 shifted values after adjustment.

One aspect taken into consideration was that yellow standard 3 has been changed to 255, 252, 101 which is close to the selected original value of 255, 255, 102. Considering the position of this circle, it indicates the main cause of the error was a light bias across the sample exposure.

7.5.2.3 Results

In order to compare the colour of the products, a photo of each pellet was cut out and put together in the numeric order according to the product system. Comparisons within the same method and between methods were made.

Figure 7.10 shows the comparison among the 6 products which were made by the 'Traditional Method'. It clearly showed that when there was no flux (NaF and NaCl) used in the system, the yellow colour was poorly developed. The colour of products No.1 (TC1350), No.2 (TC1500) and No.3 (TC1650) were closer to white rather than yellow. This indicates that the zircon structure was formed but very few praseodymium (IV) ions replaced the zirconium (IV) ions. According to the RGB

values shown in Table 7.5, it can be seen that the higher sintering temperatures, the closer the colour to yellow. In a pure white to yellow transition the blue value would fall from 255 to 0. In these materials there is a fall in blue content from 230 to 203 depending on the treatment temperature and flux content.

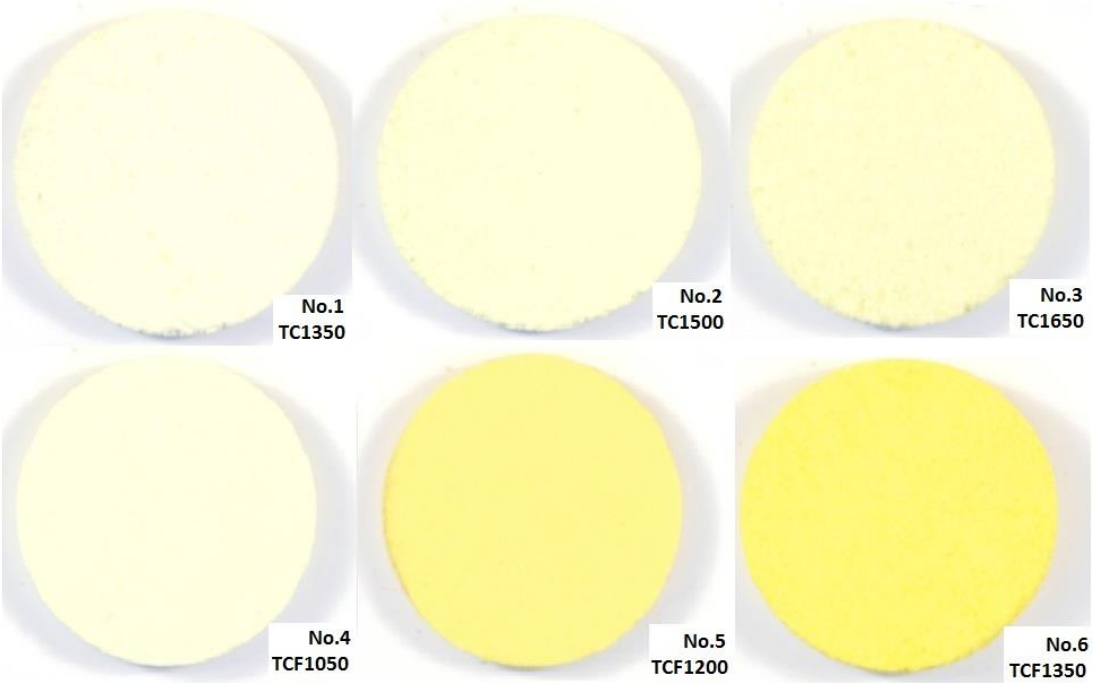

Figure 7.10 Photoshop adjusted photos of product No.1 to No.6 ('Traditional Method')

Scale: disks are 13 mm in diameter

Products No.4 (TCF1050), No.5 (TCF1200) and No.6 (TCF1350) used flux in the system, and it can clearly be seen that a greater yellow value was attained compared to no flux, but again the value increased with sintering temperature (number of blue in RGB value decreasing from about 227 to 115). Product No.6 (TCF1350) was the most yellow material in these products which showed the optimum temperature for this method was shown to be 1350 ℃ as at higher temperatures the materials melted.

Table 7.5 Average RGB value of product No.1 to No.6 (TC and TCF product)

Product	Average RGB Value (After Adjustment)
No. 1 (TC1350)	255±0, 255±0, 230±2
No. 2 (TC1500)	255±0, 255±0, 217±1
No. 3 (TC1650)	255±0, 255±0, 203±2
No. 4 (TCF1050)	255±0, 255±0, 227±1
No. 5 (TC1200)	255±1, 247±2, 142±1
No. 6 (TC1500)	255±0, 247±2, 115±1
Standard Yellow Circle	255±0, 244±2, 24±2

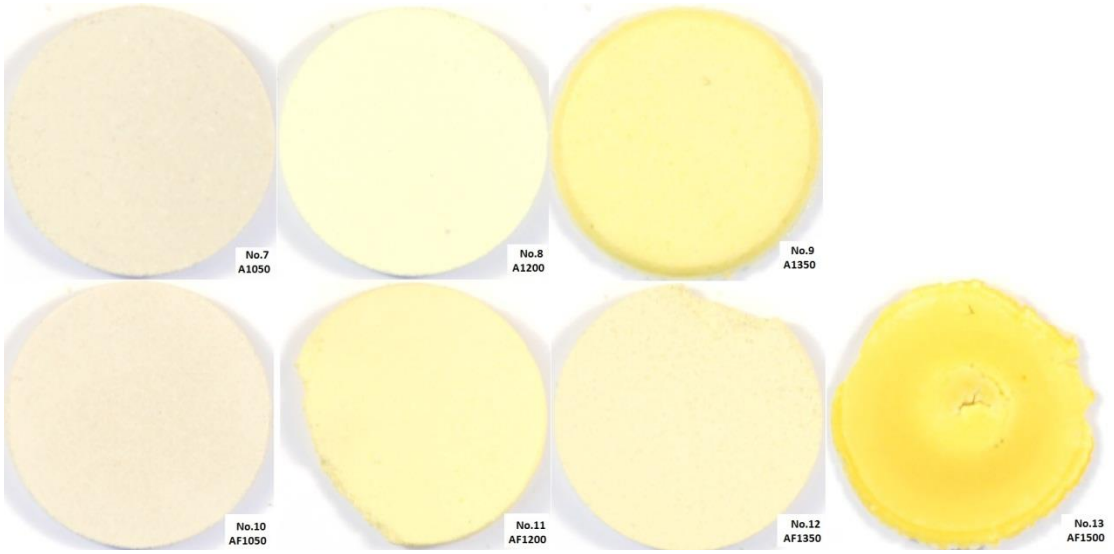

Figure 7.11 Photoshop adjusted photos of product No.7 to No.13 ('Alkali Fusion Method')

Scale: disks are 13 mm in diameter

Figure 7.11 shows the photographs of products No. 7 (A1050) to No. 13 (AF1500) which were produced by the 'Alkali Fusion Method'. By using this method, the samples made without flux (NaF and NaCl) show light yellow colour when sintered at 1200 ℃, 1350 ℃. The figure also indicates that higher sintering temperature generally improves the yellow colour formation regardless of flux content.

Table 7.6 Average RGB value of product No.7 to No.13 (A and AF product)

Product	Average RGB Value
No. 7 (A1050)	246±1, 236±2, 211±3
No. 8 (A1200)	255±0, 255±1, 213±2
No. 9 (A1350)	255±0, 249±2, 170±1
No. 10 (AF1050)	248±2, 236±3, 210±2
No. 11 (AF1200)	255±0, 251±2, 191±1
No. 12 (AF1350)	255±0, 245±2, 199±0
No. 13 (A1500)	255±2, 248±4, 93±4
Standard Yellow Circle	255±0, 244±2, 24±2

Table 7.6 shows that products No.7 (A1050) and No. 10 (AF1050) had a brown tinge, because they had a red value at about 248 and green value at about 236 compared to 255 and 250 in the other samples respectively. This may be due to the raw materials not reacting completely at the relatively low sintering temperature

employed. Some development of yellow when mixed with the grey colour of the raw materials caused the pellet to develop a brown hue.

Figure 7.12 Photoshop adjusted photos of product No.14 to No.22 ('Direct Synthesis Method') Scale: discs are 13 mm in diameter

The optimum condition of making yellow pigments by this method was sintering the raw materials with flux at 1500 ℃ for 3 hours. Sample No.13 (AF1500) has a RGB value of (255, 248, 93) which approached the adjusted standard yellow (255, 244, 24) in value.

Table 7.7 Average RGB value of product No.14 to No.22 (D, DF and DCF product)

Product	Average RGB Value
No. 14 (D1200)	255±0, 255±0, 220±0
No. 15 (D1350)	255±0, 253±1, 193±1
No. 16 (D1500)	255±0, 244±2, 161±2
No. 17 (DF1050)	255±0, 253±1, 204±2
No. 18 (DF1200)	255±0, 246±3, 178±1
No. 19 (DF1350)	255±0, 245±1, 175±3
No. 20 (DF1500)	255±0, 240±2, 95±1
No. 21 (DCF1350)	255±0, 243±2, 172±3
No. 22 (DCF1500)	255±0, 240±1, 137±1
Standard Yellow Circle	255±0, 244±2, 24±2

Figure 7.12 and Table 7.7 shows the details of the 'Direct Synthesis Method' produced yellow pigments. It can be seen that this method can produce yellow colours with and without flux. Samples which used flux were yellower than the ones without flux as the blue values of the DF products were lower than the D products at the same sintering temperature. For example DF1500 has a RGB value of (255, 240, 95) while D1500 has a RGB value of (255, 244, 161). In the same way as the 'Alkali

Fusion Method' products, higher sintering temperature can help with yellow colour formation.

Comparing the RGB values of No.19 (DF1350) to No.21 (DCF1350) and No.20 (DF1500) to No.22 (DCF1500) respectively, the ceramic waste generated zircon and the commercial zircon show similar behaviour. Treated at 1350 ℃, No.19 (DF1350) shows (255, 245, 175) and No.21 (DCF1350) shows (255, 243, 172) which are within the error of the measurement and can be considered to be the same. The ceramic waste generated zircon formed better yellow pigments than the commercial zircon at 1500 ℃ as No.20 (DF1500) and No.22 (DCF1500) have a RGB value of (255, 240 ,95) and (255, 240, 137) respectively. This may be due to the reason that the commercial zircon contains more impurities than the ceramic waste generated zircon (Figure 7.2). Thus, when the materials completely reacted the impurities reduce the yellowness of the sample as they cannot form yellow.

Figure 7.13 Photoshop adjusted photos of product No.5, No. 13 and No.20

Scale: discs are 13 mm in diameter

The most yellow pellet of each synthesis method are compared in Figure 7.13 and the details of the pellets are given in Table 7.8.

Table 7.8 Average RGB value of product No.6, No.13 and No.20

Product	Average RGB Value	Flux	Temperature
No. 6 (TCF1350)	255±0, 247±2, 115±1	Yes	1350 ℃
No. 13(AF1500)	255±2, 248±4, 93±4	Yes	1500 ℃
No. 20 (DF1500)	255±0, 240±2, 95±1	Yes	1500 ℃
Standard Yellow Circle	255±0, 244±2, 24±2		

By comparing these samples, it can be seen that the RGB values were quite similar which means similar quality pigments can be developed by using any of the approaches undertaken. This also suggested that the pigments developed from ceramic waste materials are of equal quality to those using commercial chemicals.

As standard yellow would be (255, 255, 0) in the RGB system, the absence of blue indicates a better yellow. According to the RGB value of the 22 samples, the red and green numbers remained reasonable constant at about 255 and 250 respectively. Thus, the lower the blue value, the more yellow was the sample.

Figure 7.14 shows the blue value of each sample. There were 6 types of raw powders and a line for each is shown. It can clearly be seen that under the same processing method (Traditional, Alkali Fusion, Direct Synthesis), the sample reacted with flux developed better yellow than the one without flux, for example, the DF line is under

the line for samples prefaced with D. The trend for greater yellowness with increasing temperature is also clearly illustrated.

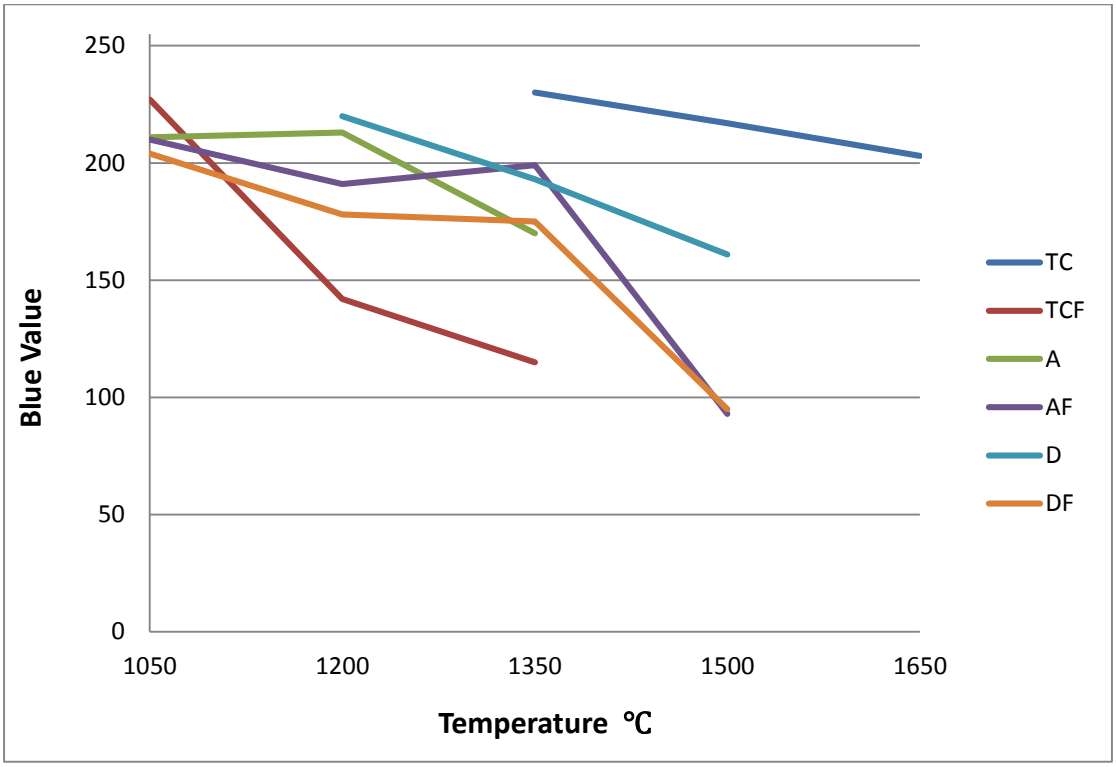

Figure 7.14 Blue values of 22 samples (categorized in 6 powder types)

The yellowest samples in this study have a blue value of about 95 while the adjusted standard yellow shows a blue value at about 24. This means if the photographing error were removed, the real RGB value of the sample should be about (255, 255, 70).

Figure 7.15 shows the software drawn yellow circle of these two RGB values. It can be seen that the sample yellow is very similar to the standard yellow. It is not easy to distinguish the difference by naked eye. This means in terms of chroma, the zircon based yellow pigment which was developed from ceramic waste materials delivered good colour.

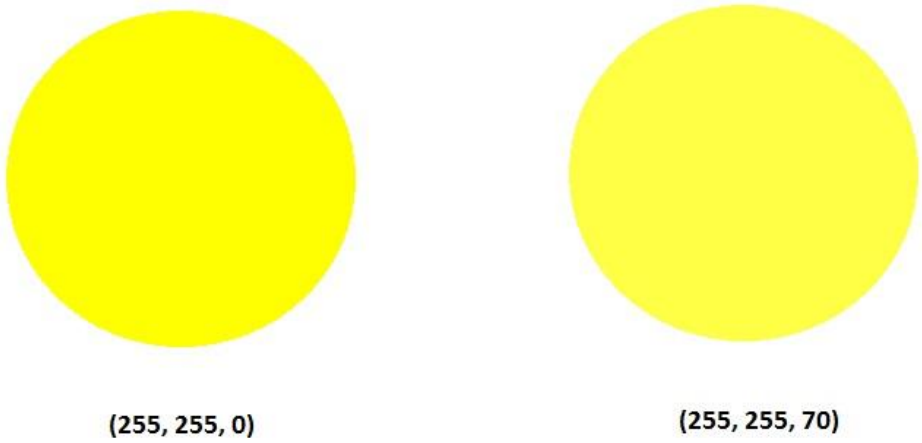

Figure 7.15 Comparison between standard yellow (255, 255, 0) and best sample yellow (255, 255, 70) - No.13 (AF1500) and No.20 (DF1500)

7.5.3 SEM Images

The pigment powders were mounted in resin, polished and observed under secondary electron mode and back scattered electron mode (refer to Section 3.4).

Figure 7.16 shows the SEM image of product No.19 (DF1350). The grey areas are resin and the dark holes are the pores in the resin. It can be seen that different sizes of spherical zircon grains were formed (shown as the bright particles in the second image).

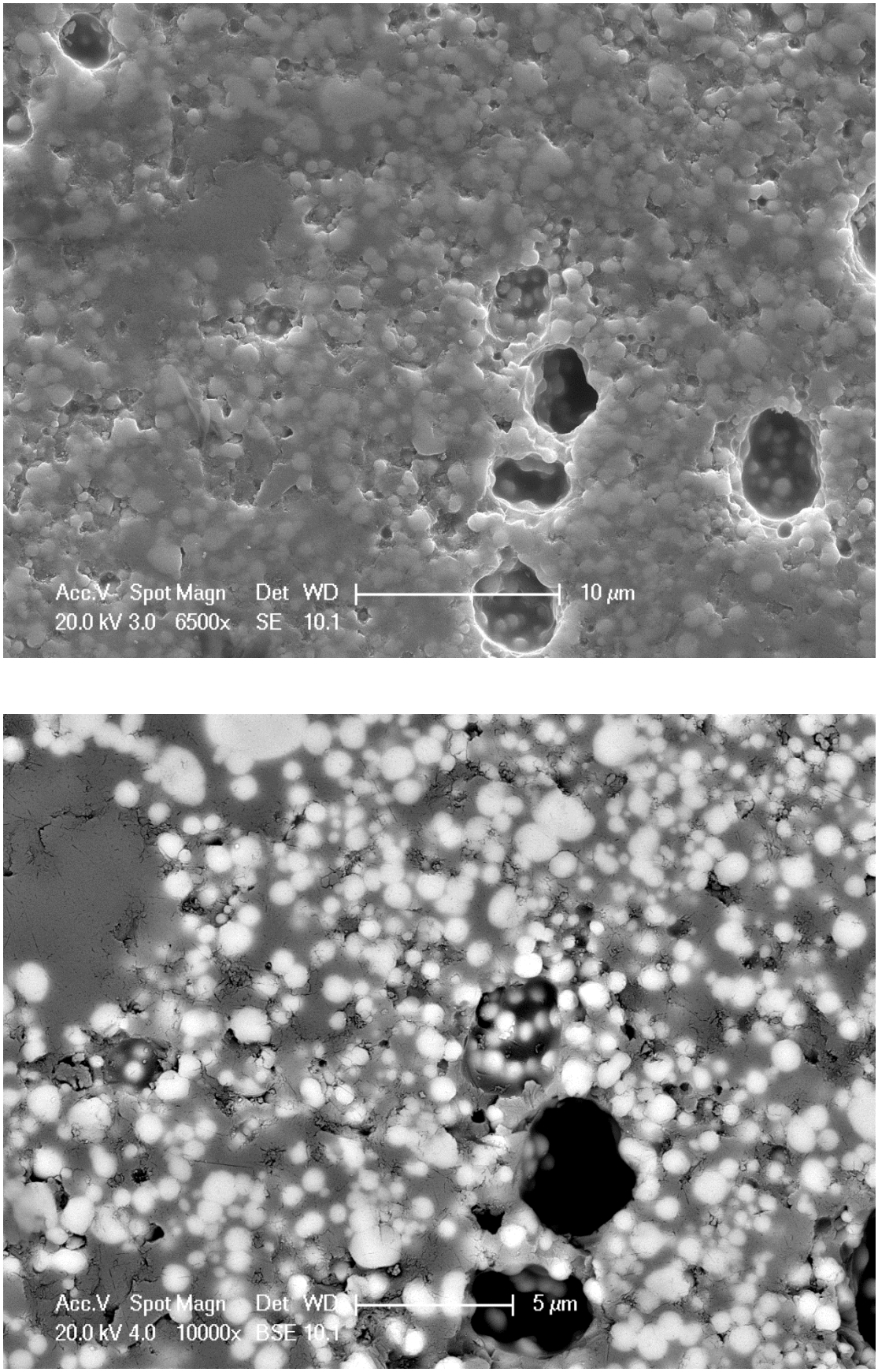

Figure 7.16 SEM image of product No.19 (DF1350) under SE and BSE mode

By horizontally and vertically drawing three lines through the picture and measuring the size of the particles, the mean particle size of sample No.19 (DF1350) can be calculated at 1.6 μm.

CHAPTER VIII CONCLUSIONS AND FUTUREWORK

Feasible processes for recycling foundry ceramic waste materials have been developed. The ceramic waste was successfully converted to either zirconia toughened mullite (ZTM) refractory materials or zircon based yellow pigments by applying a variety of various ceramic processing techniques including: size reduction, purification, shaping and sintering. The phase contents, mechanical properties, thermal characteristics and microstructures of the ZTM products were characterised. The chroma properties of the zircon based pigments were examined by digital correction and quantification. The optimum processing conditions were identified and an understanding of the material formation mechanisms gained.

8.1 Raw Materials

As stated in Section 3.3, the foundry ceramic waste used in this study was a low temperature fired (approximately 900 ℃ – 1200 ℃) ceramic, that was used to form a shell for investment casting. This material had not been through the full casting cycle but had failed during the dewaxing and pre-fire cycle. As a result, the solid pieces had relatively low strength and contamination.

8.2 Pre-Treatment Process

8.2.1 Crushing

In this study the ceramic solid components were crushed by a manual fly press due to the relatively low strength and mass (20 kg) to be processed. This crushing

technique gave a very low sample loss ratio of less than 1 %. However, manual crushing of this type is limited to small scale processing due to its low efficiency and labour intensity. Jaw crushers are widely used for primary crushing applications and would be an ideal alternative for this processing step.

8.2.2 Size Reduction

The primary crushed solids were ground down to powders effectively (from approximately 2.00 mm to 22 µm in 60 seconds for 150 ml powder) in a vibratory disc mill. However, due to the high stress and intensity, this step introduced free and smeared iron to the powder. Although this technique was very efficient, it again required significant manual labour due to the relatively low processing capacity of 150 ml per run.

A vibratory ball mill or conventional ball mill may be alternatives for large volume processing over this size reduction scale and has potential to avoid the issue caused by disc milling. Such machines come in a range of sizes suitable for this grinding duty. In both systems the mill could be lined with a hard ceramic which would prevent contamination. Zirconia media is available in many sizes to suit the mills requirement (220). Although some zirconia will be worn from the media and introduced into the ceramic powder, as the targeted product is zirconia toughened mullite or zircon based pigment, no further processes to remove the added zirconia would be required. However, the vibratory ball mill and conventional ball mills will not be as efficient as the disc mill in terms of size reduction time (68). However in the process

of total manufacture milling is not considered the rate limiting step due to the volumes that could be processed in one batch.

8.2.3 Purification

Magnetic separation significantly reduced the iron content in the milled ceramic powders to approximately 0.18 wt. %. However, the grid wet high intensity magnetic separator used in this study could only process approximately 30 g powder per batch which lead to low efficiency. Continuous wet high intensity separators are available which have the same operating principle but have much higher capacity.

The remaining impurities such as iron, sodium and calcium ions were dissolved in a 5 % H_2SO_4 solution for 8 hours. A titration method for Fe^{2+} concentration analysis confirmed 99.7 % of the remaining iron contamination was removed. However, there were difficulties in calculating the accurate kinetic constant of the leaching process due to the errors which were mainly the result of the low concentration of the solution. Increasing the leaching volume and repeating a number of times would reduce the error to give accurate kinetic data for modelling the process. Acid washing reactors are well documented in the literature and scale-up of this process would be possible (221).

A proposed flowchart of the pre-treatment and preparation of a sub 20 micron feed powder for ceramics and pigments fabrication is given in Figure 8.1.

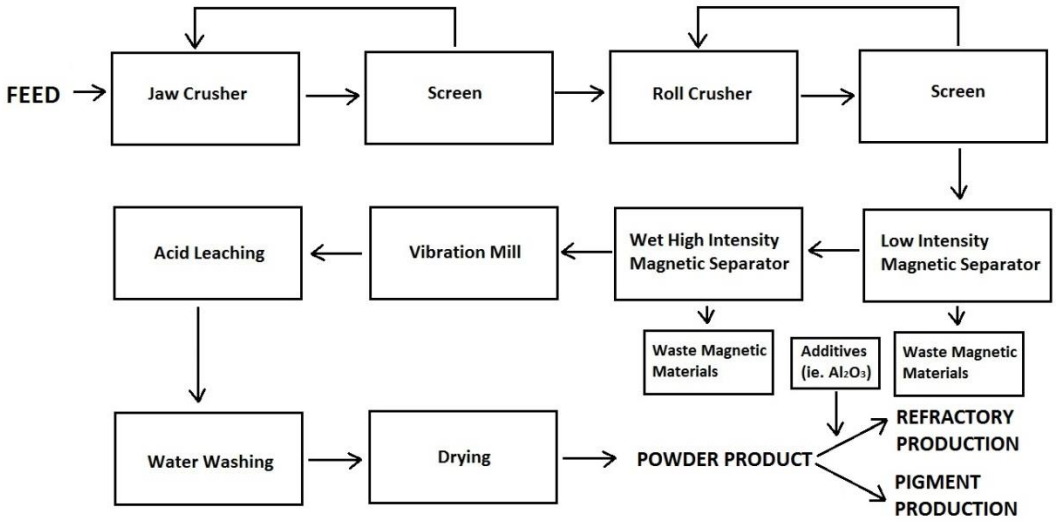

Figure 8.1 Flowchart of pre-treatment process for large scale processing

8.3 Refractory Development

8.3.1 Powder Formulation, Milling and Mixing

Accurate composition of the cleaned ceramic waste was gained by combining X-ray diffraction and X-ray fluorescence analysis. 2.351 g Al_2O_3 was added to every 10 g ceramic waste (19.03 wt. % Al_2O_3 and 80.97 wt. % ceramic waste) to give the desired final composition of 70 wt. % mullite and 30 wt. % zirconia.

It was found that attrition milling could effectively reduce the particle size of the mixture from approximately 22 µm to 1 µm in 8 hours. A ball mill was used for testing the effects of different milling fluids post attrition milling. It was found that the isopropanol processed powder had fewer and smaller agglomerates than the water processed material.

8.3.2 Paste Formulation

A water based paste and an organic based paste were developed for the extrusion process. Due to the low volatilisation rate of the chemicals, it was found the operation of water based paste system was easier and more accurate. The water based extrudates with 5 mm thickness were dried in a room environment in 24 hours, without cracking.

The organic based paste could not be dried successfully in thick sections (>1mm), and even thin section components required very controlled conditions for successful drying (15 ℃ and 70 % humidity for 48 hours).

8.3.3 Ceramic Shaping

Dry pressing and extrusion were used to form tablets and rods respectively. To form a stable green pellet that could be handled without damage, a stress of 50 MPa was required. It was found that the dry pressed samples had higher green density compared to extruded materials due to the higher applied stress. This difference between the compacted and extruded products may have contributes to the observed differences in the final properties of the ceramics.

8.3.4 Sintering

Three different sintering temperatures (1540 ℃, 1600 ℃ and 1685 ℃) were tested and the optimum condition identified as 1600 ℃. The 1600 ℃ product had better mechanical properties and less microstructural defects, with the materials processed

at lower temperatures being lower in density and not fully converted to ZTM and those processed at higher temperatures being over sintered and suffering from grain growth and micro cracking. It was found that the temperature ramp rate (3 °C·min^{-1}, 10 °C·min^{-1}) did not affect the properties of the final products. Firing on a zirconia setting powder significantly reduced the cracks developed on the sample edges as it gave a more even heat transfer.

8.3.5 Phase Contents

Phase content of the refractory samples was analysed by X-ray diffraction. Zircon, alumina, mullite and zirconia were all found in samples sintered at 1540 ℃ indicating the reactions of zircon dissociation and mullite formation were not fully complete. In samples sintered at 1600 ℃ and 1685 ℃, only mullite and zirconia were detected which suggested the materials were completely reacted and the desired composition of the final product was achieved.

8.3.6 Thermal Behaviour

The thermal behaviour of the green samples was evaluated using differential scanning calorimetry (DSC) and dilatometry. These materials reflected the reaction behaviour during the sintering process. The zircon dissociation and mullite formation were identified as occurring at the same time. It was also found that presence of the amorphous silica in the waste and greater compaction can both slightly enhance the intensity and speed of the reaction. The DSC data also showed that an addition of yttria significantly lowered the reaction temperature.

A dilatometer was also used to examine the thermal properties of the sintered samples. The monoclinic to tetragonal zirconia phase transformation was identified in all the ZTM products. The linear shrinkage data indicated that approximately 74 % of the zirconia was in a transformable tetragonal form and 26 % was monoclinic. An addition which would yield a 6 wt. % Y_2O_3 stabilised zirconia assuming full partitioning showed all the resultant zirconia to be non-transformable.

The linear thermal expansion coefficient over the temperature range from 20 °C to 1540 °C was calculated based on the dilatometry data. The ZTM materials developed from the ceramic waste had coefficient values ranging from 2.57 x 10^{-6} to 2.96 x 10^{-6} with about 2 % error which correlated well with literature value (24, 207).

Thermal shock resistance analysis showed that the ZTM material can retain its original, half and a third of the flexural strength with a ΔT of 200 °C, 700 °C and 1200 °C respectively. Again this is in good agreement with the literature (37, 216).

The low thermal expansion behaviour and high thermal shock resistance is considered to be of benefit in the potential applications of the ZTM products.

8.3.7 Microstructure

The densification ratio of the ZTM materials ranged from approximately 93 % to 98 %. The relatively high density microstructure provided good strength and hardness properties and the small amount of residual pores may also have improved the toughness of the material provided the structure is able to maintain the tetragonal phase of the zirconia at the same time (in a transformable form).

The detailed microstructures of the samples were observed by scanning electron microscopy. In all ZTM specimens, both intragranular and intergranular zirconia grains were found evenly distributed in the mullite matrix. The intergranular zirconia particles linked the lath-like mullite grains together to form a relatively dense and homogenous microstructure.

It was found that the sintering temperature significantly affected the morphology of the material. The intergranular and intragranular zirconia grains in 1600 °C sintered products were both spherical and had an average size of 1.6 μm and 0.9 μm respectively. However, in 1685 °C sintered samples, the zirconia and mullite grains both grew to a much larger size and some cracks were developed due to the zirconia transitions on cooling. The zirconia grains were more elongated and irregular in samples heat treated at 1540 °C. Under this treatment a glass phase containing Al, Si, Zr and O was found surrounding the zirconia particles which indicated the incomplete reaction of the starting powders.

The small amount of amorphous silica in the raw material may have assisted the formation of mullite and intragranular zirconia. It may also have improved the evenness of the distributed zirconia grains to yield a more homogenous microstructure. It was found that processing in isopropanol significantly reduced the agglomerates in the powder and thus prevented pore development in the structure. The higher compaction rate also improved the microstructure by helping the distribution of the zirconia particles.

Yttria appeared to change the distribution of the zirconia in the sintered product, probably by changing the intermediate glass behaviour during the reaction which caused the intergranular zirconia to form a string-like structure. This structure was less homogenous and lead to more defects and reduced properties.

8.3.8 Mechanical Properties

The mechanical behaviour of the samples was characterised by flexural strength, hardness and flexural toughness. It was found that the intermediate grain sized products with fewer pores and more homogeneous micro-structure had enhanced flexural strength and hardness. However, the lower density and more porous specimens were found to have higher toughness.

The refractory materials developed in this study had the following properties when the process was optimised: 350 MPa flexural strength, 10.4 GPa hardness, 6.12 $MPam^{1/2}$ toughness (by indentation), 2.70 x 10^{-6} $°C^{-1}$ linear coefficient and 35 % remnant strength at a ΔT of 1200 °C thermal shock. In most cases these values slightly exceed the properties of zirconia toughened mullite made by other methods (28, 38, 39, 205, 206, 208, 213).

8.4 Pigment Development

8.4.1 Alumina Elimination

The alumina content, a remnant of the refractory composition, was completely removed by solid state reaction with $K_2S_2O_7$ at 650 °C. This process was very

effective and simple to apply but energy intensive. An energy efficient alternative method could be alkali leaching, but it may be time consuming and not give such complete alumina removal as the $K_2S_2O_7$ process.

8.4.2 Processing Routes

Dissociation-synthesis methods were used in this study to form zircon based yellow pigments. The plasma dissociation method would have been more efficient and simpler than alkali dissociation approach but could not be applied effectively with the available equipment. Large scale raw material processing can be easily achieved by plasma dissociation without consuming other chemicals. The required plasma system is very specialised and for the low volumes of waste that would be processed from a foundry supply chain the chemical route is probably more favourable.

In this study, a direct sintering method was developed by the author. It was found the direct sintering route could produce yellows of equal intensity to the alkali fusion method but using a much simpler approach.

8.4.3 Chroma Properties

The chroma data of the developed yellow colour samples were obtained by digital filming, correction and quantification. During this process, about 10 % error was introduced in the system due to the light conditions and limitation of the equipment and process.

Using the optimal amount of flux and increasing the sintering temperature significantly improved the formation of yellow colour. The yellowest pigments with

same RGB value (approximately 255, 242, 93) as that produced by the traditional route, were possible from the reclamation of ceramic waste by alkali dissociation and direct sintering routes.

8.5 Future Work

Although ceramic waste materials were developed into ZTM refractory materials with high strength, hardness, thermal shock resistance and low thermal expansion, more work for further development is suggested in the following areas:

(i) The products produced in this work were manufactured on a very limited scale and for a full analysis a larger scale study would be required. This would enable the costs of such treatment and manufacturing routes to be determined. It will be important to recognise the influences of contaminants in the feed stream and to consider if the technologies could be broadened to a wider spectrum of waste streams being produced in the investment casting industry.

(ii) Miranzo et al. reveal that additives may improve the properties of ZTM composites (35). Thus, the influence of various additives such as CaO, MgO, TiO_2 or an excess amount of Al_2O_3 should be investigated in order to improve the properties of the final products.

(iii) The high temperature mechanical properties of the products should be investigated further. For this, it may be necessary to process the materials by other ceramic methods such as slip casting in order to provide the required shapes for industry.

(iv) Extrusion was only evaluated on a limited scale in this study and thus it is suggested that future studies are undertaken to more fully understand the properties of the pastes and the manufacture of useful shapes such as tubes.

(v) The reaction mechanism of the system, including zircon dissociation and mullite formation, should be investigated more thoroughly, possibly by a quenching technique combining with quantitative X-ray diffraction analysis.

A lattice type of zircon based yellow pigments was also developed, but future work could be undertaken in the following areas:

(i) Other colours of lattice type zircon based pigments, for example vanadium blue or iron pink, could be developed.

(ii) The feasibility of developing encapsulated type pigments such as Cd-Se red should be attempted.

(iii) Other colour definitive measurement method should be developed.

REFERENCES

1. Hung Y-T, Wang LK, Shammas NK, editors. Handbook of environment and waste management. Volume 2, Land and groundwater pollution control. New Jersey: World Scientific; 2014. Chapter 7, p.492-498.
2. Westlake K. Landfill waste pollution and control. Cambridge: Woodhead Publishing; 2013. Chapter 1, p.1-6. Chapter 6, p. 109-111.
3. Zanetti MC, Fiore S. Foundry waste recycling in moulding operations and in the ceramic industry. Waste Manag Res. 2003;21(3):235.
4. Schneider H, Komarneni S, editors. Mullite. 1 ed. Weinheim: Wiley VCH; 2005. Chapter 7, p. 397-467.
5. Zhao S-k, Huang Y, Wang C-a, Huang X-x, Guo J-k. Mullite formation from reaction sintering of $ZrSiO_4$/α-Al_2O_3 mixtures. Materials Letters. 2003;57(11):1716-22.
6. Carter CB, Norton MG. Ceramic materials: science and engineering. 2 ed. New York: Springer; 2013. Chapter 32, p.600-602.
7. Beeley PR. Foundry technology. 2nd ed. ed. Oxford: Butterworth-Heinemann; 2001. Chapter 1, p.27-30.
8. Woolley GR, Goumans JJJM, Wainwright PJ, editors. Waste materials in construction: science and engineering of recycling for environmental protection. International Conference on The Science and Engineering of Recycling for Environmental Protection; 2000. p. 805-821; Harrogate: Elsevier.
9. Maria CS. A study of foundry waste material. Wisconsin: University of Wisconsin--Madison; 1974. Chapter 1, p.2-7.
10. Twong DL. Waste management study of foundaries major waste streams: Phase I. Illinois: Waste Management and Research Center, 1992. p.4-23.
11. Gabriela P, Joel Barbujiani S. Waste foundry sand: Environmental implication and characterization. Geologia USP : Série Científica. 2012;12(3):57-70.
12. Guney Y, Sari YD, Yalcin M, Tuncan A, Donmez S. Re-usage of waste foundry sand in high-strength concrete. Waste Management. 2010;30(8):1705-13.
13. Beeley PR, Smart RF. Investment casting. Oxford: David Brown Book Company; 2008. p22-105.
14. Bidwell HT. Investment casting handbook. Dallas, Tex.: Investment Casting Institute; 1997. p273-290.
15. Leyland S, Smith I. Implementation of a water based shell mould investment casting process (replacement of an ethyl silicate process): Rolls-Royce plc; 1997.Chapter 1, p. 1-10.
16. Schacht CA. Refractories handbook. New York ; [London]: Marcel Dekker; 2004.
17. Lohan B. International refractories handbook & directory. [1980]. [2nd ed.]. London (5 Pond St., NW3 2PN): London and Sheffield Publishing Co. Ltd; 1980. p.66-78.
18. Minnis C. Zirconia. New York, N.Y.: Fence Books; 2001. p.34-40.
19. Cain MG. Zirconia toughened ceramics. [electronic resource]: University of Warwick; 1990. Chapter 1, p.1-8.
20. Alper AM. High Temperature Oxides: Oxides of Rare Earths, Titanium, Zirconium, Hafnium, Niobium and Tantalum: Elsevier Science; 2013.Chapter 5, p.167-188.
21. Schneider H, Fischer RX, Schreuer J. Mullite: Crystal Structure and Related Properties. Journal of the American Ceramic Society. 2015;98(10):2948-67.
22. Schneider H, Eberhard E. Thermal Expansion of Mullite. Journal of the American Ceramic Society. 1990;73(7):2073-6.
23. Yamade Y, Kawaguchi Y, Takeda N, Kishi T. Slow Crack Growth of Mullite Ceramics. Journal of the Ceramic Society of Japan. 1991;99(1150):467-71.

24. Hemra K, Aungkavattana P. Effect of zirconia content on mechanical and thermal properties of mullitezirconia composite. Advances in Applied Ceramics. 2014;113(6):323-7.
25. Prochazka S, Wallace J, Claussen N. Microstructure of Sintered Mullite-Zirconia Composites. Journal of the American Ceramic Society. 1983;66:C.
26. Zanelli C, Dondi M, Raimondo M, Guarini G. Phase composition of alumina–mullite–zirconia refractory materials. Journal of the European Ceramic Society. 2010;30(1):29-35.
27. Rupo E, Gilbart E, Carruthers T, Brook R. Reaction hot-pressing of zircon-alumina mixtures. Journal of Materials Science. 1979;14(3):705-11.
28. Claussen N, Jahn J. Mechanical Properties of Sintered, In Situ ‐ Reacted Mullite ‐ Zirconia Composites. Journal of the American Ceramic Society. 1980;63(3 ‐ 4):228-9.
29. Rodrigo PDD, Boch P. High purity mullite ceramics by reaction sintering. International Journal of High Technology Ceramics. 1985;1(1):3-30.
30. Rupo E, Anseau M. Solid state reactions in the $ZrO_2 \cdot SiO_2$ - αAl_2O_3 system. Journal of Materials Science. 1980;15(1):114-8.
31. Boch P, Giry JP. Preparation and properties of reaction-sintered mullite-ZrO 2 ceramics. Materials Science and Engineering. 1985;71:39-48.
32. Tiwari L, Mishra S, Kumar D, Sinha RK. Reaction Sintering Behaviour of Alumina-Zircon System. Transactions of the Indian Ceramic Society. 2001;60(3):130-6.
33. Koyama T, Hayashi S, Yasumori A, Okada K. Preparation and characterization of mullite-zirconia composites from various starting materials. Journal of the European Ceramic Society. 1994;14(4):295-302.
34. Degtyareva É, Romaniv O, Gud O, Fedoruk R, Khmelenko T. Effect of the type of mullite and certain additives on the sintering process of mullite-zircon specimens. Refractories. 1988;29(7):457-62.
35. Miranzo P, Pena P, Moya J, Aza S. Multicomponent toughened ceramic materials obtained by reaction sintering. Journal of Materials Science. 1985;20(8):2702-10.
36. Torrecillas R. Thermomechanical behavior of mullite. Acta Materialia. 1997;45(3):897-906.
37. Orange G, Fantozzi G, Cambier F, Leblud C, Anseau M, Leriche A. High temperature mechanical properties of reaction-sintered mullite/zirconia and mullite/alumina/zirconia composites. Journal of Materials Science. 1985;20(7):2533-40.
38. Koyama T, Hayashi S, Yasumori A, Okada K, Schmucker M, Schneider H. Microstructure and mechanical properties of mullite/zirconia composites prepared from alumina and zircon under various firing conditions. Journal of the European Ceramic Society. 1996;16(2):231-7.
39. Lathabai S, Hay DG. Reaction-bonded mullite/zirconia composites. Journal of the American Ceramic Society. 1996;79(1):248-56.
40. Eastaugh N, Walsh V, Chaplin T. Pigment Compendium: A Dictionary and Optical Microscopy of Historical Pigments: Butterworth-Heinemann; 2008. p3-6.
41. Jiang D, Zeng Y, Singh M, Heinrich J. Ceramic Materials and Components for Energy and Environmental Applications: Ceramic Transactions: Wiley; 2010. p.65-70.
42. Rosslere D. Developments in Ceramic Materials Research: Nova Science Publishers; 2007. Chapter 9, p.261-277.
43. Dimitrov T. Synthesis and structure of zircon-based ceramic pigments containing Mn, Co, and Ni AS chromophoric elements. Glass and Ceramics. 2011;67(11):383-5.
44. Eppler RA. Glazes and glass coatings. In: Eppler DR, editor. Westerville, OH: American Ceramic Society; 2000. p34-40.
45. Eppler RA. Mechanism of Formation of Zircon Stains. Journal of the American Ceramic Society. 1970;53(8):457-62.
46. Trojan M. Synthesis of a blue zircon pigment. Dyes and Pigments. 1988;9(3):221-32.

47. Trojan M. Synthesis of a yellow zircon pigment. Dyes and Pigments. 1988;9(4):261-73.
48. Ozel E, Turan S. Production of coloured zircon pigments from zircon. Journal of the European Ceramic Society. 2007;27(2):1751-7.
49. Cao Kun-Wu. Synthesis and Characterization of Pr-$ZrSiO_4$ Pigment by a Two-step Method. Journal of Inorganic Materials.27(9):984-90.
50. Minnaar EG, Neethling JH, Lee ME, Snyders E. Microstructural and analytical analysis of plasma dissociated zircon. Journal of Physics: Conference Series. 2012;371(1):012041.
51. Wong A, McPherson R. The structure of plasma dissociated zircon. Journal of Materials Science. 1981;16(6):1732-5.
52. McPherson R, Shafer BV. Microstructure of plasma dissociated zircon. Micron (1969). 1982;13(3):279-80.
53. Evans A, Williamson J. Composition and microstructure of dissociated zircon produced in a plasma furnace. Journal of Materials Science. 1977;12(4):779-90.
54. Snyders E, Potgieter JH, Nel JT. The effect of milling and percentage dissociation of plasma dissociated zircon on the colour of Pr-yellow and V-blue zircon pigments. Journal of the European Ceramic Society. 2006;26(9):1599-603.
55. Garcia A, Llusar M, Badenes J, Tena MA, Monrós G. Encapsulation of Hematite in Zircon by Microemulsion and Sol-Gel Methods. Journal of Sol-Gel Science and Technology. 2003;27(3):267-75.
56. Tu H, Duan T, Ding Y, Lu X, Tang Y. Phase and microstructural evolutions of the CeO2–ZrO2–SiO2 system synthesized by the sol–gel process. Ceramics International. 2015;41(6):8046-50.
57. Badenes J, Vicent J, Llusar M, Tena M, Monr G. The nature of Pr-ZrSiO 4 yellow ceramic pigment. Journal of Materials Science. 2002;37(7):1413-20.
58. Demiray T, Nath DK, Hummel FA. Zircon - Vanadium Blue Pigment. Journal of the American Ceramic Society. 1970;53(1):1-4.
59. Lei B, Qin W, Kang G, Peng C, Wu J. Modeling and evaluation for encapsulation efficiency of zircon-based heteromorphic encapsulation pigments. Dyes and Pigments. 2014;112:245-54.
60. Liu H, Dai W, Wang H, Zeng L, Wang Y. Study on the preparation of the CdS_xSe_{1-x} - ZrSiO 4 red ceramic pigments and its properties. Journal of Sol-Gel Science and Technology. 2015;75(1):198-205.
61. Gupta A, Yan DS. Mineral Processing Design and Operation: An Introduction: Elsevier Science; 2006. Chapter 2, p.32-61.
62. Wills BA, Hopkins DW. Mineral Processing Technology: An Introduction to the Practical Aspects of Ore Treatment and Mineral Recovery (In SI/Metric Units): Elsevier Science; 2013. Chapter 4, p.96-132.
63. Co. WCF. Fly presses and screw presses 2003 [cited 2012 Jun 06]. Available from: http://www.flypress.com/.
64. Bhandari VB. Design of Machine Elements: Tata McGraw-Hill; 2010, Chapter 6, p.184-217.
65. Black BJ. Workshop Processes, Practices and Materials: Taylor & Francis; 2015. Chapter 16, p.261-289.
66. Bawa HS. Manufacturing Processes - II: McGraw-Hill Education (India) Pvt Limited; 2004, Chapter 7, p.115-129.
67. Retsch. Size reduction with disc mills and mortar grinders [cited 2012 Jul 08]. Available from: http://www.retsch.com/products/milling/disc-mills/rs-200/.
68. Retsch. Retsch vibratory disc mill RS 200 2011 [cited 2012 July 09]. Available from: https://www.youtube.com/watch?v=rZWPz1oappA.

69. Boulton. Vibro-Energy Ultra-fine wet grinding mills [cited 2014 Mar 30]. Available from: http://williamboulton.co.uk/wp-content/uploads/2015/08/AM-AH-Range-Ultra-Fine-Wet-Grinding-Mills.pdf.
70. Lynch AJ, Rowland CA. The History of Grinding: Society for Mining, Metallurgy, and Exploration; 2005. Chapter 7, p.95-132.
71. Shin H, Lee S, Suk Jung H, Kim J-B. Effect of ball size and powder loading on the milling efficiency of a laboratory-scale wet ball mill. Ceramics International. 2013;39(8):8963-8.
72. Ferrari R. Handbook for Ball Mill Grinding: Description, Maintenance, Practice, Controls of Ball Mills to be Used for Grinding Industrial Products as: Faenza Editrice; 1985. p. 56 -77.
73. Patel VK. Analysis of Ball Mill: Lap Lambert Academic Publishing GmbH KG; 2013. p. 82-95.
74. Xiao Q, Kang H, Li B, Luo C. Optimization Study to the Ratio of Primeval Ball Loading in ϕ4.0 × 6.0 m Overflow Ball Mill of Yingezhuang Gold Mine. AASRI Procedia. 2014;7:14-9.
75. Mankosa MJ, Adel GT, Yoon RH. Effect of media size in stirred ball mill grinding of coal. Powder Technology. 1986;49(1):75-82.
76. Katubilwa FM, Moys MH. Effect of ball size distribution on milling rate. Minerals Engineering. 2009;22(15):1283-8.
77. Zhou L, Zhang H, Zhang Z. Homogeneous nanoparticle dispersion prepared with impurity-free dispersant by the ball mill technique. Particuology. 2013;11(4):441-7.
78. Fuerstenau MC, Han KN. Principles of Mineral Processing: Society for Mining, Metallurgy, and Exploration; 2003. Chapter 3, p. 61-114.
79. Mular AL, Halbe DN, Barratt DJ. Mineral Processing Plant Design, Practice, and Control Proceedings: Society for Mining, Metallurgy, and Exploration; 2002. Chapter 5, p.566-605.
80. Salman AD, Ghadiri M, Hounslow M. Particle Breakage: Elsevier Science; 2007. Chapter 2, p.487-508.
81. Neikov OD, Murashova IB, Yefimov NA, Naboychenko S, Mourachova IB, Gopienko VG, et al. Handbook of Non-Ferrous Metal Powders: Technologies and Applications: Elsevier Science; 2009, Chapter 2, p.58-59.
82. UnionProcess. Choose the right grinding mill 2010 [cited 2013 Sep 22]. Available from: http://www.unionprocess.com/tech_papers/ChooseTheRightGrindingMill.pdf.
83. Shinohara K, Golman B, Uchiyama T, Otani M. Fine-grinding characteristics of hard materials by attrition mill. Powder Technology. 1999;103(3):292-6.
84. Sadler LY, Stanley DA, Brooks DR. Attrition mill operating characteristics. Powder Technology. 1975;12(1):19-28.
85. Badmus A, Raji A, Akinoso R. Effect of Process Parameters on Work Index, Milling Efficiency and Some Technological Properties of Yam Flour Using Attrition Mill. An International Journal. 2013;6(1):160-8.
86. Greenwood R, Rowson N, Kingman S, Brown G. A new method for determining the optimum dispersant concentration in aqueous grinding. Powder Technology. 2002;123(2):199-207.
87. Park J, Jeong Y, Yang J, Jung M. Grinding time for control of the size fraction of products in the attrition milling. Korean Journal of Chemical Engineering. 1998;15(4):375-80.
88. Fuerstenau MC, Han KN. Principles of Mineral Processing: Society for Mining, Metallurgy, and Exploration; 2003.
89. Svoboda J. Magnetic Techniques for the Treatment of Materials: Springer Netherlands; 2007. Chapter 1, p. 1-10.
90. Masuda H, Higashitani K, Yoshida H. Powder Technology: Handling and Operations, Process Instrumentation, and Working Hazards: CRC Press; 2006. Chapter 1, p 161 - 173.

91. Fraas F, Mines USBo. Magnetic separation of minerals of low susceptibility and small particle size: U.S. Dept. of the Interior, Bureau of Mines; 1969, p. 1-14.
92. Sheridan R, Jordens A, Waters K, Rowson N. Processing a rare earth mineral deposit using gravity and magnetic separation. Minerals Engineering. 2014;62:9-18.
93. Robinson WD. The Solid Waste Handbook: A Practical Guide: Wiley; 1986. Chapter 11, p. 388-403.
94. Gerber R. High gradient magnetic separation In: Birss RR, editor. Chichester

New York: Research Studies Press; 1983.p. 192-200.
95. Guide. KP. Magnetic separators 2013 [cited 2015 Apr 05]. Available from: http://www.kanetec.co.jp/en/pdf/120_138.pdf.
96. Gupta CK, Mukherjee TK. Hydrometallurgy in Extraction Processes: Taylor & Francis; 1990. Chapter 1, p.39-47.
97. Gupta CK. Extractive Metallurgy of Molybdenum: Taylor & Francis; 1992. Chapter 3, p.151-173.
98. Young CA, Taylor PR, Anderson CG. Hydrometallurgy 2008: Proceedings of the Sixth International Symposium: Society for Mining, Metallurgy, and Exploration; 2008. Chapter 4, p.906-911.
99. Rogozhnikov D, Mamyachenkov S, Karelov S, Anisimova O. Nitric acid leaching of polymetallic middlings of concentration. Russian Journal of Non-Ferrous Metals. 2013;54(6):440-2.
100. Malhotra D, Taylor P, Spiller E, LeVier M. Recent Advances in Mineral Processing Plant Design: Society for Mining, Metallurgy, & Exploration; 2009. Chapter 4, p. 140-154.
101. Abdel-Aal EA. Kinetics of sulphuric acid leaching of lowgrade zinc silicate ore. Hydrometallurgy. 2000;55 (3):247–54.
102. Massaci P, Recinella M, Piga L. Factorial experiments for selective leaching of zinc sulphide in ferric sulphate media. International Journal of Mineral Processing. 1998;53:213-24.
103. Terry B, Monhemius A. Acid dissolution of willemite (Zn, $Mn)_2SiO_4$ and hemimorphite ($Zn_4Si_2O_7(OH)_2H_2O$). Metallurgical Transactions B. 1983;14(3):335-46.
104. Bodas MG. Hydrometallurgical treatment of zinc silicate ore from Thailand. Hydrometallurgy. 1996;40 (1–2):37-49.
105. Levenspiel O. Chemical reaction engineering: Wiley; 1999. p.453-455.
106. Kalinkin AM, Kalinkina EV. Modelling of the sulfuric acid leaching of mechanically activated titanite. Hydrometallurgy. 2011;108(3):189-94.
107. Bengisu M. Engineering Ceramics: Springer; 2001. Chapter 3, p. 125-127.
108. Shackelford JF, Doremus RH. Ceramic and Glass Materials: Structure, Properties and Processing: Springer US; 2008.
109. Riedel R, Chen IW. Ceramics Science and Technology, Synthesis and Processing: Wiley; 2011. Chapter 1, p.3-34.
110. Zhu X, Lü Z, Wei B, Huang X, Zhang Y, Su W. A symmetrical solid oxide fuel cell prepared by dry-pressing and impregnating methods. Journal of Power Sources. 2011;196(2):729-33.
111. Aminzare M, Golestani-fard F, Guillon O, Mazaheri M, Rezaie HR. Sintering behavior of an ultrafine alumina powder shaped by pressure filtration and dry pressing. Materials Science & Engineering A. 2010;527(16):3807-12.
112. Denny PJ. Compaction equations: a comparison of the Heckel and Kawakita equations. Powder Technology. 2002;127(2):162-72.
113. Sonnergaard JM. A critical evaluation of the Heckel equation. International Journal of Pharmaceutics. 1999;193(1):63-71.
114. Ilkka J, Paronen P. Prediction of the compression behaviour of powder mixtures by the Heckel equation. International Journal of Pharmaceutics. 1993;94(1):181-7.

115. Nordström J, Klevan I, Alderborn G. A particle rearrangement index based on the Kawakita powder compression equation. Journal of Pharmaceutical Sciences. 2009;98(3):1053-63.
116. Händle F. Extrusion in Ceramics: Springer Berlin Heidelberg; 2009. Chapter 2, p.13-30.
117. Rice RW. Ceramic Fabrication Technology: CRC Press; 2002. Chapter 4, p. 113-121.
118. Blackburn S, Wilson DI. Shaping ceramics by plastic processing. Journal of the european Ceramic Society. 2008;28(7):1341-51.
119. Richerson D, Richerson DW, Lee WE. Modern Ceramic Engineering: Properties, Processing, and Use in Design, Third Edition: Taylor & Francis; 2005. Chapter 13, p.447-454.
120. Terpstra RA, Pex P, de Vries A. Ceramic Processing: Springer Netherlands; 2012. Chapter 6, p. 174-194.
121. Bauser M, Siegert K. Extrusion: ASM International; 2006. Chapter 3, p.59-80.
122. Powell J, Blackburn S. Co-extrusion of multilayered ceramic micro-tubes for use as solid oxide fuel cells. 2010.
123. Benbow J. Paste flow and extrusion. In: Bridgwater J, editor. Oxford: Clarendon Press; 1993. p.60-72.
124. Benbow JJ, Oxley EW, Bridgwater J. The extrusion mechanics of pastes—the influence of paste formulation on extrusion parameters. Chemical Engineering Science. 1987;42(9):2151-62.
125. Russell BD, Lasenby J, Blackburn S, Wilson DI. Selection of signal processing techniques for extracting quantitative indicators of paste quality from extrusion data. Chemical Engineering Communications. 2006;193(18):986-1007.
126. Russell BD, Lasenby J, Blackburn S, Wilson DI. A study of surface fracture in paste extrusion using signal processing. Journal of Materials Science. 2006;41(10):2895-906.
127. Stanley-Wood N, Lines RW, Group RSoCPC. Particle Size Analysis: Royal Society of Chemistry; 1992. p. 1-12.
128. Syvitski JPM. Principles, Methods and Application of Particle Size Analysis: Cambridge University Press; 2007. Chapter 1, p. 1-21.
129. Allen T. Particle size measurement.: Springer US; 2013. Chapter 4. p. 133-145.
130. Merkus HG. Particle Size Measurements: Fundamentals, Practice, Quality: Springer Netherlands; 2009. Chapter 10, p. 259-280.
131. Hergert W, Wriedt T. The Mie Theory: Basics and Applications: Springer Berlin Heidelberg; 2012. Chapter 2, p.53-67.
132. Sympatec. Helos Particle size analysis with laser diffraction [cited 2013 Feb 11]. Available from: https://www.sympatec.com/EN/LaserDiffraction/HELOS.html.
133. Beckhoff B, Kanngießer B, Langhoff N, Wedell R, Wolff H. Handbook of Practical X-Ray Fluorescence Analysis: Springer; 2007. Chapter 1, p. 1-26.
134. Lachance GR, Claisse F. Quantitative X-ray fluorescence analysis: theory and application: Wiley; 1995. Chapter 6. p. 168- 194.
135. Haschke M. Laboratory Micro-X-Ray Fluorescence Spectroscopy: Instrumentation and Applications: Springer International Publishing; 2014. Chapter 1, p. 1-14.
136. Van Grieken R, Markowicz A. Handbook of X-Ray Spectrometry, Second Edition: CRC Press; 2001. Chapter 1, p.1-2.
137. Jenkins R. X-Ray Fluorescence Spectrometry: Wiley; 1999. p. 3 -32.
138. Friedbacher G, Bubert H. Surface and Thin Film Analysis: A Compendium of Principles, Instrumentation, and Applications: Wiley; 2011. Chapter 17, p. 267-287.
139. Waseda Y, Matsubara E, Shinoda K. X-Ray Diffraction Crystallography: Introduction, Examples and Solved Problems: Springer Berlin Heidelberg; 2011. Chapter 4, p. 107-126.
140. Warren BE. X-Ray Diffraction: Dover Publications; 2012. Chapter 1, p. 1-14.

141. Zachariasen WH. Theory of X-Ray Diffraction in Crystals: Dover Publications; 2004. Chapter 3, p.83-84.
142. Guinier A. X-Ray Diffraction: In Crystals, Imperfect Crystals, and Amorphous Bodies: Dover Publications; 2013. Chapter 2, p. 27-54.
143. Suryanarayana C, Norton MG. X-Ray Diffraction: A Practical Approach: Springer US; 2013. Chapter 1, p. 3-20.
144. Impact C. Match! [cited 2012 May 22]. Available from: http://www.crystalimpact.com/match/.
145. Egerton R. Physical Principles of Electron Microscopy: An Introduction to TEM, SEM, and AEM: Springer US; 2011. Chapter 1, p.8-21.
146. Hawkes PW, Reimer L. Scanning Electron Microscopy: Physics of Image Formation and Microanalysis: Springer Berlin Heidelberg; 2013. Chapter 1, p.1-12.
147. Khursheed A. Scanning Electron Microscope Optics and Spectrometers: World Scientific; 2011. Chapter 1, p.2-18.
148. Echlin P. Handbook of Sample Preparation for Scanning Electron Microscopy and X-Ray Microanalysis: Springer; 2011. Chapter 2, p. 11-21.
149. Bell D, Garratt-Reed A. Energy Dispersive X-ray Analysis in the Electron Microscope: Taylor & Francis; 2003. p.131-136.
150. Goldstein J, Newbury DE, Joy DC, Lyman CE, Echlin P, Lifshin E, et al. Scanning Electron Microscopy and X-ray Microanalysis: Third Edition: Springer US; 2012. Chapter 1, p. 3- 7.
151. Lyman CE, Newbury DE, Goldstein J, Williams DB, Romig AD, Armstrong J, et al. Scanning Electron Microscopy, X-Ray Microanalysis, and Analytical Electron Microscopy: A Laboratory Workbook: Springer US; 2012. Chapter 8, p. 51-54.
152. Kuo J. Electron Microscopy: Methods and Protocols: Humana Press; 2007. p 468-494.
153. Jones FE, Schoonover RM. Handbook of Mass Measurement: CRC Press; 2002. Chapter 13, p. 137-139.
154. Gupta SV. Practical Density Measurement and Hydrometry: CRC Press; 2002. Chapter 1, p. 2-5.
155. Gupta SV. Mass Metrology: Springer Berlin Heidelberg; 2012. Chapter 9. p. 199- 236.
156. Micromeritics. AccuPyc 1330 Pycnometer operator's manual 2001 [cited 2013 Dec 02]. Available from: https://www.dcu.ie/sites/default/files/mechanical_engineering/images/manual_pycnometer_complete.pdf.
157. da Silva VD. Mechanics and Strength of Materials: Springer Berlin Heidelberg; 2006. Chapter 5, p. 119-140.
158. Kobayashi T. Strength and Toughness of Materials: Springer Japan; 2012. Chapter 3, p. 35-52.
159. Mendes G, Lago B. Strength of Materials: Nova Science Publishers; 2009. Chapter 1, p. 1-15.
160. Rattan SS. Strength of Materials: McGraw-Hill Education (India) Pvt Limited; 2008. Chapter 5, p. 129-130.
161. Den Hartog JP. Advanced Strength of Materials: Dover Publications; 2014. Chapter 6, P. 171-211.
162. Bansal RK. Engineering Mechanics and Strength of Materials: Laxmi Publications; 2005. Chapter 14, p. 489-492.
163. Hosford WF. Mechanical Behavior of Materials: Cambridge University Press; 2005. Chapter 1, p. 29-43.
164. Chawla KK. Composite Materials: Science and Engineering: Springer New York; 2013. Chapter 2, p. 7-10.

165. Hodgkinson JM. Mechanical Testing of Advanced Fibre Composites: CRC Press; 2000. Chapter 8, p. 161-172.
166. Lara-Curzio E, Readey MJ. 28th International Conference on Advanced Ceramics and Composites B: Ceramic Engineering and Science Proceedings, Volume 25: Wiley; 2009. p. 122.
167. Börger A, Supancic P, Danzer R. The ball on three balls test for strength testing of brittle discs: Part II: analysis of possible errors in the strength determination. Journal of the European Ceramic Society. 2004;24(10–11):2917-28.
168. Börger A, Supancic P, Danzer R. The ball on three balls test for strength testing of brittle discs: stress distribution in the disc. Journal of the European Ceramic Society. 2002;22(9–10):1425-36.
169. Singh D, Salem J, Kirihara S, Widjaja S. Mechanical Properties and Performance of Engineering Ceramics and Composites VIII: Ceramic Engineering and Science Proceedings, Volume 34: Wiley; 2013. p.300-311.
170. ISFK. Ball on 3 Balls Test (web-App) 2011 [cited 2014 Mar 11]. Available from: http://wm.unileoben.ac.at:8080/webMathematica/ISFK/B3B_strength_webApp.jsp.
171. Jeong SM, Park SE, Lee HL. Fracture behaviour of alumina ceramics by biaxial ball-on-3-ball test. Journal of the European Ceramic Society. 2002;22(7):1129-35.
172. Shackelford JF, Han YH, Kim S, Kwon SH. CRC Materials Science and Engineering Handbook, Fourth Edition: CRC Press; 2015. p. 132-133.
173. Zhou Y, Yang L, Huang Y. Micro- and Macromechanical Properties of Materials: Taylor & Francis; 2013.
174. Herrmann K. Hardness Testing: Principles and Applications: ASM International; 2011. Chapter 1, p.1-20.
175. Chandler H, International A. Hardness Testing, 2nd Edition: ASM International; 1999. Chapter 1, p. 1-13.
176. Gilmore C. Materials Science and Engineering Properties, SI Edition: Cengage Learning; 2014. Chapter 6, p. 274-277.
177. Sharpe WN. Springer Handbook of Experimental Solid Mechanics: Springer; 2008. Chapter 4, p.97-121.
178. Wikipedia. Toughness 2011 [cited 2014 Jul 21]. Available from: https://en.wikipedia.org/wiki/Toughness.
179. Wunderlich B. Thermal Analysis of Polymeric Materials: Springer; 2005. Chapter 4, p. 279-303.
180. Krishnan RS, Srinivasan R, Devanarayanan S, Pamplin BR. Thermal Expansion of Crystals: International Series in The Science of The Solid State: Elsevier Science; 2013. Chapter 3, p. 54-103.
181. Bach H. Low Thermal Expansion Glass Ceramics: Springer Berlin Heidelberg; 2013. Chapter 1, p. 1-3.
182. Sibilia JP. A Guide to Materials Characterization and Chemical Analysis: Wiley; 1996. Chapter 13, p. 329-334.
183. Menard KP. Dynamic Mechanical Analysis: A Practical Introduction, Second Edition: CRC Press; 2008. Chapter 4, p.57-68.
184. NETZSCH. Operating Instructions DIL 402 PC [cited 2015 Apr 03]. Available from: https://www.dcu.ie/sites/default/files/mechanical_engineering/images/Manual_DIL402PC_e.pdf.
185. Höhne G, Hemminger WF, Flammersheim HJ. Differential Scanning Calorimetry: Springer Berlin Heidelberg; 2013. Chapter 3, p 31-63.
186. Bershteĭn VA, Egorov VM. Differential Scanning Calorimetry of Polymers: Physics, Chemistry, Analysis, Technology: Ellis Horwood; 1994. Chapter 1,p. 2-19.
187. Speyer R. Thermal Analysis of Materials: Taylor & Francis; 1993. Chapter 3, p.35-80.

188. Reading M, Hourston DJ. Modulated Temperature Differential Scanning Calorimetry: Theoretical and Practical Applications in Polymer Characterisation: Springer Netherlands; 2006. Chapter 1, p. 1-13.
189. Brown ME. Handbook of Thermal Analysis and Calorimetry: Principles and Practice: Elsevier Science; 1998. Chatper 2, p.136- 143.
190. Schneider GA, Petzow G. Thermal Shock and Thermal Fatigue Behavior of Advanced Ceramics: Springer Netherlands; 2013. Chapter 1, p. 3- 32.
191. Wirtz OM. Thermal Shock Behaviour of Different Tungsten Grades under Varying Conditions: Forschungszentrum Jülich, Zentralbibliothek; 2012. Chapter 2, p. 25-32.
192. Stuart. Hotplate stirrers, digital, CD162, SD162 [cited 2015 May 20]. Available from: http://www.stuart-equipment.com/product.asp?dsl=153.
193. Kenkel J. Analytical Chemistry for Technicians, Fourth Edition: Taylor & Francis; 2013. Chapter 5, p. 113-120.
194. Gao S, Ye X, Chu Y, Dong M. Effects of biological soil crusts on profile distribution of soil water, organic carbon and total nitrogen in Mu Us Sandland, China. Journal of Plant Ecology. 2010;3(4):279-84.
195. Sohn HY, Wadsworth ME. Rate Processes of Extractive Metallurgy: Springer US; 2013. Chapter 3, p.133-135.
196. McKetta JJ. Encyclopedia of Chemical Processing and Design: Volume 60 - Uranium Mill Tailing Reclamation in the U.S. and Canada to Vacuum System Design: Taylor & Francis; 1997. p. 249-279.
197. Dow. METHOCEL Cellulose Ethers thechnical handbook 2002 [cited 2014 Aug 16]. Available from: http://www.dow.com/dowwolff/en/pdf/192-01062.pdf.
198. Blackburn S. Personal Communication. In: Xie Y, editor. 2015.
199. Weissermel K, Arpe HJ. Industrial Organic Chemistry: Wiley; 2008. Chapter 10, p. 237-264.
200. Kuraray. Mowital B 30 H 2010 [cited 2014 Oct 20]. Available from: https://www.ulprospector.com/en/eu/Coatings/Detail/2676/47033/MOWITAL-B-30-H.
201. Kuraray. Mowital B 60 H 2010 [cited 2014 Oct 20]. Available from: https://www.ulprospector.com/en/na/Coatings/Detail/1414/47038/MOWITAL-B-60-H.
202. Abrar A, Zhang D, Su B, Button T, Kirk KJ, Cochran S. 1-3 connectivity piezoelectric ceramic-polymer composite transducers made with viscous polymer processing for high frequency ultrasound. Ultrasonics. 2004;42(1-9):479-84.
203. Wildman RD. Breakdown of Agglomerates in paste flow / by Ricky Darren Wildman. Birmingham: Thesis (Ph.D) - University of Birmingham, IRC in Materials for High Performance Applications, Faculty of Engineering, 1998.; 1997.
204. Wilson PJ. Investigating the formulation of silica-based ceramic core materials for investment casting / by Paul James Wilson. Birmingham: Thesis (Eng.D.)--University of Birmingham, School of Chemical Engineering, 2011.; 2010.
205. Bhattacharjee S, Singh SK, Galgali RK. Preparation of zirconia toughened mullite by thermal plasma. Materials Letters. 2000;43(1):77-80.
206. Liu W, Li H, Xin YJ. Properties of zirconia-toughened mullite ceramics improved by B2O3 additive. Journal of Materials Science. 1997;32(8):2151-4.
207. Yuan Qm, Tan Jq, Jin Zg. Preparation and Properties of Zirconia‐Toughened Mullite Ceramics. Journal of the American Ceramic Society. 1986;69(3):265-7.
208. Bhattacharjee S, Galgali R, Singh S. Preparation of zirconia-toughened mullite with dissociated zircon. Littleton2001. p. 200.
209. Pena P, Moya J, Aza S, Cardinal E, Cambier F, Leblud C, et al. Effect of magnesia additions on the reaction sintering of zircon/alumina mixtures to produce zirconia toughened mullite. Journal of Materials Science Letters. 1983;2(12):772-4.

210. Andrews MJ, Ferber MK, Lara-Curzio E. Mechanical properties of zirconia-based ceramics asfunctions of temperature. Journal of the European Ceramic Society. 2002;22(14):2633-9.
211. Green DJ. An Introduction to the Mechanical Properties of Ceramics: Cambridge University Press; 1998. Chapter 9, p. 285-290.
212. Insaco. The forms and phases of zirconia engineering ceramics that lead to high strength and toughness 2013 [cited 2015 Sep 22]. Available from: http://www.azom.com/article.aspx?ArticleID=5780.
213. Sahnoune F, Saheb N. Mechanical behavior of mullite-zirconia composites. EPJ Web of Conferences. 2010;6:20005.
214. Severin KP. Energy Dispersive Spectrometry of Common Rock Forming Minerals: Springer Netherlands; 2008. Chapter 2, p. 15-24.
215. Drazin JW, Castro RHR. Phase Stability in Nanocrystals: A Predictive Diagram for Yttria–Zirconia. Journal of the American Ceramic Society. 2015;98(4):1377-84.
216. Gilbert A, Kokini K, Sankarasubramanian S. Thermal fracture of zirconia–mullite composite thermal barrier coatings under thermal shock: An experimental study. Surface & Coatings Technology. 2008;202(10):2152-61.
217. Patnaik P. Handbook of Inorganic Chemicals: McGraw-Hill; 2003. p.328-337
218. Kock LD, Lekgoathi MDS, Snyders E, Wagener JB, Nel JT, Havenga JL. The determination of percentage dissociation of zircon (ZrSiO 4) to plasma ‐ dissociated zircon (ZrO 2 . SiO 2) by Raman spectroscopy. Journal of Raman Spectroscopy. 2012;43(6):769-73.
219. Yugeswaran S, Ananthapadmanabhan PV, Lusvarghi L. Zircon dissociation in air plasma through a low power transferred arc plasma torch. Ceramics International. 2014;41(1):265-73.
220. TOSOH. Environmentally friendly products with superior grinding efficiency [cited 2015 Nov 28]. Available from: http://www.tosoh.com/our-products/advanced-materials/zirconia-grinding--dispersion-media.
221. Smith RM. Chemical Process: Design and Integration: Wiley; 2005. p. 258.

APPENDIX A: DETAILS OF REFRACTORY PRODUCT SYSTEM

Product Number	Name	Type	Raw Materials	Powder Processing	Sintering (heating rate)
1	PA1600 (BIP)	Compact Pellet	Alumina	Ball milled in isopropanol	1600 ℃ (10 ℃·min^{-1})
2	PYTZ1600 (BIP)	Compact Pellet	Yttria +Zirconia	Ball milled in isopropanol	1600 ℃ (10 ℃·min^{-1})
3	PCA1600 (BIP)	Compact Pellet	Ceramic Waste + Alumina	Ball milled in isopropanol	1600 ℃ (3 ℃·min^{-1})
4	PCA1600 (BIP)	Compact Pellet	Ceramic Waste + Alumina	Ball milled in isopropanol	1600 ℃ (5 ℃·min^{-1})
5	PCA1685 (AWP)	Compact Pellet	Ceramic Waste + Alumina	Attrition milled in water	1685 ℃ (10 ℃·min^{-1})
6	PCA1685 (BWP)	Compact Pellet	Ceramic Waste + Alumina	Ball milled in water	1685 ℃ (10 ℃·min^{-1})
7	PCA1685 (AIP)	Compact Pellet	Ceramic Waste + Alumina	Attrition milled in isopropanol	1685 ℃ (10 ℃·min^{-1})
8	PCA1685 (BIP)	Compact Pellet	Ceramic Waste + Alumina	Ball milled in isopropanol	1685 ℃ (10 ℃·min^{-1})
9	PSA1685 (AWP)	Compact Pellet	Silica + Alumina	Attrition milled in water	1685 ℃ (10 ℃·min^{-1})
10	PSA1685	Compact	Silica + Alumina	Ball milled in	1685 ℃

	(BWP)	Pellet		water	(10 °C·min^{-1})
11	PSA1685 (AIP)	Compact Pellet	Silica + Alumina	Attrition milled in isopropanol	1685 °C (10 °C·min^{-1})
12	PSA1685 (BIP)	Compact Pellet	Silica + Alumina	Ball milled in isopropanol	1685 °C (10 °C·min^{-1})
13	PZA1685 (AWP)	Compact Pellet	Zircon + Alumina	Attrition milled in water	1685 °C (10 °C·min^{-1})
14	PZA1685 (BWP)	Compact Pellet	Zircon + Alumina	Ball milled in water	1685 °C (10 °C·min^{-1})
15	PZA1685 (AIP)	Compact Pellet	Zircon + Alumina	Attrition milled in isopropanol	1685 °C (10 °C·min^{-1})
16	PZA1685 (BIP)	Compact Pellet	Zircon + Alumina	Ball milled in isopropanol	1685 °C (10 °C·min^{-1})
17	PCA1600 (AWP)	Compact Pellet	Ceramic Waste + Alumina	Attrition milled in water	1600 °C (10 °C·min^{-1})
18	PCA1600 (BWP)	Compact Pellet	Ceramic Waste + Alumina	Ball milled in water	1600 °C (10 °C·min^{-1})
19	PCA1600 (BIP)	Compact Pellet	Ceramic Waste + Alumina	Ball milled in isopropanol	1600 °C (10 °C·min^{-1})
20	PCA1600 (AIP)	Compact Pellet	Ceramic Waste + Alumina	Attrition milled in isopropanol	1600 °C (10 °C·min^{-1})
21	PSA1600	Compact Pellet	Silica + Alumina	Attrition milled in water	1600 °C (10 °C·min^{-1})

	(AWP)				
22	PSA1600 (BWP)	Compact Pellet	Silica + Alumina	Ball milled in water	1600 °C (10 °C·min^{-1})
23	PSA1600 (AIP)	Compact Pellet	Silica + Alumina	Attrition milled in isopropanol	1600 °C (10 °C·min^{-1})
24	PSA1600 (BIP)	Compact Pellet	Silica + Alumina	Ball milled in isopropanol	1600 °C (10 °C·min^{-1})
25	PZA1600 (AWP)	Compact Pellet	Zircon + Alumina	Attrition milled in water	1600 °C (10 °C·min^{-1})
26	PZA1600 (BWP)	Compact Pellet	Zircon + Alumina	Ball milled in water	1600 °C (10 °C·min^{-1})
27	PZA1600 (AIP)	Compact Pellet	Zircon + Alumina	Attrition milled in isopropanol	1600 °C (10 °C·min^{-1})
28	PZA1600 (BIP)	Compact Pellet	Zircon + Alumina	Ball milled in isopropanol	1600 °C (10 °C·min^{-1})
29	EWH1685 (AWP)	Extrusion Rod	Water Based Paste	Attrition milled in water	1685 °C (10 °C·min^{-1})
30	EWH1600 (AWP)	Extrusion Rod	Water Based Paste	Attrition milled in water	1600 °C (10 °C·min^{-1})
31	EOH1685 (AWP)	Extrusion Rod	Organic Based Paste	Attrition milled in water	1685 °C (10 °C·min^{-1})
32	EOH1600 (AWP)	Extrusion Rod	Organic Based Paste	Attrition milled in water	1600 °C (10 °C·min^{-1})
33	EWI1685 (BIP)	Extrusion Rod	Water Based Paste	Ball milled in isopropanol	1685 °C (10 °C·min^{-1})

34	EWI1600 (BIP)	Extrusion Rod	Water Based Paste	Ball milled in isopropanol	1600 ℃ (10 ℃·min^{-1})
35	PCAY1600 (BIP)	Compact Pellet	Ceramic Waste + Alumina + Yttria	Ball milled in isopropanol	1600 ℃ (10 ℃·min^{-1})
36	PCA1540 (BIP)	Compact Pellet	Ceramic Waste + Alumina	Ball milled in isopropanol	1540 ℃ (10 ℃·min^{-1})

APPENDIX B: DENSITY AND FLEXURAL STRENGTH OF REFRACTORY PRODUCTS

Product Number	Name	Average Apparent Density ($kg \cdot m^{-3}$)	Average Flexural Strength (MPa)	Sintering (heating rate)
1	PA1600 (BIP)	3880	377.3	1600 °C ($10\ °C \cdot min^{-1}$)
2	PYTZ1600 (BIP)	5980	897.1	1600 °C ($10\ °C \cdot min^{-1}$)
3	PCA1600 (BIP)	3578	347.7	1600 °C ($3\ °C \cdot min^{-1}$)
4	PCA1600 (BIP)	3581	349.1	1600 °C ($5\ °C \cdot min^{-1}$)
5	PCA1685 (AWP)	3497	137.3	1685 °C ($10\ °C \cdot min^{-1}$)
6	PCA1685 (BWP)	3304	97.0	1685 °C ($10\ °C \cdot min^{-1}$)
7	PCA1685 (AIP)	3503	105.4	1685 °C ($10\ °C \cdot min^{-1}$)
8	PCA1685 (BIP)	3470	100.2	1685 °C ($10\ °C \cdot min^{-1}$)
9	PSA1685	2246	70.6	1685 °C

	(AWP)			(10 °C·min^{-1})
10	PSA1685 (BWP)	2231	58.2	1685 °C (10 °C·min^{-1})
11	PSA1685 (AIP)	n/a	n/a	1685 °C (10 °C·min^{-1})
12	PSA1685 (BIP)	2281	59.8	1685 °C (10 °C·min^{-1})
13	PZA1685 (AWP)	3535	85.0	1685 °C (10 °C·min^{-1})
14	PZA1685 (BWP)	3465	82.2	1685 °C (10 °C·min^{-1})
15	PZA1685 (AIP)	n/a	n/a	1685 °C (10 °C·min^{-1})
16	PZA1685 (BIP)	3380	135.5	1685 °C (10 °C·min^{-1})
17	PCA1600 (AWP)	3459	253.6	1600 °C (10 °C·min^{-1})
18	PCA1600 (BWP)	3505	246.0	1600 °C (10 °C·min^{-1})
19	PCA1600 (BIP)	3580	349.8	1600 °C (10 °C·min^{-1})
20	PCA1600 (AIP)	3576	321.3	1600 °C (10 °C·min^{-1})

21	PSA1600 (AWP)	2189	65.3	1600 °C (10 °C·min^{-1})
22	PSA1600 (BWP)	2145	67.5	1600 °C (10 °C·min^{-1})
23	PSA1600 (AIP)	n/a	n/a	1600 °C (10 °C·min^{-1})
24	PSA1600 (BIP)	2220	62.4	1600 °C (10 °C·min^{-1})
25	PZA1600 (AWP)	2891	123.7	1600 °C (10 °C·min^{-1})
26	PZA1600 (BWP)	2866	112.4	1600 °C (10 °C·min^{-1})
27	PZA1600 (AIP)	n/a	n/a	1600 °C (10 °C·min^{-1})
28	PZA1600 (BIP)	2950	145.2	1600 °C (10 °C·min^{-1})
29	EWH1685 (AWP)	3502	110.3	1685 °C (10 °C·min^{-1})
30	EWH1600 (AWP)	3450	196.4 ± 22.37	1600 °C (10 °C·min^{-1})
31	EOH1685 (AWP)	3487	144.7	1685 °C (10 °C·min^{-1})
32	EOH1600 (AWP)	3420	172.2	1600 °C (10 °C·min^{-1})

33	EWI1685 (BIP)	n/a	n/a	1685 ℃ (10 ℃·min^{-1})
34	EWI1600 (BIP)	3520	296.9 ± 21.74	1600 ℃ (10 ℃·min^{-1})
35	PCAY1600 (BIP)	3590	215.0 ± 23.80	1600 ℃ (10 ℃·min^{-1})
36	PCA1540 (BIP)	3240	283.8 ± 20.65	1540 ℃ (10 ℃·min^{-1})